CIVIL ENGINEERING JOURNAL

číslo 1/2026

Obsah:

1	**THE IMPACT OF MACROECONOMIC AND POLITICAL STABILITY ON NUCLEAR POWER PLANT CONSTRUCTION DURATION: DEVELOPMENT AND APPLICATION OF THE MAPSS INDEX** *Petr Talášek*
2	**NEGATIVE MOMENT ZONE IN UHPC-STRENGTHENED SIMPLY-SUPPORTED-TO-CONTINUOUS CONCRETE BOX BEAMS: CRACKING RESISTANCE ANALYSIS** *Junming Huang, Kexin Zhang, Jiaqi Qiu*
3	**DECISION-MAKING OF ECOLOGICAL SLOPE PROTECTION SCHEME BASED ON IMPROVED FUZZY SET PAIR ANALYSIS** *Xiansheng Duan, Ming Zhang, Runjuan Zhou, Yingke Sun*
4	**REGARDING SEVERAL NEW CRITERIA FOR THE ENERGY-EFFICIENT ENVELOPE¨’S POTENTIAL ASSESMENT** *Yuriy Biks, Georgiy Ratushnyak, Olga Ratushnyak*
5	**FUNDAMENTAL FREQUENCY VARIATION ANALYSIS OF CABLE-STAYED BRIDGES WITH DAMAGE CAUSED BY SUDDEN INCIDENTS** *Dandan Hu, Baozhen Yan*
6	**BONDING PROCEDURES, ARTIFICIAL AGEING AND THEIR EFFECT ON THE DURABILITY OF GLASS-TO-GLASS ADHESIVE JOINTS** *Markéta Zikmundová, Martina Eliášová, Klára V. Machalická*
7	**UNIAXIAL COMPRESSION PERFORMANCE OF ECC BASED ON NUMERICAL SIMULATION** *Zhao Jun, Yuxin Xie, Shangxin Zhang, Chunling Yan, Hongbo Xiao, Songqiang Wan, Jingli Yang, Chenjie Hao, Junhua Guo, Xingyao Wang, Chongjin Li, Han Song, Long Liu*
8	**COMPARISON OF RENOVATION AND REPLACEMENT STRATEGIES FOR IMPROVING THE THERMAL PERFORMANCE OF HISTORIC BOX-TYPE WINDOWS IN 19TH-CENTURY APARTMENT BUILDINGS** *Klára Kroftová, David Skála*
9	**CHARACTERISTICS OF INCINERATION BOTTOM ASH AS A POTENTIAL SUBSTITUTE FOR AGGREGATES AND CEMENT** *Dr.Yongzhen Cheng, Weiye Mu, Dr. Baoliang Li, Mengdi Zhou*
10	**FINITE ELEMENT ANALYSIS OF BONDED PRESTRESSED STRENGTHENED HOLLOW SLAB BEAMS** *Xilong Zheng*

Article no. 1

THE CIVIL ENGINEERING JOURNAL 1-2026

THE IMPACT OF MACROECONOMIC AND POLITICAL STABILITY ON NUCLEAR POWER PLANT CONSTRUCTION DURATION: DEVELOPMENT AND APPLICATION OF THE MAPSS INDEX

Petr Talášek

Czech Technical University in Prague, Faculty of Civil Engineering, Thákurova 7, 166 29 Prague, Czech Republic; p.talasek@gmail.com

Received:	*10.07.2025*
Received in revised form:	*28.01.2026*
Accepted:	*08.04.2026*

ABSTRACT

This study examines the impact of a country's macroeconomic and political stability on the construction duration of nuclear power plant (NPP) projects. Despite extensive research into technical and managerial causes of delays, the role of national stability remains underexplored. This research develops the Macroeconomic and Political Stability Score (MAPSS), a composite risk assessment index designed to quantify national-level risks affecting project delivery. A stratified sample of 96 NPP projects was analysed using Pearson correlation, Welch's t-tests, and multiple linear regression to evaluate the relationship between key economic indicators, political events, and construction timelines. The results show that national economic crises, international crises, government collapses, and armed conflicts are significantly associated with extended construction durations, whereas factors such as inflation and international sanctions showed no meaningful effect. The MAPSS index demonstrated a statistically significant correlation with project duration ($r = -0.390$, $p < 0.001$), confirming its practical value for early-stage risk assessment. The findings underscore that external macroeconomic and political factors are critical determinants of nuclear project delivery. This research offers a novel framework to support policymakers, investors, and planners in evaluating stability-related risks prior to committing to nuclear infrastructure investments.

KEYWORDS

Nuclear Power Plant, Construction Duration, Macroeconomic Stability, Political Stability, Risk, MAPSS, Project Delay

INTRODUCTION

The global transition towards low-carbon energy sources positions nuclear power at the centre of many national energy strategies due to its capacity to deliver reliable baseload electricity with minimal CO_2 emissions [1]. Nuclear energy is increasingly recognized as a key component of energy security and long-term climate objectives [2]. The successful deployment and continuous innovation of such sustainable energy technologies rely heavily on consistent public funding and aligned strategic policies at both national and supranational levels [3]. Despite this strategic importance, the delivery of new nuclear power plants (NPPs) continues to face persistent challenges

- most notably high capital costs and extended construction durations [4] - which frequently undermine project viability and investor confidence [5]. Given their scale, duration, and stringent safety and quality requirements, contemporary nuclear new-builds occupy the broader class of long-duration infrastructure megaprojects, where schedule performance is pivotal to overall viability. These challenges are compounded by the inherent complexity of nuclear projects.

Prior research on schedule performance in nuclear new builds has predominantly focused on internal project factors and regulatory drivers. Empirical studies link overruns and delays to design quality/changes, documentation and interface management, contractor capability, supply-chain bottlenecks, and project-management discipline, alongside licensing scrutiny and regulatory review cycles [6]. Evidence from the literature consistently highlights organizational and managerial determinants as central drivers of nuclear power plant project performance. Factor-analytic studies identify construction management practices, coordination mechanisms, and the prior experience of contractors and integrated project teams as critical success factors influencing schedule adherence and cost control [7]. Complementary evidence from structured risk-register analyses of U.S. nuclear power plant projects indicates that design-related risks constitute the most frequently occurring and systematically significant risk category, often cascading into additional procurement, rework, and interface management complications during execution [8]. Furthermore, longitudinal analyses of historical cost escalation demonstrate that more than half of observed cost increases can be attributed to management deficiencies, regulatory adaptation challenges, labour productivity shortfalls, and coordination inefficiencies, rather than to the intrinsic cost of reactor technology or major hardware components [9]. Post-accident assessments further anticipate stricter safety requirements and regulatory delays that amplify costs and timelines [10].

In contrast, a smaller but expanding body of work indicates that country-level conditions materially shape delivery risk. Multicriteria assessments for international NPPs rank policy change, political instability, and public intervention among the highest schedule-risk contributors, alongside regulatory approval and incomplete designs [11]. Cross-region analysis of 1955–2016 reactor builds shows discontinuities in both lead time and cost that are country-specific and “induced by national policies and regulatory frameworks,” underscoring macro-institutional influences on delivery performance [12]. Broader megaproject evidence also links outcomes to governance quality and external stakeholder dynamics [13], while comparative risk-management frameworks formalize national-environment risk classes (political/policy, economy/finance, legal, social) and find NPPs exhibit higher risk profiles than fossil/gas projects across the life cycle [14,15]. Program-level SWOT analyses of newcomer nuclear states, such as Ghana’s proposed nuclear energy programme, identify policy discontinuity, governance fragility, institutional capacity gaps, and security vulnerabilities as structural risks that may constrain timely and stable nuclear deployment [16].

Taken together, the literature supports the primacy of internal and regulatory explanations, but it also points to a consequential and uneven macro-political layer that remains underexplored. To address this gap, we propose the Macroeconomic and Political Stability Score (MAPSS), a composite index that integrates continuous macroeconomic indicators with discrete political-event markers to quantify country-level delivery risk. MAPSS provides a systematic way to capture national stability conditions and to test their association with construction duration in nuclear new builds.

The research is guided by the following research questions:

RQ1: To what extent are national macroeconomic and political stability conditions associated with NPP construction duration?
RQ2: Can these conditions be summarised in a composite index (MAPSS) that explains variation in construction duration more effectively than single indicators?
RQ3: Can MAPSS serve as a composite index suitable for early-stage risk screening of NPP projects?

Accordingly, we test the following hypotheses:

H1: Lower national macroeconomic and political stability (lower MAPSS) is associated with longer NPP construction durations.
H2: MAPSS explains significantly more variance in construction duration than any single constituent indicator.
H3: MAPSS demonstrates predictive accuracy consistent with early-stage risk screening.

This study addresses a critical gap in the nuclear project management literature by operationalizing macroeconomic and political stability into a composite, reactor-linked index (MAPSS) and empirically testing its association with construction duration. While prior research has emphasized project-internal and regulatory drivers of delay, systematic quantification of macro-institutional influences remains limited. By introducing and validating MAPSS, the study expands the explanatory framework for nuclear megaproject performance beyond the project boundary.

MATERIALS AND METHODS

Study design

This study employed a quantitative research design to examine whether macroeconomic and political stability during the construction phase is statistically associated with the construction duration of nuclear power plants (NPPs). The objective was to evaluate whether key indicators of national macroeconomic and political stability influence construction duration. The analytical framework was directly aligned with the three research questions outlined in the Introduction.

Data sources

The initial dataset comprised 412 nuclear reactors constructed worldwide between 1968 and 2024, all of which achieved operational status. The dataset was obtained from the Nuclear Planet database [17], an open-access and continuously updated resource that documents the development and operational history of nuclear energy infrastructure worldwide.

The Data Collection Procedure

Data required for the statistical analysis was manually collected through a structured search of official and publicly accessible databases and archives. Economic data was sourced from the World Bank Databank [18], specifically the GDP % annual growth indicator, unemployment and inflation. Political and crisis-related data was obtained from the U.S. Department of State Office of the Historian [19], which documents international crises and geopolitical events, and the U.S. Department of the Treasury's Office of Foreign Assets Control (OFAC) Sanctions List [20], which records international sanctions. Additionally, major economic crises, including the Great Recession, were verified through the Federal Reserve History archives [21]. All collected data was compiled into a structured spreadsheet and rigorously cross-checked to ensure consistency prior to statistical analysis.

Selection criteria

Prior to sample selection, projects lacking essential project-level data were excluded to ensure data completeness and consistency. The inclusion criteria required the availability of the following core project attributes: reactor name, operating country, construction start year, and commercial operation date. The dependent variable—construction duration—was measured in months, calculated from the date of physical construction commencement to the date of first grid connection.

To enable robust statistical analysis, projects were further required to have complete data for the following independent variables covering the entire construction period:

Gross Domestic Product (GDP);
Inflation Rate;
Unemployment Rate;
Economic crisis – International;
Economic crisis – National;
Government Collapse;
International Sanctions;
Armed Conflicts.

As a result of these criteria, 92 projects were excluded for lacking key economic or political data relevant to the construction period. Common reasons included prolonged geopolitical isolation, lack of independent national data during periods of political transition, or unavailability of disaggregated statistics during the Soviet era. After applying all exclusion criteria, the final dataset comprised 320 nuclear reactor projects with complete and analysable data.

From this dataset, a stratified random sample of 30% (n = 96) was selected to ensure proportional representation of projects with short, average, and extended construction durations. Stratification was based on total construction duration (in months), which served as the key variable for defining the strata. This approach balanced representativeness with analytical tractability: while the full dataset of 320 projects was theoretically available, focusing on a 30% stratified subsample preserved proportional representation across short, medium, and long-duration projects while keeping the dataset manageable for detailed manual verification, consistency checks, and cross-referencing of economic and political indicators.

First, the 33rd and 66th percentiles of construction duration were calculated using Microsoft Excel. These thresholds divided the projects into three groups: short, average, and long-duration projects. Each project was then assigned to its respective group. A random number was generated for each project. Within each group, projects were sorted in ascending order based on the generated random numbers, and the top entries corresponding to 30% of each group were selected.

This method ensured a proportionally random selection across the defined strata, preserving the original distribution of construction durations within the sample. All sampling procedures were performed in Microsoft Excel. This transparent, spreadsheet-based approach ensures that the procedure can be directly replicated by other researchers without specialist software.

DEVELOPMENT OF THE MACROECONOMIC AND POLITICAL STABILTY SCORE (MAPSS)

To enable composite analysis and reduce dimensionality among the independent variables, a unified metric—the Macroeconomic and Political Stability Score (MAPSS)—was developed. The MAPSS is an original composite index designed to quantify the level of national macroeconomic and political stability during a nuclear power plant's construction period.

Weighting Scheme

The weighting structure, which assigns the relative impact of individual events on national stability, reflects the theoretical assumption that macroeconomic conditions exert a marginally greater influence on construction timelines than political factors, primarily through effects on financing conditions, labor markets, and supply chain stability [22]. Nevertheless, political events—such as regime changes, sanctions, or armed conflicts—can trigger immediate, acute disruptions that are not necessarily preceded by economic signals [5,23].

Accordingly, the MAPSS framework distinguishes between two categories of indicators:

Continuous macroeconomic indicators—GDP growth, inflation, and unemployment—which tend to fluctuate together and collectively represent the underlying economic resilience or vulnerability of a nation; and

Discrete crisis events—government changes, international sanctions, armed conflicts, and national or international financial crises—which represent sudden, severe shocks that can disrupt goods, services, financing, and ultimately hinder national industrial capacity.

This distinction reflects well-documented patterns in economic history. For example, the 1973 oil crisis, 1979 energy crisis, 2008 global financial crisis, and the 2020 COVID-19 pandemic each produced abrupt economic contractions that led to severe supply chain disruptions, labor shortages, and capital constraints affecting infrastructure and energy projects globally [24]. These crises are explicitly included in the dataset used for this study and serve as examples of the kind of acute destabilizing events captured in the MAPSS index.

The selection of weights follows a hybrid approach combining empirical evidence from the dataset with established practices in composite index construction. The weighting is aligned with methodologies employed by international institutions such as the OECD, World Bank, and IAEA [25], where high-impact, low-frequency events—such as armed conflict or government collapse—are retained with substantial weight despite their relatively infrequent occurrence in historical data.

This reflects a widely accepted principle in risk-based composite modelling: low-frequency, high-impact events must be accounted for to preserve the predictive and practical utility of the index. For example, while inflation may exhibit a muted effect on project durations due to mitigation strategies embedded in contractual structures, the occurrence of a national economic crisis or armed conflict has the potential to disrupt construction entirely. Therefore, such discrete but critical variables are weighted comparably to continuous macroeconomic indicators.

The MAPSS is structured as a weighted aggregate of two sub-indices:
Economic Stability Sub-index - total weight 0.55 (55%);
Political Stability Sub-index - total weight = 0.45 (45%).

These two domains are further divided into eight indicators:

Economic Stability Sub-index:
GDP: Growth Rate (average % for duration) - 0.15 (15%) weight;
Inflation Rate (average % for duration) - 0.10 (10%) weight;
Unemployment Rate (average % for duration) - 0.10 (10%) weight;
Economic crisis – International (binary) – 0.10 (10%) weight;
Economic crisis – National (binary) – 0.10 (10%) weight.

Political Stability Sub-index:
Government Changes (binary) - 0.15 (15%) weight;
International Sanctions (binary) - 0.15 (15%) weight;
Armed Conflicts (binary) - 0.15 (15%) weight.

Data Transformation Process

All independent indicators identified in Section 2.4. were normalized or coded onto a standardized scale ranging from 0 (lowest stability) to 1 (highest stability).

Economic Continuous Variables - GDP, Inflation, Unemployment - was transformed using min–max normalization on scale ranging from 0 (lowest stability) to 1 (highest stability) to calculate X_norm:

$$X\_norm = \frac{X - X\_min}{X\_max - X\_min}$$

Where:
X = observed raw value;
X_min and X_max = minimum and maximum values within the dataset.

Economic and Political Binary variables — International Crisis, National Crisis, Government collapse, International sanctions, armed conflicts, and economic crises — were coded as:
1 = Event occurred (instability);
0 = event did not occur (stability).

Directionality was adjusted where necessary, so that lower values for negative factors (e.g., inflation, unemployment) corresponded to higher stability scores:
X_inv = 1 - X_norm.

Formula for MAPSS

The following outlines the computational hierarchy:
MAPSS = Economic Sub-Index + Political Sub-Index.

Where:
Economic Sub-Index = (0.15 x GDP_norm) + (0.10 x Inflation_norm) + (0.10 x Unemployment_norm) + (0.10 x Economic Crisis - International_norm) + (0.10 x Economic Crisis - National_norm);
Political Sub-Index = [0.15 x (1 – GovCollaps_norm)] + [0.15 x (1 – Sanctions_norm)] + [0.15 x (1 – Conflict_norm)].

Tools and Data Availability

All calculations were performed using Microsoft Excel 365. The Excel workbook used for MAPSS calculation, including all normalization formulas and weighting logic, is uploaded and available at: https://doi.org/10.5281/zenodo.19469868. This choice of platform was made to ensure maximum accessibility and reproducibility, so results can be verified without specialized statistical software.

Reproducibility Statement

All data sources used are publicly accessible. Data availability is unrestricted, and all computation procedures are transparent within the provided supplementary materials. No proprietary or restricted data were used.

ANALYTICAL METHODS

Statistical analysis was performed using Microsoft Excel on the dataset of 96 nuclear power plant (NPP) projects using a combination of Pearson’s correlation coefficient, Welch’s t-test, and multiple linear regression analysis. These methods were employed to investigate the existence and strength of statistically significant relationships between macroeconomic and political stability indicators and the construction duration of NPPs.

Correlation and Group Difference Analysis

Pearson’s correlation analysis was used to assess the direction and magnitude of linear associations between continuous economic indicators—such as GDP growth, inflation, and unemployment—and the construction duration.

Welch's t-test, complemented by Levene's test for homogeneity of variances, was applied to compare mean construction durations across binary categorical variables, including the occurrence of international economic crises, national economic crises, government collapse, international sanctions, and armed conflicts. Cohen's d was calculated to quantify effect sizes for all group comparisons.

Multiple Linear Regression Analysis

A multiple linear regression analysis was conducted to evaluate the combined influence of all independent variables—both continuous and binary—on construction duration. This approach enabled the identification of the most influential predictors while controlling for the effects of other variables. The regression model included GDP growth, inflation, unemployment, international and national economic crises, government collapse, international sanctions, and armed conflicts as predictors.

The statistical significance, direction, and magnitude of each predictor's coefficient were evaluated, along with overall model fit statistics, including R^2 and adjusted R^2. This analysis provided a holistic understanding of how macroeconomic and political stability factors jointly affect project timelines.

Regression Diagnostics

Prior to interpreting the regression results, key assumptions of multiple linear regression were evaluated to ensure the robustness of the analysis:

Multicollinearity: Assessed using Variance Inflation Factors (VIF), with all predictors recording VIF values below 2, indicating no multicollinearity concerns.

Homoscedasticity: Evaluated via residuals vs. fitted values plots, which showed randomly distributed residuals, indicating homoscedasticity was met.

Normality of Residuals: Assessed using histograms and Q–Q plots. Residuals were approximately normally distributed, with minor tail deviations common in applied datasets but not severe enough to undermine model validity.

Independence of Errors: Not deemed critical as the data are cross-sectional, not time-series.

Linearity: Confirmed through preliminary correlation analysis and inspection of residuals, supporting the appropriateness of the linear model form.

MAPSS Validation Analysis

Additionally, the validity of the composite MAPSS score as a predictive metric was assessed using Pearson's correlation analysis and simple linear regression against construction duration. This analysis evaluated the extent to which MAPSS functions as a reliable single-variable predictor of construction delays in NPP projects.

RESULTS

Correlation Between Economic Indicators and Construction Duration

Pearson correlation analysis revealed a moderate but statistically significant negative correlation between gross domestic product (GDP) growth and NPP construction duration ($r = -0.215$, $p = 0.036$), suggesting that higher GDP growth during the construction period was associated with shorter project durations. A simple linear regression yielded a slope of −4.82, an intercept of 115.46, and a coefficient of determination (R^2) of 0.046, indicating only modest explanatory power of GDP alone.

By contrast, Pearson correlation analysis revealed no statistically significant relationship between average inflation during the construction period and NPP construction duration ($r = 0.006$, $p = 0.954$). A simple linear regression confirmed this result, yielding a slope of 0.052, an intercept of

95.36, and an R^2 of 0.000, indicating that inflation exerted no meaningful influence on project duration within the sample.

Similarly, Pearson correlation analysis identified a moderate and statistically significant positive correlation between average unemployment during the construction period and NPP construction duration ($r = 0.226$, $p = 0.027$), indicating that higher unemployment was associated with longer project durations. A simple linear regression yielded a slope of 5.03, an intercept of 67.26, and an R^2 of 0.051, suggesting that unemployment alone accounts for a modest portion of the variability in construction timelines.

Welch's t-test indicated a statistically significant difference in construction durations between projects executed during periods of international economic crisis and those constructed in more stable economic conditions (mean = 102.07 months vs. 71.75 months; $t = 3.20$, $p = 0.002$). Levene's test confirmed that the assumption of equal variances was not violated ($W = 1.88$, $p = 0.173$). The corresponding Cohen's d of 0.622 suggests a moderate effect size, indicating that international economic crises had a meaningful adverse impact on project timelines.

A similar pattern was observed for national economic crises. Welch's t-test revealed a statistically significant difference in construction durations between projects affected by national economic crises and those that were not (mean = 121.3 months vs. 77.5 months; $t = 3.35$, $p = 0.0016$). Levene's test indicated a violation of the assumption of equal variances ($W = 6.03$, $p = 0.016$), justifying the use of Welch's correction. The computed Cohen's d of 0.739 indicates a moderate to large effect size, demonstrating that national economic crises substantially increased project durations.

Impact of Political Disruptions, and Conflict on Construction Duration

In the case of government collapse, Welch's t-test revealed a difference in construction durations that did not reach statistical significance (mean = 122.88 months vs. 86.20 months; $t = 1.81$, $p = 0.082$). Levene's test indicated a significant violation of the equal variance assumption ($W = 8.29$, $p = 0.0049$), warranting the use of Welch's correction. Despite the lack of statistical significance, the computed Cohen's d of 0.497 suggests a moderate effect size, indicating that projects undertaken during periods of government collapse tended to experience longer durations, though this trend was not conclusive within the sample.

In contrast, the analysis revealed no statistically significant relationship between the presence of international sanctions during the construction period and NPP construction duration (mean = 99.65 months vs. 94.30 months; $t = 0.484$, $p = 0.630$). Levene's test indicated that the assumption of equal variances was satisfied ($W = 0.026$, $p = 0.873$). The computed Cohen's d of 0.099 reflects a negligible effect size, suggesting that international sanctions had no observable influence on project timelines within this dataset.

Finally, Welch's t-test demonstrated a statistically significant difference in construction durations between projects affected by armed conflicts and those not affected (mean = 108.00 months vs. 74.40 months; $t = 3.31$, $p = 0.0013$). Levene's test indicated that the assumption of equal variances was not violated ($W = 2.27$, $p = 0.135$). The computed Cohen's d of 0.639 represents a moderate effect size, highlighting that armed conflicts were associated with substantially longer project durations.

Multiple Linear Regression Analysis

To assess the combined influence of all macroeconomic and political stability indicators on NPP construction duration, a multiple linear regression analysis was conducted. The overall model was statistically significant ($F(8, 87) = 3.94$, $p = 0.0005$), explaining 26.6% of the variance in construction duration ($R^2 = 0.266$; adjusted $R^2 = 0.198$).

The results indicated that national economic crises ($\beta = 44.24$, $p = 0.001$) and government (regime) collapse ($\beta = 29.24$, $p = 0.040$) were significant predictors of longer construction durations. A near-significant effect was also observed for international economic crises ($\beta = 29.11$, $p = 0.079$).

Other variables, including GDP growth, inflation, unemployment, international sanctions, and armed conflicts, did not achieve statistical significance in the multivariate model, despite some showing significance in bivariate analyses. This suggests that certain contextual factors—particularly major national-level economic and political disruptions—exert a disproportionately stronger influence on project timelines when considered jointly with other factors.

Composite Stability Index (MAPSS) and Project Duration

Finally, the MAPSS composite index was tested as a single aggregated predictor of construction duration. Pearson correlation analysis revealed a moderate but statistically significant negative correlation between MAPSS and NPP construction duration ($r = -0.390$, $p = 0.000087$), indicating that higher macroeconomic and political stability was associated with shorter project durations. A simple linear regression yielded a slope of −114.46, an intercept of 159.91, and an R^2 of 0.152. This suggests that MAPSS alone explains over 15% of variance in construction duration, outperforming any individual variable. These findings provide initial evidence that MAPSS captures stability-related risks more effectively than single measures and offers preliminary predictive value for early-stage risk screening.

DISCUSSION

The results of this study provide robust empirical evidence within the analysed dataset that macroeconomic and political stability can significantly influence the construction duration of nuclear power plant (NPP) projects. This finding aligns with and extends the existing body of literature, which increasingly acknowledges that the performance of large-scale infrastructure projects depends not only on internal technical and managerial factors but also on broader national and geopolitical conditions [26]. It reinforces the perspective that external contextual factors, often overlooked in traditional project management models, play a critical role in shaping project delivery outcomes [27]. In particular, the results confirm that external crises and instability operate as significant schedule risks, thereby supporting the hypothesis set out in this study.

GDP Growth and Project Duration

A modest but statistically significant negative correlation between GDP growth and construction duration supports the hypothesis that stronger economic performance facilitates more efficient project execution. Economies experiencing continuous growth are typically characterized by higher industrial output, more resilient supply chains, robust labour markets, and reliable access to financing—all of which are critical enablers for delivering capital-intensive, technologically complex projects such as NPP construction. This outcome is consistent with broader infrastructure literature, which links favorable macroeconomic conditions to improved project performance [11]. For instance, the competitiveness and resilience of foundational sectors, such as the steel industry, are closely tied to macroeconomic stability and decarbonization policies, acting as essential prerequisites for the secure material supply chains required in large-scale energy infrastructure [28].

Within the MAPSS index, GDP growth is retained as a continuous stabilizing indicator, reflecting the long-term economic resilience that underpins project delivery.

Unemployment and Project duration

The observed positive correlation between unemployment and construction duration further reinforces this relationship from the inverse perspective. Higher unemployment typically signals broader economic weakness, translating into market uncertainty, reduced investment, labour productivity challenges, and disruptions within critical supply chains.

Within MAPSS, unemployment is retained as a negatively weighted indicator, capturing the vulnerability of projects situated in fragile labour market contexts and constrained industrial environments.

Inflation and Project Duration

By contrast, the analysis revealed no statistically significant relationship between inflation and construction duration. This null result is best explained by the contractual and financial structures characteristic of nuclear megaprojects. Inflationary pressures typically influence financing costs rather than schedules. Risk is mitigated at the contract stage through mechanisms such as forward pricing, escalation clauses, currency hedging, and indexation. These provisions anticipate cost growth over long lifecycles and reduce the likelihood of direct schedule disruption. Thus, while inflation remains a standard macroeconomic indicator, its impact on construction duration appears limited in practice.

Despite the absence of a significant effect, inflation is retained within the MAPSS index to maintain consistency with broader macroeconomic theory, where it remains a standard indicator of economic stability and recessionary risk [29]. Its inclusion ensures that MAPSS remains generalizable beyond the nuclear domain, thereby reinforcing its value as a composite tool for early-stage risk screening.

International Economic Crisis and Project Duration

Projects executed during periods of international economic crisis experienced substantially longer construction durations compared to those constructed under stable economic conditions. The corresponding effect size is consistent with established evidence that systemic downturns constrain liquidity, destabilize supply chains, and heighten uncertainty in capital-intensive megaprojects [30]. Similar findings were observed following the COVID-19 pandemic, where global supply chain disruptions and inflationary pressures caused severe project delays across major infrastructure sectors [31].

Within MAPSS, international crises are retained as discrete, high-impact indicators, complementing the continuous measures of GDP, unemployment, and inflation.

National Economic Crisis and Project Duration

A similar but even more pronounced effect was observed for national economic crises. Projects affected by national-level crises exhibited a mean construction duration of 121.3 months compared to 77.5 months for unaffected projects. These results are consistent with existing literature on megaproject vulnerability under financial distress and highlight how crises at both global and national scales can disrupt supply chains, strain labour markets, and create financing constraints [32].

The comparable magnitude of impact across international and national crises supports their equal weighting in the MAPSS framework. Their inclusion ensures that MAPSS captures both gradual macroeconomic conditions and severe financial shocks, providing a balanced and practical tool for risk assessment in nuclear construction projects.

Government Collapse as Delay Drivers

While government collapse was associated with considerable delays, the finding did not reach conventional statistical significance. This may be attributable to the limited sample size or to the heterogeneity of what constitutes a “collapse,” ranging from transitional governments to full regime breakdowns. Nonetheless, qualitative evidence suggests that such political disruptions can have substantial and long-lasting effects on nuclear project delivery.

A well-documented example of a project affected by full regime collapse is Iran’s Bushehr Nuclear Power Plant, which was originally initiated in the 1970s with German assistance but experienced severe delays following the 1979 Islamic Revolution and the subsequent imposition of international sanctions. The regime change led to the withdrawal of Western contractors and a prolonged construction halt; the project only resumed years later under Russian cooperation and was ultimately completed in 2011—more than three decades after its initial start [3,33]. This case illustrates how profound political transitions can destabilize project governance, financing, and international cooperation, causing multidecade schedule overruns.

Beyond full regime collapse, a broader spectrum of political instability may also contribute to delivery risks. Administrative failures, legislative deadlocks, and frequent leadership turnovers—though less visible than regime change—can similarly delay project approvals and implementation. For instance, the inability of authorities to operationalize newly adopted permitting laws has been shown to prolong construction approvals at the national level [34]. Such forms of governance dysfunction, while short of formal collapse, still represent systemic political instability with tangible effects on project delivery.

Despite the lack of statistical significance within this dataset, the substantial effect size and multiple documented historical examples support the decision to retain government collapse within the MAPSS framework. This aligns with established practices in risk-based modelling, where high-impact but lower-frequency events are incorporated due to their disproportionate potential to disrupt project delivery.

International Sanctions as Delay Drivers

The presence of international sanctions did not exhibit a statistically significant effect on project timelines within this dataset. This finding warrants closer examination, as the consequences of sanctions may operate through mechanisms not fully captured by construction-duration metrics alone. Sanctions can exert delayed or lagged effects, particularly when imposed prior to project initiation, by constraining access to financing, technology transfer, or international partnerships. In such cases, sanctions may inhibit project approval, financial close, or commencement rather than extend duration once physical construction has begun.

Moreover, sanctions vary considerably in severity, scope, and sectoral targeting. Some states may partially offset their effects through alternative suppliers, domestic industrial substitution, or geopolitical realignment, thereby attenuating direct impacts on ongoing construction activities.

Historical evidence nevertheless demonstrates that sanctions can exert profound and prolonged effects under specific conditions. India, for example, faced comprehensive international sanctions following its 1974 nuclear test, resulting in the withdrawal of foreign suppliers and the termination of fuel and technology agreements with Canada and the United States. These measures constrained elements of India’s civilian nuclear programme, including operations at Tarapur, and necessitated the development of indigenous technological capabilities. A subsequent wave of sanctions in 1998 further restricted international cooperation until the early 2000s [35]. This case illustrates that when sanctions directly target nuclear policy and supply chains, they can materially disrupt civilian nuclear infrastructure development.

Therefore, while sanctions did not emerge as a statistically significant determinant of construction duration across the broader sample, their effects may be conditional, temporally lagged, or manifested through project non-initiation or cancellation rather than extended build times. For this reason, international sanctions are retained within the MAPSS framework as a low-frequency but potentially high-impact indicator, consistent with the index’s objective to capture both structural macroeconomic conditions and episodic geopolitical disruptions.

Armed Conflicts as Delay Drivers

Armed conflict emerges as a substantial external determinant of nuclear construction performance. Projects undertaken in conflict-affected environments required, on average, approximately 34 additional months to complete compared with those in stable conditions. This magnitude of delay underscores that geopolitical instability constitutes a material and operationally significant risk factor for nuclear megaproject delivery.

This finding aligns with theoretical expectations and historical evidence. Armed conflicts can disrupt construction directly through physical damage to infrastructure, restrictions on labour mobility, and supply chain interruptions, while also indirectly affecting financing and logistics as national resources are diverted toward defence activities [36]. Even conflicts that occur outside the immediate project area can generate ripple effects through regional instability, trade constraints, and heightened security requirements, collectively extending construction schedules [3].

Historical examples further illustrate this relationship. The construction of Ukraine's Khmelnytskyi and Rivne nuclear power plants experienced significant delays amid the geopolitical turbulence surrounding the collapse of the Soviet Union and later regional conflicts. Similarly, armed conflicts in the Middle East have historically delayed energy infrastructure projects—including nuclear initiatives—through logistical constraints, workforce displacement, and security-related suspensions [37].

Given both the statistical evidence and extensive historical documentation of conflict-induced disruption, armed conflict is retained as a high-impact indicator within the MAPSS framework. Its capacity to halt work, sever supply chains, or necessitate extraordinary security measures justifies its weighting as a critical component of national stability assessment for nuclear construction projects.

Combined effects on Model Interpretation

The multiple linear regression analysis confirmed that not all variables exert independent effects when considered simultaneously. The overall model was statistically significant indicating that approximately 26.6% of the variance in construction duration can be explained by the combined macroeconomic and political stability indicators. Notably, national economic crises and government collapse emerged as the most significant predictors of prolonged construction durations.

Variables that were significant in the bivariate analyses—such as GDP growth, unemployment, and armed conflict—did not achieve significance in the multivariate model, suggesting that their effects may be mediated through or overshadowed by crisis-level disruptions. This finding reinforces the conclusion that acute destabilizing events, rather than gradual economic trends, are among significant drivers of large-scale construction delays [38,39].

MAPSS Index and Practical Implications

The statistically significant correlation between the MAPSS score and construction duration ($r = -0.390$, $p < 0.001$) provides preliminary empirical support for the conceptual validity of this composite index. MAPSS integrates a broad range of macroeconomic and political indicators—continuous measures such as GDP growth and unemployment, together with discrete, event-based risks including economic crises, government collapses, and armed conflicts—into a single stability metric. The negative relationship between MAPSS and project duration indicates that lower national stability scores are associated with longer nuclear power plant construction periods. Although the index explains approximately 15% of the variance in project duration, its performance surpasses that of any single constituent variable, suggesting initial predictive relevance.

MAPSS is intended primarily as an early-stage screening tool for assessing macroeconomic and political risks in nuclear infrastructure projects. It offers decision-makers an objective measure of whether a host country's stability conditions are conducive to successful project execution and can help identify areas where systemic risks require mitigation. By consolidating both structural and event-based risk factors, the MAPSS framework enables transparent risk communication and informed decision-making at the national or intergovernmental level. Even in contexts where projects proceed under suboptimal stability conditions, MAPSS can assist stakeholders in prioritizing mitigation strategies and contingency planning. This aligns with emerging research that integrates composite indices and multidimensional metrics for evaluating systemic risk in infrastructure delivery. Recent frameworks for infrastructure-risk quantification and resilience modelling likewise highlight the value of aggregated indicators for early-stage decision support [40]. Furthermore, the development and application of advanced composite indexing have become a proven methodological standard for comprehensively measuring complex socio-economic parameters, regional development, and national sustainability statuses [41]. Such approaches collectively strengthen the rationale for adopting MAPSS as a standardized screening tool in the nuclear domain.

Limitations and Future Research

This study is subject to several limitations. While the dataset of 96 nuclear power plant projects was carefully compiled and stratified, it represents only a subset of the global fleet. Data availability constrained the inclusion of some projects, particularly in countries with limited transparency or incomplete historical records. As a result, certain geographic regions or political contexts may be underrepresented.

The analysis employs primarily linear modelling techniques. While this approach is appropriate for the study's objectives, more complex methods — including nonlinear models, machine learning algorithms, or stochastic simulations — could be explored in future studies to capture potential interaction effects between variables and improve predictive accuracy.

Future research could also refine and validate the MAPSS framework by testing it against other types of infrastructure megaprojects beyond the nuclear sector, such as renewable energy, transportation, or defence projects. Additionally, longitudinal studies examining how stability conditions evolve throughout the full lifecycle of a project — from planning to commissioning — could offer deeper insights into risk dynamics.

CONCLUSION

This study provides empirical evidence that national macroeconomic and political stability is a material determinant of nuclear power plant (NPP) construction duration and should be treated as a core schedule-risk domain rather than a background contextual condition. Using a stratified sample of 96 reactor projects and complementary bivariate and multivariate tests, the analysis shows that destabilizing shocks—especially national economic crises and severe political disruption—are associated with systematically longer delivery timelines. These results reinforce the view that nuclear new-build performance is shaped not only by project-internal capabilities and regulatory processes, but also by the macro-institutional environment that conditions financing continuity, industrial capacity, supply-chain reliability, and governance stability over extended delivery horizons.

A central contribution of the paper is the development and validation of the Macroeconomic and Political Stability Score (MAPSS), a composite index that integrates continuous economic indicators with low-frequency, high-impact political and crisis events. MAPSS demonstrates a statistically significant association with construction duration ($r = -0.390$, $p < 0.001$) and explains more variance than any single constituent indicator, indicating that the stability environment is better captured as a multidimensional construct than through isolated macroeconomic metrics. While MAPSS is not intended to function as a deterministic forecasting model, its explanatory performance is meaningful in the context of infrastructure megaproject research, where outcomes are typically driven by multicausal and interacting factors. In this setting, even moderate macro-level explanatory power represents substantive insight, because it isolates a systemic layer of risk that is often omitted from conventional project appraisal and schedule-risk baselines.

The findings have direct implications for nuclear investment governance. Because nuclear projects are highly capital intensive, long-duration, and path dependent once construction begins, exposure to instability-related shocks has asymmetric consequences: disruptions can propagate through financing structures, contracting regimes, labour availability, and international supply chains, amplifying delay effects and increasing the probability of schedule collapse. MAPSS offers a transparent and replicable mechanism for incorporating this exposure into early-stage screening, enabling policymakers, investors, and planners to differentiate between host-country contexts where schedule risk is structurally elevated versus those where delivery conditions are comparatively resilient. In practical terms, MAPSS can support portfolio-level siting decisions, the calibration of contingency allowances, and the design of governance safeguards (e.g., staged commitments, enhanced contractual protections, resilience-oriented procurement strategies, and political-risk mitigation instruments).

At the same time, the results should be interpreted as complementary to—rather than substitutive of—project-level explanations. The model explains a substantive but partial share of variance in construction duration, consistent with the established multilevel nature of nuclear project performance. This underscores the need for future research that integrates macro-institutional indicators with project-internal variables (e.g., reactor type, delivery model, supply-chain localization, regulatory regime maturity, and owner/contractor experience), and that tests nonlinearities and interaction effects under compound crises. Further validation on larger samples and across other long-duration infrastructure sectors would also clarify the generalizability and boundary conditions of MAPSS as a stability-risk screening framework.

In conclusion, the study advances nuclear project management and megaproject research by quantifying the macroeconomic and political stability environment as a measurable risk domain and by demonstrating its systematic association with construction duration. By operationalizing national stability conditions into MAPSS, the paper offers a replicable tool and an extended explanatory lens for understanding why delivery performance diverges across countries even under broadly similar technological and regulatory demands. Embedding macro-institutional risk screening within nuclear project appraisal can therefore improve the realism of early schedule baselines, strengthen governance design, and reduce the likelihood that strategic nuclear investment decisions are made without explicit recognition of the stability conditions required for timely delivery.

ACKNOWLEDGEMENTS

The author gratefully acknowledges the financial support for the research that led to this paper that was provided by the Czech Technical University in Prague, Czech Republic, Grant SGS25/081/OHK1/2T/11 Technicko-ekonomická metodika efektivního řízení výstavby nových jaderných zdrojů.

REFERENCES

[1] Sovacool B.K., Schmid P., Stirling A., Walter G., MacKerron G., 2020. Differences in carbon emissions reduction between countries pursuing renewable electricity versus nuclear power. Nature Energy, vol. 5, p. 928–935. https://doi.org/10.1038/s41560-020-00696-3

[2] Hong S., Bradshaw C.J.A., Brook B.W., 2019. Global zero-carbon electricity pathways using nuclear and renewable energy. Energies, vol. 12, p. 3770. https://doi.org/10.3390/en12193770

[3] Kurekova L., Cermakova K., Hromada E., Kaderabkova B., 2023. Public funding in R&D and R&D outcome sustainable development: Analysis of Member States EU. International Journal of Economic Sciences, vol. 12(2), p. 40-62. https://doi.org/10.52950/ES.2023.12.2.003

[4] Sovacool B.K., Gilbert A., Nugent D., 2014. Risk, innovation, electricity infrastructure and construction cost overruns: Testing six hypotheses. Energy, vol. 74, p. 906–917. https://doi.org/10.1016/j.energy.2014.07.070

[5] Benson A.G., 2022. Global divergence in nuclear power plant construction: The role of political decentralization. Nuclear Technology, vol. 208(6), p. 947–989. https://doi.org/10.1080/00295450.2021.1991762

[6] Lovering J.R., Yip A., Nordhaus T., 2016. Historical construction costs of global nuclear power reactors. Energy Policy, vol. 91, p. 371–382. https://doi.org/10.1016/j.enpol.2016.01.011

[7] Wright J., Cho C.-S., Hastak M., 2014. Assessment of Critical Construction Engineering and Management Aspects of Nuclear Power Projects. Journal of Construction Engineering and Management, vol. 140, p. 04014020. https://doi.org/10.1061/(ASCE)CO.1943-7862.0000872
[8] Sherman J., Parrish K., Lamanna C., 2017. Identifying and Categorizing Risks Incumbent in US NPP Construction. Journal of Construction Engineering and Management, vol. 143, p. 04017070. https://doi.org/10.1061/(ASCE)CO.1943-7862.0001369
[9] Eash-Gates P., Petroski H., Buongiorno J., Trancik J.E., 2020. Sources of Cost Overrun in Nuclear Power Plant Construction: Call for a New Approach to Engineering Design. Joule, vol. 4, p. 1575–1599. https://doi.org/10.1016/j.joule.2020.05.018
[10] Kessides I.N., 2012. The future of the nuclear industry reconsidered: Risks, uncertainties, and continued promise. Energy Policy, vol. 48, p. 185–208. https://doi.org/10.1016/j.enpol.2012.05.008
[11] Hossen T., Kang H.-S., Kim J.-M., 2015. Construction Schedule Delay Risk Assessment by Using Combined AHP–RII Methodology for an International NPP Project. Nuclear Engineering and Technology, vol. 47, p. 362–379. https://doi.org/10.1016/j.net.2015.01.008
[12] Portugal-Pereira J., Szklo A., Soria R., Schaeffer R., Lucena A.F.P., Szklo A.S., Rathmann R., 2018. Better Late than Never, but Never Late Is Better: Risk Assessment of Nuclear Power Construction Projects. Energy Policy, vol. 120, p. 158–170. https://doi.org/10.1016/j.enpol.2018.05.029
[13] Brookes N.J., Locatelli G., 2015. Power Plants as Megaprojects: Using Empirics to Shape Policy, Planning, and Construction Management. Utilities Policy, vol. 36, p. 57–66. https://doi.org/10.1016/j.jup.2015.09.005
[14] Kim J.-H., Lee S.-W., Jung W., 2017. International Project Risk Management for Nuclear Power Plant Construction Featuring Comparative Analysis with Fossil and Gas Power Plants. Sustainability, vol. 9, p. 1735. https://doi.org/10.3390/su9101735
[15] Escobar-Rangel L., Lévêque F., 2015. Nuclear power plant construction costs: Regulation and innovation. Energy Policy, vol. 82, p. 118–130. https://doi.org/10.1016/j.enpol.2015.02.019
[16] Agyekum E.B., Amponsah O., Aboagye E., 2020. Nuclear Energy for Sustainable Development: SWOT Analysis on Ghana's Nuclear Agenda. Energy Reports, vol. 6, p. 107–115. https://doi.org/10.1016/j.egyr.2019.11.140
[17] Nuclear Planet, 2025. Nuclear Power Plants Database [online]. [cit. 2025-06-25]. Available from: https://app.nuclearplanet.ch/nuclearplanet/kkw-world
[18] The World Bank, 2025. World Development Indicators: GDP Growth (Indicator: NY.GDP.MKTP.KD.ZG) [online]. [cit. 2025-06-25]. Available from: https://databank.worldbank.org/indicator/NY.GDP.MKTP.KD.ZG
[19] U.S. Department of State, Office of the Historian, 2025. Foreign Relations of the United States [online]. [cit. 2025-06-25]. Available from: https://history.state.gov/
[20] U.S. Department of the Treasury, Office of Foreign Assets Control (OFAC), 2025. Sanctions List Service (SLS) [online]. [cit. 2025-06-25]. Available from: https://ofac.treasury.gov/sanctions-list-service
[21] Federal Reserve History, 2025. The Great Recession and Its Aftermath [online]. [cit. 2025-06-25]. Available from: https://www.federalreservehistory.org/essays/great-recession-and-its-aftermath
[22] Ahiaga-Dagbui D.D., Smith S.D., Love P.E.D., Ackermann F., 2017. Toward a systemic view to cost overrun causation in infrastructure projects: A review and implications for research. Project Management Journal, vol. 48, p. 88–98. https://doi.org/10.1177/875697281704800107
[23] Locatelli G., Invernizzi D.C., Brookes N.J., Meredith J., 2017. Managing the project finance risks of nuclear power plants: Lessons from the UK. International Journal of Project Management, vol. 35, p. 552–566. https://doi.org/10.1016/j.ijproman.2016.12.003
[24] Hannon M., Bolton R., Martiskainen M., 2021. The Covid-19 crisis: Agility and sustainability in the energy sector. Energy Research & Social Science, vol. 69, p. 101718. https://doi.org/10.1016/j.erss.2020.101718
[25] OECD, 2003. Emerging Risks in the 21st Century: An Agenda for Action. OECD Publishing: Paris, France. https://doi.org/10.1787/9789264101227-en
[26] Ansar A., Flyvbjerg B., Budzier A., Lunn D., 2014. Should we build more large dams? The actual costs of hydropower megaproject development. Energy Policy, vol. 69, p. 43–56. https://doi.org/10.1016/j.enpol.2013.10.069

[27] Li Y., Guo F., Zhang L., Chen S., 2020. Investigating the Impact of Governmental Governance on Megaproject Performance: Evidence from China. Technological and Economic Development of Economy, vol. 26, p. 1134–1155. https://doi.org/10.3846/tede.2020.11334
[28] Hromada E., Cermakova K., Kaderabkova B., Kurekova L., Krasnicka M., 2025. Strategic Challenges and Opportunities for the Czech Steel Industry: A Path Toward Sustainable Competitiveness. International Journal of Economic Sciences, vol. 14(1), p. 333-350. https://doi.org/10.31181/ijes1412025207
[29] Blanchard O., Johnson D.R., 2017. Macroeconomics, 7th ed., Pearson: Harlow, UK.
[30] Flyvbjerg B., 2023. How Big Things Get Done. Currency: New York, NY, USA.
[31] Alsharef A., Banerjee S., Uddin S.M.J., Albert A., 2023. Analyzing the Factors Affecting Construction Project Schedules amidst COVID-19 Pandemic. Plast. Res., vol. 3, p. 100100.
[32] Flyvbjerg B., 2014. What You Should Know About Megaprojects and Why: An Overview. Project Management Journal, vol. 45, p. 6–19. https://doi.org/10.1002/pmj.21409
[33] Ramana M.V., 2009. Nuclear power in the Persian Gulf: Implications for Iran and the UAE. Bulletin of the Atomic Scientists, vol. 65, p. 38–49. https://doi.org/10.2968/065004007
[34] Reuters, 2024. Czech PM dismisses outgoing junior party chief from cabinet. Reuters, 24 September 2024 [online]. [cit. 2025-07-01]. Available from: https://www.reuters.com/world/europe/czech-pm-dismisses-outgoing-junior-party-chief-cabinet-2024-09-24
[35] Ramana M.V., 2007. India’s nuclear energy program: Past, present, and future. Annual Review of Environment and Resources, vol. 32, p. 285–310. https://doi.org/10.1146/annurev.energy.32.053006.141535
[36] Saqib M., Alqurashi M., Alhammadi Y., Khan K., 2023. The Construction Industry in a War-Ravaged Region: Examination of Challenging Factors. Applied Sciences, vol. 15, p. 2900. https://doi.org/10.3390/app15062900
[37] Bazilian M., Sovacool B.K., Miller M., Rogner H., Mulvaney D., Jacome G., Peak R., 2014. Energy resources and the geopolitics of conflict. Energy Policy, vol. 68, p. 654–667. https://doi.org/10.1016/j.enpol.2013.10.056
[38] Mahmood S., Sun H., Abdein M.A., Qadri S.U., Iqbal A., Abdelkader M.F.M., Mahmoud M.H., Hewedy O., 2023. Exploring the China-Pakistan Economic Corridor project performance during Covid-19 pandemic. Heliyon, vol. 9(12), p. e22835. https://doi.org/10.1016/j.heliyon.2023.e22835
[39] Ling F.Y.Y., Zhang Z., Yew A.Y.R., 2022. Impact of COVID-19 Pandemic on Demand, Output, and Outcomes of Construction Projects in Singapore. Journal of Management in Engineering, vol. 38(2), p. 04021097. https://doi.org/10.1061/(ASCE)ME.1943-5479.0001020
[40] OECD Nuclear Energy Agency (NEA), 2023. Meeting the Nuclear Energy Challenge: Policy Frameworks for Sustainable Expansion. OECD Publishing: Paris, France.
[41] Luczak A., Cermakova K., Kalinowski S., Hromada E., Mec M., 2025. Measurement of Sustainable Development and Standard of Living in Territorial Units: Methodological Concept and Application. Sustainable Development, vol. 33(3), p. 4604-4630. https://doi.org/10.1002/sd.3366

Article no. 2

THE CIVIL ENGINEERING JOURNAL 1-2026

NEGATIVE MOMENT ZONE IN UHPC-STRENGTHENED SIMPLY-SUPPORTED-TO-CONTINUOUS CONCRETE BOX BEAMS: CRACKING RESISTANCE ANALYSIS

Junming Huang[1], Kexin Zhang[2] and Jiaqi Qiu[2]

1. *School of Management, Shenyang Jianzhu University, Shenyang, No.25 Hunnan Zhong Road, China; 2423805749@qq.com*
2. *School of Transportation and Geomatics Engineering, Shenyang Jianzhu University, Shenyang, No.25 Hunnan Zhong Road, China; jt_zkx@sjzu.edu.cn*

Received: *28.05.2025*

Received in revised form: *21.01.2026*

Accepted: *19.03.2026*

ABSTRACT

In this study, to investigate the cracking resistance of UHPC-strengthened simply-supported-to-continuous concrete box beams in the negative moment zone, a total of nine specimens were designed: one reinforced concrete box beam (comparison beam), seven UHPC-RC composite box beams (reinforced beams), and one prestressed concrete box beam (prestressed beam). The research focuses on evaluating the influence of key parameters - including reinforcement ratio, UHPC casting length in the negative moment zone, UHPC thickness, and the joint configuration between UHPC and ordinary concrete - on the cracking resistance of these beams. The results demonstrate that, under the same reinforcement ratio, UHPC strengthening in the negative moment zone significantly enhances the cracking performance of the test beams, with the cracking load increasing by 46%. As the UHPC casting length increases, the maximum crack width at the vertical interface between the full normal concrete (NC) section and the UHPC-NC composite section decreases markedly. Additionally, increasing the UHPC thickness leads to a substantial reduction in the maximum crack width at both the UHPC-NC composite section and the intermediate diaphragm section.

KEYWORDS

Simply-supported to continuous concrete box beam, Negative moment zone, UHPC, Cracking resistance

INTRODUCTION

Simply-supported to continuous beam bridge has been widely used in highway construction by virtue of its advantages of simple structure, high degree of assembly, low cost and fast construction speed [1-2]. Accompanied by the rapid development of the economy, the pressure of highway traffic is also gradually increased, the simply-supported to continuous beam bridge of some problems have begun to appear [3-5], which in turn to the top of the abutment negative bending moment region of the problem is most prominent. Due to the low tensile strength of ordinary concrete and insufficient crack resistance, cracks are produced in the negative moment region at the top of the abutment of simply-supported to continuous concrete beam bridges, which seriously affects the durability and normal service life of the bridge [6]. Therefore, improving the crack resistance in the negative moment zone of simply-supported to continuous beam bridges to improve the durability of bridge operation has become the focus of research [7-8].

The traditional mechanical tensioning prestressing method is to limit the crack development in the negative moment zone by tensioning the prestressing bundles in the negative moment zone at the top of the pier [9]. The crack resistance of the beams is improved by applying prestressing to the negative moment region of the combined beams, but its construction is complicated, inefficient, costly and difficult to ensure the construction quality [10-13]. Therefore, it aims to solve the cracking problem in the negative moment zone of simply-supported to continuous beam bridges, and on this basis, effectively improve the construction efficiency and reduce the construction difficulty and cost.

In recent years, with the vigorous development of material science, many new materials have emerged to provide new solutions to the cracking problem in the negative moment region of beam bridges. Ultra-High Performance Concrete (UHPC), as a new type of cementitious composite material, has the characteristics of ultra-high strength, high toughness, and high durability, and its compressive strength can reach more than 150 MPa and tensile strength can reach more than 6 MPa [14-17]. Long G. [18] carried out a study on UHPC-RC combination beams, and analysed in-depth the effect of the thickness of UHPC on the crack resistance of bridges as well as the ultimate load carrying capacity. Liu X. [19] conducted a study on UHPC-steel composite beams and analysed in-depth the influence of UHPC on improving the crack resistance of composite beams. Wan Z. [20] conducted a study on UHPC-steel-concrete composite beams and analysed in-depth the influence of several parameters, such as the type of overlaying concrete, the arrangement of interfacial shear reinforcement, and the presence of steel wire mesh, on the structural performance of the added composite beams. At present, the research on the structural aspects of UHPC mainly focuses on the combined beams, while there are few studies on the negative moment region of UHPC-strengthened simply-supported to continuous structures.

To address the cracking issue in the negative moment zone of simply-supported-to-continuous beam bridges, this study innovatively applies UHPC to the negative moment zone of simply-supported-to-continuous concrete box beams, forming a locally UHPC-strengthened structural system. This approach effectively mitigates cracking in the negative moment zone. Owing to UHPC's superior tensile properties, it replaces the conventional bridge system conversion method, which involves “pouring concrete over the pier continuous section (at the joint) + mechanically tensioned prestressing.” This innovation not only enhances construction efficiency but also reduces associated risks. Although UHPC materials are more expensive than ordinary concrete, their exceptional performance and durability significantly lower long-term maintenance costs, ensuring economic viability over the service life of the structure. This paper investigates the structural behavior of such composite box beams by considering variables including reinforcement ratio, UHPC length and thickness, prestressing tendon arrangement, and the presence of bearers. The findings provide a theoretical foundation for the practical application of this innovative beam type.

TEST PROCEDURE

Materials

Mechanical Properties of Ordinary Concrete

The grade of plain concrete used is C40 and the specific mix is shown in Table 1.

Tab. 1 - C40 concrete mix

Material	Quality ratio (kg/m^3)
Water	0.33
cement	1
sand	1.15
cobble	2.26
Water reducing agent	0.004

In order to determine the specific mechanical properties of the C40 concrete used in the test beams, three cubic specimens of 150 mm × 150 mm × 150 mm, three prismatic specimens of 100 mm × 100 mm × 400 mm, and three prismatic specimens of 100 mm × 100 mm × 300 mm were poured and cast, and the tests of compressive strength, flexural strength, and modulus of elasticity were carried out respectively. The specimens were all poured at the same time as the concrete of the precast section of the test beam, and the curing was completed under the same conditions. The tests were carried out in accordance with the standard test methods in the Standard Test Methods for Concrete Structures (GB/T 50152-2012), and the average values of the basic mechanical properties of each group of specimens are shown in Table 2.

Tab. 2 - C40 concrete mix

Concrete type	Cubic compressive strength（MPa）	Flexural strength（MPa）	Modulus of elasticity（MPa）
C40	40.9	2.47	26500

Mechanical Properties of UHPC

The UHPC matrix was doped with steel fibers of end-hook type at a dosage of 2% and the specific mixing ratios are shown in Table 3.

Tab. 3 - UHPC material mix ratios

Composition	Quality ratio (kg/m^3)
Cement	956
Medium Sand	214.2
Fine Sand	856.8
Silica Fume	159
Quartz Powder	159
Water Reducing Agent	25.5
Water	216.7

With reference to the specification “Activated Powder Concrete” (GB 50010-2010), three 100 mm × 100 mm × 100 mm cubic compression specimens, three 100 mm × 100 mm × 400 mm prismatic flexural specimens, and three dumbbell-shaped tensile specimens were cast to test the compressive and flexural strengths and tensile strengths of the UHPC. The specimens were cast in the same batch with the test beams, and the maintenance was completed under the same conditions, and the average values of the material performance test results are shown in Table 4, and the axial tensile diagram is shown in Figure 1.

Fig. 1 – Tensile strength test

Tab. 4 - UHPC mechanical properties test results

Cubic compressive strength (MPa)	Flexural strength (MPa)	Tensile strength (MPa)
122	23.3	7.91

Mechanical properties of steel bars

The tensile steel bars used in the test are HRB400 grade, and the pull-out test is carried out to test the yield strength and ultimate tensile strength of the steel bars, and the mechanical properties of the steel bars are shown in Table 5.

Tab. 5 - Test results of mechanical properties of reinforcing steel

Reinforcement diameter (mm)	Modulus of elasticity (MPa)	Yield strength (MPa)	Ultimate tensile strength (MPa)
10	2.0×10^5	422	578
12	2.0×10^5	428	587
14	2.0×10^5	437	592

Test Beam Design and Casting Process

The main steps for making the test beam are as follows: reinforcement cage tying, concrete material preparation, concrete pouring, cast-in-place section reinforcement tying, concrete pouring for end beams as well as beams in the negative moment zone, UHPC pouring in the negative moment zone, formwork dismantling, and maintenance of the test beam. The steps of box beam casting are shown in Figure 2.

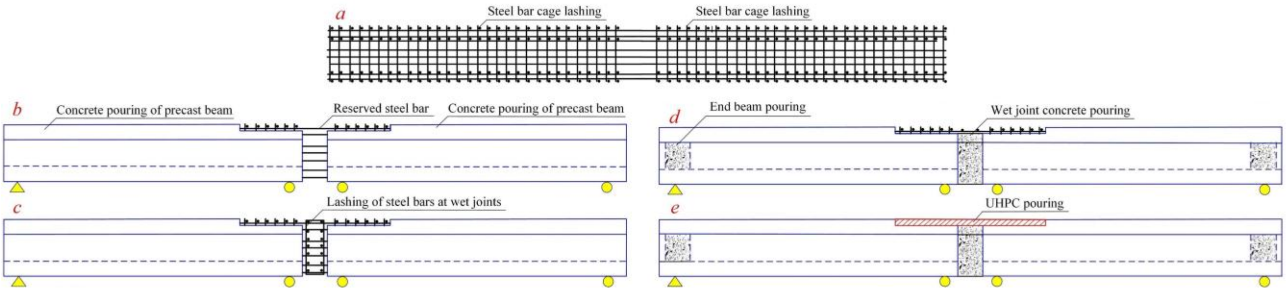

Fig. 2 – Schematic diagram of UHPC reinforced simply-supported to continuous concrete box beams in negative moment zone: (a) – precast beams reinforcement cage tying; (b) – precast beams concrete pouring; (c) – wet joints reinforcement tying; (d) – wet joints and end beams concrete pouring; (e) – UHPC pouring.

Site Pouring Process

The fabrication process of box beams is depicted in Figure 3, primarily involving two main steps: the construction of formwork and the tying of reinforcement cages, followed by the pouring of both conventional concrete materials and UHPC.

Formwork Production and Reinforcement Cage Tying

After the completion of the template production, in accordance with the design drawings of the size of the rebar and the location of the cage will be tied, the rebar between the use of fine steel wire bonding, the test of the reinforcing steel used for the HRB400 level, to be strain gauges paste can be poured, the template and the cage as shown in Figure 3 (a).

Pouring of Concrete Materials

Prepare the concrete mixture, and then slowly pour it into the formwork. During the pouring process, continuously vibrate the concrete using a vibrator to ensure it is uniformly distributed and compacted. After allowing the poured concrete to set for approximately 2 h, smooth the concrete surface again with a trowel. To minimize water loss and prevent cracking after the concrete has been poured, cover the surface with cling film after sprinkling it with water, and regularly moisten the surface thereafter. After about 7 d of curing, concrete can be poured for the end beams as well as the beams in the negative moment region. The specific pouring process is illustrated in Figure 3(b) and Figure 3(c).

UHPC Pouring

After the curing of the plain concrete region was finished, the UHPC-NC interface was chiseled using a chisel hammer. During the chiseling process, efforts were made to partially expose the coarse aggregate on the surface. Once chiseling was complete, any debris on the chiseled surface was cleaned off using an air pump. Subsequently, the UHPC material was prepared and poured into the negative moment zone of the box beam. Given that UHPC possesses self-compacting and self-leveling properties, it was not necessary to use vibrating instruments during the pouring process. After pouring, the surface was smoothed with a trowel and then covered with a plastic film to prevent moisture loss. The formwork was removed, and the structure was allowed to cure at room temperature for 28 d before testing. The UHPC pouring and curing process is illustrated in Figures 3(d) to 3(f).

DOI 10.14311/CEJ.2026.01.0002

Fig. 3 – Box beam fabrication process: (a) – supporting formwork and tying reinforcement, (b) – pouring precast concrete, (c) – pouring concrete for center diaphragm, (d) – mixing UHPC, (e) – pouring UHPC, and (f) – curing after UHPC pouring

Test Procedure

Taking the length of UHPC in the negative moment zone, the thickness of the UHPC layer, and the reinforcement ratio of ordinary steel as the primary variables, a total of nine test beams were designed for the experiment. Among these, one was a simply-supported-to-continuous ordinary reinforced concrete box beam, another was a simply-supported-to-continuous prestressed reinforced concrete box beam, and the remaining seven were simply-supported-to-continuous concrete box beams locally strengthened with UHPC. The parameters for each test beam are detailed in Table 6, while the specific dimensions of the test beams are illustrated in Figures 4 to 6.

Tab. 6 - Pilot programme

Test beam number	Length of UHPC L/mm	Plain steel reinforcement ratio（%）	Prestressing tendon	Thickness of UHPC /mm	Forms of Concrete Undertaking
B0	—	0.43	—	—	Groove
B1	1600	0.36	—	60	Groove
B2	1600	0.43	—	60	Groove
B3	1600	0.50	—	60	Groove
B4	800	0.43	—	60	Groove
B5	1200	0.43	—	60	Groove
B6	—	0.43	2Φs15.2	—	—
B7	1600	0.43	—	120	Bearing
B8	1600	0.43	—	120	Unsupported

The test beam has a longitudinal length of 5000 mm, a clear span of 4600 mm, and a beam height of 450 mm. The flange plate thickness is 120 mm, with a bottom plate width of 1200 mm and a top plate width of 700 mm. The concrete cover thickness is 20 mm, the ordinary concrete used has a strength grade of C40, and all ordinary reinforcing bars are of HRB400 grade. Additionally, cross beams with thicknesses of 300 mm and 200 mm are installed at both ends and the middle of the beam, respectively. In this experiment, key analysis factors include varying ordinary steel reinforcement ratios, UHPC casting lengths and thicknesses, as well as the interfacial bonding forms between ordinary concrete and UHPC.

Among the test beams, beams B1, B2, and B3 all featured a UHPC casting length of 1.6 meters, but they had different ordinary reinforcement ratios, specifically 0.36%, 0.43%, and 0.50%, respectively. Beams B2, B4, and B5 shared the same ordinary reinforcement ratio, yet their UHPC casting lengths varied, measuring 1.6 m, 0.8 m, and 1.2 m, respectively. For beam B6, based on the configuration of beam B0, two nominally symmetrical UHPC sections were arranged. The thicknesses of the UHPC castings for beams B2, B7, and B8 were 60 mm, 120 mm, and 120 mm, respectively. Notably, the interface between UHPC and NC (normal concrete) for beam B7 utilized a bracket-supported bearing form, whereas for beam B8, it was without bracket support.

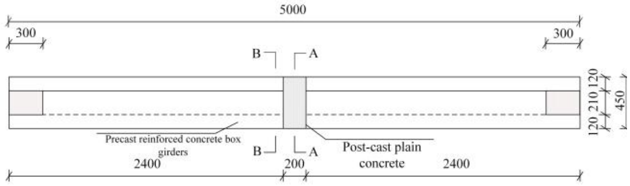

(a) –Beam B0

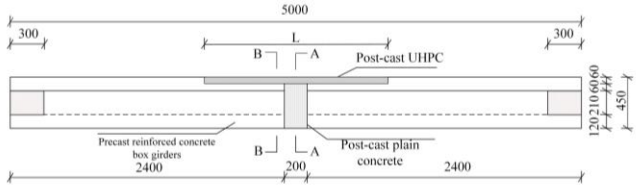

(b) – Beams B1, B2, B3, B4, B5

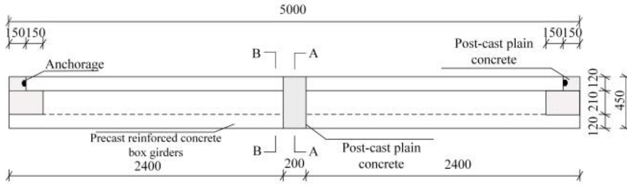

(c) – Beam B6

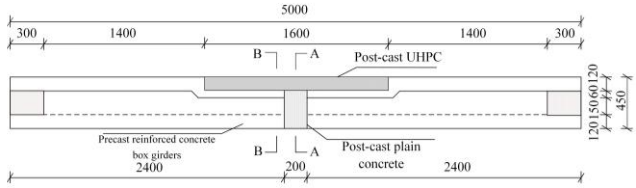

(d) – Beam B7

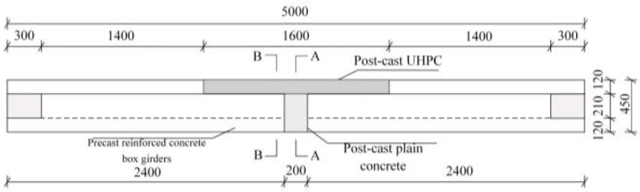

(e) – Beam B8

Fig. 4 – Elevation of test beam (unit: mm)

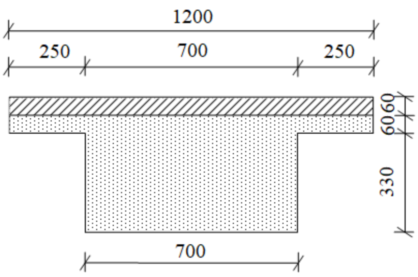

(a) – Beams B1, B2, B3, B4, B5

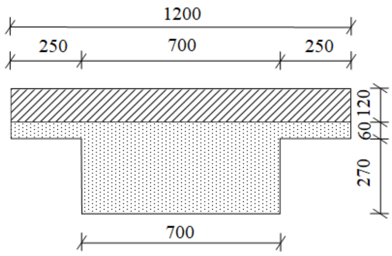

(b) –Beam B7

Fig. 5 – Section A-A of test beam (unit: mm)

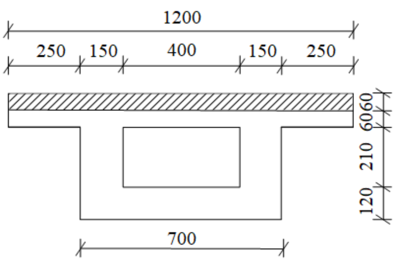

(a) – Beams B1, B2, B3, B4, B5

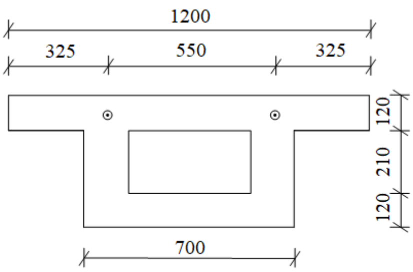

(b) – Beam B8

Fig. 6 – section B-B of test beam (unit: mm)

Load and Measurement Point Arrangement

The test beams were inverted, and reversed loading was employed to simulate the negative bending moment acting on the main beams. Loading was applied using 1000 kN hydraulic jacks, with the beam ends supported on steel piers spaced 4600 mm apart. The test was conducted with four loading points, and the distance between each loading point was set at 600 mm. Schematic diagrams of the loading setup for the test beams, along with on-site photographs, are presented in Figures 7 and 8.

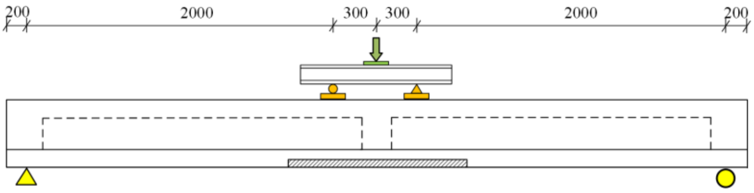

Fig. 7 – Schematic diagram of test loading (unit: mm)

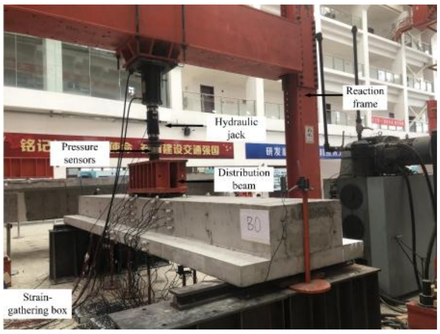

Fig. 8 –Pictures of the test site

RESULTS AND DISCUSSION

Effect of Crack Distribution Under Different Influencing Factors

Factors for Reinforcement Ratio of Ordinary Steel Bars

The simply-supported-to-continuous concrete box beam locally strengthened with UHPC is categorized into four distinct regions, as illustrated in Figure 9. Region Ⅰ represents the full normal concrete (NC) section located outside the UHPC-strengthened area; Region Ⅱ denotes the vertical interface between the combined UHPC-NC section and the full NC section; Region Ⅲ corresponds to the combined UHPC-NC section itself; and Region Ⅳ signifies the intermediate diaphragm beam section. The variations in maximum crack width with respect to applied load for each region in beams B1, B2, and B3 are depicted in Figure 10. Additionally, a comparative analysis of the load versus maximum crack width curves for each region across the test beams is presented in Figure 11.

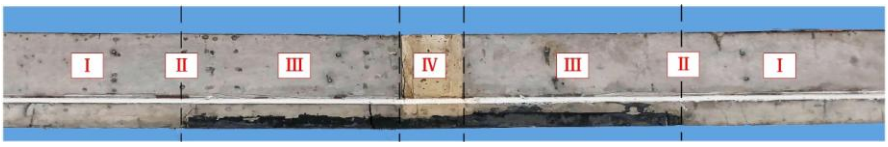

Fig. 9 – Map of the division of the test beam region (B2 beam)

CIVIL ENGINEERING JOURNAL

Article no. 2

THE CIVIL ENGINEERING JOURNAL 1-2026

As illustrated in Figure 10(a), when the external load reaches 85 kN, the first crack emerges in Region Ⅰ of beam B1, followed sequentially by cracks in Regions Ⅱ, Ⅳ, and Ⅲ. As the load increases, the maximum crack widths in all four regions—Ⅰ, Ⅱ, Ⅲ, and Ⅳ—generally exhibit a linear growth trend. When the load surpasses 200 kN, the stiffness of the UHPC-NC composite cross-section significantly decreases, leading to a relatively slower increase in crack width in Regions Ⅰ and Ⅱ, while the crack width in Region Ⅳ grows more rapidly. Ultimately, the beam fails at the intermediate diaphragm cross-section.

From Figure 10(b), it is evident that the first crack in beam B2 appears in Region Ⅰ when the load reaches 95 kN, followed by cracks in Regions Ⅱ, Ⅳ, and Ⅲ in sequence. When the load increases to approximately 120 kN, the crack width in Region Ⅰ is the first to reach 0.2 mm, followed by a crack width of 0.1 mm in Region Ⅱ, while cracks in Regions Ⅲ and Ⅳ have not yet appeared. As the load continues to rise, the maximum crack widths in all four regions—Ⅰ, Ⅱ, Ⅲ, and Ⅳ—generally show linear growth, albeit at a relatively slow rate. When the load exceeds 270 kN, some of the reinforcement in Region Ⅱ yields, causing the crack width there to increase sharply with further load increase.

From Figure 10(c), it can be observed that when beam B3 is loaded to 100 kN, cracks successively appear in Regions Ⅰ, Ⅱ, and Ⅳ, with widths of 0.02 mm, 0.1 mm, and 0.1 mm, respectively. Cracks in Region Ⅲ emerge when the external load reaches 120 kN, at which point the maximum crack width in Region Ⅰ has already reached 0.2 mm, and the maximum crack widths in Regions Ⅱ, Ⅲ, and Ⅳ are approximately 0.15 mm, 0.1 mm, and 0.15 mm, respectively.

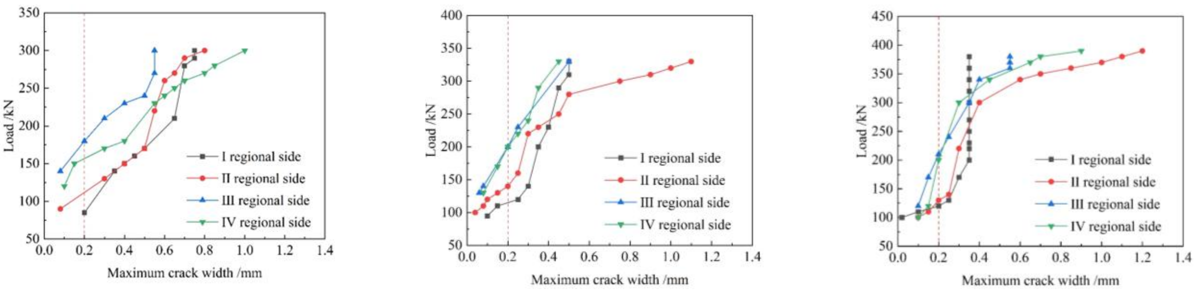

(a) – Beam B1 *(b) – Beam B2* *(c) – Beam B3*

Fig. 10 – Load-maximum crack width curves for beams B1, B2 and B3

The comparison of load-maximum crack width curves for Regions Ⅰ, Ⅱ, Ⅲ, and Ⅳ is presented in Figure 11. From Figure 11(a), it is evident that when the load is less than 150 kN, the maximum crack widths in Region Ⅰ of beams B1, B2, and B3 continuously increase with the rising load. However, when the load exceeds 150 kN, the crack widths grow at a relatively slower rate. At lower loads, the stiffness of the full normal concrete (NC) section is smaller than that of the UHPC-NC composite section, causing cracks to appear first in Region Ⅰ. As the load increases, both the number and width of these cracks expand. Once the load surpasses 150 kN, numerous cracks emerge at the vertical interface between the UHPC-NC composite section and the full NC section, as well as within the UHPC-NC composite section itself, leading to a significant reduction in the composite section's stiffness. Additionally, the bending moment in the composite section is greater than that in the outer full NC section, resulting in a less pronounced increase in maximum crack width in Region Ⅰ, while crack widths in other regions grow relatively faster.

From Figure 11(b), it can be observed that when the load is less than 150 kN or more than 280 kN, the crack width in Region Ⅱ of beams B1, B2, and B3 continuously increases with the rising load. However, when the load is between 150 kN and 280 kN, the crack width in Region Ⅱ changes insignificantly with the load. At loads below 150 kN, since Region Ⅱ is located at the vertical interface between the UHPC-NC composite section and the full NC section, the concrete there experiences a larger bending moment than the outer full NC section, causing both Region Ⅱ and Region Ⅰ to crack earlier and exhibit faster crack width growth at lower loads. When the load exceeds 150 kN, numerous cracks appear in the UHPC-NC composite section, significantly reducing its stiffness. The bending moment in the composite section becomes larger than that at the vertical interface, resulting in a less pronounced increase in crack width in Region Ⅱ, while the crack width in the UHPC-NC composite section grows rapidly with the load. When the load exceeds 280 kN, the reinforcement in Region Ⅱ of beams B1, B2, and B3 yields or is about to yield, leading to a significant increase in crack width with the rising load.

From Figure 11(c), it can be seen that the load and crack width in Region Ⅲ of beams B1, B2, and B3 generally exhibit a linear relationship, with the crack width gradually decreasing as the reinforcement ratio increases under the same load. This is because, with an increased reinforcement ratio, more tensile stress is borne by the steel reinforcement under the same load, reducing the tensile stress borne by the UHPC and effectively suppressing the crack width in the UHPC-NC composite section.

From Figure 11(d), it is evident that the cracks in Region Ⅳ of beam B1 increase sharply with the rising load due to its lower reinforcement ratio, causing more tensile stresses to be borne by the UHPC as the load increases, leading to faster crack width development. In the pre-loading stage, the crack width growth in Region Ⅳ of beams B2 and B3 is relatively slow. However, when the load exceeds 300 kN, the crack width growth accelerates.

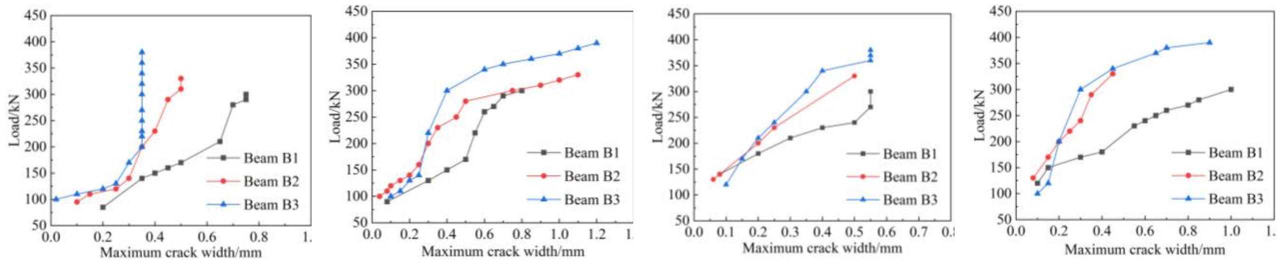

(a) – Region Ⅰ *(b) – Region Ⅱ* *(c) – Region Ⅲ* *(d) – Region Ⅳ*

Fig. 11 – Comparison of load-maximum crack width curves for regions Ⅰ, Ⅱ, Ⅲ and Ⅳ

UHPC Coverage Length Factors

The division of the test beam regions is illustrated in Figure 12. The variations in maximum crack width with respect to the applied load for each region of beams B4 and B5 are depicted in Figure 13. Additionally, a comparative analysis of the load versus maximum crack width curves for each region of the test beams is presented in Figure 14.

Fig. 12 – Map of the division of the test beam region (Beam B4)

As depicted in Figure 13(a), when beam B4 was loaded to 70 kN, cracks were observed in Region Ⅰ. As the load continued to increase, cracks successively appeared in Regions Ⅱ, Ⅲ, and Ⅳ. Upon reaching a load of 100 kN, the maximum crack width in Region Ⅰ was the first to reach 0.2 mm, while the maximum crack width in Region Ⅱ was 0.1 mm at that time; cracks had not yet appeared in Regions Ⅲ and Ⅳ. During the pre-loading stage, the crack widths in Regions Ⅰ and Ⅱ increased with the rising load. After loading reached 150 kN, cracks began to emerge in Regions Ⅲ and Ⅳ, and their widths increased accordingly with the load. However, the growth rate of crack widths in Regions Ⅰ and Ⅱ became relatively slower. When the load exceeded 190 kN, the crack width in Region Ⅱ increased sharply with the rising load, ultimately leading to the failure of the test beam at the middle diaphragm section. After the load surpassed 240 kN, the crack width in Region Ⅰ also increased sharply with the rising load as part of the tensile reinforcement yielded.

From Figure 13(b), it can be observed that when beam B5 was loaded to 75 kN, cracks appeared in Region Ⅰ, followed by successive cracks in Regions Ⅱ, Ⅳ, and Ⅲ. When the load reached 110 kN, the maximum crack width in Region Ⅰ was the first to reach 0.2 mm, while the crack width in Region Ⅱ was 0.1 mm, and no cracks had appeared in Regions Ⅲ and Ⅳ. As the load continued to increase, the crack widths in all four regions generally exhibited linear growth. Notably, the crack widths in Regions Ⅲ and Ⅳ were similar and consistently smaller than those in Regions Ⅰ and Ⅱ. This was attributed to the "bridge-linking" effect of the steel fibers after the UHPC cracked, which effectively restricted the further development of the cracks. When the load exceeded 250 kN, the crack width in Region Ⅱ increased sharply with the rising load, ultimately leading to the failure of the test beam in this region.

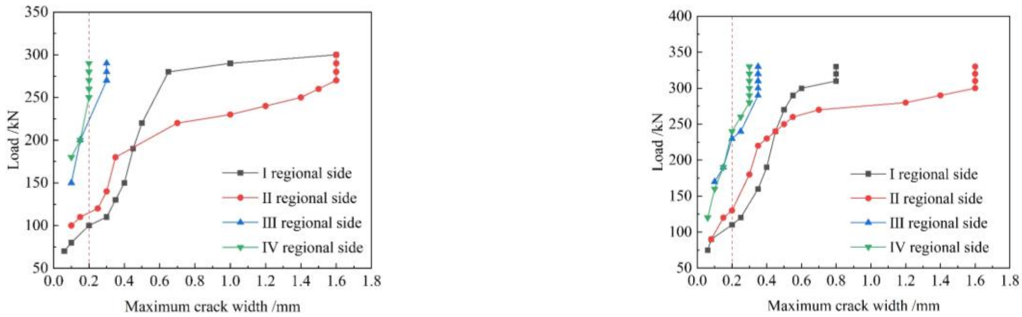

(a) – Beam B4 *(b) – Beam B5*

Fig. 13– Load-maximum crack width curves for beams B4 and B5

From Figure 14(a), it is evident that when the load is less than 150 kN, the crack widths in Region I of beams B2, B4, and B5 all increase with the rising load. However, when the load exceeds 150 kN, the rate of change in crack widths slows down. The crack width in the full NC section increases more gradually because cracks begin to appear in the UHPC-NC composite section at a load of 150 kN. Consequently, the crack widths in Regions Ⅲ and Ⅳ start to increase slowly with the increasing load, and the stiffness of the UHPC-NC composite section decreases significantly. As the load continues to rise, the crack width in Region I decreases with the increasing length of the UHPC-NC composite section. This is because a shorter UHPC-NC composite section results in a longer full NC section, which bears a larger bending moment. Additionally, the internal force redistribution in ordinary concrete is more pronounced, making it difficult to withstand larger bending moments. Therefore, under the same load, the crack widths in Region I of beams B4, B5, and B2 decrease in sequence. When the load exceeds 250 kN, the crack widths of beams B4 and B5 increase sharply with the rising load, while the crack width of beam B2 does not change significantly. This is because, at this point, the reinforcement in Region I of beams B2, B4, and B5 has already yielded or is about to yield, and more tensile stresses are borne by the UHPC. However, the cross-section of the UHPC-NC composite in beams B4 and B5 is shorter, leading to more steel fibers being extracted from the matrix.

From Figure 14(b), it can be observed that when the load is less than 150 kN, the crack widths in Region II of beams B2, B4, and B5 continuously increase with the rising load. This is because the bending moments at the vertical interface between the UHPC-NC and the full NC cross-sections are larger than those at the full NC cross-section, causing both Region II and Region I to crack earlier, and the crack widths to increase relatively rapidly during the preloading period. After the load exceeds 150 kN, with the decreasing stiffness of the UHPC-NC composite section, the crack

DOI 10.14311/CEJ.2026.01.0002

width in Region II increases relatively slowly. From Figures 14(c) and 14(d), it can be seen that the crack widths in Regions III and IV of beams B2, B4, and B5 generally increase linearly with the rising load. When the load exceeds 250 kN, the crack widths of beams B4 and B5 basically remain unchanged with the increasing load, while the crack widths of beam B2 continue to grow linearly.

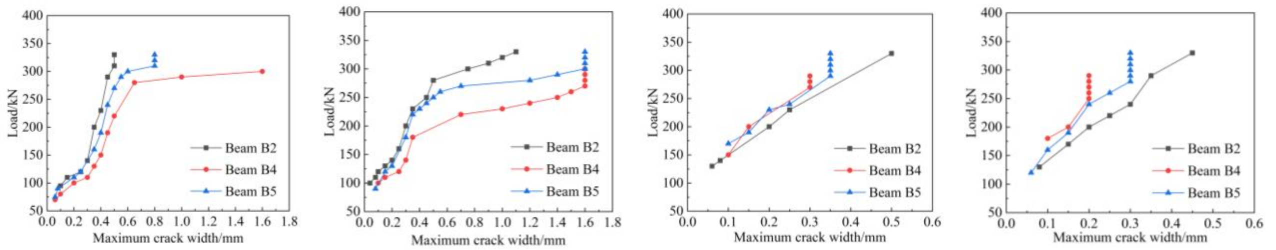

(a) – Region Ⅰ (b) – Region Ⅱ (c) – Region Ⅲ (d) – Region Ⅳ

Fig. 14 – Comparison of load-maximum crack width curves for regions Ⅰ, Ⅱ, Ⅲ and Ⅳ

UHPC Thickness and Form of Support

The division of the test beam regions is shown in Figure 15. The variation of maximum crack width with load in each region of beams B7 and B8 under load is shown in Figure 16, and the comparison of load-maximum crack width curves in each region of the test beams is shown in Figure 17.

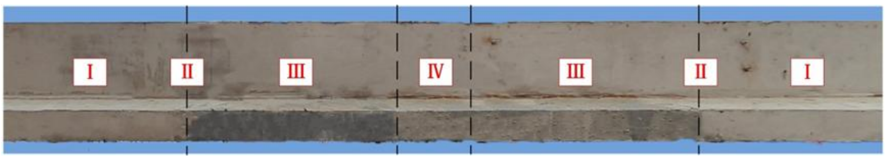

Fig. 15 – Map of the division of the test beam region (Beam B8)

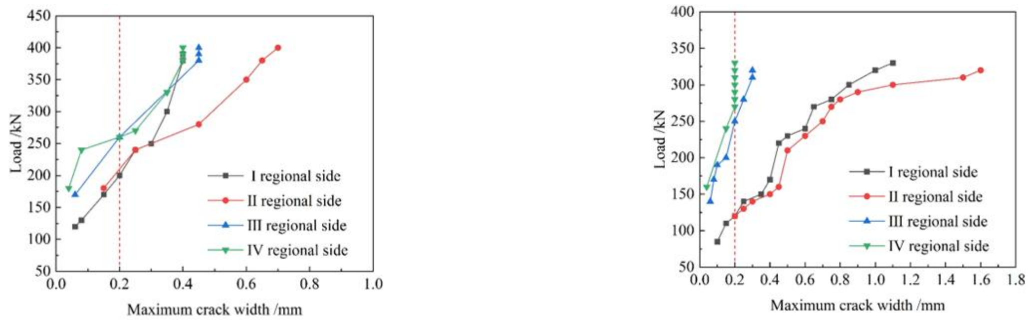

(a) – Beam B7 (b) – Beam B8

Fig. 16 – Load-maximum crack width curves for beams B7 and B8

As illustrated in Figure 18(a), the first crack emerged in Region Ⅰ when beam B7 was loaded to 120 kN. Subsequently, with the continuous increase in load, cracks successively appeared in Regions Ⅲ, Ⅱ, and Ⅳ. When the load reached 200 kN, the crack width in Region Ⅰ was the first to attain 0.2 mm, while the crack widths in Regions Ⅱ, Ⅲ, and Ⅳ were 0.15 mm, 0.1 mm, and 0.05 mm, respectively. As the load continued to rise, the crack widths in each region generally increased linearly, with those in Regions Ⅰ and Ⅱ being larger than those in Regions Ⅲ and Ⅳ.

From Figure 18(b), it can be observed that when beam B8 was loaded to 85 kN, cracks appeared in Region Ⅰ. As the load increased, cracks subsequently emerged in Regions Ⅱ, Ⅲ, and

Ⅳ in turn. When the load reached 120 kN, the crack widths in Regions Ⅰ and Ⅱ simultaneously reached 0.2 mm, while no cracks had yet appeared in Regions Ⅲ and Ⅳ. During the early stage of loading, the crack widths in Regions Ⅰ and Ⅱ grew with the increasing load. When the load exceeded 150 kN, as the crack widths in Regions Ⅲ and Ⅳ began to increase, the cross-sectional stiffness of the UHPC-NC composite section decreased, leading to a relatively steeper slope in the load-crack width curves for Regions Ⅰ and Ⅱ. When the load surpassed 290 kN, the crack widths in Regions Ⅲ and Ⅳ essentially remained unchanged, while some of the reinforcement in Regions Ⅰ and Ⅱ had yielded, resulting in a sharp increase in crack width at the section with the rising load. Ultimately, the test beam failed at the vertical interface between the UHPC-NC composite section and the full NC section.

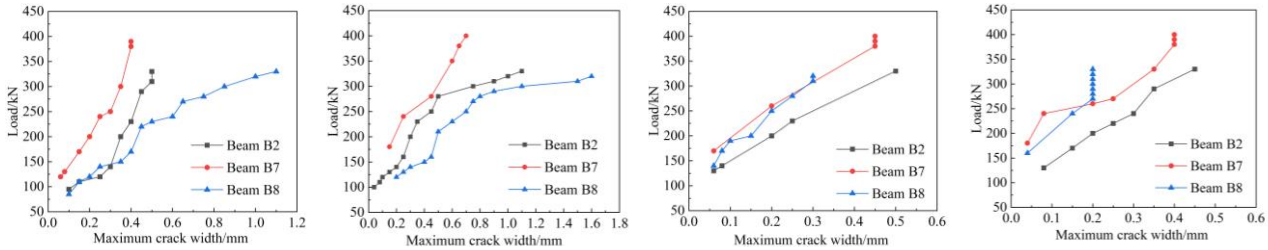

(a) – Region Ⅰ *(b) – Region Ⅱ* *(c) – Region Ⅲ* *(d) – Region Ⅳ*

Fig. 17 – Comparison of load-maximum crack width curves for regions Ⅰ, Ⅱ, Ⅲ and Ⅳ

From Figure 17(a), it is evident that as the load increases, the crack width in Region Ⅰ of beam B7 exhibits linear growth. Moreover, under the same load, the crack width in this region is smaller than that of beam B8. This is because the UHPC underlay enhances the flexural stiffness of the test beams, effectively suppressing crack development in Region Ⅰ. When the load is less than 150 kN, the crack widths in Region Ⅰ of beams B2 and B8 are similar, both increasing with the rising load. However, when the load exceeds 150 kN, the growth rate of crack width slows down. Under the same load, the crack width of beam B2 is smaller than that of beam B8.

At the early stage of loading, the stiffness of the full NC section is relatively low, causing the crack width in Region Ⅰ to develop more rapidly. When the load surpasses 150 kN, as the crack width in the UHPC-NC composite section increases, its sectional stiffness decreases. Coupled with the larger bending moment in the UHPC-NC composite section, the crack widths in Regions Ⅲ and Ⅳ grow faster, resulting in a relatively slower growth rate of crack width in Region Ⅰ. The thickness of the UHPC layer in beam B8 is greater than that in beam B2, providing a higher degree of steel fiber bridging. Consequently, the stiffness of the UHPC-NC composite section in beam B8 decreases more slowly, leading to smaller crack widths compared to beam B2. Furthermore, the decrease in cross-sectional stiffness is slower, and the crack widths and number of cracks in Regions Ⅲ and Ⅳ grow at a slower rate than in beam B2. Therefore, under the same loading conditions, the crack width in Region Ⅰ of beam B2 is smaller than that of beam B8.

From Figure 17(b), it can be observed that the crack width in Region II of beam B7 increases linearly with the rising load. Under the same load, the crack width of beam B7 is smaller than that of beam B8 because the UHPC underlay enhances the flexural stiffness of the test beams, effectively suppressing crack development in Region II. When the load is less than 150 kN, the crack widths of beams B2 and B8 increase with the load due to the larger bending moment at the vertical interface between the UHPC-NC composite section and the full NC section compared to the full NC section alone. Consequently, cracks in both Region Ⅱ and Region Ⅰ appear earlier, and the crack widths develop more rapidly.

From Figure 17(c), it is apparent that as the load increases, the crack widths in Region III of beams B7 and B8 are generally similar and both are smaller than that of beam B2 under the same load. This is because with the increase in UHPC thickness, the degree of bridging provided by steel fibers becomes greater, and its crack-arresting effect is more pronounced. From Figure 17(d), it can be seen that when the load is less than 270 kN, the crack widths in Region Ⅳ of beams B7 and B8 are similar and both are smaller than that of beam B2 under the same load.

Analysis of Maximum Crack Width in Pure Bending Zone

Reinforcement Ratio

Beams B1, B2, and B3 were tested to compare the effects of different reinforcement rates—0.36%, 0.43%, and 0.5%, respectively—on the flexural performance of a UHPC-strengthened simply-supported-to-continuous concrete box beam in the negative moment region. As illustrated in Figure 18, with an increase in the reinforcement rate, the cracking load of the UHPC-locally-reinforced simply-supported-to-continuous concrete box beam increased by 11.8% and 17.6%, the yield load rose by 17.4% and 47.8%, and the ultimate load increased by 14.8% and 28.5%. For the same reinforcement rate, the cracking load, yield load, and ultimate load of beam B2 increased by 46%, 12.5%, and 25%, respectively, compared to those of beam B0. Moreover, when the crack width in the purely curved section of beam B0 reached 0.2 mm, the crack width in beam B2 was only 0.1 mm.

The analysis revealed that reinforcing the negative moment zone of simply-supported-to-continuous concrete box beams with UHPC significantly enhanced the flexural performance of the test beams. As the reinforcement rate increased, the load-carrying capacity, stiffness, and ductility of the test beams improved markedly, and all test beams experienced damage at the intermediate diaphragm section. Compared to beam B0, the cracking load, yield load, and ultimate load of beam B6 increased by 38%, 4%, and 21%, respectively. When the maximum crack width in the purely curved section of beam B0 reached 0.2 mm, the crack width in beam B6 was 0.15 mm, which was closer to that of beam B2. This indicates that beam B2, which features UHPC reinforcement with a length of 1600 mm and a thickness of 60 mm, demonstrates comparable load-carrying and crack-limiting capabilities to a simply-supported-to-continuous prestressed concrete box beam reinforced with two additional prestressing strands of diameter 15.2 mm (with a tensile stress of 1000 MPa).

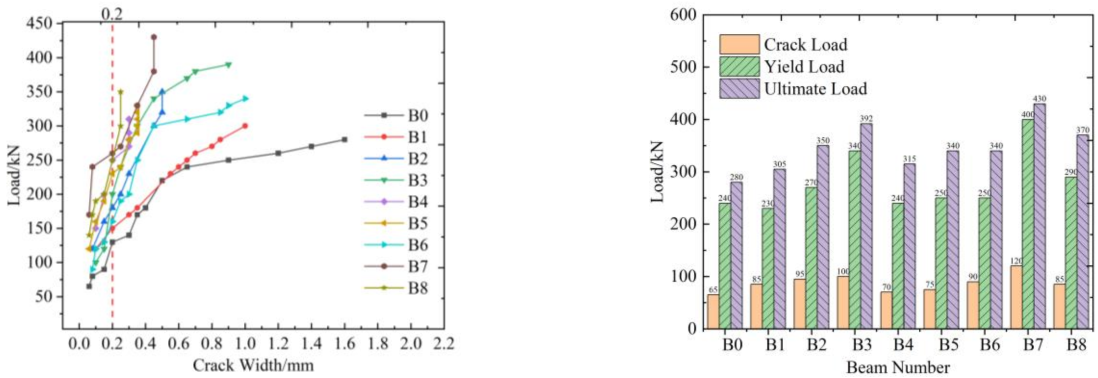

(a) – Load-maximum crack width curve for purely curved section

(b) – Eigenvalues of loads

Fig. 18 – Different reinforcement rates, UHPC lengths, UHPC thicknesses and support forms

UHPC Length

Beams B2, B4, and B5 were primarily tested to investigate the influence of varying UHPC cover lengths on the bending performance of UHPC-strengthened simply-supported-to-continuous concrete box beams in the negative moment zone. As depicted in Figure 18, when the UHPC cover

DOI 10.14311/CEJ.2026.01.0002

lengths were 1600 mm, 800 mm, and 1200 mm, the cracking load of the UHPC-locally-strengthened simply-supported-to-continuous concrete box beams increased by 46%, 7.7%, and 15%, respectively, compared to the control beam. The yield load increased by 12.5%, 0%, and 4%, while the ultimate load rose by 25%, 12.5%, and 21%, respectively. These results indicate that an adequate UHPC cover length is crucial, as shorter cover lengths result in less pronounced improvements in cracking load, yield load, and ultimate load.

When the crack width in the pure bending section of beam B0 reached 0.2 mm, the crack widths in beams B2, B4, and B5 were 0.1 mm, 0 mm, and 0.08 mm, respectively. This discrepancy can be attributed to the shorter cross-sectional lengths of the UHPC-NC combinations in beams B4 and B5, which caused a greater proportion of the external loads to be borne by the full NC section, thereby reducing the crack width in the pure bending section.

UHPC Thickness and Form of Support

Beams B2, B7, and B8 were primarily examined to explore the impact of varying UHPC thicknesses and bearing methods on the bending performance of UHPC-strengthened simply-supported-to-continuous concrete box beams in the negative moment zone. As illustrated in Figure 18, the cracking loads of UHPC-locally-strengthened simply-supported-to-continuous concrete box beams with UHPC thicknesses of 60 mm, 120 mm (with load bearing underneath the UHPC), and 120 mm (without specific load-bearing mention, assumed standard configuration) were 46%, 84.6%, and 30% higher, respectively, than those of the comparison beams. The yield loads were 12.5%, 66.7%, and 20.8% higher, while the ultimate loads were 25%, 53.6%, and 32% higher, respectively, compared to the comparison beams.

When the maximum crack width in the pure bending section of beam B0 reached 0.2 mm, the crack widths in beams B2, B7, and B8 were 0.1 mm, 0 mm, and 0 mm, respectively. The analysis revealed that UHPC with load bearing underneath significantly enhanced the stiffness, load-carrying capacity, and crack-controlling ability of the test beams. However, under larger loads, the UHPC in the tensile zone of beam B7 entered the stress-softening stage, and the steel fiber "bridging" effect was not as pronounced as in beam B2 (assuming the comparison was intended to be with B2 or another relevant beam; if not, please adjust accordingly).

CONCLUSION

1. When the crack width in the pure bending section of a plain reinforced concrete box beam reaches 0.2 mm under the same reinforcement ratio, the crack width in a UHPC-reinforced beam is only 0.1 mm. Reinforcing the negative moment zone of a simply-supported-to-continuous concrete box beam with UHPC can significantly enhance the cracking performance of the test beam. When the UHPC length is small, a greater portion of the external loads is borne by the full NC (normal concrete) section, resulting in a smaller crack width in the pure bending section. Therefore, to achieve optimal crack resistance, it is essential to ensure an adequate UHPC length.
2. The reinforced beams were categorized into four regions: the full NC section, the vertical interface between the UHPC-NC combined section and the full NC section, the UHPC-NC combined section, and the intermediate diaphragm section. The crack development patterns in each region of the test beams were systematically analyzed under varying reinforcement rates, UHPC lengths, and UHPC thicknesses. The analyses revealed the following:

(1) As the UHPC length increases, the maximum crack width at the vertical interface between the full NC section and the UHPC-NC combined section, as well as within the full NC section itself, decreases significantly. However, the crack width at the UHPC-NC combined section and the intermediate diaphragm section increases slightly. When the UHPC length is relatively small, its crack-limiting ability is not pronounced, showing performance similar to that of the comparison beams.
(2) Increasing the thickness of the UHPC leads to a significant reduction in the maximum crack width at the UHPC-NC combined section and the intermediate diaphragm section. Conversely, the

crack width at the vertical interface between the UHPC-NC combined section and the full NC section increases notably.

(3) When the reinforcement ratio of ordinary steel bars is the same, beam B2 demonstrates superior crack-limiting ability compared to beam B0. Specifically, when the crack width in the pure bending section of beam B0 reaches 0.2 mm, that of beam B2 is only 0.1 mm. Furthermore, the crack width in the pure bending section of a simply-supported-to-continuous prestressed concrete box beam reinforced with two additional 15.2-diameter prestressing strands is 0.15 mm, indicating comparable performance between beams B2 and B6.

REFERENCES

[1] Hu Tie - ming, He Cheng - kui, Chen Xiao - feng, et al., 2010. Fatigue experiment of concrete bridges strengthened by simple - supporting to continuous construction method. China Journal of Highway and Transport, vol. 23, p. 76. https://doi.org/10.19721/j.cnki.1001-7372.2010.05.012.

[2] Nielson B G, DesRoches R., 2007. Seismic performance assessment of simply supported and continuous multispan concrete girder highway bridges. Journal of Bridge Engineering, vol. 12, p. 611 - 620. https://doi.org/10.1061/(ASCE)1084-0702(2007)12:5(611)

[3] Arrayago I, Real E., 2016. Experimental study on ferritic stainless steel simply supported and continuous beams. Journal of Constructional Steel Research, vol. 119, p. 50 - 62. https://doi.org/10.1016/j.jcsr.2015.12.006

[4] Mohamed A M, Mahmoud K, El - Salakawy E F., 2020. Behavior of simply supported and continuous concrete deep beams reinforced with GFRP bars. Journal of Composites for Construction, vol. 24, p. 04020032. https://doi.org/10.1061/(ASCE)CC.1943-5614.0001039

[5] Sun Q, Yang Y, Fan J, et al., 2014. Effect of longitudinal reinforcement and prestressing on stiffness of composite beams under hogging moments. Journal of Constructional Steel Research, vol. 100, p. 1 - 11. https://doi.org/10.1016/j.jcsr.2014.04.017

[6] Su Q, Yang G, Bradford M A., 2015. Behavior of a continuous composite box girder with a prefabricated prestressed - concrete slab in its hogging - moment region. Journal of Bridge Engineering, vol. 20, p. B4014004. https://doi.org/10.1061/(ASCE)BE.1943-5592.0000698

[7] Chen S., 2005. Experimental study of prestressed steel–concrete composite beams with external tendons for negative moments. Journal of Constructional Steel Research, vol. 61, p. 1613 - 1630. https://doi.org/10.1016/j.jcsr.2005.05.005 https://doi.org/10.1016/j.jcsr.2005.05.005

[8] Gong W, Li X, Ge Z, et al., 2023. Steel - concrete composite beams strengthened with NSM CFRP systems at the hogging - moment regions. Engineering Structures, vol. 292, p. 116576. https://doi.org/10.1016/j.engstruct.2023.116576

[9] Liu X, Tang L, Jing Y, et al., 2022. Behaviour of continuous steel–concrete composite beams strengthened with CFRP sheets at hogging - moment region. Composite Structures, vol. 291, p. 115695. https://doi.org/10.1016/j.compstruct.2022.115695

[10] Maghsoudi A A, Bengar H A., 2009. Moment redistribution and ductility of RHSC continuous beams strengthened with CFRP. Turkish Journal of Engineering & Environmental Sciences, vol. 33, p. 1. https://doi.org/10.3906/MUH-0901-6

[11] Abdullah A Q, Mansor A A, Mohammed A S, et al., 2021. Hybrid and external strengthening of T - reinforced concrete beams under negative bending moment using steel plates and CFRP. IOP Conference Series: Earth and Environmental Science, vol. 856, p. 012027. https://doi.org/10.1088/1755-1315/856/1/012027

[12] Gholamhoseini A, Khanlou A, MacRae G, et al., 2018. Short - term behaviour of reinforced and steel fibre–reinforced concrete composite slabs with steel decking under negative bending moment. Advances in Structural Engineering, vol. 21, p. 1288 - 1301. https://doi.org/10.1177/1369433217739710

[13] Liu R, Yang Y, Zhou X., 2018. Experimental study on fatigue performance of composite beam with steel - plate - concrete composite decks. Construction and Building Materials, vol. 188, p. 833 - 849. https://doi.org/10.1016/j.conbuildmat.2018.08.108

[14] Ibrahim A, Salem S, Khalil A, et al., 2020. Experimental Investigation for Moment Redistribution in Continuous RC Beams Top Strengthened with CFRP and Steel Plates. IOP Conference Series: Materials Science and Engineering, vol. 809, p. 012007. https://doi.org/10.1088/1757-899X/809/1/012007

[15] Lin W, Yoda T, Taniguchi N, et al., 2014. Mechanical performance of steel - concrete composite beams subjected to a hogging moment. Journal of Structural Engineering, vol. 140, p. 04013031. https://doi.org/10.1061/(ASCE)ST.1943-541X.0000800

[16] Russell H G, Graybeal B A, Russell H G., 2013. Ultra - high performance concrete: A state - of - the - art report for the bridge community. United States. Federal Highway Administration. Office of Infrastructure Research and Development.

[17] Zhang P, Hu R, Zou X, et al., 2021. Experimental study of a novel continuous FRP - UHPC hybrid beam. Composite Structures, vol. 261, p. 113329. https://doi.org/10.1016/j.compstruct.2020.113329

[18] Long G, Zhou R, Ma H, et al., 2022. Experimental and Numerical Study on UHPC–RC Decks within Hogging Moment Region. Applied Sciences, vol. 12, p. 11446. https://doi.org/10.3390/app122211446

[19] Liu X, Zhang J, Cheng Z, et al., 2021. Experimental and numerical studies on the negative flexural behavior of steel - UHPC composite beams. Advances in Civil Engineering, vol. 2021, p. 1 - 15. https://doi.org/10.1155/2021/8828175

[20] Wan Z, Fang Z, Liang L, et al., 2022. Structural performance of steel–concrete composite beams with UHPC overlays under hogging moment. Engineering Structures, vol. 270, p. 114866. https://doi.org/10.1016/j.engstruct.2022.114866

CIVIL ENGINEERING JOURNAL

Article no. 3

THE CIVIL ENGINEERING JOURNAL 1-2026

DECISION-MAKING OF ECOLOGICAL SLOPE PROTECTION SCHEME BASED ON IMPROVED FUZZY SET PAIR ANALYSIS

Xiansheng Duan[1], Ming Zhang[1], Runjuan Zhou[2], and Yingke Sun[2]

1. *School of Architecture and Civil Engineering, Anhui Polytechnic University, Wuhu 241000, Anhui, China; zhangming@ahpu.edu.cn, dxscg18@163.com*

2. *School of Chemical and Environmental Engineering, Anhui Polytechnic University, Wuhu 241000, Anhui, China; rjzhou@mail.ahpu.edu.cn, syingke158900@163.com*

Received:	*26.06.2025*
Received in revised form:	*08.03.2026*
Accepted:	*26.04.2026*

ABSTRACT

The study evaluates the effectiveness of various ecological slope protection strategies for riverbank stabilization by systematically analyzing several critical factors: slope coefficient, durability, impact resistance to flow, biodiversity index, biochannel fluency, vegetation coverage, construction and maintenance costs, landscape aesthetics, and recreational function. The Fuzzy Set Pair Analysis Assessment Method was utilized to create a comprehensive evaluation model, employing normalized benefit-type indices and incorporating the Analytic Hierarchy Process (AHP) with an Accelerated Genetic Algorithm (AGA) to determine the weight of each evaluation index. This model assesses the linkage degree of single indices and uses a confidence criterion to classify evaluation samples across different risk tolerance levels. The results show that plant berms are most effective at a confidence level of 0.50, while gabion revetments perform best at levels of 0.60 and 0.70. The findings suggest that plant berms are suitable for higher risk tolerance, while gabion revetments are better for risk-averse decisions. This methodology offers a novel and robust tool for scientifically assessing and selecting optimal river slope protection strategies.

KEYWORDS

Ecological slope protection, Scheme decision-making, accelerated genetic algorithm, Hierarchical analysis, Fuzzy set-pair analysis

INTRODUCTION

The escalating impacts of climate change, characterized by frequent extreme hydrological events, have intensified the global challenge of riverbank erosion and ecological degradation [1,2]. Traditional hard engineering revetments, such as riprap and concrete linings, while effective in flood control, have been widely criticized for disrupting the fluvial continuum, fragmenting aquaticterrestrial habitats, and diminishing the self-purification capacity of rivers [3-5]. Consequently, there is a global consensus on the urgent need to transition towards ecological slope protection (ESP) that harmonizes flood defence with ecosystem conservation [6].

To address this challenge, extensive research has been conducted worldwide on the evaluation and selection of optimal ESP schemes. In Europe and North America, multi-criteria decision-making (MCDM) methods have been increasingly applied to prioritize river restoration and river-floodplain conservation by jointly considering hydromorphological, ecological, and socio-economic criteria [7-9]. In parallel, soil and water bioengineering has been widely recognized as a nature-based strategy capable of reconciling natural hazard control with ecological restoration in riverbank protection [10]. Similarly, in Japan, the “nature-oriented river works” approach has long emphasized the integration of ecological indices into engineering practice and river management standards [11].

China, with its massive scale of water conservancy construction and rapid urbanization, faces analogous challenges. Existing studies have evaluated ESP schemes under Chinese conditions from the perspectives of comprehensive performance comparison, ecological revetment assessment, and project-level effect verification [12-17]. However, much of the existing literature remains case-specific, and the applicability of these methods is still constrained by methodological limitations in weight consistency, uncertainty propagation, and fuzzy grade transitions.

Among these, AHP is the most widely adopted due to its simplicity and systematic structure. However, as Jin et al. [18] critically noted, the conventional AHP treats weight calculation and consistency verification as separate steps. Once the judgment matrix is established, the consistency index is fixed, leaving no room for optimization, which can compromise the accuracy of derived weights [19]. Furthermore, other methods present their own drawbacks: PCA often leads to information loss during dimensionality reduction [20], and traditional set pair analysis (SPA) assumes rigid boundaries for grading criteria and equal weights for all indicators, which fails to capture the fuzzy and uncertain nature of ecological systems [21].

To overcome these deficiencies, this study proposes an integrated evaluation model that couples an Accelerated Genetic Algorithm-optimized Analytic Hierarchy Process (AGA-AHP) with a Fuzzy Set Pair Analysis (FSPAAM) . The AGA addresses the consistency optimization problem in AHP, enhancing the objectivity of weight determination, while the FSPAAM effectively handles the uncertainty and fuzziness inherent in ecological grading criteria. This hybrid approach not only refines the evaluation of ESP schemes for Chinese rivers but also offers a robust decision-making framework applicable to similar contexts worldwide, providing both theoretical contributions and practical guidance for sustainable river management [22,23].

RESEARCH METHODS

A scientific and robust evaluation framework is essential for assessing river slope protection schemes. Based on the analytic hierarchy process optimized by an accelerated genetic algorithm (AGA-AHP) and fuzzy set pair analysis (FSPA), this study develops an integrated evaluation model for ecological riverbank protection risk assessment [22,24-27]. The procedure is summarized as follows.

First, an evaluation index system was established to comprehensively characterize the ecological shore protection scheme. Let the selected indicators be denoted as x_1, x_2, ..., xm, where m is the total number of indicators. A three-level hierarchical structure was then constructed, consisting of the objective layer (A), subsystem layer (B), and indicator layer (C).

Second, AGA-AHP was used to determine indicator weights. Pairwise comparison matrices were constructed for elements in each layer with respect to their upper-level criterion. Using the conventional 1-9 scale and its reciprocal, the judgment matrix for layer B relative to the objective layer A is expressed as A = $\{a_{ij}\}$, and the matrices for layer C relative to each subsystem B**k** are denoted as $B_k = \{b_{ij}k\}$. The relative weights of indicators were obtained through hierarchical single ranking and total ranking, while matrix consistency was optimized and tested using the AGA-based consistency index function:

$$a_{ij} = w_i/w_j \tag{1}$$

$$min \cdot \mathrm{CIF}(n_b) =\cdot (1/n_b) \cdot 2_{k=1}^{n_b} \cdot l \cdot 2_{i=1}^{n_b} \cdot \frac{a_{ik}w_k}{\cdot n_b w_k} \cdot l \tag{2}$$

subject to:$w_k > 0, \mathrm{and} Z_{k=1}^{n_b} w_k \cdot=\cdot 1$

where w_k denotes the ranking weight of each element and CIF(nb) is the consistency index function. The final total ranking weights of layer C with respect to layer A were taken as the comprehensive weights of the evaluation indicators.

Third, FSPA was employed to evaluate the relationship between the observed indicator values and the predefined risk grading criteria. For the l-th indicator, let Al denote the observed value set and Bk the k-th evaluation grade criterion. The K-element linkage degree of the set pair H(Al, Bk) is expressed as:

$$\mu_{A_l-B_k} =\cdot a_l +\cdot b_{l,1}l_1 +\cdot b_{l,2}l_2 +\cdots + \cdot b_{l,K-2}l_{K-2} +\cdot c_l J \tag{3}$$

where al, $b_{l,1}$, ..., $b_{l,K-2}$, and cl represent the identity, discrepancy, and opposition degrees, respectively, between the indicator value and the grading standard.

After determining the weight wl of each indicator, the overall linkage degree of the evaluation sample is calculated as:

$$\mu_{A-B} = \sum_{l=1}^{m} w_l \cdot \mu_{A_l-B_l} \tag{4}$$

Let

$$f_1 = \sum_{l=1}^{m} w_l a_l, f_2 = \sum_{l=1}^{m} w_l b_{l,1}, \dots, f_K = \sum_{l=1}^{m} w_l c_l \tag{5}$$

then Equation (7) can be rewritten as:

DOI 10.14311/CEJ.2026.01.0003

$$\mu_{A-B} = f_1 + f_2 I_1 + f_3 I_2 + \cdots + f_{K-1} I_{K-2} + f_K J \tag{6}$$

where f_1, f_2, ..., f_K indicate the likelihood that the evaluation sample belongs to each risk level.

For positive indicators, the fuzzy linkage degree was calculated according to the corresponding grading intervals. When K > 2, the K-element linkage degree was determined using the piecewise formulation in Eq. (8), and when K = 2, the binary linkage degree was calculated using Equation (9).

Finally, the confidence criterion was adopted to determine the risk level of the evaluation sample:

$$h_k = f_1 + f_2 + \cdots + f_k > \lambda, k = 1,2, \ldots, K \tag{7}$$

where λ is the confidence level. Following previous studies, λ was selected within the range of 0.50-0.70 [28]. Based on this criterion, the final risk grade of the ecological riverbank protection scheme was identified.

EXAMPLE ANALYSIS

Determination of evaluation index system and evaluation criteria

This study exemplifies the evaluation of ecological shore protection and further elaborates on the application process of evaluation based on the AGA-AHP fuzzy set approach. This paper references the evaluation index system for assessing the effectiveness of ecological slope protection as established in the existing literature[29]. The impact of ecological slope protection is comprehensively analysed from three perspectives: structural stability, ecological functionality, and socio-economic factors. To establish a comprehensive, objective, and rational evaluation index system for ecological shore protection, the following factors are considered: slope coefficient, durability, impact resistance flow rate, biodiversity index, biological channel patency, vegetation coverage, construction and maintenance costs, landscape aesthetics, and recreational value. The final risk evaluation index system is illustrated in Figure 1.

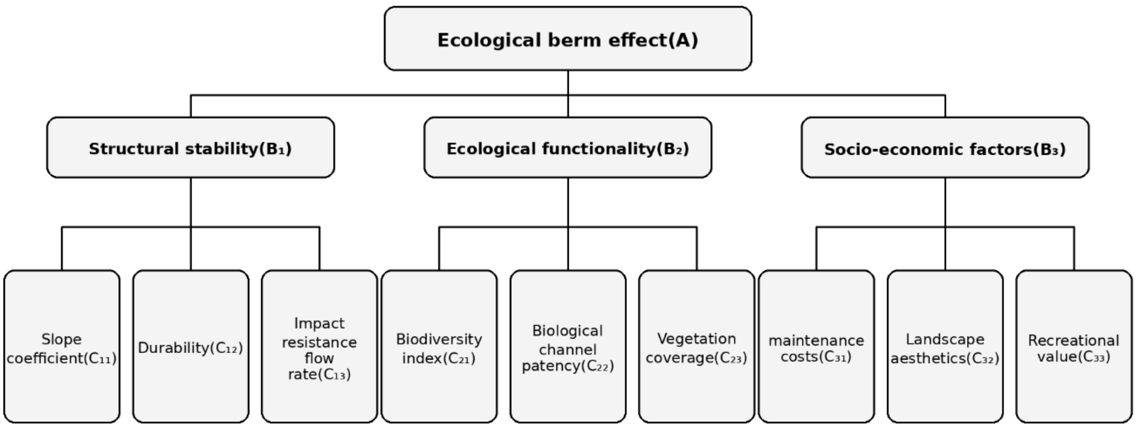

Fig. 1 - Evaluation system of ecological riparian effect

Referencing both domestic and international research standards and literature on ecological shore protection, this study adopts a four-level evaluation criteria system[30-33]. These levels, ranging from the strongest to the weakest, are denoted as Level 1 through Level 4 (see Table 1).

Tab.1 - Evaluation criteria for each index of ecological shore protection measures

Criterion	Index	Level 1	Level 2	Level 3	Level 4
Structural stability	Slope coefficient	≥3.5	2~3.5	1~2	<1
	Durability（year）	≥50	10~50	1~10	<1
	Impact resistance flow rate (m/s)	≥4	3~4	2~3	<2
Ecological functionality	Biodiversity index	≥1.5	0.8~1.5	0.2~0.8	<0.2
	Biological channel patency	≥30%	10%~30%	5%~10%	<5%
	Vegetation coverage (%)	≥50%	20%~50%	10%~20%	<10%
Socio-economic factors	Construction and maintenance costs (Yuan /m^2)	≥1	0.5~1	0.3~0.5	<0.3
	Landscape aesthetics	≥0.7	0.5~0.7	0.3~0.5	<0.3
	Recreational value	≥0.7	0.5~0.7	0.3~0.5	<0.3

Determining the weights of indicators

Based on the referenced literature, ten experts specializing in ecological bank design, construction, maintenance, economy, and environmental protection were invited to evaluate the importance of each factor at all levels of the evaluation through pairwise comparisons. The survey results were organized to form the A-B, B1-C, B2-C, and B3-C judgment matrices (Tables 2 to 5). In this paper, we utilize Matlab software and employ the AGA-AHP method to efficiently verify the consistency of the judgment matrix and calculate the weights of each indicator layer. The results are presented in Table 6.

Tab.2 - A-B judgment matrix and weights of each criterion

	Structural stability(B_1)	Ecological functionality(B_2)	Slope coefficient(C_{11})
Structural stability(B_1)	1	1	3
Ecological functionality(B_2)	1	1	3
Socio-economic factors(B_3)	0.33	0.33	1

Tab.3 - B_1-C judgment matrix and weights of each criterion

	Slope coefficient(C_{11})	Durability(C_{12})	Impact resistance flow rate(C_{13})
Slope coefficient(C_{11})	1	2	0.33
Durability(C_{12})	0.5	1	0.33
Impact resistance flow rate(C_{13})	3	3	1

Tab.4 - B_2-C judgment matrix and weights of each criterion

	Biodiversity index(C_{21})	Biological channel patency(C_{22})	Vegetation coverage(C_{23})
Biodiversity index(C_{21})	1	0.5	0.33
Biological channel patency(C_{22})	2	1	0.5
Vegetation coverage(C_{23})	3	2	1

Tab.5 - B_3-C judgment matrix and weights for each criterion

	maintenance costs(C_{31})	Landscape aesthetics(C_{32})	Recreational value(C_{33})
maintenance costs(C_{31})	1	2	3
Landscape aesthetics(C_{32})	0.5	1	2
Recreational value(C_{33})	0.33	0.5	1

Tab.6 - Results of AGA-AHP and AHP method for calculating the ranking weights of judgment matrices

Methodology	Judgment matrix	Sorting weight			Coherence indicator function value
		w1	w2	w3	
AHP[29]	A	0.429	0.429	0.143	0
AGA-AHP	A	0.429	0.429	0.143	0
AHP[29]	B_1	0.249	0.157	0.594	0.027
AGA-AHP	B_1	0.200	0.200	0.600	0.033
AHP	B_2	0.163	0.297	0.594	0.005
AGA-AHP	B_2	0.182	0.272	0.546	0.015
AHP[29]	B_3	0.163	0.297	0.594	0.005
AGA-AHP	B_3	0.546	0.273	0.182	0.015

Calculation of Contact Degree

The index data for six types of bank protection measures for a riverbank, obtained through investigation and data review, are presented in Table 7. All the type of indicator in Table 7 is efficiency-oriented. This paper utilizes the weights calculated by the AGA-AHP method combined with the fuzzy set-pair evaluation method to explore the effectiveness of ecological slope protection.

Tab..7 - Results of the survey on indicators of ecological riparian measures

No.	Scheme	Structural stability(B_1)			Ecological functionality(B_2)			Socio-economic factors(B_3)		
		Slope coefficient	Durability(year)	Impact resistance flow rate(m/s)	Biodiversity index	Biological channel patency	Vegetation coverage	Construction and maintenance costs	Landscape aesthetic	Recreational value
1	vegetated slope protection	1.5	5	1	5	40%	80%	26/26	0.6	0.6
2	Reynolds Shore Protection	1.5	30	2	6	30%	80%	26/77	0.6	0.6
3	Gabion shore protection	1	30	3	10	30%	60%	26/257	0.6	0.8
4	Ecological concrete berms	1	20	2.5	13	25%	60%	26/180	0.8	0.4
5	Self-embedded retaining wall	0.5	20	2.5	11	20%	60%	26/470	0.8	0.6
6	dry-stone revetment	2	15	1.5	9	30%	50%	26/214	1	0.6

Representative examples of the ecological slope protection schemes considered in this study are shown in Figure 2, which helps visualize the engineering forms corresponding to the alternatives listed in Table 7.

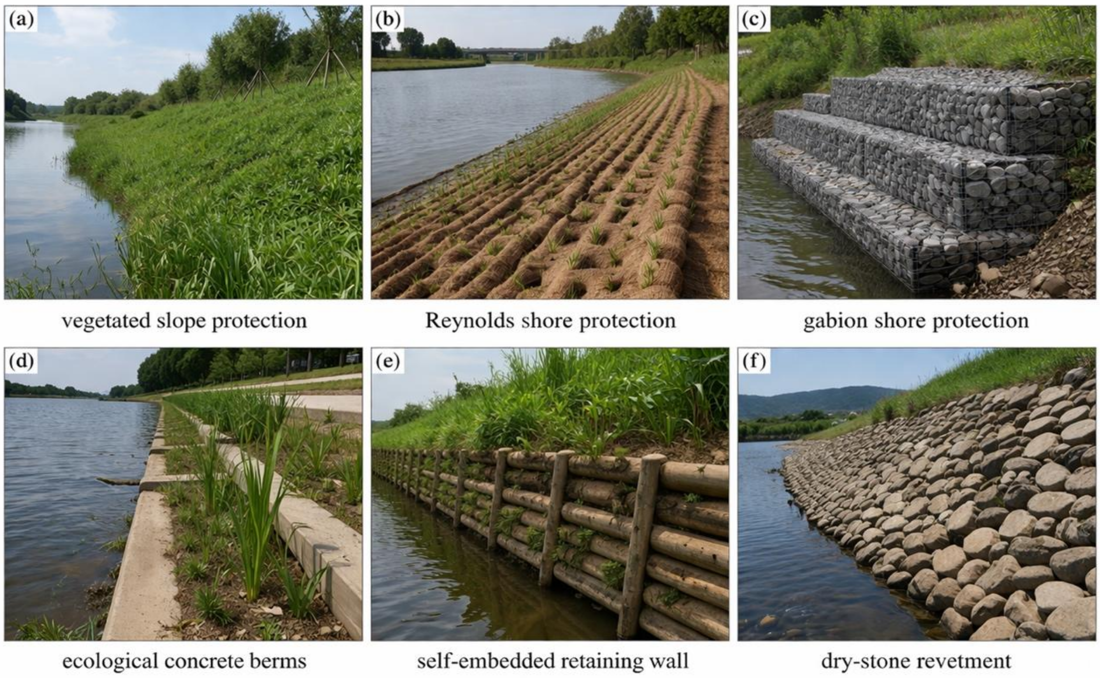

Fig. 2 - Representative examples of ecological slope protection schemes considered in this study: (a) vegetated slope protection; (b) Reynolds shore protection; (c) gabion shore protection; (d) ecological concrete berms; (e) self-embedded retaining wall; (f) dry-stone revetment.

From Tables 1 through 6, we determine that the evaluation level is K=4, with nine indicators (*m*=9). The weights of C_{11}-C_{33} are 0.086, 0.086, 0.257, 0.078, 0.117, 0.234, 0.078, 0.039, and 0.026.Using plant bank protection as an example, define the I-th indicator x_I (I = 1, 2,…, 9) as the set A_I, and the corresponding level 1 evaluation criteria as the set B_1. Construct the set pair $H(A_I,B_1)$ for (I= 1, 2,…, 9).In this example, all indicators are positive. Therefore, formula (8) is used to calculate the 4-element linkage $\mu_{AI\sim B1}=a_I+b_{I,1}I_1+ b_{I,2}I_2+c_IJ$ for each set pair $H(A_I，B_1)$(I=1,2,…,9). The results are presented in Table 8. The nine index values of plant berms constitute the set A, while the level 1 grade standards of the nine indexes constitute the set B. The linkage degree of the set pair *H*(A,B) is calculated using Eqs. (10) and (11) as $\mu_{A\sim B}=f_1+f_2I_1+f_3I_2+f_3J=0.507+0.065I_1+0.162I_2+0.267J$. Similarly, the linkage degree of each set pair for Reynolds mats, geobringer banks, eco-concrete, self-embedded retaining walls, and dry masonry slopes can be calculated. The results are shown in Table 9.

Tab.8 - Calculation of the linkage of each set to $H(A_l,B_1)$

Scheme	degree of contact	$\mu_{A1\sim B1}$	$\mu_{A2\sim B1}$	$\mu_{A3\sim B1}$	$\mu_{A4\sim B1}$	$\mu_{A5\sim B1}$	$\mu_{A6\sim B1}$	$\mu_{A7\sim B1}$	$\mu_{A8\sim B1}$	$\mu_{A9\sim B1}$
vegetated bank protection	a_l	0	0	0	1	1	1	1	0	0
	$b_{l,1}l_1$	0	0	0	0	0	0	0	1	1
	$b_{l,2}l_2$	1	0.889	0	0	0	0	0	0	0
	c_l	0	0.111	1	0	0	0	0	0	0
Reynolds Shore Protection	a_l	0	0	0	1	1	1	0	0	0
	$b_{l,1}l_1$	0	1	0	0	0	0	0	1	1
	$b_{l,2}l_2$	1	0	0	0	0	0	0.052	0	0
	c_l	0	0	1	0	0	0	0.948	0	0
Gabion shore protection	a_l	0	0	0	1	1	1	0	0	1
	$b_{l,1}l_1$	0	1	0.5	0	0	0	0	1	0
	$b_{l,2}l_2$	0	0	0.5	0	0	0	0	0	0
	c_l	1	0	0	0	0	0	1	0	0
Ecological concrete berms	a_l	0	0	0	1	0.5	1	0	1	0
	$b_{l,1}l_1$	0	0.592	0	0	0.5	0	0	0	0
	$b_{l,2}l_2$	0	0.409	1	0	0	0	0	0	1
	cl	1	0	0	0	0	0	1	0	0
Self-embedded retaining wall	a_l	0	1	0	1	0	1	0	1	0
	bl,1l1	0	0.592	0	0	1	0	0	0	1
	$b_{l,2}l_2$	0	0.408	1	0	0	0	0	0	0
	c_l	1	0	0	0	0	0	1	0	0
dry-stone revetment	a_l	0	0	0	1	1	1	0	1	0
	$b_{l,1}l_1$	0.4	0.388	0	0	0	0	0	0	1
	$b_{l,2}l_2$	0.6	0.612	0	0	0	0	0	0	0
	c_l	0	0	1	0	0	0	1	0	0

Tab.9 - Calculation results of the linkage degree of H(A,B) for each program set

Scheme / degree of contact $\mu_{A\sim B}$	vegetated bank protection	Reynolds Shore Protection	Gabion shore protection	Ecological concrete berms	Self-embedded retaining wall	dry-stone revetment
f_1	0.507	0.429	0.455	0.91	0.351	0.468
f_2	0.065	0.151	0.353	0.109	0.194	0.094
f_3	0.162	0.089	0.129	0.318	0.292	0.104
f_4	0.267	0.331	0.164	0.164	0.164	0.335

DOI 10.14311/CEJ.2026.01.0003

RESULTS AND DISCUSSION

Taking λ = 0.5 for plant revetment, h_1=f_1=0.507>λ, thus the ecological effect of plant revetment is judged to be level 1 according to the confidence criterion. Similarly, the ecological effect evaluation grade for Reynolds mat, gabion bank protection, ecological concrete, self-embedded retaining wall, and dry masonry slope protection is determined. The evaluation results using the original AHP-TOPSIS method and various λ values are presented in Table 10.

Tab.10 - Comparison of evaluation results of different methods

Scheme	AHP-TOPSIS[29]	AGA-AHP Fuzzy Set Pairs		
		λ=0.5	λ=0.6	λ=0.7
vegetated bank protection	4	1	3	3
Reynolds Shore Protection	2	3	4	4
Gabion shore protection	1	2	1	1
Ecological concrete berms	3	6	2	2
Self-embedded retaining wall	5	5	2	2
dry-stone revetment	6	4	5	4

Table 6 shows that the weights of the indicators calculated by the AHP and AGA-AHP methods differ between B_1 and C_{11}, B_1 and C_{12}, and B_1 and C_{13}.The results calculated by AGA-AHP are 0.200, 0.200, and 0.600, while those calculated by AHP are 0.2493, 0.1571, and 0.5936. AGA-AHP indicates that the weights of C_{11} and C_{12} are the same, whereas AHP shows that the weight of C_{11} is greater than that of C_{12}. Furthermore, AGA-AHP ranks the weights of C_{31}, C_{32}, and C_{33} from largest to smallest, while AHP ranks them from smallest to largest. The main reason for this discrepancy is that the AHP method calculates weights independently of the consistency test of the judgment matrix, leading to potential inaccuracies in the final weights. In contrast, the AGA-AHP method overcomes this limitation, resulting in more efficient and accurate weight calculations. Therefore, the original literature lacks sufficient accuracy in evaluating the effectiveness of slope protection, leading to discrepancies with the results of this study. The evaluation method applied in this paper is more efficient and yields more accurate evaluation results.

Table 10 shows that three different confidence values have been chosen in this paper, allowing experts with different risk preferences and in various geographic environments to select the appropriate confidence value. When λ is set to 0.5, it is suitable for experts with a higher risk tolerance, who prioritize ecological functionality indicators such as biodiversity index, biological channel patency, and vegetation cover. This paper finds that plant revetment scores higher on these ecological functionality indicators compared to the other five types of revetment. Therefore, at λ = 0.5, plant revetment is the most effective option and aligns with the preferences of experts who are more risk-tolerant and emphasize ecological functionality. In addition, when λ is set to 0.6 or 0.7, the effects of the six bank protection methods are largely similar, with gabion bank protection proving to be the most effective. Under these conditions, the evaluation results are more reliable and stable, making them well-suited for conservative experts. These experts not only consider ecological functionality but also incorporate structural aspects such as durability, impact resistance, and flow velocity. The integration of these multiple factors enhances the accuracy and realism of the evaluation results.

The existing AHP method calculates weights without considering the consistency of the judgment matrix. The weights are calculated independently of the consistency test, and once the judgment matrix is determined, the weights and consistency metrics are fixed and cannot be improved. In this paper, AGA-AHP is utilized to overcome these shortcomings. By integrating the weight calculation into the process, the final evaluation results are more stable and reliable. In addition, AGA-AHP is combined with the fuzzy set-pair evaluation method and employs a confidence criterion to determine the rank of the sample. This approach avoids the subjectivity typically involved in determining the uncertainty component coefficients of the linkage difference.

The methodology of this study scientifically and effectively evaluated the effectiveness of six types of ecological slope protection; however, there were some shortcomings. The AGA-AHP method overcomes the defects of the traditional AHP method in weight calculation, but it is still influenced by subjective factors to a certain extent. To mitigate these subjective influences, objective weighting methods such as entropy weighting, CRITIC weighting, and informativeness weighting can be used. In addition, the selection of slope protection schemes in this study is not exhaustive. Further exploration of various slope protection schemes is needed to make the evaluation results more comprehensive, applicable, and integrated.

Limitations and Future Work

Several limitations should be noted. First, although AGA-AHP improves the consistency of weight calculation, the judgment matrix still depends on expert pairwise comparisons, meaning the final weights remain sensitive to expert selection and subjective preferences. Future work should compare the present weighting strategy with more objective or hybrid methods, such as Entropy, CRITIC, or combined subjective-objective weighting approaches. Second, the current indicator system is static and case-specific. It does not explicitly represent non-linear interactions or time-varying drivers such as extreme rainfall, climate-change-induced hydrological shifts, vegetation succession, or long-term deterioration of protection materials. Extending FSPAAM to incorporate dynamic criteria, multi-period monitoring data, and larger datasets would improve its scalability and engineering realism. Third, while the current verification relies on surveyed engineering schemes and their known performance characteristics, it lacks long-term empirical validation from active construction sites. Therefore, our immediate future research will focus on practical field implementation. We plan to apply this framework to ongoing ecological slope projects in diverse geological regions and conduct long-term field monitoring to track post-construction performance (e.g., vegetation survival rates, structural displacement, and erosion control efficiency). By comparing model predictions with real-world observational data, we aim to calibrate the model parameters and rigorously validate its robustness under varying environmental conditions. This transition from theoretical evaluation to practice-oriented validation will be crucial for bridging the gap between decision-making models and engineering applications.

CONCLUSION

This study evaluated six representative ecological slope protection schemes using the proposed AGA-AHP–FSPAAM framework and obtained differentiated decisions under different confidence levels.

(1) The principal finding is that the preferred scheme changes with risk preference. Plant revetment is the preferred option at $\lambda = 0.5$, indicating better suitability for restoration-oriented and higher-risk-tolerance scenarios, whereas gabion revetment is preferred at $\lambda = 0.6$ and 0.7, indicating stronger suitability for conservative decisions requiring higher structural reliability.

(2) Compared with the reference AHP-TOPSIS approach, the proposed framework better captures the joint influence of weight consistency and decision uncertainty. Its main advantage is that it can translate the same dataset into transparent scheme rankings for different confidence levels, which is valuable for multi-objective ecological slope protection planning.

(3) For engineering implementation, plant-based schemes are recommended where ecological recovery, landscape quality, and habitat connectivity are primary targets and hydraulic conditions are relatively moderate. Gabion revetment is recommended for reaches with stronger flow action or stricter safety requirements. In practice, the framework can be used as a screening tool at the planning and preliminary design stages, and should be combined with site-specific hydraulic, geotechnical, and long-term maintenance assessments before final selection.

ACKNOWLEDGEMENTS

We would like to thank undergraduate students Shi Haoran and Li Ming for their contributions to the evaluation data analysis.

This research was supported by Open Research Fund Program of State Key Laboratory of Water Disaster Prevention (Grant No. 2024490411, 2023490211); National College Students' Innovation and Entrepreneurship Training Program (202310363003); The Key project of University Natural Science Research Project of Anhui Province (KJ2021A0505, 2024AH050111).

REFERENCES

1. WANG, B.; WANG, S.; WANG, B., **2024** Root reinforcement effect of three ecological slope protection plants. *Journal of Hebei Agricultural University*, 47, (04), 117-125, https://link.cnki.net/doi/10.13320/j.cnki.jauh.2024.0062
2. Shen, Y.; Li, Q.; Pei, X.; Wei, R.; Yang, B.; Lei, N.; Zhang, X.; Yin, D.; Wang, S.; Tao, Q., **2023** Ecological Restoration of Engineering Slopes in China—A Review. *Sustainability*, 15, (6), https://www.mdpi.com/2071-1050/15/6/5354
3. Song, G.; Song, X.; He, S.; Kong, D.; Zhang, S., **2022** Soil Reinforcement with Geocells and Vegetation for Ecological Mitigation of Shallow Slope Failure. *Sustainability*, 14, (19), https://www.mdpi.com/2071-1050/14/19/11911
4. Su, H.; Wu, D.; Lu, Y.; Peng, X.; Wang, X.; Chen, W.; Wang, S., **2021** Experimental and numerical study on stability performance of new ecological slope protection using bolt-hinge anchored block. *Ecological Engineering*, 172, https://www.sciencedirect.com/science/article/pii/S0925857421002640
5. Capobianco, V.; Robinson, K.; Kalsnes, B.; Ekeheien, C.; Høydal, Ø., **2021** Hydro-Mechanical Effects of Several Riparian Vegetation Combinations on the Streambank Stability—A Benchmark Case in Southeastern Norway. *Sustainability*, 13, (7), https://www.mdpi.com/2071-1050/13/7/4046
6. Huang, Z.; Peng, Z.; Jiao, W.; Liu, Y.; Xu, Y.; Ma, S., **2024** Field study on vegetation eco-protection technology for red sandstone fill slope against water damage. *Case Studies in Construction Materials*, 20, https://www.sciencedirect.com/science/article/pii/S2214509524004625

7. Ioana-Toroimac, G.; Zaharia, L.; Minea, G.; Moroșanu, G. A., 2017 Using a multi-criteria analysis to identify rivers with hydromorphological restoration priority: Braided rivers in the south-eastern Subcarpathians (Romania). *Science of The Total Environment*, 599-600, 700-709, https://doi.org/10.1016/j.scitotenv.2017.04.209
8. Lu, W.; Arias Font, R.; Cheng, S.; Wang, J.; Kollmann, J., 2019 Assessing the context and ecological effects of river restoration – A meta-analysis. *Ecological Engineering*, 136, 30-37, https://doi.org/10.1016/j.ecoleng.2019.06.004
9. Funk, A.; Martínez-López, J.; Borgwardt, F.; Trauner, D.; Bagstad, K. J.; Balbi, S.; Magrach, A.; Villa, F.; Hein, T., 2019 Identification of conservation and restoration priority areas in the Danube River based on the multi-functionality of river-floodplain systems. *Science of The Total Environment*, 654, 763-777, https://doi.org/10.1016/j.scitotenv.2018.10.322
10. Rey, F.; Bifulco, C.; Bischetti, G. B.; Bochet, E.; Bourrier, F.; Buffin-Bélanger, T.; Cavaillé, P.; Dutoit, T.; Florineth, F.; Graf, F.; et al., 2019 Soil and water bioengineering: Practice and research needs for reconciling natural hazard control and ecological restoration. *Science of The Total Environment*, 648, 1210-1218, https://doi.org/10.1016/j.scitotenv.2018.08.217
11. Koji IKEUCHI, Kenji KANAO , 2003. The approach and the issue to conservation and restoration for river environment in Japan. *Ecology and Civil Engineering*, 5(2), 205–216. https://doi.org/10.3825/ece.5.205
12. Tisserant, M.; Cavaillé, P.; Evette, A.; Poulin, M., 2020 Diversity and succession of riparian plant communities along riverbanks bioengineered for erosion control: a case study in the foothills of the Alps and the Jura Mountains. *Ecological Engineering*, 152, 105880, https://doi.org/10.1016/j.ecoleng.2020.105880
13. Wang Xiaowen; Tan, C.; Sun, D.; Li, J., **2022** Preferred ecological protection scheme for earthquake-damaged slopes of Sichuan-Kowloon Highway. *Highway*, 67, (08), 394-398, https://link.cnki.net/urlid/11.1668.U.20220805.1136.134
14. Tisserant, M.; Cavaillé, P.; Evette, A.; Poulin, M., 2021 Controlling erosion while fostering plant biodiversity: A comparison of riverbank stabilization techniques. *Ecological Engineering*, 172, 106387, https://doi.org/10.1016/j.ecoleng.2021.106387
15. Zhang Xu; Chen, J.; Huang, B., **2021** Experiment and effect evaluation of eco-protection slope on yellow river downstream dik. *Yellow Rrivr*, 43, (06), 46-49+54, https://kns.cnki.net/kcms2/article/abstract?v=_GofKS1StuSmexSxtNaARyJjWSiFxBRNJ3jIemu8_2X98lb6us7f0cS_eSfgMnnkVTqhne3ub0nOwjdnnSaajViMiJWldMmF7OG4K5iySmpIFL6zJI0Ny9O37cl0Cd2uQF7iVybq9iVZTtgsU50nkOeLBbrWk3j7ZvIqyRc5ra4NP9PMVCu7K556kqapm8JS&uniplatform=NZKPT&language=CHS
16. Tisserant, M.; Cavaillé, P.; Evette, A.; Poulin, M., 2024 A functional characterization of bioengineered plant communities along riverbanks. *Ecological Engineering*, 204, 107279, https://doi.org/10.1016/j.ecoleng.2024.107279
17. Wan Bingtong; Bao, X.; Li, A., **2019** Quality evaluation systemand application of ecological slope protection project based on Unascertained-set pair coupling. *Bulletin of Soil and Water Conservation*, 39, (02), 108-114, https://kns.cnki.net/kcms2/article/abstract?v=iJorCDPRxqoaZK7lRfDTLa8KulQPgqU6iFFeobiA6r1977DSt5GVLBnW5lV1LEEjrwimFt5XlD_15gwogEAX3EFJ1Qg4Q8mywERFDmY8TfKzZVVIxMDjX-mgs7VjaRAGtetA9W8eZoMyunSBX_eGDg==&uniplatform=NZKPT&language=CHS
18. Juliang, J.; Yiming, W.; Qiang, F.; Jing, D., **2002** An Accelerated Genetic Algorithm for Computing Ranking Weights in Hierarchical Analysis. *Systems Engineering Theory and Practice*, (11), 39-43, https://kns.cnki.net/kcms2/article/abstract?v=OHSidZhWKUnentoicX0_Rym-D7oH0pOkgE8_ixJe3dxkhIQnI4MBx7lCPCS8bYmYJZ3Fh4iHg0OXwU2cBp2yxc-RON3He93XrP24O8CR0UI-Kf5vsFpFisqxn2HZMmK1QeIYzf4W3ic=&uniplatform=NZKPT&language=CHS
19. Zhou Ke, **2022** Comprehensive evaluation on water resources carrying capacity based on improved AGA-AHP method. *Applied Water Science*, 12, (5), 103, https://doi.org/10.1007/s13201-022-01626-2
20. Ouyang, Y., 2005 Evaluation of river water quality monitoring stations by principal component analysis. *Water Research*, 39, (12), 2621-2635, https://doi.org/10.1016/j.watres.2005.04.024
21. Minatour, Y.; Bonakdari, H.; Aliakbarkhani, Z. S., **2016** Extension of Fuzzy Delphi AHP Based on Interval-Valued Fuzzy Sets and its Application in Water Resource Rating Problems. *Water Resources Management*, 30, (9), 3123-3141, https://link.springer.com/article/10.1007/s11269-016-1335-5
22. Wan, X.; Yang, T.; Zhang, Q.; Yan, X.; Hu, C.; Sun, L.; Zheng, Y., 2021 A novel comprehensive model of set pair analysis with extenics for river health evaluation and prediction of semi-arid basin - A case study of

Wei River Basin, China. *Science of The Total Environment*, 775, 145845, https://doi.org/10.1016/j.scitotenv.2021.145845
23. Zeng, L.; Luo, J.-T.; Yang, Z.-R.; Yu, H.-C.; Wen, W.; Gao, Q.-F.; Zhang, H.-R., **2024** Performance evaluation of vegetation concrete with carbonaceous mudstone aggregates in slope protection under wet-dry conditions. *Bulletin of Engineering Geology and the Environment*, 83, (9), https://link.springer.com/article/10.1007/s10064-024-03827-2
24. Zou, Q.; Zhou, J.; Zhou, C.; Song, L.; Guo, J., 2013 Comprehensive flood risk assessment based on set pair analysis-variable fuzzy sets model and fuzzy AHP. *Stochastic Environmental Research and Risk Assessment*, 27, 525-546, https://doi.org/10.1007/s00477-012-0598-5
25. Jin Juliang; Chen, J.; Zhang, Y., **2005** Fuzzy comprehensive evaluation model based on accelerated parallel genetic algorithm. *Water Resources and Power*, (06), 1-4+89, https://kns.cnki.net/kcms2/article/abstract?v=_GofKS1StuT_YokP3zqkcciGAUdZCD4GMGWCEDkNom061UoxjkzN-IGM2ICDkXk7vl-pivZC-2HVAn96zZVUY6UOtzbig2aq5e8UUS_oT7OF1iNjKFaGAdCHG8y4xqLOsSXVy9E8FnK-p8iiaaecA204TyrTTHUTafMLTcbzfM7KbV_3M1_Y3JgfgKNGa02i&uniplatform=NZKPT&language=CHS
26. Yang, Z.; Wang, Y., 2020 The cloud model based stochastic multi-criteria decision making technology for river health assessment under multiple uncertainties. *Journal of Hydrology*, 581, 124437, https://doi.org/10.1016/j.jhydrol.2019.124437
27. Yang, Z.; Yang, K.; Su, L.; Hu, H., 2020 Two-dimensional grey cloud clustering-fuzzy entropy comprehensive assessment model for river health evaluation. *Human and Ecological Risk Assessment*, 26, (3), 726-756, https://doi.org/10.1080/10807039.2018.1536519
28. Libing, Z.; Yachao, B.; Juliang, J.; Guan, Y. H.; Yuliang, Z.; Ting, Z., **2022** Optimisation of dry limit water level and water supply strategy in irrigation reservoirs based on fuzzy set-pair analysis. *SHUILI XUEBAO*, 53, (10), 1154-1167, https://link.cnki.net/doi/10.13243/j.cnki.slxb.20211136
29. Yi, X., **2020** Evaluation model and application of ecological shore protection based on AHP-TOPSIS. https://link.cnki.net/doi/10.26985/d.cnki.gcsjc.2020.000528
30. Foss, O.; Blenkinsopp, C. E.; Bayle, P. M.; Martins, K.; Schimmels, S.; Almeida, L. P., **2023** Comparison of dynamic cobble berm revetments with differing gravel characteristics. *Coastal Engineering*, 183, https://www.sciencedirect.com/science/article/pii/S0378383923000364
31. Tang, W.; Mohseni, E.; Wang, Z., **2018** Development of vegetation concrete technology for slope protection and greening. *Construction and Building Materials*, 179, 605-613, https://www.sciencedirect.com/science/article/pii/S0950061818312911
32. Cavaillé, P.; Ducasse, L.; Breton, V.; Dommanget, F.; Tabacchi, E.; Evette, A., 2015 Functional and taxonomic plant diversity for riverbank protection works: Bioengineering techniques close to natural banks and beyond hard engineering. *Journal of Environmental Management*, 151, 65-75, https://doi.org/10.1016/j.jenvman.2014.09.028
33. Shutao, Z.; Jun, P.; Hang, C.; Tiancheng, W., **2024** Study on the shallow stability of new assembled ecological protection slopes. *Yangtze River*, 55, (05), 172-177+185, https://link.cnki.net/doi/10.16232/j.cnki.1001-4179.2024.05.023

CIVIL ENGINEERING JOURNAL

Article no. 4

THE CIVIL ENGINEERING JOURNAL 1-2026

REGARDING SEVERAL NEW CRITERIA FOR THE ENERGY-EFFICIENT ENVELOPE'S POTENTIAL ASSESSMENT

Yuriy Biks[1], Georgiy Ratushnyak[2] and Olga Ratushnyak[3]

1. *Vinnytsia National Technical University, Faculty of Construction, Civil and Environmental Engineering, Department of Construction, Architecture and Urban Planning, Vinnytsia, Politekhnichna 7, Ukraine; biks@vntu.edu.ua*
2. *Vinnytsia National Technical University, Faculty of Construction, Civil and Environmental Engineering, Department of Engineering Systems in Construction, Vinnytsia, Politekhnichna 7, Ukraine; ratushnyak@vntu.edu.ua*
3. *Vinnytsia National Technical University, Faculty of Management and Information Security, Department of Business Economics and Production Management, Vinnytsia, Khmelnytske Highway 95, Ukraine; ratushniak@vntu.edu.ua*

Received:	*28.05.2025*
Received in revised form:	*21.01.2026*
Accepted:	*19.03.2026*

ABSTRACT

This paper introduces a set of new criteria for assessing the energy-efficiency potential of multilayered building envelopes, focusing on physically measurable aspects of dynamic thermal performance and LCA parameters. Based on EN ISO 13786:2023, the study considers thermal transmittance (U-value), internal areal heat capacity (k_1), and decrement factor (f) as thermal performance parameters, along with assembly mass (m) and embodied energy (EE) as additional LCA objective indicators. Five wall assemblies common in the Ukrainian market - hempcrete, AAC + Rockwool, Porotherm brickwork + Rockwool, wood-chip cement-bonded blocks (Woodcrete) and ICF systems were evaluated through numerical modelling and comparative analysis. To eliminate subjectivity in criteria weighting, three new interconnected criteria were proposed: Dynamic Thermal Performance Efficiency per mass ($DTPE_m$), per embodied energy ($DTPE_{EE}$), and per both ($DTPE_{m\&EE}$). Results indicate that AAC + Rockwool (Wall B) consistently ranks as the most efficient assembly according to the $DTPE_{m\&EE}$ criteria. At the same time, Wall E (ICF) aligns with the recommended thermal inertia ranges but exhibits the highest embodied energy, resulting in the lowest $DTPE_{m\&EE}$. The study highlights the complexity of MCDA in envelope design and provides physically grounded criteria that can support more objective predesign decision-making.

KEYWORDS

Dynamic thermal performance efficiency, Multilayered assembly, Envelopes, Energy efficiency, Physical parameters

INTRODUCTION

The diverse range of building materials and construction techniques in modern practice has drawn significant attention from multicriteria decision analysis (MCDA) methods [1], particularly for determining building energy efficiency, as evidenced in papers [1], [2], [3], [4]. From a practical perspective, such research aims to identify criteria for energy efficiency that are both interpretable and adjustable [5]. Such criteria are results of complex interconnection of thermal and physical behaviour parameters of the multilayered envelope itself (e.g. U-value [5], [6], [7] thermal inertia [4], [8], [9], internal area heat capacity [5], [10] decrement factor [5], [9]), climate influence (e.g. hot degree days HDD, cool degree days CDD), building orientation towards the sun (e.g. Trombe wall in the south façade, opaque north-oriented wall [11]), etc. All of the studies mentioned above demonstrate that efforts to establish comprehensive criteria for evaluating envelope energy efficiency remain relevant [8]. Meanwhile, one of the major, if not the most crucial, ongoing predesign stage challenges for developers is selecting the "best" option from the vast array of available building envelopes. However, comparisons between alternatives typically involve trade-offs, making the selection of the optimal or "best" solution inherently complex. The term "best" is used here with caution, as a multicriteria assessment of real-life alternatives often suggests that only options within the Pareto set can be deemed the "best" or optimal alternatives [2], [3], [4], [5], [12], [13]. In practice, new criteria could allow the decision-maker to pick the better Pareto-set solution that dominates others by this additional criterion, and provides the most advantageous overall compromise [13].

To facilitate the decision-making process during the early stages of building design, easily calculable physical criteria were chosen, including thermal transmittance (U-value), W/m²K, mass (m, kg/m²), decrement factor (f) and internal area heat capacity (k_1), kJ/m²K, based on dynamic thermal performance standards outlined in Ukraine National Standard DSTU EN ISO 13786 [6] and embodied energy or primary energy of the wall component MJ/m², as the objective LCA marker [14], [15].

LITERARY ANALYSIS AND PROBLEM STATEMENT

In recent decades, the performance assessment of building envelopes has shifted gradually from simple one-dimensional thermal resistance comparisons to integrative frameworks that include dynamic, environmental, and lifecycle-aware indicators [2], [4], [7], [8]. Traditionally, steady-state criteria, such as the thermal transmittance coefficient (U-value), have served as the primary determinant of envelope efficiency. However, as numerous authors have pointed out [8], [15], [16], [17], this parameter alone fails to accurately reflect the dynamic thermal behaviour of constructions and their inertia-related performance, especially under real-time climatic fluctuations [15], [16]. In climates with sharp day-night cycles or seasonally variable thermal loads, parameters such as thermal mass, decrement factor, and phase shift have emerged as crucial in describing a wall's ability to modulate indoor comfort and energy demand [15], [17].

At the same time, material-related physical and mechanical properties, including density, specific heat capacity, and moisture behaviour, influence not only dynamic heat flow but also structural performance and lifecycle impacts. This intersection of thermal behaviour and material ecology has prompted scholars to develop composite indicators aligned with Life Cycle Assessment (LCA) methodologies [5], [18], [19]. Several studies suggest that the embodied energy of materials, coupled with their service life, should be internalised in envelope selection, particularly when aiming to balance operational and embodied performance [15].

However, a comparative deficiency remains in the literature regarding integral metrics that connect physical, mechanical, and lifecycle properties as an actionable selection tool for design optimisation. While LCA tools provide environmental insights, U-value (W/m²K), internal area heat capacity (k_1), kJ/m²K, and the decrement factor (f) reflect thermal parameters that are primary influencers of envelope winter and summer behaviour [8], there is limited methodological convergence between them. Some attempts to bridge this include thermal mass assessments [20], [21] or dynamic-to-static performance coefficients [15]; however, such indicators have yet to be standardised or validated across material groups.

Thus, the current research aims to critically explore new criteria, grounded in physical and mechanical properties, such as internal area heat capacity and decrement factor, as dynamic thermal inertia indices, in conjunction with environmental durability parameters, including Life Cycle Assessment (LCA).

PURPOSE AND TASKS OF RESEARCH

The current research aims to formulate additional criteria for early-stage multilayered assembly design assessment of envelope energy-efficiency potential, based exclusively on physical parameters of envelope materials and taking into account dynamic thermal characteristics as well as embodied energy as the LCA component, which can provide a more objective comparison of different envelope types in terms of their thermophysical and physical-mechanical parameters. This direction is particularly relevant given the rising need for buildings that harmonise material rationality, climate adaptability, and lifecycle sustainability.

To achieve this goal, the following tasks should be solved:

a) a list of envelope types for the medium cost segment of residential buildings, based on the conducted data review, should be revealed.

b) the most significant physical and thermophysical parameters for the complex multi-criteria should be chosen;

c) a complex multi-criteria parameter should be proposed, and the benchmarking of the proposed envelope types should be calculated.

MATERIALS AND METHODS

The physical criteria that could easily be calculated in the early-stage multi-layered assembly design of the construction, such as thermal transmittance (U-value), W/m^{2}K, mass (m, kg/m^2), and internal area heat capacity (k_1), kJ/m^{2}K, as a dynamic thermal performance parameter under EN ISO 13786 [1] for the wall assembly, were taken.

For the calculation of the EE (research LCA framework is limited to the material production stages A1-A3 values only), the MJ/m² of relevant assembly materials was mainly determined using the Baubook Eco2soft online tool [22] and data from the research papers.

The numerical assessment of dynamic thermal performance efficiency parameters, such as thermal transmittance (U-value), W/m²K, the decrement factor (f), and internal area heat capacity (k1), kJ/m²K, was performed using the HTflux [23] freely downloadable Excel-based calculator spreadsheets.

For numerical simulation setup of the dynamic thermal performance efficiency parameters, as well of EE parameter, five types of multilayered wall assemblies, were chosen as popular assemblies in the Ukrainian construction market, namely: Wall A (Hempcrete) as energy efficient and eco-friendly type, Wall B (Aerated autoclaved concrete (AAC) D300 + Rockwool as insulation material) as the affordable cost-efficient type of energy efficient solution; Wall C (Hollow brickwork masonry (Porotherm 38) + Rockwool as insulation material) as traditional reliable ceramic brickwork masonry with energy efficient porous brick, Wall D (Wood-chip cement bonded block) as energy efficient and “retrofitted” technology and Wall E (wood-chip cement bonded block, as one of the promising type of Insulated concrete formwork (ICF), which gained a significant traction in EU, North American and Australian construction market and is commercially distributed under trademarks as ISOTEX [24], [25], Fixolite [26], Isolabloc [27], Isospan [28], Fasswall [29], Nexcem [30], Durisol [31] etc.) as well-known wall construction technology in European, North American and Australian construction markets and new construction technology competitor at the Ukrainian one. In Figures 1-5, there are photos from real construction sites showing the investigated assemblies, and in Figure 6, a detailed cross-section drawing.

Fig. 1 – Hempcrete wall performed by tamping method (Photo taken from [32])

Fig. 2 – AAC façade insulated with stone-wool wall insulator (Photo taken from [33])

Fig. 3 – Layering of hollow ceramic blocks (Porotherm 38, Photo taken from [34])

Fig. 4 – Layering of wood-chip cement-bonded blocks (Photo taken from [35][34])

Fig. 5 – Layering of ISOTEX - ICF wood-chip cement-bonded blocks (Photo taken from [36][35][34])

The dynamic thermal characteristics of each multilayered assembly were determined below under ISO 13786 [6] using the following sequence:

1) Definition of thermophysical properties (ρ, c, λ) for each layer (see Tab.1);
2) Calculation of penetration depth;
3) Determination of dimensionless thickness;
4) Construction of layer transfer matrices;
5) Assembly of the global transmittance matrix;
6) Extraction of dynamic parameters: internal areal heat capacity (k_1), decrement factor (f).

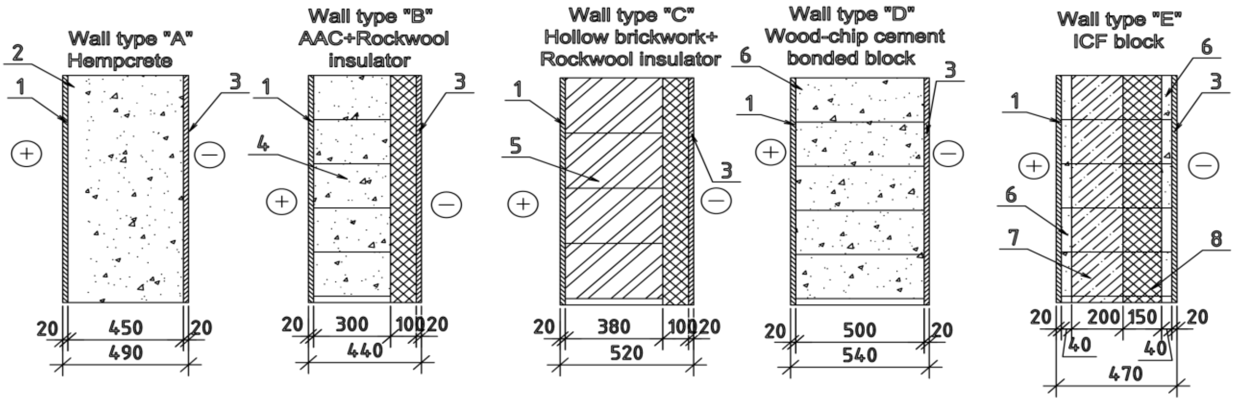

Fig. 6 – Cross-sectional scheme of investigated wall assemblies: (1 - internal lime-sand plaster, 2 - hemcrete, 3 - external lime-sand plaster, 4 - aerated autoclaved concrete (AAC), 5 - hollow brick-work, 6 - wood-chip cement bonded block (woodcrete), 7 - reinforced concrete, 8 - BASF Neopor insulator)

The calculations were implemented in a spreadsheet environment [23] and verified through consistency checks and comparison with literature values (given below).

Thermal transmittance (U-value) under [37] of the aforementioned multilayered assemblies is calculated as follows in Equation (1)

$$\mathrm{U-value} = \frac{1}{R_{si}+\sum_{i=1}^{n}\frac{d_i}{\lambda_i}+R_{se}}, \tag{1}$$

where R_{si}=1/8.7- interior layer thermal resistance, m^{2}K/W [38];
R_{se}=1/23 – exterior layer thermal resistance, m^{2}K/W [38];

DOI 10.14311/CEJ.2026.01.0004

d_i, λ_i – the thickness and thermal conductivity coefficient of the *i*-th layer, respectively.

Penetration depth of the *i*-th layer under [6] is calculated according to the formula (2)

$$\delta_i = \sqrt{\frac{\lambda_i \times T}{\pi \times \rho_i \times c_i}}, \tag{2}$$

where T=24hours – oscillation time, considered for envelopes;
ρ_i, c_i – the density and specific heat capacity of the *i*-th layer.

Dimensionless penetration depth under [6] is calculated as represented in the formula (3)

$$\xi = \frac{d_i}{\delta_i}. \tag{3}$$

Thermal transmittance matrix component of each i-th layer under [6] is calculated as follows in formulae (4)-(6)

$$z11_i = z22_i = \ cos(\ \xi_i \times (1i - 1)), \tag{4}$$

where $1i = \sqrt{-1}$.

$$z12i = -\frac{\delta_i}{2 \times \lambda_i} \times (-1i - 1) \times \ sin(\ \xi_i \times 1i - \xi_i); \tag{5}$$

$$z21i = -\frac{\lambda_i}{\delta_i} \times (-1i - 1) \times \ sin(\ \xi_i \times 1i - \xi_i). \tag{6}$$

Thus, the transmittance matrix of the i-th layer is defined as [6] and is to be arranged as in formula (7)

$$Z_i = \begin{bmatrix} z11_i & z12_i \\ z21_i & z22_i \end{bmatrix}. \tag{7}$$

In case we have a multilayered envelope, the total transmittance matrix will be the product of the total transmittance matrix Z_{tot} of each *i*-th layer, from the interior to exterior, in terms of envelope cross-section, as it is represented in formula (8)

$$Z_{tot} = \prod_{i=1}^{k} Z_i, \tag{8}$$

where $k = 1,2, \ldots, n$ – number of layers.

The boundary layer thermal transmittance matrix under [6] is calculated as follows in formula (9)

$$Z_{s1} = \begin{bmatrix} 1 & -R_{se} \\ 0 & 1 \end{bmatrix}; \tag{9}$$

$$Z_{s2} = \begin{bmatrix} 1 & -R_{si} \\ 0 & 1 \end{bmatrix}. \tag{10}$$

Construction thermal transmittance matrix of multilayered envelope from environment to environment, according to [6], to be calculated as defined in formula (11)

$$Z_{ee} = Z_{s2} \times Z_{tot} \times Z_{s1} \tag{11}$$

Internal area heat capacity (k_1) and decrement factor (f) under [6] are to be calculated as defined in formulae (12)-(13)

$$k_1 = \left| \frac{Z_{ee_{2,2}} - 1}{Z_{ee_{1,2}}} \right| \times \frac{T}{2 \times \pi}; \tag{12}$$

$$f = \frac{\left| \frac{Z_{ee_{2,2}} - 1}{Z_{ee_{1,2}}} \right| \times \frac{T}{2 \times \pi}}{U\text{-}value}, \tag{13}$$

where $Z_{ee2,2}$, $Z_{ee1,2}$–elements of the second column of the second row and the second column of the first row of the construction thermal transmittance matrix, respectively.

The initial thermophysical parameters of the assembly materials used in the current numerical experiment (numerator), obtained from the referenced data range (denominator), are aggregated in Table 1.

Tab. 1 - The initial thermophysical parameters of assembly materials

Assembly material	The thermophysical parameters of materials			Data reference
	Specific heat capacity, *c* (J/kgK)	Density ρ, (kg/m³)	Thermal conductivity λ, (W/m·K)	
Lime-sand plaster	1000	1500	0.67	[39][39]
Hempcrete	$\frac{1200}{1000-1600}$	$\frac{450}{200-627}$	$\frac{0.08}{0.05-0.18}$	[40], [41], [42], [43], [44]
Aerated autoclaved concrete (AAC)	100	275	0.09	[39]
Hollow brickwork masonry (Porotherm 38 W)	1000	745	0.112	[39], [45], [46]
Wood-chip cement-bonded block	$\frac{1400}{1000-1700}$	$\frac{475}{475-587}$	$\frac{0.12}{0.1-0.12}$	[24], [25], [26], [27], [28], [29], [30], [31]
Reinforced concrete	1000	2200	1.65	[22], [39]
BASF Neopor insulator	$\frac{1450}{1200-1600}$	$\frac{16}{15-25}$	$\frac{0.031}{0.031-0.032}$	[39][22], [39], [47]
Stone wool wall insulator (Rockwool®)	$\frac{1030}{800-1030}$	$\frac{70}{30-200}$	$\frac{0.034}{0.033-0.045}$	[39]

For the calculation of the EE (research focuses only on the material production stages A1-A3 values of the LCA framework), the MJ/m² of each assembly was determined using the Baubook Eco2soft online tool [22]. The output influence parameters for all the assemblies are calculated in Table 2.

Tab. 2 - Calculated parameters for researched assemblies

Influence parameter	Wall type "A"	Wall type "B"	Wall type "C"	Wall type "D"	Wall type "E"
U-value, W/m²K	0.17*	0.15	0.15	0.22	0.17
m, kg/m²	262.50	149.50	350.10	335.00	540.39
k_1, kJ/m²K	39.955	37.369	43.742	43.551	40.073
f	0.013	0.115	0.007	0.007	0.052
EE, MJ/m²	833.55**	594	951	889	770

*For simplicity, the timber frame input is not taken into consideration;
**For Wall A, the *EE* value was calculated as:

$$3.5 \cdot 0.45 \cdot 450 + 2.08 \cdot 2 \cdot 0.02 \cdot 1500 = 833.55 \frac{MJ}{m^2},$$

where 3.5 – *EE* of hemp-lime composite, MJ/kg, taken from [44];

2.08 – *EE* for one-layer plastering mortar for external OC lime (1500 kg/m³), MJ/kg, taken from Eco2soft database [22][22];

0.45, 0.02 – hempcrete wall and external and internal plaster thicknesses, respectively, m;

450, 1500 – densities of the hempcrete wall and plaster, respectively, kg/m³ (see Table 1).

From the analysis of Table 2, it can be seen that all the researched assemblies meet the minimum permissible reduced heat transfer resistance for enclosing structures of residential and public buildings, as required in Ukraine. $R_{qmin} = 4.0 \frac{m^2\mathrm{K}}{\mathrm{W}}$ [49][49], or by a more convenient unit $\mathrm{U-value} = \frac{1}{R_{qmin}} = 0.25 \frac{\mathrm{W}}{m^2\mathrm{K}}$ with significant energy efficiency potential (wall B and wall C, respectively, with the same $\mathrm{U-value} = 0.15 \frac{\mathrm{W}}{m^2\mathrm{K}}$. Wall A and Wall E also demonstrate a sufficient level of $\mathrm{U-value} = 0.17 \frac{\mathrm{W}}{m^2\mathrm{K}}$. The last preferable Wall type from the perspective of thermal transmittance is Wall D with $\mathrm{U-value} = 0.22 \frac{\mathrm{W}}{m^2\mathrm{K}}$.

To ensure the reliability of the results, the calculated dynamic parameters were compared with reference ranges reported in several relevant studies on the thermal inertia of building envelopes [8], [15], [16], [50], [51], [52] The values of the decrement factor and internal specific heat capacity fall within expected ranges for similar constructions, confirming the validity of the applied methodology.

From the dynamic performance characteristics, such as (k_1) and (f), together with the U-value, which are considered significant influencers of summer and winter behaviour [8], the overall picture of the preferred wall assembly becomes more complicated. The comparison of the (k_1) versus density shows that the massive wall assemblies will possess a higher value of internal area heat capacity (k_1), which is neither good nor bad. The higher (k_1) value should provide more comfortable interior temperatures on a hot summer day due to its greater heat-accumulation capacity.

Geographically, Vinnytsia city, a representative city of central Ukraine, was selected as an example city. The construction of the aforementioned assemblies was numerically modelled on a typical July day (to see the "true" picture without HVAC intervention) to provide a graphical representation of temperature and heat-flow attenuation, as an additional aspect of wall dynamic behaviour. The climate of the aforementioned city can be described as follows:

- Humid continental climate - warm summer, no dry season (climate zone Dfb by Köppen–Geiger Classification) [53]; Cold winters often below 0 °C, warm summers (average July ≈ 19 - 21 °C [53][54]), precipitation fairly evenly distributed year-round [55]; Climate is heating-dominated. Heating Degree Days for a typical year (HDD) = 3676 °C·days/year (base 20 °C, [55]); Indicates high heating demand during a long heating season (roughly October–April);
- Reflects low cooling demand, with only short periods of summer overheating. Cooling Degree Days (CDD) are not presented in the current version of Norm [55], but could be approximately evaluated for a typical year as $D \times (T_{av} - T_{base}) \approx 8 \times (23.5 - 22) \approx 12$ °C·days/year, where D – days through the year with average diurnal temperature T_{av} higher than the threshold T_{base} = 22°C;
- Thermal design focus: insulation, thermal mass, and minimising heat losses; Summer overheating is moderate, but it can matter for lightweight buildings. Input data for HTflux modelling [23] are presented in Table 3.

Tab. 3 - Initial data for dynamic simulation of the Wall A

Mean temperature side 1 (ext.):	25.5°C	Mean temperature side 2 (int.):	25.0°C
Temp. Amplitude side 1 (ext.):	9.0°C	Temp. Amplitude side 2 (int.):	1.5°C
Time of max. Temp side 1 (ext.):	15:00	Time of max. Temp side 2 (int.):	17:00

Figure 7 illustrates results from the dynamic heat-flow simulation on both the external and internal sides of each wall, including heat flow and temperature fluctuations, as output from the HTflux spreadsheet [23].

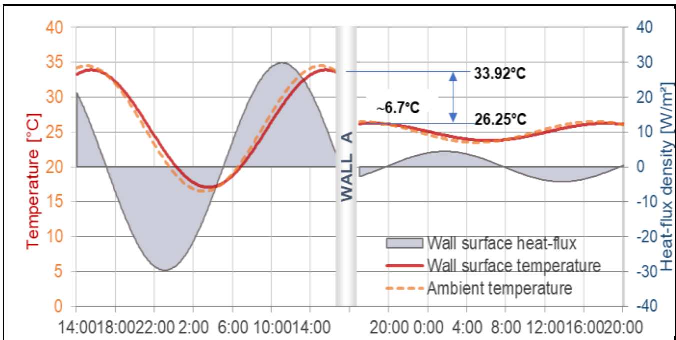

Building component surface temperature	
side 1	side 2
Max: 33.92°C	Max: 26.25 °C
Min: -17.08°C	Min: 23.77 °C
Range: 16.84°C	Range: 2.47 °C
Building component heat flux	
side 1	side 2
Max: 29.85W/m²	Max: 4.43 W/m²
Min: -29.68 W/m²	Min: -4.26 W/m²
Range: 59.52 W/m²	Range: 8.69 W/m²

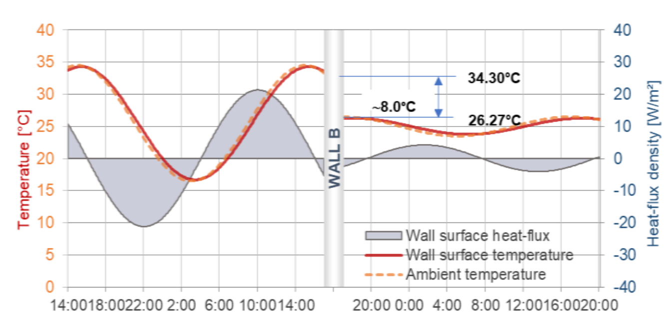

Building component surface temperature	
side 1	side 2
Max: 34.30 °C	Max: 26.27 °C
Min: -16.69 °C	Min: 23.75 °C
Range:17.60 °C	Range: 2.52 °C
Building component heat flux	
side 1	side 2
Max: 21.35 W/m²	Max: 4.23 W/m²
Min: -21.20 W/m²	Min: -4.07 W/m²
Range: 42.55 W/m²	Range: 8.30 W/m²

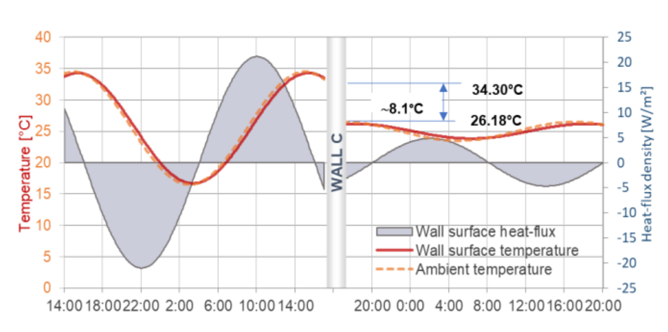

Building component surface temperature	
side 1	side 2
Max: 34.30 °C	Max: 26.18 °C
Min: -16.70 °C	Min: 23.84 °C
Range:17.60 °C	Range: 2.34 °C
Building component heat flux	
side 1	side 2
Max: 21.17 W/m²	Max: 4.84 W/m²
Min: -21.02 W/m²	Min: -4.69 W/m²
Range: 42.19 W/m²	Range: 9.53 W/m²

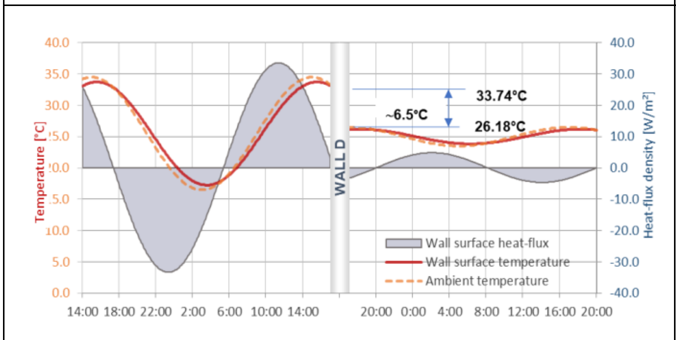

Building component surface temperature	
side 1	side 2
Max: 33.74 °C	Max: 26.18 °C
Min: -17.25 °C	Min: 23.84 °C
Range: 16.49 °C	Range: 2.34 °C
Building component heat flux	
side 1	side 2
Max: 33.56 W/m²	Max: 4.85 W/m²
Min: -33.34 W/m²	Min: -4.64 W/m²
Range: 66.90 W/m²	Range: 9.49 W/m²

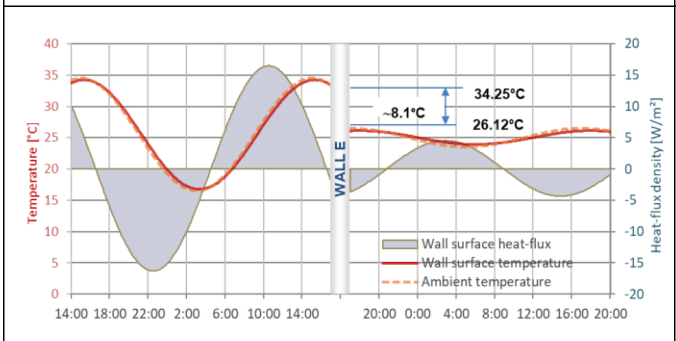

Building component surface temperature	
side 1	side 2
Max: 34.25 °C	Max: 26.12 °C
Min: -16.74 °C	Min: 23.90 °C
Range: 17.50 °C	Range: 2.21 °C
Building component heat flux	
side 1	side 2
Max: 16.49 W/m²	Max: 4.53 W/m²
Min: -16.32 W/m²	Min: -4.36 W/m²
Range: 32.81 W/m²	Range: 8.89 W/m²

Fig. 7 – Diurnal heat flow simulation for walls in July

Analysis of Figure 7 tabled data and a quantitative picture of heat-flaw and temperature behaviour leads to such intermediate takeaways:

- Despite significant differences in material composition, all wall types demonstrate a comparable internal thermal response. The interior surface temperature amplitudes remain within a narrow range (2.2 - 2.5 °C), while the internal heat flux amplitudes are similarly limited (4 - 5 W/m²). This indicates that all configurations provide an adequate level of indoor thermal stability under the considered climatic excitation.
- Substantial differences are observed at the external surface. The maximum external heat flux varies significantly between wall types (≈16–34 W/m²), indicating that the interaction between the building envelope and the outdoor environment is highly dependent on the wall structure.

The results confirm a clear functional separation of roles within multilayer assemblies:

- The external layer primarily governs the intensity of heat exchange with the environment, as reflected by the external heat flux amplitude ($q_{max,\ ext}$). This behaviour is strongly linked to the surface layer's thermal effusivity.
- The internal mass distribution controls the attenuation of the thermal wave, quantified by the decrement factor (f), and the heat storage capacity, expressed by (k_1).
- A low decrement factor does not necessarily imply a low external heat flux. In particular, the wood-chip concrete wall (Type D) exhibits one of the lowest decrement factors while simultaneously producing the highest external heat flux. This behaviour can be interpreted as a "high-intensity thermal accumulator", which efficiently absorbs heat but interacts strongly with the external environment.
- In contrast, configurations incorporating external insulation (notably wall Type C) effectively decouple the external environment from the internal thermal mass. This leads to both reduced external heat flux and strong attenuation of the thermal wave. As a result, such assemblies achieve a more balanced performance.
- The hempcrete wall (Type A) demonstrates a well-balanced behaviour, combining moderate external heat flux with satisfactory attenuation and heat capacity. Conversely, the AAC-based wall (Type B) shows limited thermal inertia despite low external fluxes. In contrast, the ICF-type wall (Type E) minimises external heat exchange but utilises internal mass less effectively.
- The comparison between hempcrete and wood-chip cement-bonded concrete walls further highlights that, when boundary layers are identical, differences in performance are primarily driven by the internal core properties. In this case, variations in thermal effusivity of the core material have only a secondary influence on the external/internal flux ratio. At the same time, the decrement factor remains the dominant parameter governing internal heat flux.
- The study demonstrates that the dynamic thermal performance of building envelopes cannot be fully characterised by traditional parameters such as thermal transmittance or decrement factor alone. Instead, a multi-criteria perspective is required.
- An extended evaluation framework incorporating (k_1), (f), and (q_{max}) provides a more comprehensive basis for optimising multilayer wall assemblies than existing standards. This approach enables a more physically consistent interpretation of heat transfer processes and supports the development of energy-efficient and thermally stable building envelopes.

All the aforementioned evidence demonstrates that thermal inertia plays a crucial role in dynamic simulation and can be incorporated into multi-criteria optimisation and the pre-design assessment of building energy efficiency performance.

On the other hand, as stated in [40], in the case of countries with a hot summer climate, to which, as we evident, Ukraine can also be enlisted, in retrospect of harsh climate changes, especially in the recent few decades, the recommended range of dynamic thermal parameters, valid for energy efficient envelopes with $\mathrm{U-value} < 0.3\frac{\mathrm{W}}{m^2\mathrm{K}}$ are $0.04 \le f \le 0.08$ for decrement factor and $k_1 \ge 40\frac{kJ}{m^2\mathrm{K}}$ for internal area heat capacity. This is also correlated with revealed recommendations for designers – a range of high thermal inertia levels $k1 \ge 30\frac{kJ}{m^2\mathrm{K}}$ for assemblies with no too low a decrement factor value $f{\sim}0.07$ [8].

To determine which of the assemblies considered in current research meet the recommended ranges for both dynamic characteristics, a scatterplot in Figure 8 shows the dependence of internal area heat capacity (k_1) on the decrement factor (f) for five assemblies.

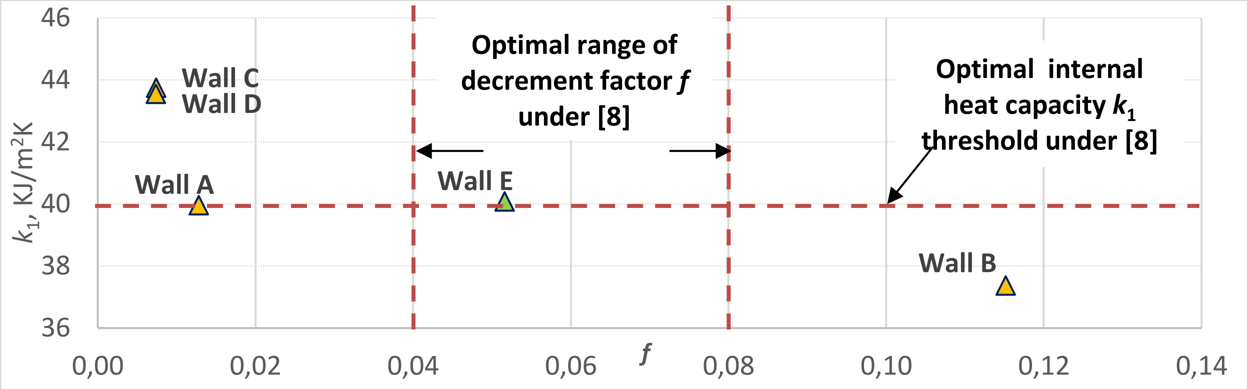

Fig. 8 – Factual arrangement of researched assemblies in terms of recommended (k_1) and (f) values

From Figure 8, it can be seen that only Wall E (marked in green) of all the researched types of assemblies falls within the recommended range of the (k_1) and (f) values. Wall B has the highest decrement factor (f) and the lowest (k_1) value, indicating that it has the lowest damping effect on the incoming heat flow, according to [2]. Walls A, C and D have a low decrement factor (f) with a good (k_1) value.

Thus, since this research involves more than one characteristic to compare (in the current study, there are five physical parameters), multicriteria decision analysis (MCDA) is applicable.

In this regard, new physically based criteria for energy efficiency assessment are proposed, which are aimed at eliminating the subjectivity of parameter weights, weighted sums, and other commonly used data manipulations that involve different units for calculating the goal function (e.g. weighted aggregation), aimed at interconnecting physical parameters to obtain global super criteria, which should be minimised or maximised.

For such a purpose, three criteria were proposed:

1) Dynamic thermal performance efficiency per mass m of the assembly, $DTPE_m$. This metric demonstrates how good the considered assembly is if we need to assess how much heat a material can store in terms of its mass, as shown in formula (14)

$$DTPE_m = \frac{k_1}{m} \tag{14}$$

2) Dynamic thermal performance efficiency per (EE) of the assembly, $DTPE_{EE}$, criteria which reflect how much thermal inertia of the assembly (k_1) is represented in terms of assembly (EE), as follows in formula (15)

$$DTPE_{EE} = \frac{k_1}{EE} \tag{15}$$

3) Dynamic thermal performance efficiency per mass (m) and (EE) of the assembly, $DTPE_{m\&EE}$, criteria which reflect how much thermal inertia of the assembly (k_1) is represented in terms of assembly mass (m) and (EE), as follows in formula (16)

$$DTPE_{m\&EE} = \frac{k_1}{EE \times m} \tag{16}$$

This formula provides a measure of how much heat a material can store relative to the energy required to produce it (EE) and its mass (m). It helps choose materials that are both energy-efficient and environmentally friendly - a higher value means the material is better at storing heat for less environmental cost (lower embodied energy); a lower value means the material requires more energy to produce for the amount of heat it stores, indicating lower thermal efficiency in terms of its environmental impact. As can be seen from the constituents of formulae (14)-(16), all the proposed criteria should be maximised.

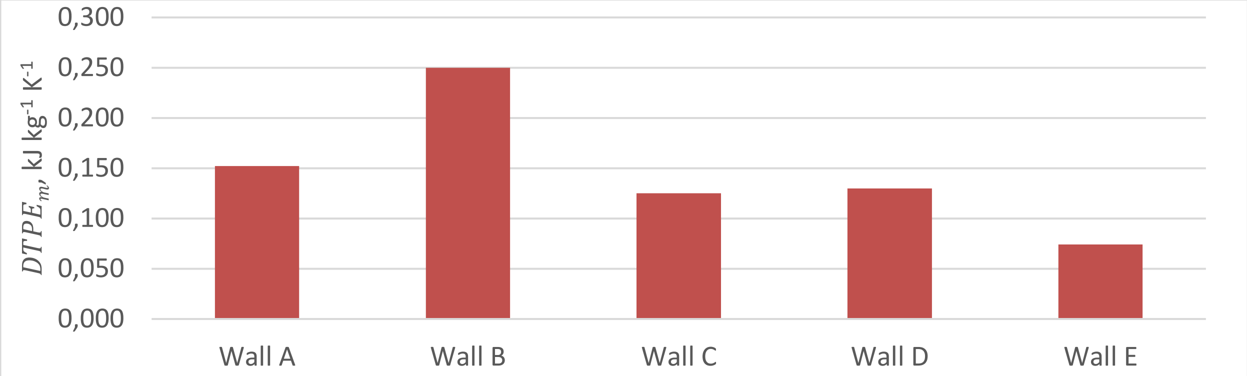

Fig. 9 – Dynamic thermal performance efficiency per mass m of the assembly $DTPE_m$, KJ/Kkg

From Figure 9, it can be seen that Wall B is the better alternative in terms of mass, as per the proposed criteria. Walls A, D and C have the same level of dynamic thermal performance. The Wall E can be considered the least preferable assembly in terms of the mass criteria. On the other hand, if we consider the EE criteria, the overall picture of the wall's preferences will change slightly (see Figure 10).

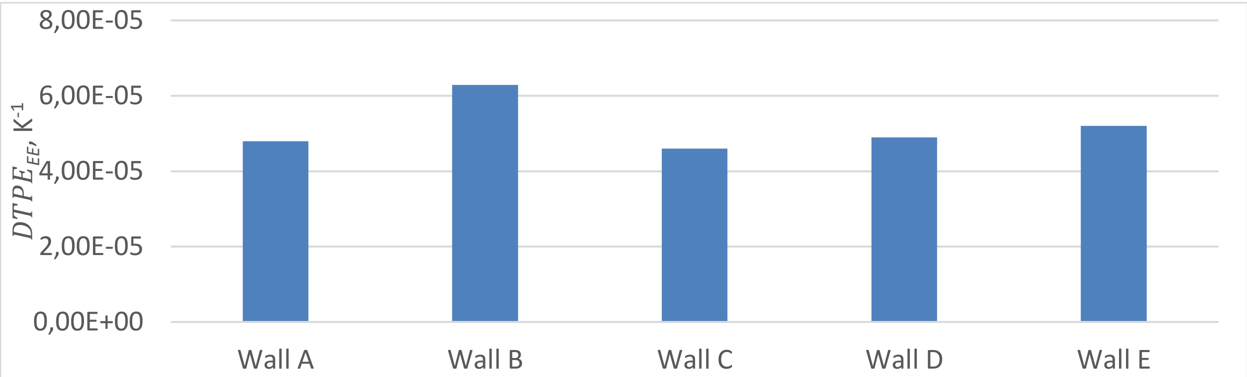

Fig. 10 – Dynamic thermal performance efficiency per embodied energy EE of the assembly $DTPE_{EE}$, 1/K

From Figure 10, it can be seen that Wall B remains the best alternative according to the proposed criteria; the remaining assemblies, namely Walls A, C, D, and E, exhibit approximately equal levels of (*EE*). Figure 11 illustrates the impact of both (*m*) and (*EE*) parameters on the proposed criteria.

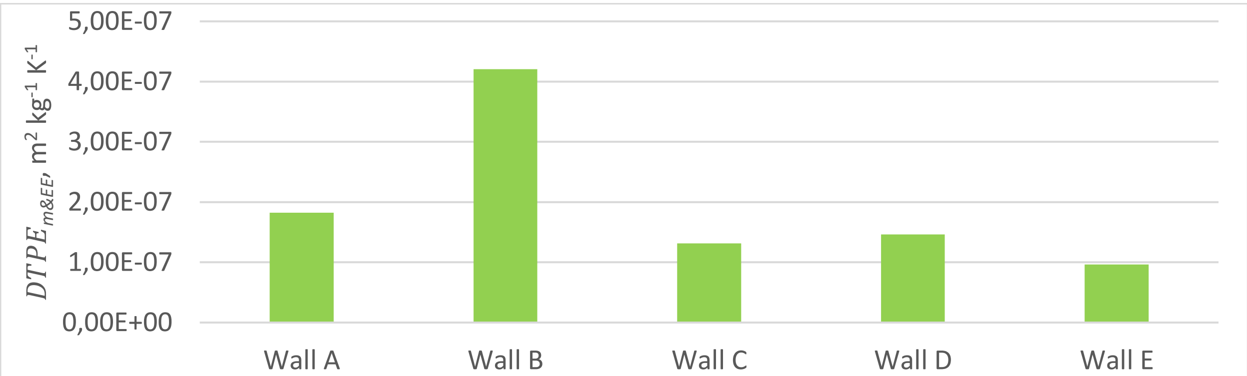

Fig. 11 - Dynamic thermal performance efficiency per mass m and embodied energy EE of the assembly $DTPE_{m\&EE}$, m^2/Kkg

From Figure 11, which illustrates how the value preferences change due to the product of the assembly mass (*m*) and embodied energy (*EE*), according to formula (16), been slightly changed with domination of Wall B as the best assembly and Wall E as the worst one, meanwhile, the relative values of the wall alternatives evaluations differences, given in Figure 9 and Figure 11, are non-evident. It can be concluded that the preference tendency of wall assemblies, reflected in Figure 9 (mass (*m*) parameter) and Figure 11 (mass (*m*) and embodied energy (*EE*) parameters), follows a similar pattern. This can be explained by minor differences in the (*EE*) parameter (Figure 10), which, when multiplied by (m), directly influence the values illustrated in Figure 11.

To perform a comparative analysis of the obtained results, illustrated in Figures 9 - 11, the ranking of the suggested criteria results, both with the factual criteria values, is aggregated in Table 5.

Tab. 5 - Factual arrangement of researched assemblies in terms of proposed criteria

Govern criteria		Wall A	Wall B	Wall C	Wall D	Wall E
Absolute value	$DTPE_m$, [kJ kg^{-1} K^{-1}]	0.152	0.250	0.125	0.130	0.074
	$DTPE_{EE}$, [K^{-1}]	4.79E-05	6.29E-05	4.60E-05	4.90E-05	5.20E-05
	$DTPE_{m\&EE}$, [m^2 kg^{-1} K^{-1}]	1.83E-07	4.21E-07	1.31E-07	1.46E-07	9.63E-08
Results ranking*	$DTPE_m$	4	1	5	3	2
	$DTPE_{EE}$	2	1	4	3	5
	$DTPE_{m\&EE}$	2	1	4	3	5

*1- the best, 5 - the worst.

From Table 5, it can be seen that Wall B is the best alternative according to all three of the proposed criteria. Wall D possess the third position. The rest of the assemblies, namely Wall A, C and E, have different ranks according to the proposed criteria, and their preference are arguable.

DISCUSSION OF THE RESULTS OF THE RESEARCH

The comparative analysis of the investigated multilayer wall assemblies reveals several fundamental aspects of their dynamic thermal behaviour under periodic boundary conditions:

Assessing the typical wall assemblies in terms of the proposed dynamic thermal performance inertia *DTPE* criteria has shown that Wall B is the “undisputable best” assembly, considering both mass *m* and embodied energy *EE* parameter with rank 1 (Excellent); Wall D possesses the medium position with rank 3 (Satisfactory); Wall A, C, and E have non-obvious and arguable preference order, thus they can have unexpectedly competitive options. Meanwhile, the $DTPE_{EE}$ preference order has the same pattern as well in $DTPE_{m\&EE}$ case considerations, with rank 2 (Good) for Wall A, rank 4 (Poor) for Wall C and rank 5 (Unsatisfactory) for Wall E. Dynamic thermal performance criteria $DTPE_m$ slightly differs from the evaluations of embodied energy $DTPE_{EE}$ and $DTPE_{m\&EE}$ considerations given above with rank 4 (Poor) for Wall A, rank 5 (Unsatisfactory) for Wall C and rank 2 (Good) for Wall E.

Notably, Wall E aligns with the recommendations of the (k_1) and f values ranges, and thermo-physically, but in terms of embodied energy, it occupies the last position.

It should be noted that the proposed criteria do not aim to replace traditional optimisation methods but rather to complement them by providing physically interpretable indicators. The results demonstrate that different criteria can yield conflicting rankings, highlighting the inherently multi-objective nature of envelope design, even when based solely on the physical properties of envelope materials, while accounting for dynamic thermal characteristics and embodied energy as the LCA component.

CONCLUSION

Among the results of the research, the following can be considered the most valuable:

(1) Three new criteria for providing early-stage multilayered assembly design assessment of envelope energy-efficiency potential, based exclusively on physical parameters of envelope materials, by considering dynamic thermal characteristics (decrement factor (*f*), internal area heat capacity (k_1), kJ/m²K as well as embodied energy (*EE*), MJ/m² as the LCA component, were proposed in current research.

(2) The thermal transmittance coefficient (U-value) can be considered only in the early stages of decision-making as the primary determinant of envelope efficiency; however, this parameter alone fails to accurately reflect the dynamic thermal behaviour of constructions and their inertia-related performance.

(3) Dynamic thermal performance parameters, such as, but not restricted to, decrement factor (*f*) and internal area heat capacity (k_1), are valuable parameters for effective assembly design in the early multilayered design stage, by utilising the recommended ranges of both for different climate zones, respectively, for energy-efficient envelopes with $\mathrm{U-value} < 0.3\frac{\mathrm{W}}{m^2\mathrm{K}}$, such as $0.04 \leq f \leq 0.08$ and $k_1 \geq 40\frac{kJ}{m^2\mathrm{K}}$ for internal area heat capacity for hot climates. In the current research, the Wall E (ICF block) is the only one that met the recommended range of (*f*) and (k_1) for the five assemblies used in the research.

(4) The easily calculable physical dynamic thermal performance efficiency criteria *DTPE* can be used as a predesign metric for both, based on inertia-related performance assembly performance, outlined in EN ISO 13786 [1]. Consideration of the embodied energy (*EE*) or primary energy of the wall component MJ/m², as the objective LCA marker [14], [15] was proposed.

(5) Benchmarking of considered assemblies in terms of dynamic thermal performance efficiency criteria based on assembly mass m ($DTPE_m$), assembly embodied energy (*EE*) ($DTPE_{EE}$), and both assembly mass (*m*) and (*EE*) ($DTPE_{m\&EE}$) revealed that:

a) Wall A and C have a non-obvious and arguable preference order based on the proposed criteria - rank 2 (Good) and rank 4(Poor) for Wall A, and rank 4(Poor) and rank 5 (Unsatisfactory) for Wall C, respectively;
b) Wall B is the "undisputable best" assembly, considering both mass (*m*) and the embodied energy (*EE*) parameter with rank 1 (Excellent). However, it is out of the recommended range of decrement factor (*f*) that is shown in limited thermal inertia despite low external fluxes;
c) Wall D possesses the medium position with rank 3 (Satisfactory);
d) Wall E meets the recommended range of decrement factor *f* and internal area heat capacity k_1, but has the rank 2 (Good) only from the term of $DTPE_m$ (mass (*m*) consideration). However, Wall-E shows the rank 5 (Unsatisfactory) in terms of assembly embodied energy (*EE*) ($DTPE_{EE}$) and both assembly mass (*m*) and (*EE*) ($DTPE_{m\&EE}$).

It is essential to highlight that the assembly's ranking will vary depending on the alternatives being compared. In one case, "the worst" can be the optimal given the available assemblies; in another, "the best" can be the unsatisfactory rank, and the results may be contradictory, requiring additional verification and analysis to confirm the "best" choice among the proposed alternatives.

Current research can be determined as the next step in the conceptual evaluation attitude, exclusively based on measurable physical parameters with emphasise on the dynamic thermal characteristics and embodied energy as the LCA component, which can provide a more objective comparison of different envelopes types in terms of their thermophysical and physical-mechanical parameters, by elimination of the subjectivity of any data manipulations, such as parameter weights, weighted sums, and other commonly used methodologies that involve normalising the different parameter's units for calculating the goal function (e.g. weighted aggregation).

LIST OF SYMBOLS

c	Specific heat capacity [kJ kg^{-1} K^{-1}]
f	Decrement factor
k_1	Internal area heat capacity of assembly [kJ m^{-2} K^{-1}]
$q_{max,\ ext}$	External heat flow intensity, [W m^{-2}]
T	Oscillation period [h]
U-value	Thermal transmittance coefficient of assembly [W m^{-2} K^{-1}]
Z_{ee}	Thermal transmittance matrix of a multilayered assembly
Z_i	Thermal transmittance matrix of the i-th layer of assembly
Z_{s1}	Boundary layer thermal transmittance matrix (exterior)
Z_{s2}	Boundary layer thermal transmittance matrix (interior)
$z11_i$	Thermal transmittance matrix component of the i-th layer of assembly
$z12_i$	Thermal transmittance matrix component of the i-th layer of assembly [m^2 K W^{-1}]
$z21_i$	Thermal transmittance matrix component of the i-th layer of assembly [W m^{-2} K^{-1}]
$z22_i$	Thermal transmittance matrix component of the i-th layer of assembly

Abbreviations

$DTPE_m$	Dynamic thermal performance efficiency per mass of the assembly [kJ kg^{-1} K^{-1}]
$DTPE_{EE}$	Dynamic thermal performance efficiency per embodied energy of the assembly [K^{-1}]
$DTPE_{m\&EE}$	Dynamic thermal performance efficiency per mass and embodied energy of the assembly [m^2 kg^{-1} K^{-1}]
EE	Embodied energy of assembly [MJ m^{-2}]

Greek symbols

λ	Thermal conductivity coefficient [W m^{-1} K^{-1}]
δ	Heat flux penetration depth [m]
ρ	Density [kg m^{-3}]
ξ	Dimensionless heat flux penetration depth

REFERENCES

[1] Thakkar, J. J. (2021). Multi-criteria decision making (Vol. 336, pp. 1-365). Singapore: Springer. https://doi.org/10.1007/978-981-33-4745-8

[2] Basińska, M. (2017). The use of multi-criteria optimisation to choose solutions for energy-efficient buildings. Bulletin of the Polish Academy of Sciences. Technical Sciences, 65(6). https://doi.org/10.1515/bpasts-2017-0084

[3] Wang, J. J., Jing, Y. Y., Zhang, C. F., & Zhao, J. H. (2009). Review of multi-criteria decision analysis in aid of sustainable energy decision-making. Renewable and sustainable energy reviews, 13(9), 2263-2278. https://doi.org/10.1016/j.rser.2009.06.021

[4] Biks Y., Ratushnyak, G., & Ratushnyak, O. (2019). Energy performance assessment of envelopes from organic materials. Architecture, Civil Engineering, Environment, 12(3), 55-67. https://doi.org/10.21307/acee-2019-036

[5] Brojan, L., Petric, A., Clouston, P. L. (2013). A comparative study of brick and strawbale wall systems from environmental, economical and energy perspectives. ARPN Journal of Engineering and Applied Sciences, 8, 920–926.

[6] Ukrainian National Standard. DSTU EN ISO 13786:2023 Thermal performance of building components – Dynamic thermal characteristics – Calculation methods (2023). (Official edition) Kyiv: Institute of Technical Thermophysics of the National Academy of Sciences of Ukraine (in Ukrainian).

[7] Alkhatib, H., & Lemarchand, P. (2024). Assessing Thermal Performance: An Experimental Study on U-Value Variability in Building Fabric Elements. Results in Engineering. https://doi.org/10.1016/j.rineng.2024.103730

[8] Stazi, F. (2017). Thermal Inertia in Energy Efficient Building Envelopes. Butterworth-Heinemann. https://doi.org/10.1016/C2016-0-00641-1

[9] Humaish, H.H., Marmoret, L., & Beji, H. (2018). Effect of thermal inertia (time lag and decrement factor) on the insulation thermal capacity. 2018 International Conference on Advance of Sustainable Engineering and its Application (ICASEA), 137-141. https://doi.org/10.1109/icasea.2018.8370971

[10] Ferrari, S., & Zanotto, V. (2016). Approximating Dynamic Thermal Behaviour of the Building Envelope. https://doi.org/10.1007/978-3-319-24136-4_2

[11] Pérez, G., Allegro, V.R., Alonso, C., Martín-Consuegra, F., Oteiza, I., Frutos, B., & Guerrero, A. (2019). Selection of suitable materials for the development of an innovative thermochromic Trombe wall. Advances in Building Energy Research, 15, 146 - 160. https://doi.org/10.1080/17512549.2019.1684364

[12] Auf Hamada, A., Raslan, R., & Hong, S. (2023). A framework for parametric multi-criteria decision analysis (P-MCDA) for building retrofits. Building Simulation Conference Proceedings. https://doi.org/10.26868/25222708.2023.1519

[13] Kovalenko, I., Davydenko, Y., Shved, A. (2020). Searching for Pareto-Optimal Solutions. In: Shakhovska, N., Medykovskyy, M.O. (eds) Advances in Intelligent Systems and Computing IV. CSIT 2019. Advances in Intelligent Systems and Computing, vol 1080. Springer, Cham. https://doi.org/10.1007/978-3-030-33695-0_10

[14] Asdrubali, F., Grazieschi, G., Roncone, M., Thiébat, F., & Carbonaro, C. (2023). Sustainability of Building Materials: Embodied Energy and Embodied Carbon of Masonry. Energies. https://doi.org/10.3390/en16041846

[15] Reilly, A., Kinnane, O., & O'Hegarty, R. (2020). Energy embodied in, and transmitted through, walls of different types when accounting for the dynamic effects of thermal mass. Journal of Green Building, 15(4), 43-66. https://doi.org/10.3992/jgb.15.4.43

[16] Oktay, H., Argunhan, Z., Yumrutaş, R., Işık, M. Z., & Budak, N. (2016). An investigation of the influence of thermophysical properties of multilayer walls and roofs on the dynamic thermal characteristics. Mugla Journal of Science and Technology, 2(1), 48-54

[17] Verbeke, S., & Audenaert, A. (2018). Thermal inertia in buildings: A review of impacts across climate and building use. Renewable and sustainable energy reviews, 82, 2300-2318. https://doi.org/10.1016/j.rser.2017.08.083.

[18] Barbhuiya, S., & Das, B. B. (2023). Life Cycle Assessment of construction materials: Methodologies, applications and future directions for sustainable decision-making. Case Studies in Construction Materials, 19, e02326. https://doi.org/10.1016/j.cscm.2023.e02326.

[19] Young, L., Kaminski, S., Kovacs, M., & Zea Escamilla, E. (2024). A Comparative Life Cycle Assessment (LCA) of a Composite Bamboo Shear Wall System Developed for El Salvador. Sustainability, 16(17), 7602. https://doi.org/10.3390/su16177602

[20] Childs, K. W., Courville, G. E., & Bales, E. L. (1983). Thermal mass assessment: an explanation of the mechanisms by which building mass influences heating and cooling energy requirements (No. ORNL/CON-97). Oak Ridge National Lab.(ORNL), Oak Ridge, TN (United States). https://doi.org/10.2172/5788833

[21] Reilly, A., & Kinnane, O. (2017). The impact of thermal mass on building energy consumption. Applied Energy, 198, 108-121. https://doi.org/10.1016/j.apenergy.2017.04.024

[22] Eco2soft. Life cycle assessment of buildings. Retrieved June 28, 2025, from: https://www.baubook.at/eco2soft/?SW=27&LU=1823785713&qJ=1&LP=b4BKI&lng=2.

[23] A brief guide and free tool for the calculation of the thermal mass of building components. Retrieved February 18, 2026, from: https://www.htflux.com/en/free-calculation-tool-for-thermal-mass-of-building-components-iso-13786/

[24] Isotex. (n.d.). Isotex: Wood-cement blocks for construction. Retrieved June 5, 2025, from https://en.blocchiisotex.com/

[25] Isotex Srl. (2025) Product catalogue. Retrieved July 19, 2025 from https://www.blocchiisotex.com/wp-content/uploads/2025/02/product-catalogue-isotex-worldwide.pdf

[26] Fixolite. (2009). Brochure: Blocs de construction isolants en aggloméré bois-ciment. La performance au service de l'éco-construction [document PDF]. Retrieved June 22, 2025, from http://www.fixolite.be/sites/fixolite.be/files/Brochure_Blocs_Fixolite_ENTETE_VERTEmodif.pdf

[27] Isolabloc. (2025). Le futur se construit. Retrieved June 22, 2025, from http://www.isolabloc.fr

[28] Isospan. (2025). Technical Data and Product Range. Retrieved June 29, 2025, from https://www.isospan.eu/cms/upload/dlmstat/index.php?sprache=en

[29] Fasswall®. Build your natural, non-toxic home with this remarkable wood-chip concrete building block. Retrieved March 20, 2026, from https://faswall.com/

[30] Nexcem. Insulated Concrete Forms without Styrofoam. Retrieved March 20, 2026, from https://nexcembuild.com/

[31] Durisol. DURISOL ICF INSULATED CONCRETE FORMS FOR AUSTRALIA. Retrieved March 20, 2026, from https://www.durisol.com.au/

[32] Костробетон — революційна новинка на ринку екобудівництва (Hemcrete – a new revolutionary innovation on the ecobuilding maket) Retrieved March 20, 2026, from https://zelenasadyba.com.ua/dim-i-podvirya/kostrobeton.html (in Ukrainian)

[33] Утеплення будинку з газобетону зовні: як правильно це зробити? (House exterior insulation – how to perform it correctly?) Retrieved March 20, 2026, from http://gazobloki.lviv.ua/uteplennya-budinku-z-gazobetonu-zovni-yak-pravilno-ce-zrobiti/ (in Ukrainian)

[34] Porotherm 38 P+W. Retrieved March 20, 2026, from https://info-haus.com/product/porotherm-38-p-w/ (in Ukrainian)

[35] Будинок з арболіта — будівництво будинку своїми руками (House made of arbolit — DIY construction). Retrieved March 20, 2026, from https://stroyfibra.com.ua/budinok-z-arbolita-budivnictvo-budinku-svoimi-rukami/ (in Ukrainian)

[36] Building Better with ISOTEX. Retrieved March 20, 2026, Retrieved March 20, 2026, from https://murotex.co.uk/about-us/

[37] Ukrainian National Standard. DSTU N B V.2.6-101:2010. (2010). Constructions of buildings and structures. Method for determination of thermal resistance of building envelopes. Kyiv, Institute of Technical Thermophysics of the National Academy of Sciences of Ukraine (in Ukrainian).

[38] Filonenko, O. I., Yurin, O. I. (2015). (Construction and Thermal Physics of Building Enclosures: A manual (Poltava: Poltava National Technical University named after Yuri Kondratyuk), (in Ukrainian).

[39] Ukrainian National Standard. DSTU 9191:2022. (2022). Thermal insulation of buildings. Method for selecting thermal insulation material for building insulation. (Official edition). Kyiv: Ministry of Economy of Ukraine (in Ukrainian).

[40] Shea, A., Lawrence, M., & Walker, P. (2012). Hygrothermal performance of an experimental hemp-lime building. Construction and Building Materials, 36, 270–275. https://doi.org/10.1016/j.conbuildmat.2012.04.123

[41] Le, A. T., Maalouf, C., Mai, T. H., Wurtz, E., & Collet, F. (2010). Transient hygrothermal behaviour of a hemp concrete building envelope. Energy and buildings, 42(10), 1797-1806. https://doi.org/10.1016/j.enbuild.2010.05.016

[42] Evrard, A. (2008, May). Transient hygrothermal behaviour of lime-hemp materials (Doctoral thesis). Ecole Polytechnique de Louvain, Unité d'Architecture.

[43] Walker, R., & Pavia, S. (2014). Moisture transfer and thermal properties of hemp-lime concretes. Construction and Building Materials, 64, 270-276. https://doi.org/10.1016/j.conbuildmat.2014.04.081

[44] Florentin, Y., Pearlmutter, D., Givoni, B., & Gal, E. (2017). A life-cycle energy and carbon analysis of hemp-lime bio-composite building materials. Energy and Buildings, 156, 293-305. https://doi.org/10.1016/j.enbuild.2017.09.097

[45] Porotherm – Wall solutions. Retrieved July 20, 2025 from https://porotherm.com.ua/pdf/Porotherm_P_W_RU.pdf

[46] Porotherm Technical datasheet Porotherm BIO Inc. 38 T. Retrieved July 20, 2025, from https://www.infobuild.it/wp-content/uploads/Porotherm-BIO-inc-38-25-19-T.pdf

[47] Neopor® – a Raw Material for Diverse Solutions. Retrieved July 19, 2025 from https://neopor.de/portal/load/fid1225927/Neopor_Thermal_insulation.pdf

[48] Rockwool SIUPERROCK. Retrieved July 20, 2025, from https://www.rockwool.com/ua/products-and-applications/products/ua-diy/SUPERROCK-UA/

[49] Ukrainian National Building Code. Thermal insulation and energy efficiency of buildings: DBN V.2.6-31:2021 (2021). (Official edition). Kyiv: Ministry for Communities and Territories Development of Ukraine. (in Ukrainian).

[50] Stazi, F., Ulpiani, G., Pergolini, M., & Di Perna, C. (2018). The role of areal heat capacity and decrement factor in case of hyper insulated buildings: An experimental study. Energy and Buildings, 176, 310-324. https://doi.org/10.1016/j.enbuild.2018.07.034

[51] Shaik, S., & Setty, A. B. T. P. (2013). Analytical computation of admittance, decrement factor, time lag and surface factors for different exterior wall materials of the buildings in Dakshina Kannada district. In Proc. 22th Natl. 11th Int. ISHMT-ASME Heat Mass Transf. Conf.
[52] Kalinović, S. M., Djoković, J. M., Nikolić, R. R., & Hadzima, B. (2019). Calculation of the thermal dynamic performance of the residential buildings' walls. Quality Production Improvement-QPI, 1.
[53] Kottek, M., Grieser, J., Beck, C., Rudolf, B., & Rubel, F. (2006). World map of the Köppen-Geiger climate classification updated
[54] Ukrainian National Standard. Energy efficiency of buildings. Method for calculating energy consumption during heating, cooling, ventilation, lighting and hot water supply: DSTU 9190:2022 (2022). (Official edition). Kyiv: Ministry for Communities and Territories Development of Ukraine. (in Ukrainian).
[55] Ukrainian National Standard. Energy efficiency of buildings. Building climatology: DSTU N B V.1.1-27:2010 (2010). (Official edition). Kyiv: Minregionbud of Ukraine. (in Ukrainian).

CIVIL ENGINEERING JOURNAL

Article no. 5

THE CIVIL ENGINEERING JOURNAL 1-2026

FUNDAMENTAL FREQUENCY VARIATION ANALYSIS OF CABLE-STAYED BRIDGES WITH DAMAGE CAUSED BY SUDDEN INCIDENTS

Hu Dandan[1], Baozhen Yan[2]

1. *School of Intelligent and Construction Engineering, Harbin University, No.109 Zhongxing Road, Harbin, Heilongjiang Province, China; Hardandan@163.com*
2. *Heilongjiang Province Highway Bridge Survey Design Co. Ltd., No. 90 Qingbin Road, Harbin 150040, China*

Received: 07.12.2024

Received in revised form: 10.09.2025

Accepted: 27.03.2026

ABSTRACT

Cable-stayed bridges have become one of the fastest growing and most competitive bridge types in modern bridge engineering due to their large spanning capacity and novel structure. Rapid economic development has led to a gradual increase in the number of vehicles transporting flammable and explosive products, as well as an increase in the incidence of bridge fires. Cable-stayed cables are usually close to the carriageway, and a fire will inevitably cause varying degrees of harm to the cable-stayed cables of a bridge in the event of a fire, leading to significant economic losses. Dynamic performance of cable-stayed bridges after fire is investigated by different simulation analyses of fire-induced damage to the tension cables. Results show that different tie damage has different effects on the dynamic characteristics of the whole bridge, and the tie damage has the greatest effect on the vertical symmetric bending formation, and almost no effect on the longitudinal drift, transverse bending and torsion formations. Damage to the outer cables near the transition span and side spans has a large effect on the low-order frequency variation of cable-stayed bridges, especially when the damage to the outermost back cables of S13+N13 occurs, it has the largest effect on the 2nd and 3rd order frequency variation, with a maximum value of 9.6%. Different levels of damage to the tension cables affect the dynamic performance of the bridge in terms of quantitative changes, with the frequency of a certain order formation increasing as the level of damage increases. It is particularly important to quickly and accurately analyze and evaluate the mechanics of overfire cable-stayed bridges to provide an accurate basis for decision-making.

KEYWORDS

Cable-stayed bridges, Cable-stayed cables, Sudden incidents, Fire, Fundamental frequency variation

INTRODUCTION

In recent years, with the increase in the number of automobiles and the acceleration of bridge construction, the probability of fire in the process of bridge construction and operation has increased, and the hazards of fire for bridges have received more and more attention. Fires caused by vehicles account for the majority of bridge fires [1-4]. Cable-stayed cables are usually in close proximity to the travel lanes, and fires, when they occur, will inevitably cause varying degrees of harm to the cable-stayed cables of a bridge [5-8].

Vehicle fire is a fortuitous event, due to the type of vehicle at the time of the incident is different, so that when the fire occurs cable-stayed cables in the fire at different temperatures, resulting in cable-stayed cables with varying degrees of damage, mild impact to the cable-stayed cables outside the HDPE sheath, so that the sheath charred and melted, and the serious can lead to the entire cable-stayed cables fracture [9-12]. In recent years, scholars at home and abroad have carried out more researches on the fire resistance of prestressed concrete structures, but there are fewer researches on the damage of cable-stayed bridges under fire, among which there are even fewer analyses on the force effects of cable-stayed bridges after damage of the cables [13-15].

In August 2011, a tanker loaded with 24 tons of gasoline had a rear-end collision with another coal hauling truck at Caogou Bridge in Yulin City's YuYang District, severely damaging the tank, leaking a large amount of gasoline, and starting a fire [16]. In January 2013, an oil truck in the Anqiu section of National Highway 206, Qingyunhu Lake bridge accidentally hit the bridge abutment, resulting in the rupture of the tank, the tank 30 tons of 93 gasoline leakage, the formation of a fire, gasoline plus the wind, the fire burned for a whole day, causing serious damage to the bridge [17].

At present, there is a lack of research on cable damage, especially in the case of cable fire damage, the overall performance of the bridge is more prominent impact and evaluation. This paper takes the bridge fire accident as the engineering background, and it is especially important to study the dynamic performance of cable-stayed bridges after the fire through different simulation analyses of fire-induced damages of tie cables by using the damage theory and finite element theory, which provides an accurate basis for decision makers to make decisions.

ENGINEERING BACKGROUND

In 2011 the bridge had a traffic accident, the car on fire near the cable-stayed cables burned, the accident damaged cable-stayed cables a total of two, respectively, for the north bank upstream of the N13, upstream of the N12 two back of the cable-stayed cables, two cable-stayed cables PE protective materials partially burned, cable-stayed cables there are obvious traces of damage by the fire, the two cable-stayed cables all appear to be exposed steel wire, cable-stayed cables of high-strength steel wire did not find the protruding deformation, wire breakage phenomenon. Upstream N12 cable-stayed cables PE protective material burned length of 16.5 m, upstream N13 cable-stayed cables PE protective material burned length of 5 m, set aside the burnt material, revealing the cable-stayed cables steel wire, steel wire surface color has a certain degree of discoloration. The damage to the cable is shown in Figure 1.

Fig.1 - Fire diagram of two back cables on the downstream side of the north bank

Main bridge adopts double-tower and double-surface semi-floating system combined with cable-stayed bridges, and approach bridge adopts prestressed concrete continuous box girder structure length of the bridge is 1268.86 m, the main bridge is 696 m long, the approach bridge is 572.86 m long, the main bridge adopts the form of 44 m (transition span)+136 m (side span)+336 m (main span)+136 m (side span)+44 m (transition span) bridge span arrangement, the design load: automobile-super 20 level, trailer-120, four lanes in both directions. Four lanes in both directions. The overall arrangement of the whole bridge and the panoramic arrangement of the whole bridge, as shown in Figure 2.

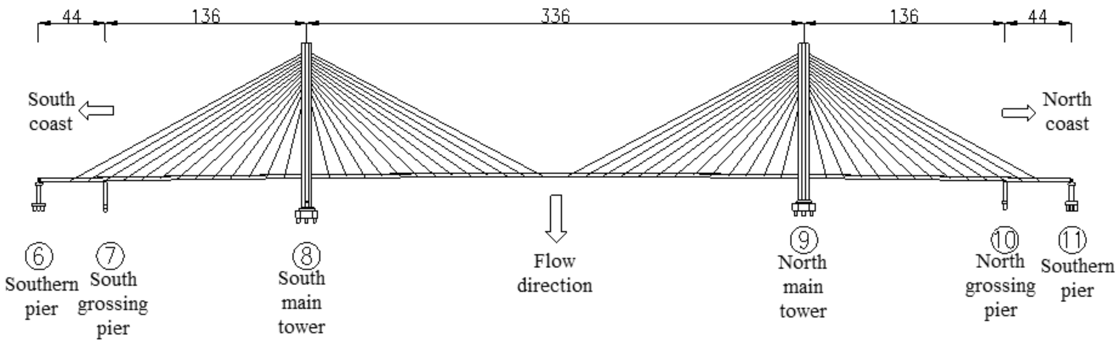

Fig.2 - Overall layout of the main bridge (unit: m)

(1) Bridge tower

Cable tower is a portal tower, set up the upper and lower beams. There is a lower crossbeam below the bridge deck and an upper crossbeam above the bridge deck, and the 2 crossbeams divide the bridge tower into three parts: the upper, middle and lower pylons. South tower is 110.80 m high, north tower is 106.10 m high, and the crossbeam of the tower is hollow box girder. Cross-sections of beams and tower columns are enlarged and strengthened with chamfers. A stiffening skeleton is provided in the wall of the tower. Inside the tower, there is a pedestrian ladder leading to the top of the tower. Pedestrian entrances are located at the top of the lower beam and the tower wall at the bridge deck.

(2) Main girder of the main bridge

Main girder section with two I-beam side beam ribs, cross girder and small longitudinal girder in the middle, combined with concrete deck slabs to form a combined section. Rib spacing of the two

I-beam side girders is 29.2 m. The girder height at the Bussel Road is 2.2 m, and the girder height at the centerline of the bridge is 2.47 m. The ratio of the girder height to the main span is 1/136, and the height-to-width ratio of the cross-section is 1/13.4.

(3) Cable-stayed cables

This bridge adopts hot-extruded polyethylene semi-parallel cable-stayed cables, and the cable-stayed cables are made of φ7 low relaxation prestressed galvanized high strength steel wire. Concentric and concentric twisting 2°~4°, outsourcing PE protective material. The total number of 52 pairs of cables in the bridge is 163~367 wires. The design cable strength is 3940 kN~8870 kN, and the layout of the cables on the north and south banks is shown in Figure 3.

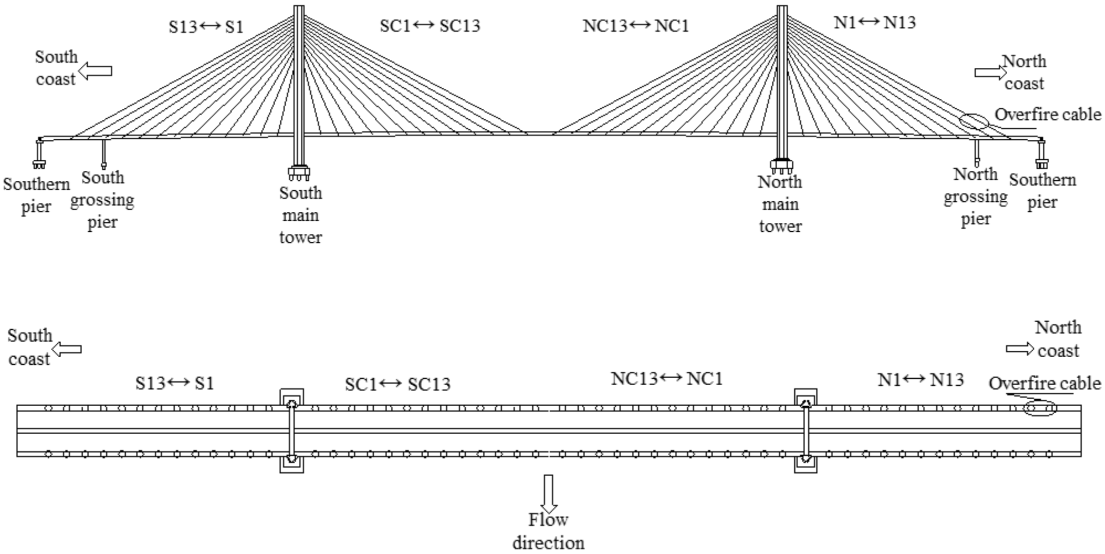

Fig.3 - Layout of cable on the north and south banks

DAMAGE MECHANISM of CABLE-STAYED CABLES

To study damage in structures, it is first necessary to choose the appropriate state parameter, damage variable, that characterizes the damage. Damage varies due to the diversity of substances. Differences in damage exogenous factors lead to different damage for the same substance [18-22].

Cable-stayed cables subjected to fire damage, according to the previous description of the damage mechanism of the cable-stayed cables for simulation, for the fire caused by high-strength steel wire bundle strand fracture, fracture of the steel wire part of the complete withdrawal from the work, for the fire did not melt off the steel wire, according to the occurrence of the temperature of the member of the overfire when the modulus of elasticity, ultimate strength calculations, the calculation of the specific method of calculation in combination with the previous high-temperature after the material characteristics of the steel for the calculations. Load carrying capacity of a cable is only related to the effective load bearing area of the cable $\tilde{A}$, and the study of cable damage is based on statistical theory. Take the entire high-strength steel wire bundle strand of the cable-stayed cables as a continuous medium, the ratio of the area of the fractured high-strength steel wire $(A-\tilde{A})$ to the area of the original high-strength steel wire of the cable-stayed cables is defined as the damage rate, as the damage variable *D* in the damage mechanism of the cable-stayed cables, then:

$$\zeta = \left(A-\tilde{A}\right)/A = 1-\tilde{A}/A \tag{1}$$

After the damage to the material is assumed to break part of the steel wire for the second group of composite materials, according to the “law of mixing” of composite materials, after the damage to the cable-stayed cables of the modulus of elasticity, the ultimate strength of the cable-stayed cables for:

$$E_\xi = E(1-\zeta) + E_K\zeta$$

$$\sigma_\xi = \sigma(1-\zeta) + \sigma_K\zeta \tag{2}$$

Among them: ζ —Proportion of voids to the whole wire rope;

E —Modulus of elasticity of the non-destructive high-tensile steel wire;

E_K —Elastic modulus of the cavity;

σ_K —Limiting strength of the cavity.

Due to the elastic modulus of the cavity $E_K = 0$, the ultimate strength $\sigma_K = 0$ then:

$$E_\xi = E(1-\zeta)$$

$$\sigma_\xi = E(1-\zeta) \tag{3}$$

For partially ablated cable-stayed cables the modulus of elasticity and ultimate strength shall be discounted in accordance with the above formula, and for cable-stayed cables affected by overfire the modulus of elasticity and ultimate strength of the steel wire after high temperatures shall be discounted in accordance with the degradation law of elasticity and ultimate strength of the steel wire after high temperatures as described in the preceding paragraphs.

Take a cable-stayed cables as an example, assuming that the cable-stayed cables are multiple parallel steel wire cable-stayed cables, and some of the steel wires are melted after the fire, and assuming that the cable-stayed cables have a damage rate ζ of 30%, then according to equation (3) $E_\xi = E(1-\zeta) = E(1-30\%) = 70\%E$; $\sigma_\xi = \sigma(1-\zeta) = \sigma(1-30\%) = 70\%\sigma$.

Assuming that the temperature of the high-tensile steel wire in the cable-stayed cables under the action of fire is 900 ℃, and then according to the degradation model of elastic modulus and ultimate strength of the high-tensile steel wire after the fire, the modulus of elasticity and the ultimate strength of the cable-stayed cables after the fire will be reduced to 80.5% and 17.12% respectively of the original one, then the modulus of elasticity of the cable-stayed cables will be equivalent to $E^* = 70\%E80.5\% = 1.0988\times10^5 MPa$, the limiting strength equivalent is $\sigma^* = 70\%\sigma80.5\% = 884MPa$

Therefore, the modulus of elasticity and ultimate strength of the cable-stayed cables after overfire are calculated as:

$$E_\xi = (1-\zeta)E_{st}$$

$$\sigma_\xi = (1-\zeta)\sigma_{st} \tag{4}$$

Among them: E_{ξ} —Modulus of elasticity of the whole cable after overfiring;

σ_{ξ} —Ultimate strength of the whole cable after overfiring;

ζ —Proportion of fused wire to the entire wire rope;

E_{st} —Modulus of elasticity of the unfused high-tensile steel wire in the cross-section of the cable after overheating at high temperature;

σ_{st} —Ultimate strength of the high-tensile steel wire after high temperature without fusing in the cross section of the cable after overheating.

FINITE ELEMENT ANALYSIS

Modeling

Finite element model of cable-stayed bridges was established by Midas/Civil. Main girder, small longitudinal beams, crossbeam: Both sides of the steel main girder ribs, small longitudinal beams and crossbeams are simulated by beam units, the steel main girder ribs are the main load-bearing members, which are connected with the middle small longitudinal beams through steel crossbeams to form a space girder lattice structure, the steel crossbeams are connected with the main girder and the small longitudinal beams through the common nodes. Concrete bridge deck slabs are simulated by means of a uniform force form, which is loaded on the main girder ribs, small longitudinal girders and cross girders connected to them. Bridge towers are modeled using beam units. Top and bottom beams are connected to the portal tower columns by shared nodes. The simulation of cable-stayed cables is carried out by using truss unit, the upper end of the cable establishes a node at the outer edge of the bridge tower, the lower end establishes a node at the outer edge of the steel main girder, and the two ends of the cable are connected with the bridge tower and the main girder by stiffening arms. A total of 1,933 nodes and 2,272 units are established for the whole bridge. A total of 104 cable-stayed cables are simulated by truss units, and the main tower and main girder, which are subject to bending pressure, are simulated by beam units. The damage to the cables in the text is achieved by reducing the elastic modulus of the stay cables. By adjusting the elastic modulus of the stay cables, the mechanical performance changes of the cables under different degrees of damage can be equivalently simulated. Structural finite element discretization diagram is shown in Figure 4.

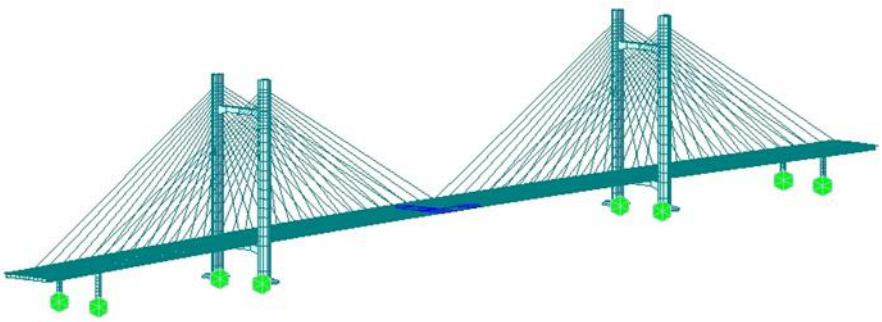

Fig.4 - Structural finite element discretization

DOI 10.14311/CEJ.2026.01.0005

Analysis of Structural Dynamics Under Symmetric Fire-Induced Meltdown of Cables

S1+N1, S3+N3 are selected as two working conditions for the fused damage of cables at the tower root, S6+N6, S8+N8 are two working conditions for the fused damage of cables at the middle of the span, and S11+N11, S13+N13 are two working conditions for the fused damage of cables at the outer back cables, and in total, six conditions are selected for the comparative analysis of the impacts of the auxiliary spans and side spans of the cable power. Table 1 shows the frequency and formation results of different symmetrical fusion damage of cables in the main span. SC1+NC1 and SC3+NC3 are selected as two working conditions for the fusion damage of cables at the tower root of the main span, SC6+NC6 and SC8+NC8 are selected as two working conditions for the fusion damage of cables at the 1/4L of the main span, SC11+NC11 and SC13+NC13 are selected as two working conditions for the fusion damage of cables at the middle of the span, which is a total of 6 working conditions for the comparative analysis of the impact of main span cable dynamics. conditions for the comparative analysis of the dynamic impact of the main span cables.

Tab. 1 - Structural intrinsic frequencies and formations for different cable symmetric fire-induced fusion cases in the main span

Ordinal number	Non destructive model frequency	Formation	Ordinal number	Non destructive model frequency	Formation
1	0.127	Drifting vertically	11	1.133	Beam positive symmetrical vertical bending + tower positive symmetrical smooth bending
2	0.363	First-order symmetrical vertical bending of beams	12	1.219	Beam antisymmetric vertical bending + tower antisymmetric smooth bending
3	0.460	First-order antisymmetric vertical bending of beams	13	1.244	Beam positive symmetrical vertical bend
4	0.472	South towerfirst-order lateral bend	14	1.364	Beam opposes symmetrical vertical bend
5	0.488	North tower first-order lateral bend	15	1.447	Beam symmetric torsion + tower symmetric lateral bending
6	0.651	First-order symmetric transverse bending of beams	16	1.531	Beam positive symmetrical vertical bending + tower positive symmetrical smooth bending
7	0.733	Second-order symmetric vertical bending of beam + symmetric smooth bending of tower	17	1.566	Beam symmetric transverse bending + tower positive symmetric downward bending
8	0.839	Second-order antisymmetric vertical bending of beam + antisymmetric smooth bending of tower	18	1.606	Beam positive symmetrical vertical bending + tower positive symmetrical smooth bending
9	0.890	Positive symmetric vertical bending at beam height order	19	1.649	Beam antisymmetric torsion + tower antisymmetric side bending
10	1.003	Beam high-order antisymmetric vertical bending + tower antisymmetric smooth bending	20	1.687	Beam antisymmetric transverse bending + tower antisymmetric smooth bending

Figures 5 and 6 show the frequency-order plots and frequency-variation-order plots for the first 20 orders of various operating conditions for different cables fused at the transition span and side spans. It can be seen that the amount of change in frequency is very small, with the largest variation in the S13+N13 condition, where the maximum frequency variation is only 9.6%.

In order to facilitate the analysis of the frequency variation-order diagrams for different working conditions are listed separately, and Figures 7 to 9 show the frequency comparison diagrams for the transition span and inside side span, mid-span and outside working conditions, respectively.

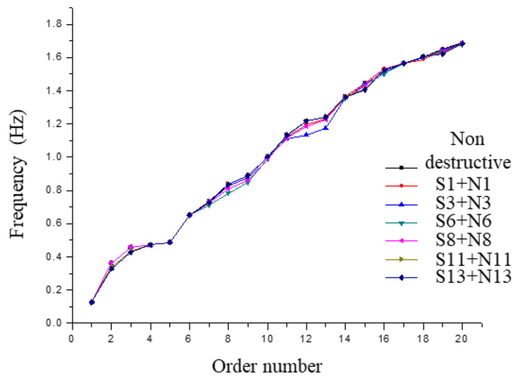

Fig.5 - Frequency-order variation under fire-induced meltdown of different cables in transition span and side spans

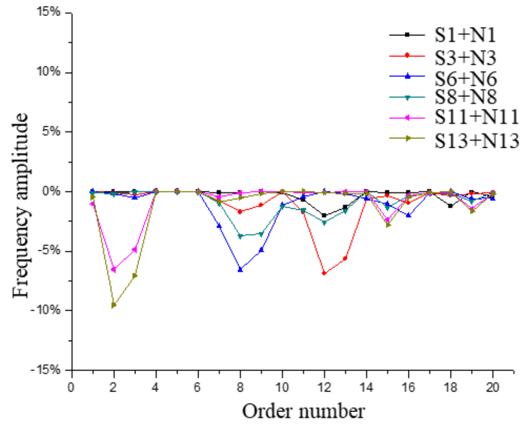

Fig.6 - Frequency variation-order variation plots under fire-induced fusing of different cables for transition and side spans

From Figures 7 to 9, it can be concluded that the transition span and side span cable damage has an effect on the vertical bending formation of the whole bridge and has the greatest effect on the vertical symmetric bending formation, and the damage of the cable near the outer side has the greatest frequency on the formation.

Damage to the outer cables near the transition span and side spans has a large effect on the low-order frequency variation of cable-stayed bridges, especially when the damage to the outermost back cables of S13+N13 occurs, it has the largest effect on the 2nd and 3rd order frequency variation, with a maximum value of 9.6%. Transition span and side span cable damage has almost no effect on the longitudinal drift, transverse bending and torsional formations of the cable-stayed bridges.

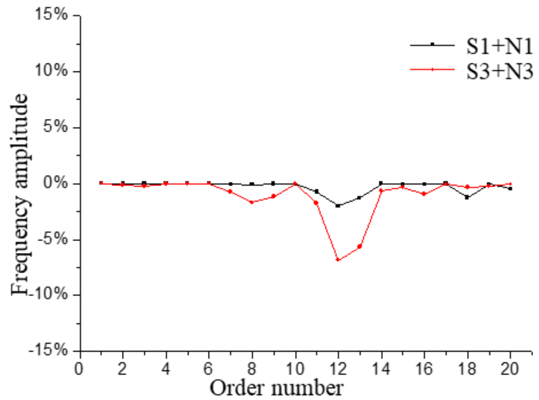

Fig.7 - Frequency amplitude order diagram of transition span and inner side span

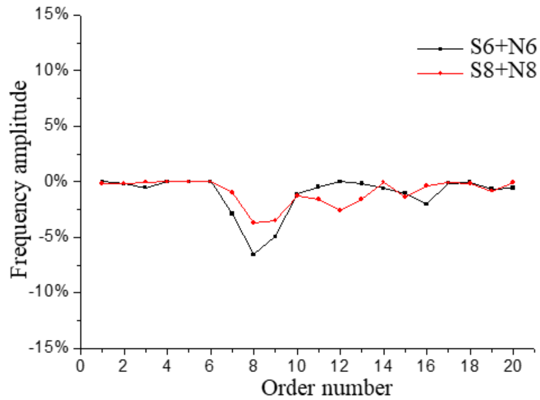

Fig.8 - Frequency amplitude order diagram of transition span and edge span

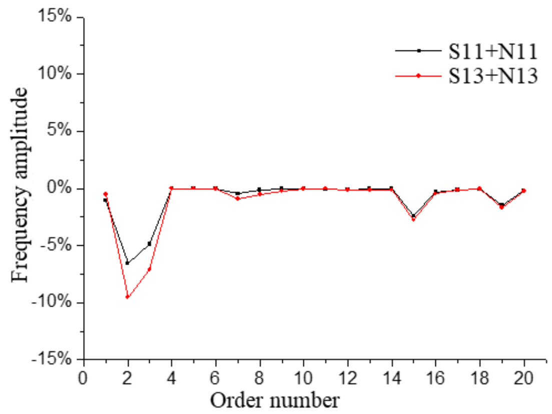

Fig.9 - Transition span and side span outer frequency variation-order plot

Figures 10 and 11 show the frequency-order and frequency variation-order plots for the first 20 orders of various working conditions for different cables fused on the main span. It can be seen that the amount of frequency change is very small, the SC13+NC13 condition has the largest variation, and the maximum frequency variation is only 11.1%.

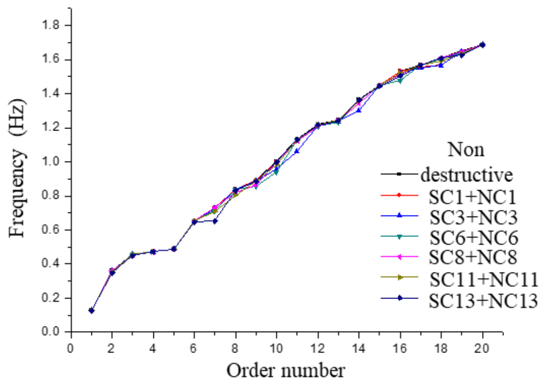

Fig.10 - Frequency-order variation under different cable fusing in main span

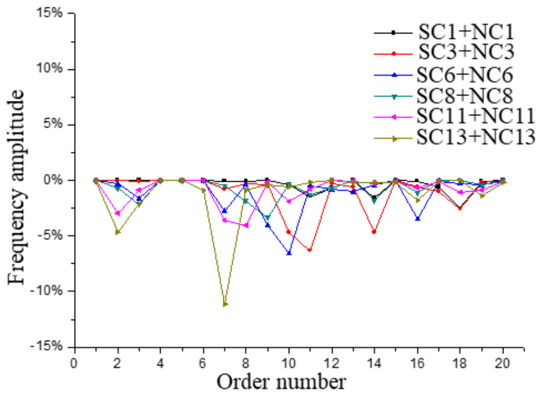

Fig.11 - Plot of frequency variation-order change under fire-induced fusing of different cables in the main span

In order to facilitate the analysis of the frequency amplitude-order plots for different conditions are listed separately. Figures 12 to 14 show the comparison of the frequency amplitude for the main span near the bridge tower, 1/4L and mid-span damage conditions, respectively.

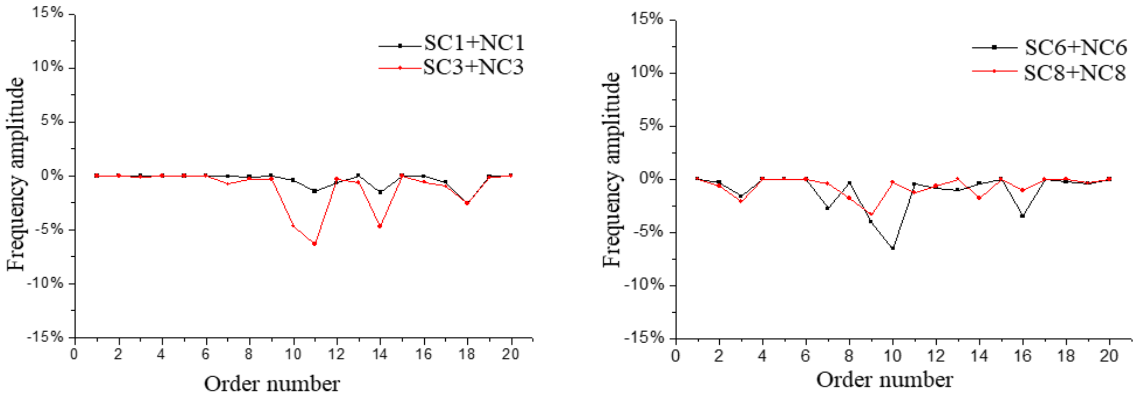

Fig.12 - Frequency variation-order plot of the main span near the side of the bridge tower

Fig.13 - Frequency variation-order plot at 1/4L of main span

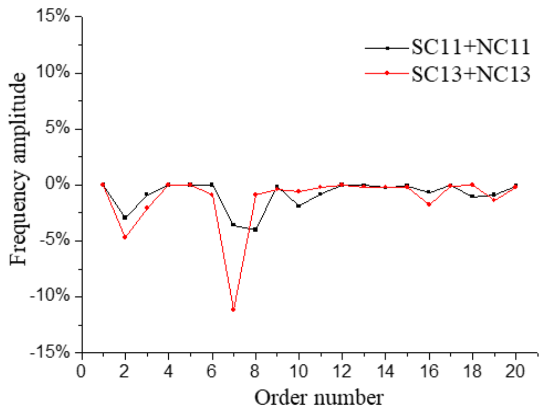

Fig.14 - Main span mid-span frequency variation-order plot

From Figures 12 to 14, it can be seen that the main span cable damage has an effect on all vertical bending formations of the whole bridge, with the greatest effect on the vertical symmetric bending formations, and the damage close to the outer cables has the greatest effect on the frequency of the formations. The mid-span cable has a large effect on the low-order frequency, and near the bridge tower has a large effect on the high-order frequency.

Damage to the cable near the mid-span of the main span has a large effect on the lower order frequencies of the cable-stayed bridges, especially when the damage to the outermost back cables of SC13+NC13 occurs, it has the largest effect on the 7th order frequencies, with a maximum value of 11.1%. Transition span and side span cable damage has almost no effect on the transverse bending and torsional formations of the cable-stayed bridges structure.

Structural Dynamic Analysis of The Whole Bridge Under Different Cable Fire Damage

Analysis of Structural Dynamics Under Asymmetric Fire-Induced Fusing of Cables

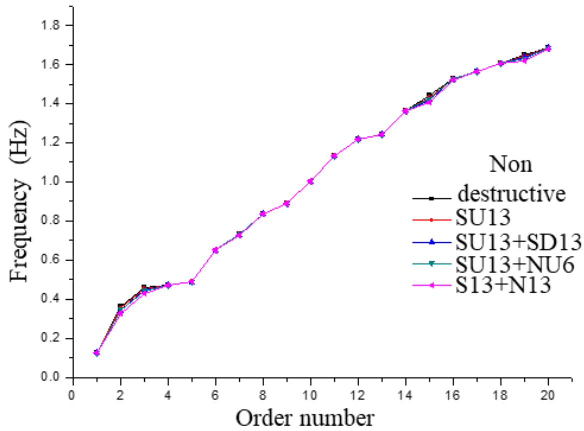

Fig.15 - Frequency-order diagram under asymmetric damage of transition span and side span

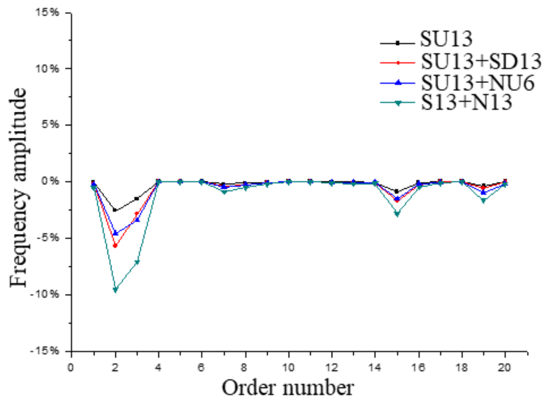

Fig.16 - Frequency variation-order plot under asymmetric damage of transition span and side span

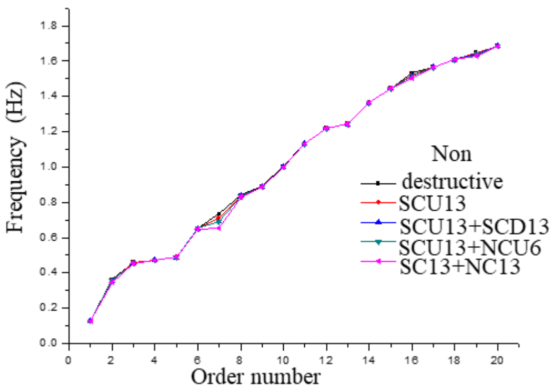

Fig.17 - Frequency-order diagram under asymmetric damage in the main span

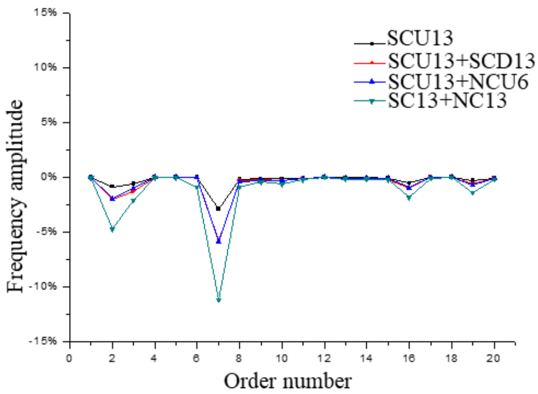

Fig.18 - Frequency variation-order plot under asymmetric damage of main span

From the previous section, it is concluded that the long cable fusion has the greatest effect on the lower order frequencies, so the transition span and side span outermost back cables are used to represent the auxiliary and side span cable asymmetric damage, and the main span outermost back cable is used to represent the main span cable asymmetric damage. Table 3-13 shows the first 20 orders of frequency values for the transition span, side span cable asymmetry and main span cable asymmetry damage cases, which are analyzed by taking four working conditions (both asymmetric span and asymmetric axis, symmetric longitudinal axis but asymmetric span, symmetric span but asymmetric longitudinal axis, and both symmetric span and symmetric longitudinal axis), respectively.

Figures 15 and 16 show the frequency-order and frequency-variation-order plots under asymmetric fusing damage in the transition span and side spans, as shown in the two figures:

Transition span and side span asymmetric damage had a large effect on the frequency of 2nd and 3rd order vertical bending formations (first order vertical symmetric and antisymmetric formations), and on the frequency of 15th and 19th order torsional formations (positive symmetric torsion and antisymmetric torsion), which increased with the increase in the number of fused cables, and had almost no effect on the frequency of the other side bending formations.

Figures 17 and 18 show the frequency-order and frequency-variation-order plots under the main-span asymmetric fusion damage. It can be seen from the two plots that the main-span asymmetric damage has a greater effect on the frequency of the vertical bending formations, with the maximum effect being on the 2nd and 7th orders, and has a greater effect on the frequency of the 19th-order torsional formations (antisymmetric torsion), and with the increase in the extent of the damage, the formation frequency variation increases, and has almost no effect on the frequency of other lateral bending

Structural Dynamic Analysis of The Whole Bridge with Different Degrees of Fire Damage to The Cables

In order to analyze the structural dynamic characteristics of the whole bridge under different degrees of fire damage, two pairs of back cables and their adjacent cables are selected for the analysis of the dynamic characteristics under different degrees of damage, S13 and S12 are taken to represent different degrees of damage in the transition span and side spans at the same time, and SC13 and SC12 are taken to represent different degrees of damage in the main span at the same time. Table 3-14 shows the values of the first 20 orders of formation frequency for the whole bridge structure at different damage levels of auxiliary and side spans and different damage levels of main spans.

Figures 19 and 20 show the frequency-order and frequency-variation-order plots of the structural formations at different levels of damage in the transition span and side spans.

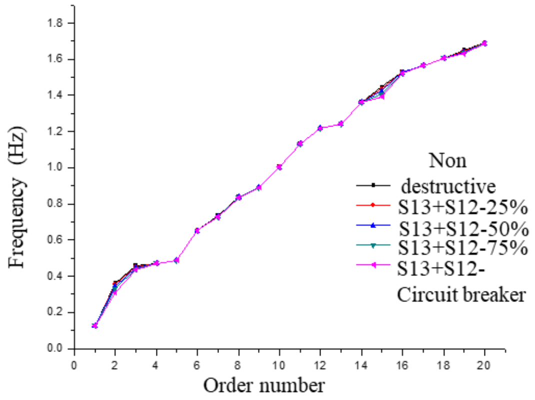

Fig.19 - Frequency-order diagrams for different degrees of damage in the transition span and side spans

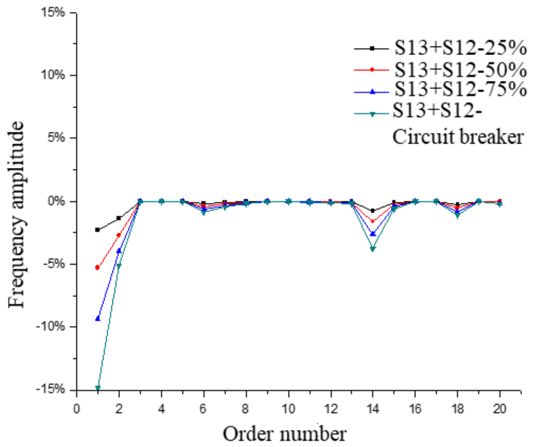

Fig.20 - Frequency variation-order plots for different degrees of damage in the transition span and side spans

As can be seen from Figures 19 and 20, the effect on the frequency of the longitudinal floating formation (1st order) is larger for different damage levels of the transition span and side spans, and the effect on the bending formation of the antisymmetric vertical bending (2nd and 14th order) is larger, and the change in the frequency of the formations is larger with the increase of the damage level. There is almost no effect on the transverse bending and twisting formations.

Figures 21 and 22 show the frequency-order and frequency-variation-order plots for structural formations with different degrees of damage to the main span.

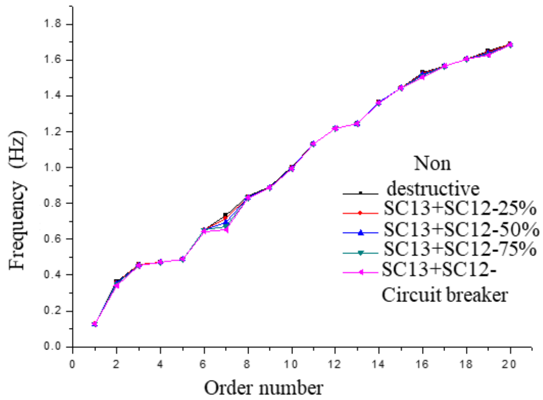

Fig.21 - Frequency-order diagrams for different degrees of damage to the main span

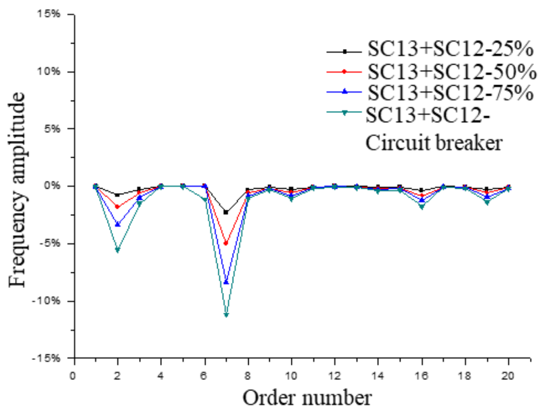

Fig.22 - Frequency variation-order plot for different degrees of damage to the main span

From Figures 21 and 22, it can be seen that different degrees of damage to the main span cables have a greater effect on the vertical antisymmetric bending formations (2nd and 7th order) of the structure, and the change in the frequency of the structural formations increases with the increase in the degree of damage. There is almost no effect on the longitudinal drift, transverse bending and torsion formations.

CONCLUSION

In this paper, the dynamic characteristics of the entire bridge under different cable fires and different degrees of cable fire damage were analyzed. The research results can provide references for the assessment of cable-stayed bridge damage, and also offer valuable insights for design. The main conclusions are as follows:

1. Fire-induced damage to the cables has an effect on the vertical bending formation of the whole bridge, with the greatest effect on the vertical symmetrical bending formation. Fire-induced damage to the whole bridge cables had little effect on the longitudinal drift, transverse bending and torsional formations of the cable-stayed bridges structure. Effects of different levels of damage to the cables on the dynamic performance of the bridge are reflected in quantitative changes, with the frequency of a certain order formation increasing as the level of damage increases.

2. At different levels of damage in the transition and side spans, the effect on the frequency of the longitudinal drift formation (1st order) is greater, and on the antisymmetric vertical bending (2nd and 14th order) bending formations, and the change in the frequency of the formations is greater with the increase in the level of damage. There is almost no effect on the transverse bending and twisting formations.

3. Damage to the outer cables near the transition span and side spans has a large effect on the low-order frequency variation of cable-stayed bridges, especially when the damage to the outermost back cables of S13+N13 occurs, it has the largest effect on the 2nd and 3rd order frequency variation, with a maximum value of 9.6%

4. The amplitude of frequency variation under the damage of the middle span cable is very small, while in the case of SC13 + NC13, the variation amplitude is the largest, with the maximum frequency variation being only 11.1%.

REFERENCE:

[1] Zhang S, Shen R, Dai K, et al. A methodology for cable damage identification based on wave decomposition [J]. Journal of Sound and Vibration, 2019, 442: 527-551. https://doi.org/10.1016/j.jsv.2018.11.018

[2] Hua X G, Ni Y Q, Chen Z Q, et al. Structural damage detection of cable-stayed bridges using changes in cable forces and model updating [J]. Journal of structural engineering, 2009, 135(9): 1093-1106. https://doi.org/10.1061/(ASCE)0733-9445(2009)135:9(1093)

[3] Tang Z F, Sui X D, Duan Y F, et al. Guided wave-based cable damage detection using wave energy transmission and reflection[J]. Structural Control and Health Monitoring, 2021, 28(5): e2688. https://doi.org/10.1002/stc.2688

[4] Kotsovinos P, Judge R, Walker G, et al. Fire performance of structural cables: Current understanding, knowledge gaps, and proposed research agenda [J]. Journal of Structural Engineering, 2020, 146(8): 03120002. https://doi.org/10.1061/(ASCE)ST.1943-541X.0002703

[5] Zhao S, Li G, Wang C. Bridge cable damage identification based on acoustic emission technology: A comprehensive review [J]. Measurement, 2024: 115195. https://doi.org/10.1016/j.measurement.2024.115195
[6] Iordachescu M, Valiente A, De Abreu M. Damage tolerance and failure analysis of tie-down cables after long service life in a cable-stayed bridge [J]. Engineering Failure Analysis, 2021, 125: 105437. https://doi.org/10.1016/j.engfailanal.2021.105437
[7] Feng J, Gao K, Gao W, et al. Machine learning-based bridge cable damage detection under stochastic effects of corrosion and fire [J]. Engineering Structures, 2022, 264: 114421. https://doi.org/10.1016/j.engstruct.2022.114421
[8] Baltazar A, Hernandez-Salazar C D, Manzanares-Martinez B. Study of wave propagation in a multiwire cable to determine structural damage [J]. Ndt & E International, 2010, 43(8): 726-732. https://doi.org/10.1016/j.ndteint.2010.08.007
[9] Ren J, Zhang B, Zhu X, et al. Damaged cable identification in cable-stayed bridge from bridge deck strain measurements using support vector machine[J]. Advances in Structural Engineering, 2022, 25(4): 754-771.
[10] Lin S W, Yi T H, Li H N, et al. Damage detection in the cable structures of a bridge using the virtual distortion method [J]. Journal of Bridge Engineering, 2017, 22(8): 04017039. https://doi.org/10.1061/(ASCE)BE.1943-5592.0001072
[11] Kildashti K, Alamdari M M, Kim C W, et al. Drive-by-bridge inspection for damage identification in a cable-stayed bridge: Numerical investigations[J]. Engineering structures, 2020, 223: 110891. https://doi.org/10.1016/j.engstruct.2020.110891
[12] Yan B, Wang Y. Cable-stayed bridge Static performance with different cable damage condition caused by fire [J]. Civil Engineering Journal, 2025, 34(3). https://doi.org/10.14311/CEJ.2025.03.0027
[13] Yang L, Shi G, Yin H, et al. Full-scale experimental study on the influence of damages on the static behavior of the single-layer cable net structure[C]//Structures. Elsevier, 2015, 3: 153-162. https://doi.org/10.1016/j.istruc.2015.04.002
[14] Wang G, Ye J. Localization and quantification of partial cable damage in the long-span cable-stayed bridge using the abnormal variation of temperature-induced girder deflection [J]. Structural Control and Health Monitoring, 2019, 26(1): e2281. https://doi.org/10.1002/stc.2281
[15] Bennetts I, Moinuddin K. Evaluation of the impact of potential fire scenarios on structural elements of a cable-stayed bridge [J]. Journal of Fire Protection Engineering, 2009, 19(2): 85-106.
[16] Yang W, Huang J, Wang P, et al. An intelligent distributed sensor developed for power cable external damage monitoring [J]. Procedia Computer Science, 2021, 183: 166-174. https://doi.org/10.1016/j.procs.2021.02.046
[17] Wu G M, Yi T H, Yang D H, et al. Damage identification of tie-down cables in cable-stayed bridges using vehicle-induced displacement[J]. Journal of Performance of Constructed Facilities, 2021, 35(3): 04021011. https://doi.org/10.1061/(ASCE)CF.1943-5509.0001590
[18] An Y, Zhong Y, Tan Y, et al. Experimental and numerical studies on a test method for damage diagnosis of stay cables [J]. Advances in Structural Engineering, 2017, 20(2): 245-256.
[19] Lonetti P, Pascuzzo A. Vulnerability and failure analysis of hybrid cable-stayed suspension bridges subjected to damage mechanisms [J]. Engineering Failure Analysis, 2014, 45: 470-495. https://doi.org/10.1016/j.engfailanal.2014.07.002
[20] Serra S, Montanari G C, Mazzanti G. Theory of inception mechanism and growth of defect-induced damage in polyethylene cable insulation [J]. Journal of applied physics, 2005, 98(3). https://doi.org/10.1063/1.1978986
[21] Gao Q, Duan M, Liu X, et al. Damage assessment for submarine photoelectric composite cable under anchor impact [J]. Applied Ocean Research, 2018, 73: 42-58. https://doi.org/10.1016/j.apor.2018.01.006
[22] Hao H, Tang E K C. Numerical simulation of a cable-stayed bridge response to blast loads, Part II: Damage prediction and FRP strengthening [J]. Engineering Structures, 2010, 32(10): 3193-3205. https://doi.org/10.1016/j.engstruct.2010.06.007

CIVIL ENGINEERING JOURNAL

Article no. 6

THE CIVIL ENGINEERING JOURNAL 1-2026

BONDING PROCEDURES, ARTIFICIAL AGEING AND THEIR EFFECT ON THE DURABILITY OF GLASS-TO-GLASS ADHESIVE JOINTS

Markéta Zikmundová[1], Martina Eliášová[1] and Klára V. Machalická[2]

1. *Czech Technical University in Prague, Faculty of Civil Engineering, Department of Steel and Timber Structures, Thákurova 7, 166 29 Prague 6, Czech Republic; marketa.zikmundova@fsv.cvut.cz, eliasova@fsv.cvut.cz*
2. *Klokner Institute, Czech Technical University in Prague, Šolínova 7, 16608 Prague, Czech Republic, klara.machalicka@cvut.cz*

Received: *30.11.2025*

Received in revised form: *15.03.2026*

Accepted: *23.04.2026*

ABSTRACT

In the context of modern architecture, glass is widely regarded as a fundamental design element, representing a material of increasing interest to architects and engineers. The fundamental challenge in using glass is to design convenient connections. Adhesive joints are more convenient connections compared to mechanical fixings due to ensuring uniform stress distribution. This study focuses on small glass-to-glass specimens: (i) bonding of the specimens, (ii) artificial ageing, and (iii) shear tests. Two different transparent adhesives were tested, 2-component epoxy and UV-cured acrylate.

Proper specimen bonding is essential. Two-component epoxy required careful sealing during curing to prevent leakage. The UV-cured acrylate adhesive needed a careful curing process to avoid bubble formation due to shrinkage of the adhesive. To determine resistance to environmental effects, a combination of DVS 1618 procedure and UV radiation was used for artificial ageing of specimens. Shear tests on the reference set showed excellent results for the acrylate adhesive, which achieved an average shear strength of 10.17 MPa. Problems with adhesion appeared after artificial ageing. Epoxy adhesive achieved an average shear strength of 4.55 MPa in the reference set. Two specimens had problems with adhesion to glass. After ageing, the specimens achieved a higher average shear strength (4.86 MPa) than in the reference set. The aged specimens failed only by glass breakage. Both adhesives showed high potential for use in glass construction joints.

KEYWORDS

Transparent adhesives, Glass, Bonded joints, Artificial ageing, Double-lap shear joint, Epoxy adhesive, Acrylate adhesive

INTRODUCTION

Structural glass has gained significance in contemporary architecture due to the continuous demand for transparency and the aesthetic lightness of structures. Given the limited dimensions of glass panes and transportation of them, it is often necessary to join individual components into larger, load-bearing units. Traditional mechanical joints, such as bolted or clamped connections, have a major disadvantage as drilling holes weakens the glass panes and indicate local stress concentrations [1, 2].

Adhesive bonds (or joints) represent a promising alternative to mechanical connections. They enable a more uniform transfer of forces distributed across the entire bonded area, thereby minimizing stress peaks. This feature is critical for brittle glass, which is unable to plastically redistribute stresses [1, 2]. Bonded joints are used in a wide range of applications, including facades made of solid glass blocks (e.g., the Crystal Houses façade, constructed from glass masonry bonded with UV-curing adhesive) [3, 4] or in creating structural glass components where they ensure composite behaviour as fully glazed enclosure in Dresden [5], glass-timber structure [6], tensegrity floor [7] etc.

A critical aspect for the reliable use of adhesives in construction is their long-term durability, as they are exposed to external environmental factors. Factors that can significantly affect the strength, stiffness, and optical properties of adhesives include humidity (or moisture), temperature, and UV radiation. For transparent adhesives, UV radiation, in particular, can lead to unfavourable changes in material properties and discoloration. Therefore, ageing evaluation is critical for lifespan prediction.

This work focuses on the experimental analysis of adhesively bonded small glass-to-glass specimens, which is key to obtaining fundamental information on the mechanical characteristics of the adhesives and the adhesive joint. For bonded joints, shear behaviour is particularly important, as it is critical for transferring loads in composite and façade systems. The shear strength of the joint is highly dependent on the adhesion of the adhesive to the substrate, the cohesion of the adhesive, joint geometry, and the bond line thickness.

The aim of this article is to examine in detail:

1. The bonding process and the preparation of small glass-to-glass specimens with particular attention to the use of two distinct adhesives.
2. The determination of the shear strength of bonded joints.
3. The influence of artificial ageing on the mechanical properties of the adhesives.

Problem of artificial ageing

The long-term service life, or durability, of adhesive joints in constructions, is a critical aspect, as they are exposed to complex and interactive environmental factors such as moisture, temperature, and UV radiation [8, 9]. Any property of the joint can deteriorate, but changes of mechanical properties and failure behaviour are essential from the engineering point of view. Material constants and strength values obtained only from short-term tests are insufficient for the reliable design of bonded constructions [10, 11], which often require a service life of 20 to 25 years [12] (though civil engineering applications may require service lives above 50 years [13]).

To determine the effects of these influences in a relatively short time, methods of artificial (accelerated) ageing are therefore used. These procedures are typically based on guidelines or standards such as ETAG 002 (for structural sealant glazing systems (SSGS)) [14], which describes procedure involving immersion in water. Other relevant standards include EN ISO 9142 [15], which guides the selection of standard atmospheric laboratory conditions for cyclic ageing. Other general tests and standards that are applied include: EN ISO 9227 [16] (often used for salt spray/corrosion tests), EN ISO 4892 [17] (commonly used for radiation exposure), ASTM D904 [18] or ASTM D1828 [19] (Atmospheric exposure). Tests are also often developed based on individual assessment by engineers [11] or developed internally by manufacturers [12].

Test scenarios include exposure to high relative humidity (such as 90 % R.H. or 100 % R.H.), immersion in water, thermal cycling, or exposure to corrosive atmospheres, such as SO_2 (sulphur dioxide atmosphere) [8, 11, 20]. UV radiation is particularly critical for transparent adhesives, where the absorption of high-energy, short-wavelength photons can trigger photochemical ageing processes. This subsequently leads to changes in both mechanical and optical properties. [9, 21]

However, conversion to actual years of natural ageing is very difficult and is not typically declared as a simple coefficient. There is no universal artificial test plan nor a precise method for

DOI 10.14311/CEJ.2026.01.0006

predicting the lifespan of adhesive joints, because every adhesive-substrate interface is unique [12]. The extrapolation of mechanical properties over a longer period than tested is not obvious [11]. Sometimes, it is even shown that the applied artificial ageing protocols can "completely overstate" the long-term behaviour. [8, 12]

Overall, it is often concluded that accelerated tests tend to overestimate the reduction in joint strength compared to natural ageing [9, 10].

Research objective

The objective of the research was to find an adhesive or adhesives suitable for bonding load-bearing glass structures, especially for the purpose of bonding the glass frame corner, as illustrated in Figure 1. As mentioned above, in order to ensure the successful bonded joint, it is necessary to meet a number of requirements which are described in detail below.

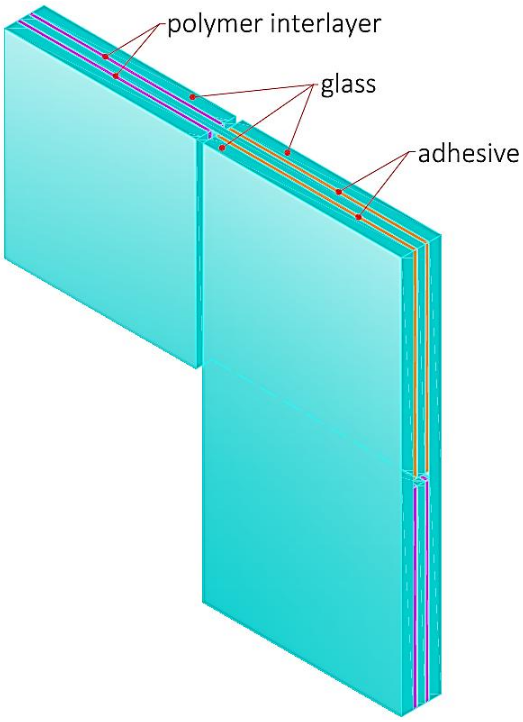

Fig. 1 - Glass frame corner (purple colour - polymer interlayer, orange colour - adhesive)

A fundamental requirement is that adhesives must be transparent. The adhesive is not visible in the glass, and the joint must appear as though it is non-existent, with the glass itself being the only visible component. Critical requirement is that adhesives must demonstrate resistance to the effects of environment. This includes exposure to elevated and low temperatures (ranging from -20 °C to 80 °C), humidity, and UV radiation.

The thickness of the adhesive layer and size of bonded area are other criteria of the selection. The thickness of the adhesive layer depends on the geometry of the glass joint. It has been determined that the double-lap shear joint will be realised. The thickness of the adhesive is thus given by the thickness of the polymer interlayer in laminated glass used in the joined construction, see Figure 1. It is expected that three PVB layers will be used (each 0.38 mm thick), which would result in a bonded layer thickness of approximately 1 mm. Because of the joint geometry, adhesives suitable for bonding medium to large bonded areas (for joints with an area of 10,000 - 90,000 mm²) were selected.

The final requirements relate to the technology for manufacturing the bonded joint. The following parameters are to be considered: the viscosity of the adhesive, and the open time (time from application of the adhesive to its solidifying). The bonded joint is created by the pouring of adhesive into the gap between the glass panes. The application method requires an adhesive with a low viscosity, thereby ensuring its flow into the comparatively narrow space between the glass panes. Furthermore, a sufficiently prolonged open time is required to prevent the adhesive from hardening during its flowing into the gap. An open time at least 20 minutes is suitable.

Adhesives that met the above-mentioned requirements for use in load-bearing glass structures in civil engineering were selected. In the initial phase of the research, the behaviour of the selected adhesives was verified through experimental testing of small specimens. The aim of this article is to present data of two selected rigid adhesives.

MATERIALS AND METHODS

Two rigid adhesives were subjected to experimental testing on two sets of specimens. Firstly, a reference set of specimens was prepared. Subsequently, a second set of specimens was subjected to artificial ageing. Technical parameters of each tested adhesive are stated in Table 1.

Tab. 1 - Technical parameters of adhesives in technical data sheets [22, 23]

Adhesive	Araldite 2020	Loctite AA 3491
Company	Huntsman	Henkel
Technology	Epoxy	Acrylic
Components	2 components	1 component
Curing	Chemical reaction	UV light
Viscosity	Ca 150 mPas	750-1500 mPas
Open time/curing time	40-50 min	seconds
Glass transition temperature	App. 39,5 °C	Not written

For the purpose of the experiment, float glass, characterised by a nominal thickness of 19 mm and dimensions 50 x 50 mm, was used for the bonding of the small specimens. Mechanical properties of the float glass are stated in Table 2. Thick glass panes were cut by water jet. The using of a water jet technique during the manufacturing process of the glass panes ensures that the glass panes does not crack.

Tab. 2: Mechanical properties of float glass [24, 25]

	Soda lime glass
Density	2500 kg/m3
Hardness (Knoop)	6 GPa
Bending strength	45 MPa
Modulus of elasticity	70 000 MPa
Thermal expansion	9·10-6 K-1
Poisson's ratio	0.23

Specimens were prepared as double-lap shear joints, see Figure 2. Each specimen was prepared using 3 glass panes. Middle glass pane was bonded 10 mm above outer glass panes. This geometry ensures possibility of punch test which leads in shear stress in adhesive layers.

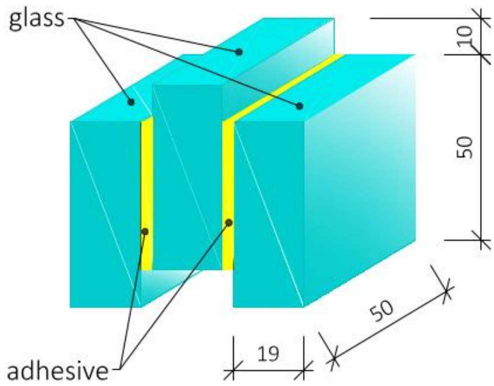

Fig. 2 - Geometry of small specimens

Number of bonded specimens for each adhesive is listed in Table 3.

Tab. 3: Number of bonded specimens

Adhesive	Epoxy adhesive	Acrylate adhesive
Reference set	5	4
Set exposed to artificial ageing	5	3

Bonding specimens

Nitrile gloves were used during both cleaning and bonding to prevent contamination of the bonded surface. Surface of glass panes was cleaned with lint-free wipes soaked in isopropyl alcohol; Figure 3 left. Following the cleaning of the surface, the bonding process was completed within approximately 30 minutes. This duration was sufficient for the isopropyl alcohol to evaporate from the bonded surface. Geometry of specimens was given by plastic device which was made on 3D printer. Gap between glasses was ensured with 1 mm plastic inserts. The assembled specimen was secured with clamps.

In the case of the two-component adhesive, the individual components had to be weighed out and subsequently mixed. The mixture was stirred with a wooden spatula for approximately 1 minute. The process of mixing resulted in the generation of air bubbles within the mixture. In order to remove the bubbles, the mixture was filtered through a nano-mesh sieve, which effectively captured the bubbles.

Whole specimen had to be sealed around bond line. This ensured no adhesive flown out of the specimen. Proper sealing of the specimens was very important due to low viscosity of adhesives. It was especially important for Araldite adhesive, which has longer open time. The adhesive has therefore more time to find any small aperture in sealing. Firstly, it was attempted to seal the specimen with tape only, but this proved insufficient. The adhesive was able to flow out of the specimen through the folds. Due to the thin gap, even a small amount of adhesive leaking out resulted in the gap being filled only halfway, for example. The use of silicone for sealing was not possible due to the possibility of adhesive contamination and thus the invalidation of the results. At last, using plastic material similar to modelling clay proved to be the most suitable method of sealing. Specimen prepared for bonding is shown in Figure 3 right.

Fig. 3 - Cleaning of the glass panes (left), specimen prepared for bonding (right)

Using UV adhesive showed different problems and that was curing. Specimens with UV adhesive were cured using handheld UV-light source. In this case LOCTITE CL32 LED Spot with wavelength 405 nm was used, see Figure 4. During bonding, two problems occurred. Ensuring geometry by clamps showed problem, how to lighten and thereby cure the adhesive. The problem was solved by using tape instead of clamps. Tape was used from sides with small overlap on front and back side of the specimen, see Figure 4. The second problem was shrinkage of adhesive during curing. Curing had to be carried out carefully from bottom part of the specimen. After curing small area on the bottom of the specimen can be cured area above. This specific procedure eliminated bubbles caused by shrinkage in the adhesive layer (Figure 5) and make addition adhesive into the bonding gap possible.

Specimens with two-component adhesive were cured at room temperature for 24 hours. For specimens with UV adhesive, the complete curing of the entire bonded surface was achieved within approximately 10 minutes.

Fig. 4 - Set-up for bonding specimen with UV adhesive - from left: specimen secured by tape, UV protecting glasses, UV adhesive with dispenser gun and application needle, LED spot

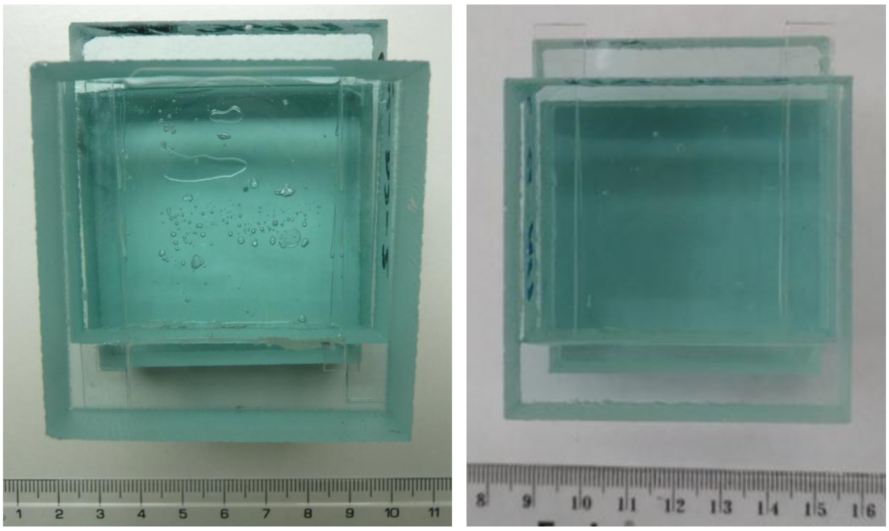

Fig. 5 - Bonded specimen with bubbles caused by shrinkage (left), better bonded specimen with less bubbles (right)

Artificial ageing

It was necessary to select or develop artificial ageing method capable of simulating natural ageing. In this research, technical guideline DVS 1618 [25] and UV radiation was combined. Technical guideline DVS 1618 was designed for elastic thick layer adhesives used in rail vehicle applications. It contains procedure of artificial ageing which is described in Table 4.

Tab. 4 - Accelerated ageing according to DVS 1618

Part	Processing	Duration
1	Conditioning at temperature 23 °C and 50 % RH	7 days
2	Immersion in distilled water at temperature 20 °C	7 days
	Conditioning at temperature 23 °C and 50 % RH	2 hours
3	Exposure to temperature 80 °C	1 day
4	Conditioning at temperature 23 °C and 50 % RH	2 hours
5	Cataplasm test (exposure to the temperature 70 °C and 100 % RH)	7 days
	Conditioning at temperature 23 °C and 50 % RH	2 hours
Extension	Shock cooling at -30 °C	1 day

This procedure was further extended by 500 h of UV radiation exposure, following Method E3 of the ČSN EN ISO 9142 standard. The whole artificial ageing method lasted app. 6 weeks, see Figure 6.

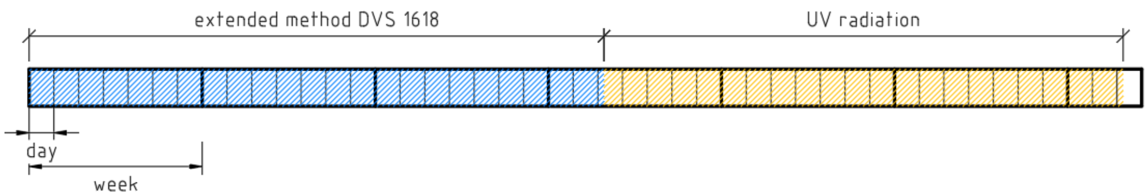

Fig. 6 - Ageing method based on DVS 1618

Combination of these two approaches ensures that the specimens were exposed to all related external effects including elevated and sub-zero temperatures, high humidity, and UV radiation.

Experimental set-up

The specimens were subjected to the punch test. In this experiment, a compressive load was applied on the central glass pane, thereby inducing shear stress in the adhesive. Glass is a brittle material and has never been in direct contact with hard materials such as steel due to stress concentrations. The specimen was equipped with elastic pads on both the inferior and superior surfaces. The elastic pads ensure uniform stress distribution and thereby eliminate stress peaks in the glass; see Figure 7.

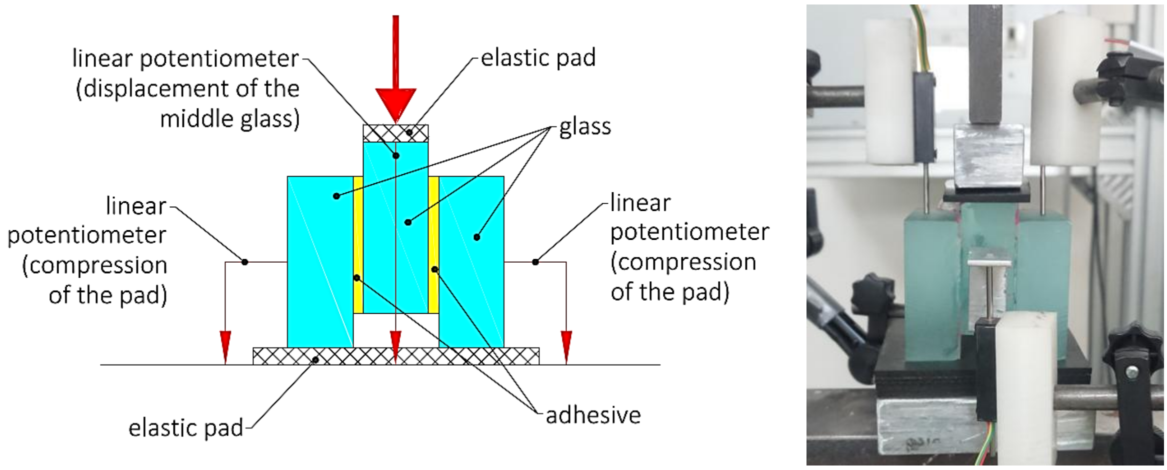

Fig. 7 - Schema of the experiment (left), photo of the experiment (right)

DOI 10.14311/CEJ.2026.01.0006

The experiment was conducted under displacement control, with displacement applied continuously until specimen failure. Crosshead speed was 0.05 mm/min. The slow crosshead speed of the test is intended to represent static or quasi-static load. Adhesives are viscoelastic materials, and the duration of the applied load is a critical factor in determining their load-bearing capacity.

The displacement of the glass panes was measured by four linear potentiometers. Two potentiometers measured displacement of the middle glass and two potentiometers measured compression of the glass panes to the pad. Used measurement equipment is written in Table 5.

Tab. 5: Details of the experiment equipment

Test machine	Shimadzu AGS-X
Linear potentiometers	Megatron MMR-1011 (measurement range 11 mm)
Test controlled by	displacement
Crosshead speed	0.05 mm/min
Measurement device	SPIDER 8, software CATMAN32
Sampling frequency	5 Hz

RESULTS

Reference set

The reference set of specimens demonstrated significant variations in shear strength among the adhesives. The epoxy adhesive achieved an average shear strength of 4.53 MPa (44.8 % of acrylic shear strength); see Table 6. A significant difference in shear strength is evident with epoxy adhesive, as illustrated in Figure 8. One specimen achieved a shear strength of less than 2 MPa. This specimen failed as a result of loss of adhesion; see Figure 9. In one specimen, failure occurred in a combined failure mode with dominant substrate failure; however, loss of adhesion was a contributing factor to the overall failure. This specimen also exhibited reduced shear strength. Other specimens failed due to glass breakage (Figure 10), and their shear strength was found to be similar at approximately 5.7 MPa.

Tab. 6 - Reference set

Adhesive	Average shear strength τ [MPa]	Standard deviation [MPa]	Dominant failure mode	τi/τi,max [%]
Epoxy	4.55	1.80	S*	44.8 %
Acrylate	10.17	0.52	S*	100.0 %

S* - substrate failure mode

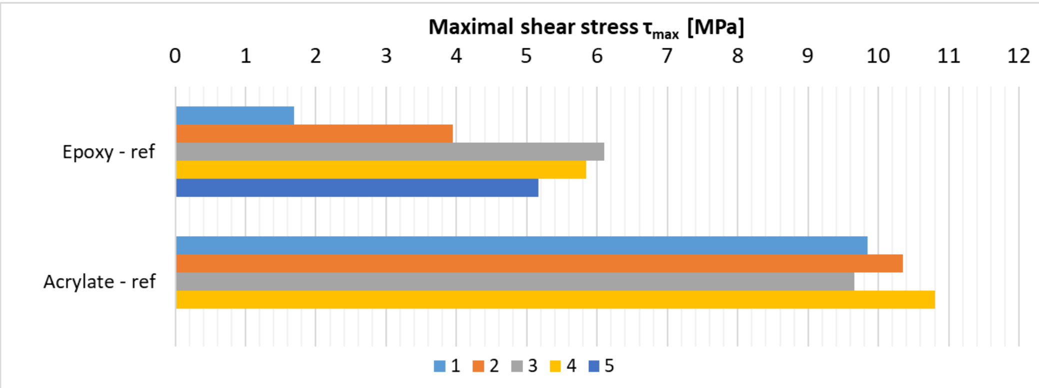

Fig. 8 - Shear strength of individual specimens in the reference set

The shear strength τ was calculated using Equation 1.

$$\tau = \frac{F}{A}, \tag{1}$$

where F is the force at breakage [N], and A is the bonded area [mm2] (the measured bonded area of both shear planes, excluding the area of the inserts).

In comparison, the acrylic adhesive achieved an average shear strength of 10.17 MPa. All specimens that were bonded with acrylate adhesive exhibited failure due to glass breakage (Figure 8, Figure 9, Figure 11). The standard deviation of these specimens is low, at only 0.52 MPa (Table 6).

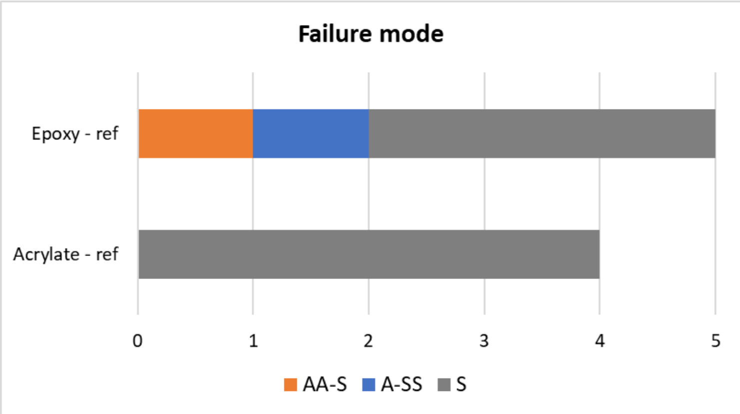

Fig. 9 - Failure mode of specimens in reference set (AA-S - combined failure mode with dominant adhesion failure, A-SS - combined failure mode with dominant substrate failure, S - substrate failure)

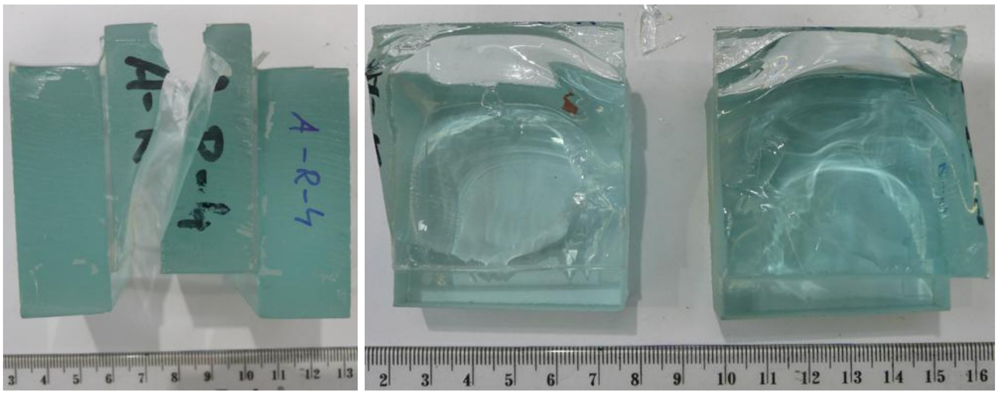

Fig. 10 - Specimen with epoxy adhesive in reference set after shear test - substrate failure

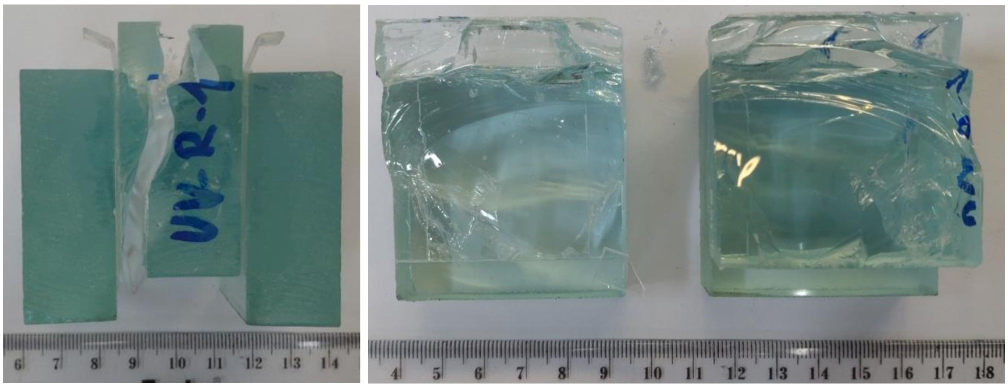

Fig. 11 - Specimen with acrylic adhesive in reference set after shear test - substrate failure

DOI 10.14311/CEJ.2026.01.0006

Artificial ageing

The importance of artificial ageing is not only in its role in determining mechanical properties, but also in its ability to influence visual properties. Visual properties cover especially colour changes and cracks or bubbles occurrence.

Specimens before and after artificial ageing are shown in Figure 12 and Figure 13. Both adhesives achieved excellent visual properties. Adhesives stayed transparent and no additional cracks or bubbles appeared. Delamination proved to be problematic, as is shown especially in Figure 13 right. It is important to note that delamination is only visible from a specific angle. Delamination was more visible in specimens with acrylate adhesive, where delamination occurred on approximately 25 – 75 % of the bonded surface. In the case of the epoxy adhesive, delamination was observed on no more than 10 % of the bonded surface.

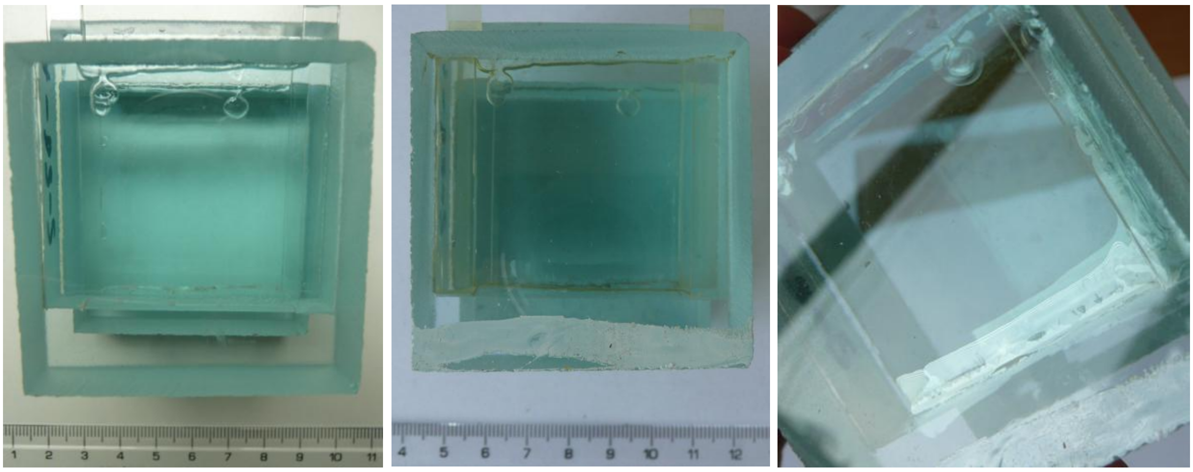

Fig. 12 - Specimen with epoxy adhesive before artificial ageing (left), after artificial ageing (middle), detail of the specimen after artificial ageing (right)

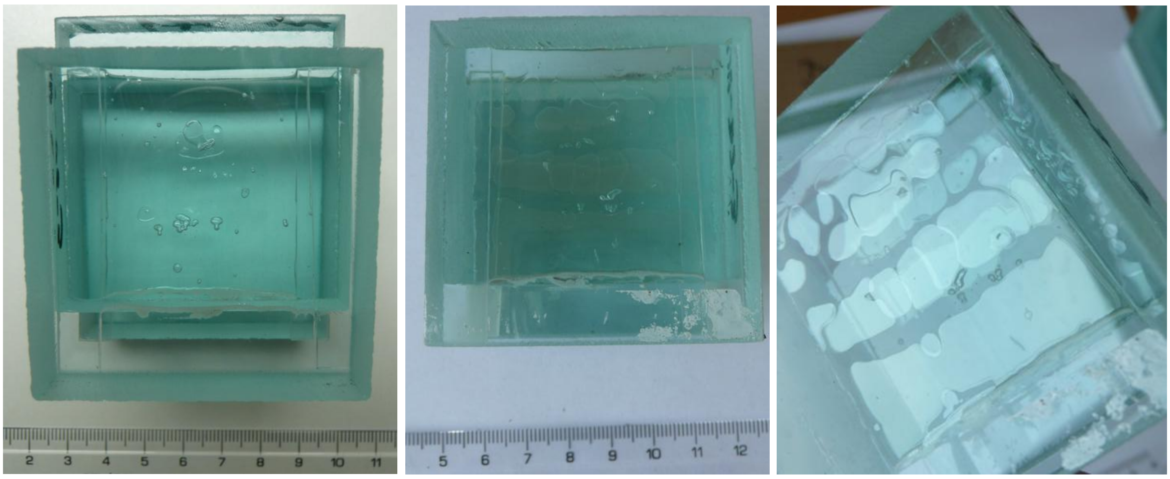

Fig. 13 - Specimen with acrylate adhesive before artificial ageing (left), after artificial ageing (middle), detail of the specimen after artificial ageing (right)

Epoxy adhesive also achieved excellent ageing resistance in terms of mechanical properties. Average shear strength after artificial ageing increased to 106.6 % of average shear strength of the reference set; see Table 7. Specimens failed by rupture of glass. A combined failure mode was observed in only two specimens, characterised by dominant substrate failure; see Figure 14. However, the shear strength of these two specimens was similar as specimens which failed only due to rupture of glass; see Figure 15. The standard deviation for epoxy adhesive after artificial ageing is only 0.40 MPa which is much lower according to the reference set; see Table 7 and Figure 16. Specimen after the shear test failed by rupture of glass is in the Figure 17.

Tab. 7 - Reference set and set of specimens exposed to artificial ageing

Adhesive	Average shear strength τ [MPa]	Standard deviation [MPa]	Dominant failure mode	τi/τi,ref [%]
Epoxy - ref	4.55	1.80	S*	100.0 %
Epoxy - DVS	4.86	0.40	S*	106.6 %
Acrylate - ref	10.17	0.52	S*	100.0 %
Acrylate - DVS	5.09	4.94	AA-S*	50.1 %

S* - substrate failure mode, A-SS* - combined failure mode with dominant substrate failure

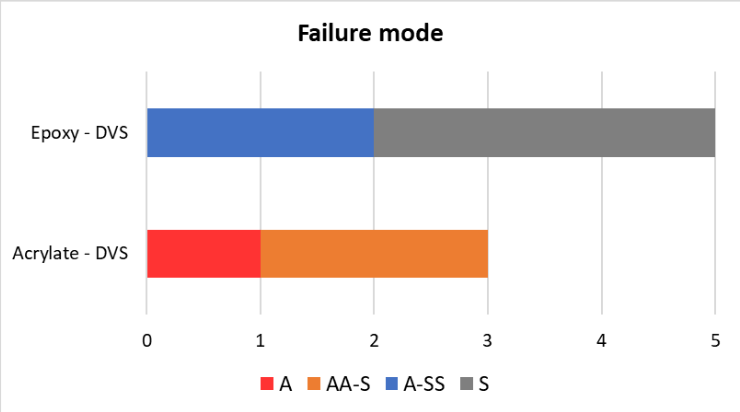

Fig. 14 - Failure mode of specimens in set exposed to artificial ageing (A - adhesion failure, AA-S - combined failure mode with dominant adhesion failure, A-SS - combined failure mode with dominant substrate failure, S - substrate failure)

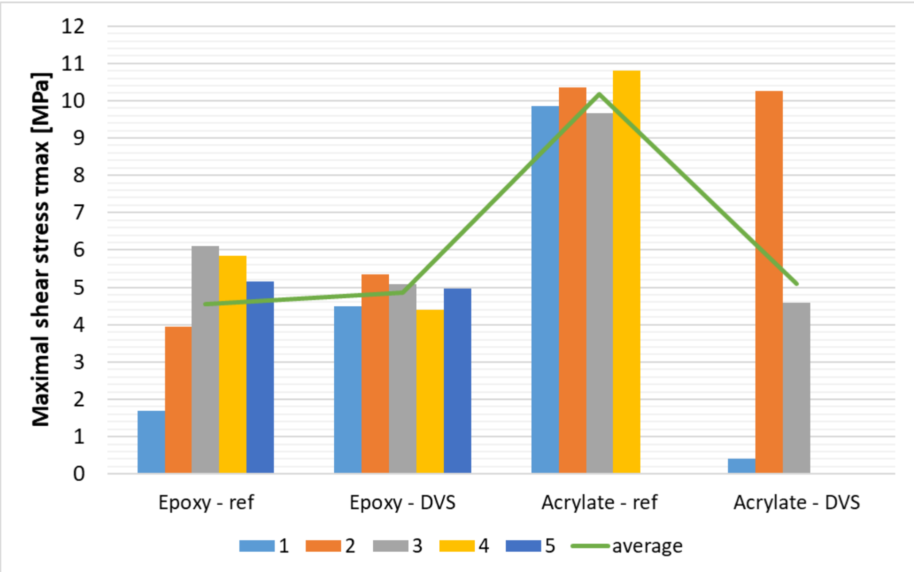

Fig. 15 - Shear strength of individual specimens in the reference set and set exposed to artificial ageing

Specimens with acrylate adhesive showed very different results; see Figure 15 and Table 7. One specimen achieved extremely high shear strength, more than 10 MPa which is similar to shear strength in reference set. One specimen showed extremely low shear strength, less than 0.5 MPa. This specimen failed due to loss of adhesion; see Figure 14. And the third specimen failed at shear stress 4.6 MPa which is app. average of shear strength of specimens in the set exposed to artificial ageing. High differences in shear strength with acrylate adhesive are also evident in Figure 16.

Specimens with higher shear strength failed in combined failure mode with dominant adhesion failure; see Figure 14 and Figure 18.

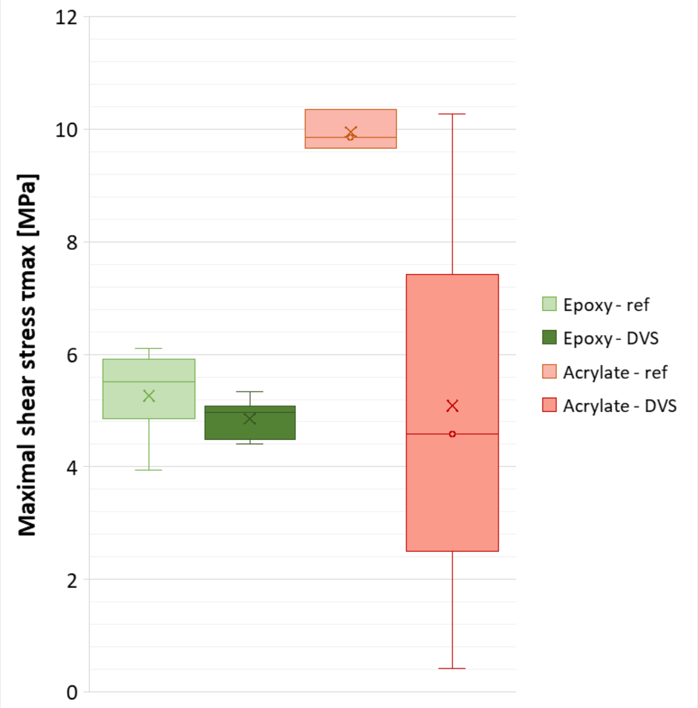

Fig. 16 - Shear strength of individual specimens in the reference set and set exposed to artificial ageing

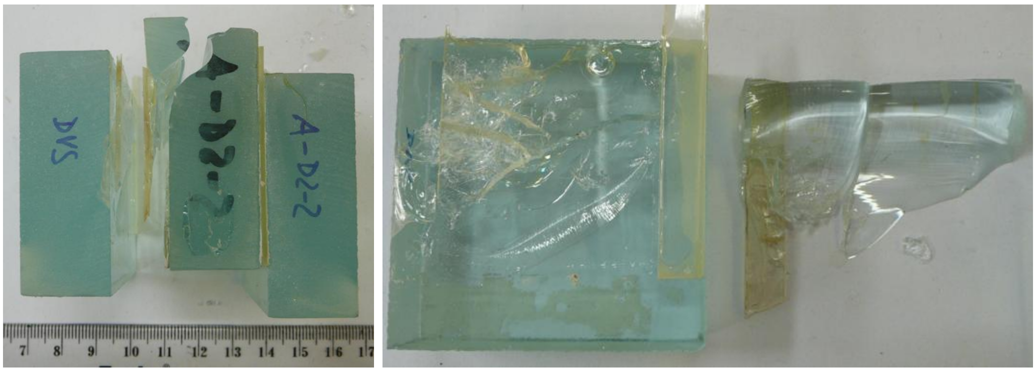

Fig. 17 - Specimen with epoxy adhesive exposed to artificial ageing after shear test - substrate failure

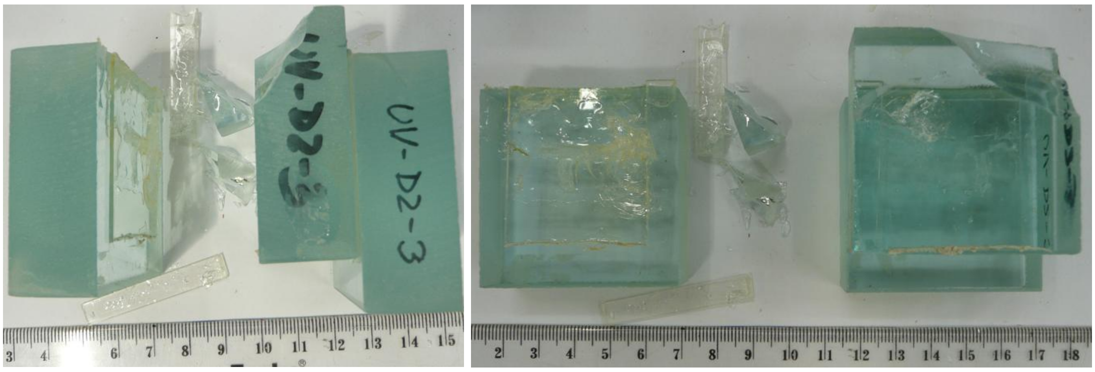

Fig. 18 - Specimen with acrylate adhesive exposed to artificial ageing after shear test - combined failure mode with dominant adhesion failure

During the testing, the deformation and subsequent displacement of the centre glass were measured. Average displacement of the center glass was calculated using Equation 2.

$$\overline{u_c} = \overline{u}_t - \overline{u_z}\,, \qquad (2)$$

where $\overline{u_c}$ is average displacement of the central glass pane [mm], $\overline{u}_t$ is average displacement of the specimen [mm], and $\overline{u_z}$ is average compression of the pad [mm].

Subsequently, the shear strain was determined from Equation 3.

$$\gamma = \frac{\overline{u_c}}{\overline{t}}\,, \qquad (3)$$

where γ is shear strain [-], and $\overline{t}$ is the average thickness of the adhesive layer [mm].

It was not possible to compile a relevant stress-strain diagram for epoxy adhesive due to the very low deformation and the influence of the elastic pads. The stress-strain diagram for acrylic adhesive is illustrated in Figure 19. In this instance, the curve exhibits a wavy pattern; however, the trend is evident in the graph. The shear modulus of the aged specimens was found to be lower than that of the specimens in the reference set.

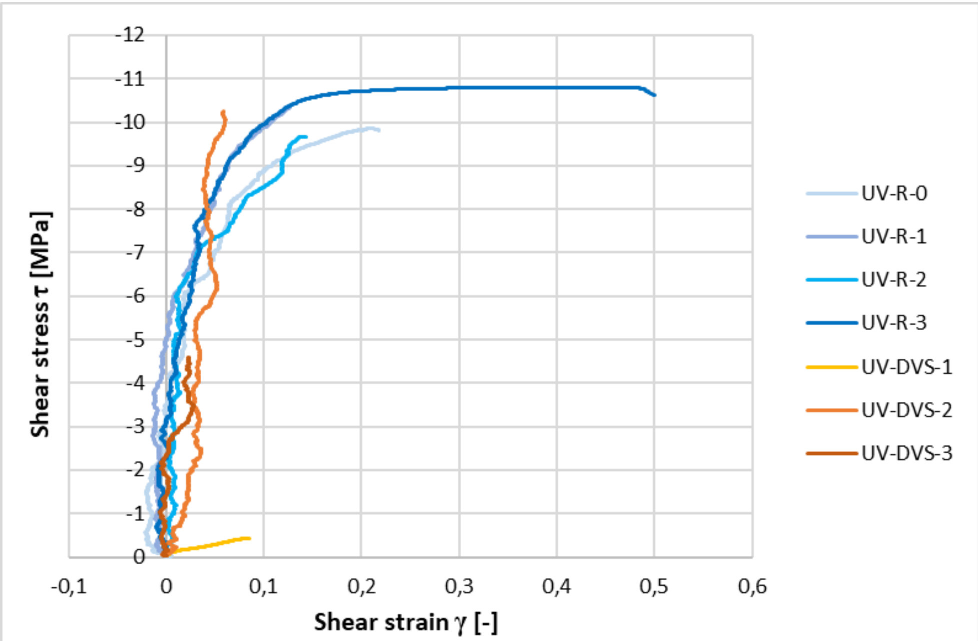

Fig. 19 - Stress-strain diagram of UV acrylate adhesive

Table 8 summarizes the experimental observations and key performance parameters for both adhesives. It highlights the differences in workability, visual appearance after ageing, resulting shear strength, and observed failure modes across the tested specimens.

Tab. 8 - Experimental observations and comparative assessment of adhesives

Adhesive	Epoxy	Acrylate
Bonding challenges	Proper sealing of the specimens due to low viscosity of the adhesive	Lighting/curing of the bonding area, shrinkage of the adhesive
Average shear strength (reference set)	4.55 MPa	10.17 MPa
Typical failure mode (reference set)	Substrate failure	Substrate failure
Ageing trend	Stability over time	Highly variable ageing resistance
Visual stability	Excellent	Stable colour, frequent delamination
Average shear strength (artificial ageing)	4.86 MPa	5.09 MPa
Typical failure mode (artificial ageing)	Substrate failure	Combined adhesive-substrate failure with dominant adhesive failure

DISCUSSION

Similar geometry, and mechanical test was performed in different researches [26, 27]. The punch test is convenient due to low tensile strength of glass. Substrate failure is not an appropriate mode of failure during the testing of bonded specimens. The substrate failure mode does not reveal the actual strength of the adhesive itself; rather, it provides an indication of the strength of the substrate. The testing of glass specimens is an issue that is complicated by the material's inherent brittleness and its sensitivity to stress peaks. In the majority of cases, the glass failed; thus, the ultimate strength of the adhesive could not be fully determined, but the results established the minimum stress level the bond can withstand without failure.

Specimens with epoxy adhesive

In the reference set, the epoxy adhesive showed a high standard deviation. This was caused by the low shear strength of specimens that failed due to loss of adhesion. The weaker was the adhesion, the lower was the resulting shear strength. However, this premature loss of adhesion occurred in only two out of five specimens. Therefore, it cannot be generally concluded that the Araldite adhesive has insufficient adhesion to glass. Nevertheless, there are studies indicating that epoxies may have issues with adhesion to glass [28]. For a more reliable assessment, higher number of shear tests should be performed.

Specimens with epoxy adhesive after artificial ageing failed due to breakage of glass or in combined failure mode but with dominant substrate failure. According to the literature [8, 9], artificial ageing, especially effect of water, may lead to a loss of adhesion. Thus, another possible reason for the insufficient adhesion to glass may be related to limited experience with the bonding process. This interpretation is supported by the fact that the specimens bonded in the reference set belonged to the first specimens prepared, where insufficient adhesion was also most pronounced.

Epoxy adhesive after artificial ageing achieved higher average shear strength compered to reference set (106.6 %). But, reduction of shear strength was expected. If specimens with lower adhesion are removed from the reference set, then there was a slight decrease in strength after laboratory ageing. However, there are studies where shear strength increased after laboratory ageing [12, 13]. The authors attributed this to the post-cure process or to water adsorption due to high temperatures during ageing, i.e., partial restoration of properties (recovery).

Specimens with acrylate adhesive

Acrylate adhesive achieved excellent results in the reference set accompanied by a low standard deviation. The low standard deviation may be related to the good quality of bonding, characterized by a minimal presence of air bubbles. During bonding, adhesive shrinkage was observed, which is a common issue associated with UV-cured adhesives [5, 11]. In this study, an adhesive with very low shrinkage was selected. Owing to the relatively thick bond line (1 mm), compared to the more commonly used thinner joints of only a few tenths of a millimetres, the effect of shrinkage was more pronounced. Nevertheless, the specimens were bonded with only a minimal occurrence of bubbles and cracks.

The laboratory ageing results proved to be more problematic than expected. Only three specimens were tested, and each specimen exhibited different behaviour, which significantly complicates the evaluation. The observed failure modes included loss of adhesion or a combined failure mode with dominant adhesion loss. Compared to the epoxy adhesive, specimens with the acrylate adhesive for laboratory ageing were bonded first. This bonding and curing approach differs substantially from that of two-component epoxy adhesives and may require a certain level of experience and skill. The durability of the joint may therefore have been influenced by the quality of the bonding process; however, further tests would be required to verify this assumption. The present results are consistent with observations reported in the literature, indicating that adhesion may be weakened during ageing, particularly under water exposure [8, 9, 29]. It should also be noted that one specimen after artificial ageing achieved approximately the same shear strength as the specimens in the reference set. Given that only three specimens were subjected to laboratory ageing and their results exhibited considerable variability, any conclusions drawn from these tests must be interpreted with caution.

CONCLUSION

This paper focused on all process of experimental testing bonded specimens - bonding of the specimens, artificial ageing and shear test.

Although scientific articles typically do not provide a detailed description of the bonding process, the present study has shown that the quality and consistency of specimen bonding play a critical role in the reliability of the obtained results. Consequently, the present work has highlighted specific challenges encountered during bonding with both two-component epoxy and UV-cured acrylate adhesives. In particular, adequate sealing of the bond line proved to be necessary to prevent leakage of the highly fluid adhesive prior to curing, a requirement typical for low-viscosity adhesive systems. The acrylate adhesive required careful bottom-up curing to prevent the formation of bubbles and to maintain the integrity of the bonded layer, taking into account adhesive shrinkage during the curing process.

The selection of an appropriate ageing method represents a major challenge. In this study, laboratory ageing according to DVS 1618 was applied, followed by additional UV radiation exposure, in order to simulate a range of external environmental influences relevant to real construction applications. The selected laboratory ageing procedure is considered to have a significant degrading effect on the specimens. The epoxy adhesive demonstrated a high resistance to the applied laboratory ageing procedure. The average shear strength obtained after laboratory ageing was slightly higher than that of the reference set (106.6 %). However, this result may have been influenced by the presence of low adhesion in two specimens in the reference set.

In contrast, specimens bonded with the acrylate adhesive exhibited, on average, significantly lower shear strength after ageing compared to the reference set, which was primarily associated with complete or partial loss of adhesion. While only three acrylate specimens were subjected to laboratory ageing, their behaviour varied considerably, reflecting varying extents of adhesion loss and delamination. These adhesion-related defects were subsequently manifested in the shear test results.

After the ageing process, both adhesives demonstrated excellent visual stability, with no signs of yellowing. Nevertheless, several specimens exhibited indications of delamination. This loss of adhesion was subsequently reflected in the results of shear tests. Further investigation would be necessary to confirm assumptions regarding adhesion failure in relation to bonding quality. Despite these limitations, both adhesives demonstrate a high potential for application in structural glass assemblies.

ACKNOWLEDGEMENTS

This work was supported by the Czech Science Foundation, grant number GA22-14105S and Student Grant Competition of Czech Technical University, grant number SGS18/169/OHK1/3T/11.

I would also like to express my gratitude to the technician Tomáš Vorlíček from Henkel, who assisted in selecting the adhesive and provided me with comprehensive instruction on its application.

Gen AI:

For language improvement and editing support, DeepL and DeepL Write was used. NotebookLM was used for reformulation and assistance with citations in the Introduction section. Additionally, Consensus was utilized for literature search and citation assistance.

REFERENCES

[1] Bedon Ch., Santarsiero M., 2018. Transparency in Structural Glass Systems Via Mechanical, Adhesive, and Laminated Connections - Existing Research and Developments. Advanced Engineering Materials, vol. 20, no. 5, 18 pp. ISSN 1438-1656, https://doi.org/10.1002/adem.201700815

[2] Lavko M., Kvočák V., 2020. Comparison of Mechanical and Adhesive Joints for Structural Glass – A review. IOP Conference Series Materials Science and Engineering, vol. 867, no. 1. ISSN 1757-8981, https://doi.org/10.1088/1757-899x/867/1/012027

[3] Oikonomopoulou F., Veer F., Nijsse R., Baardolf K., 2015. A completely transparent, adhesively bonded soda-lime glass block masonry system. Journal of Facade Design and Engineering, vol. 2, No. 3-4, pp. 201-221. ISSN 2213-302X, https://doi.org/10.3233/fde-150021

[4] Oikonomopoulou F., Bristogianni T., 2022. Adhesive solutions for cast glass assemblies: ground rules emerging from built case studies on adhesive selection and experimental validation. Glass Structures & Engineering, vol. 7, no. 2, pp. 293-317. ISSN 2363-5142, https://doi.org/10.1007/s40940-022-00178-w

[5] Weller B., Nicklisch F., Prautzsch V., Döbbel F., Rücker S., 2018. All Glass Enclosure with Transparently Bonded Glass Frames. In: Challenging Glass Conference Proceedings, vol. 2, edited by Louter Ch., Bod F., Belis J., TU Delft Open, 10 pp., ISBN 978-90-8570-524-6, https://doi.org/10.7480/cgc.2.2319

[6] Nicklisch F., Weller B., 2016. Adhesive bonding of timber and glass in load-bearing façades - Evaluation of the ageing behaviour. In: WCTE 2016 - World Conference on Timber Engineering, Vienna University of Technology, 8 pp., ISBN 978-390303900-1

[7] Alderucci T., Terlizzi V., Urso S., Borsellino Ch., Munafo P., 2018. Experimental study of the adhesive glass-steel joint behavior in a tensegrity floor. International Journal of Adhesion and Adhesives, vol. 85, pp. 293-302. ISSN 0143-7496, https://doi.org/10.1016/j.ijadhadh.2018.04.017

[8] Petrie E. M., 2006. Epoxy adhesive formulations, chapter 15, McGraw-Hill, p. 291-341, ISBN 9780071455442

[9] Adams R. D., 2005. Adhesive bonding: science, technology and applications, chapter 6, CRC Press, p. 123-142, ISBN 978-1-85573-741-9

[10] Da Silva L. F. M.; Öchsner A., Adams R. D., 2011. Handbook of adhesion technology, 2. ed., Springer, 1790 pp., ISBN 978-3-642-01168-9

[11] Possart W., Brede M., 2019. Adhesive Joints: Ageing and Durability of Epoxies and Polyurethanes, John Wiley, 526 pp., ISBN 9783527341856

[12] Van Lancker B., Dispersyn J., De Corte W., Belis J., 2016. Durability of adhesive glass-metal connections for structural applications. Engineering Structures, vol. 126, pp. 237-251. ISSN 0141-0296, https://doi.org/10.1016/j.engstruct.2016.07.024

[13] Sousa J. M., Correia J. R., Cabral-Fonseca S., 2017. Durability of an epoxy adhesive used in civil structural applications. Construction and Building Materials, vol. 161, pp. 618-633. ISSN 0950-0618, https://doi.org/10.1016/j.conbuildmat.2017.11.168

[14] ETAG 002: Guideline for European Technical Approval for Structural Sealant Glazing Systems (SSGS). 2013.

[15] EN ISO 9142: Adhesives - Guide to the selection of standard laboratory ageing conditions for testing bonded joints. 2004.

[16] EN ISO 9227: Corrosion tests in artificial atmospheres: salt spray tests. 2023.
[17] EN ISO 4892: Plastics - Methods of exposure to laboratory light sources. 2025.
[18] ASTM D904: Standard Practice for Exposure of Adhesive Specimens to Artificial Light. 2021.
[19] ASTM D1828: Standard Practice for Atmospheric Exposure of Adhesive-Bonded Joints and Structures. 2021.
[20] Assmus E., Popp Ch., Weller B., 2018. Permanent Hydrothermal Exposure on Load-bearing Adhesives in Glass Constructions. In: Challenging Glass Conference Proceedings, vol. 6, edited by Louter Ch., Bod F., Belis J., TU Delft Open, ISBN 978-94-6366-044-0, https://doi.org/10.7480/cgc.6.2154
[21] Kothe Ch., Wünsch J., Weller B., 2022. Discoloration of transparent adhesives for building applications due to aging under solar exposure. International Journal of Adhesion and Adhesives, vol. 116. ISSN 0143-7496, https://doi.org/10.1016/j.ijadhadh.2022.103137
[22] Technical data sheet - Araldite 2020, Huntsman Advanced Materials [online]. 2004. Available at: https://products.huntsman.com/products/araldite-2020-1-adhesive
[23] Technical Data Sheet - Loctite AA 3491, Henkel [online]. 2014. Available at: https://datasheets.tdx.henkel.com/LOCTITE-AA-3491-en_GL.pdf
[24] Haldiman M., Luible A., Overend M., 2008. Structural Use of Glass. IABSE. ISBN 978-3-85748-119-2
[25] EN 16612: Glass in building - Determination of the lateral load resistance of glass panes by calculation. 2020.
[26] Vokáč Machalická K., Horčičková I., Eliášová M., 2015. Shear Adhesive Connections for Glass Structures. IOP Conference Series Materials Science and Engineering, vol. 96. ISSN 1757-8981, https://doi.org/10.1088/1757-899x/96/1/012069
[27] Campione G., Orlando F., Fileccia G., Pauletta M., 2019. Bond characterization of monolithic and layered glass panels and ultrasonic tests to control glued surfaces. Engineering Structures, Vol. 198. ISSN 0141-0296, https://doi.org/10.1016/j.engstruct.2019.109545
[28] Boutar Y., Eliášová M., Tichá P., Zikmundová M., 2023. Assessment of the mechanical behavior of bonded glass-to-glass transparent epoxy adhesive joint at elevated temperatures for load-bearing elements. International Journal of Adhesion and Adhesives, Vol. 127. ISSN 0143-7496, https://doi.org/10.1016/j.ijadhadh.2023.103526
[29] Machalická K., Eliášová M., 2017. Adhesive joints in glass structures: effects of various materials in the connection, thickness of the adhesive layer, and ageing. International Journal of Adhesion and Adhesives, Vol. 72, pp. 10-22. ISSN 0143-7496, https://doi.org/10.1016/j.ijadhadh.2016.09.007

CIVIL ENGINEERING JOURNAL

Article no. 7

THE CIVIL ENGINEERING JOURNAL 1-2026

UNIAXIAL COMPRESSION PERFORMANCE OF ECC BASED ON NUMERICAL SIMULATION

Jun Zhao[1], Yuxin Xie, Shangxin Zhang[2], Chunling Yan[1], Hongbo Xiao[1], Songqiang Wan[1], Jingli Yang[1], Chenjie Hao[1], Junhua Guo[1], Xingyao Wang[1], Chongjin Li[1], Han Song[1], Long Liu[1]

1. *Henan Province Engineering Research Center of Material for Reinforcing Concrete Structure & Anyang Engineering Research Center of High ductility Concrete Structure, Anyang Institute of Technology, West section of Yellow River Avenue, Anyang 455000, China; 20160913@ayit.edu.cn*
2. *Hennan Changming Engineering Consulting Co., Ltd., 626880991@qq.com*

Received: *12.12.2024*

Received in revised form: *19.07.2025*

Accepted: *23.03.2026*

ABSTRACT

In many studies on the compressive properties of engineering cement-based composites (ECC), there are relatively few mesoscopic studies on the dosage and length of PVA fibers. To explore the influence of internal fibers of ECC on its compressive performance, this paper established a two-dimensional distribution model of PVA fibers in the matrix through random placement and generation algorithms. Firstly, an overview of previous experiments was provided. The ECC finite element (FE) model was developed using ABAQUS, and the simulation outcomes were contrasted with the experimental stress-strain curves to validate the model's viability. On this basis, parameter analysis was carried out to study the impact of different PVA fiber content and length in ECC on its compressive characteristics under vertical axial compression, and the characteristic values of the stress-strain curves of ECC with differing PVA fiber content and length under vertical axial compression were analyzed. The findings indicate that the ECC containing 2% PVA fiber with a length of 12 mm exhibits optimal compressive strength, and the yield stress and peak stress can reach 47.25 MPa and 54.96 MPa, respectively. When the fiber content is below 2% and the length ranges from 10 mm to 12 mm, the yield stress and peak stress of ECC progressively rise with increasing fiber content and length. Conversely, when the fiber content exceeds 2% within the same length range, the yield stress and peak stress of ECC exhibit a declining trend as fiber content increases. This research offers a reference for the judicious choice of fiber content and length to enhance the compressive capabilities of ECC.

KEYWORDS

ECC; FE model, PVA fiber, Uniaxial compression, Stress-strain curve

INTRODUCTION

Concrete is now recognised as the most widely utilised man-made material globally due to its superior physical and mechanical characteristics, easy access to materials and low cost.

However, because to its inadequate crack resistance and ductility, reinforced concrete (RC) structures will develop microcracks under large compressive stress, causing serious durability problems [1]. In the 1990s, Victor Li developed a high-ductility concrete called engineered cement composite (ECC) [2,3]. With the help of internal fibers, this material can improve the toughness and ductility of concrete and show good material properties. Among them, PVA fiber possesses approximately 1/8 the strength of high modulus PE fiber, while exhibiting superior tensile strength and elastic modulus compared to polypropylene (PP) fiber [4]. It has excellent mechanical properties [5], durability [6] and crack resistance [7], and has been widely used in various fiber reinforcement technologies. ECC is mainly used in bridge deck paving, RC beams and columns, dam repair and other projects [8]. The application scenario is shown in Figure 1. Its excellent compressive performance can effectively improve the compressive bearing capacity of the structure.

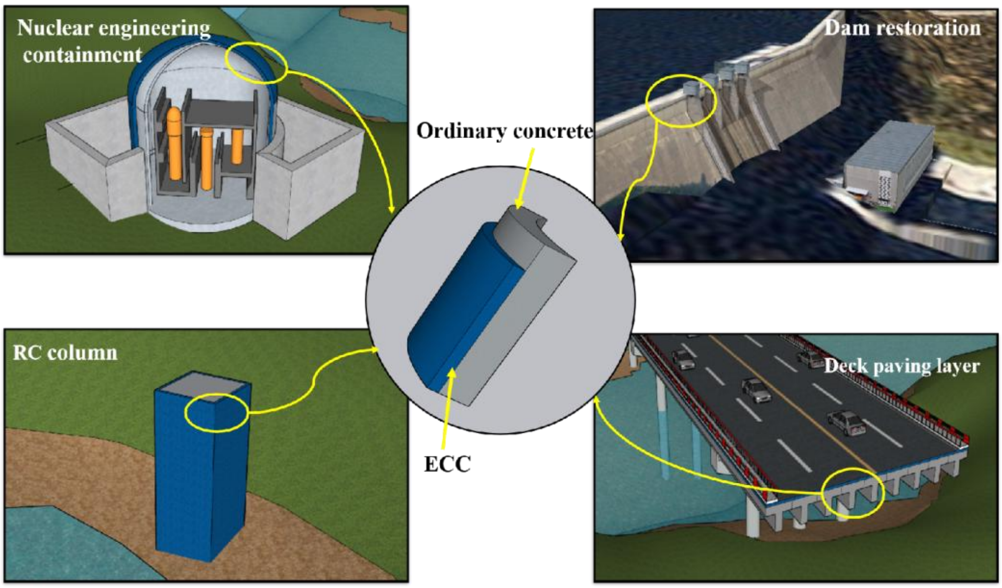

Fig. 1 – Application scenarios of ECC

In previous studies, scholars have conducted extensive research and discussions on the compression performance of ECC. Zhou et al. [9] performed an experimental investigation on the compression properties of ECC and revealed that the compressive strength of ECC is 20 to 80 MPa. Fischer et al. [10] found through uniaxial compression tests that the strength of ECC materials approaches that of high-strength concrete. In addition, the distribution of fibers has affected the ultimate compressive strain of ECC. Hu et al. [11] made uniaxial compression evaluation on ECC. The outcome showed that including fibers can improve the toughness of the matrix, altering its failure mode from brittle to ductile. The axial compressive stress-strain curve of ECC after peak load is gentler than that of ordinary concrete, and the ultimate compressive strain is considerably greater than that of conventional concrete. Singh [12] showed through experimental research that within a certain range, as the fiber length and fiber diameter increase, the flexural strength and final tensile strength of ECC increase accordingly. However, these studies are limited to experiments, which require a lot of time and effort, are costly, and cannot accurately observe the internal compression of ECC. Therefore, it is necessary to adopt a new method to study the compressive performance of ECC.

Finite element (FE) model can be used as an effective method to study the stress condition of materials [13-15]. At present, a large number of scholars have established numerical models from macroscopic and microscopic perspectives to study the compressive performance of ECC. Hung et al. [16] established a three-dimensional FE model of ECC and embedded the constitutive model material subroutine UMAT into LS-DYNA to describe the mechanical behavior of ECC. At

DOI 10.14311/CEJ.2026.01.0007

the same time, a three-dimensional FE model of ECC plate and two-span continuous beam was established for numerical calculation. Gencturk et al. [17] applied a macroscopic numerical model that simulated the stress performance of ECC under cyclic load and contrasted it to experimental findings. The simulation results were consistent with the experimental results, proving the correctness of the model. Li et al. [18] used ABAQUS to numerically simulate the ECC frame node under low-cycle reciprocating load. The results showed that the axial compression ratio significantly influenced the compressive performance of the ECC frame node. On the other hand, the microscopic scale can study ECC materials at a deeper level, and many scholars have undertaken research related to the microscopic numerical simulation of concrete and fiber concrete. Ren [19] implemented a random placement algorithm for concrete aggregates through MATLAB and established a microscopic geometric model of fiber concrete, laying the foundation to support the subsequent research of the mechanical properties of concrete through microscopic FE methods. Liang et al. [19] successfully established a three-dimensional microscopic model of steel fiber concrete based on Delaunay triangulation and verified it.

Compared with the microscopic numerical simulation of traditional fiber concrete, the small diameter and large number of PVA fibers in ECC materials will bring certain challenges to the random placement of fibers in the matrix. In addition, the connection between PVA fibers and the matrix is crucial and it is necessary to reflect it in the numerical simulation. However, in many studies on the compressive performance of ECC, there are relatively few mesoscopic studies on the dosage and length of PVA fibers. Therefore, this paper conducts an in-depth study on the compressive properties of ECC with varying PVA fiber content and fiber length. First, ECC is simplified into a two-phase composite material of cement mortar matrix and fiber, and a fiber random generation algorithm is developed using Python software. The FE model constructed with ABAQUS is applied to analyze the mechanical properties of ECC under uniaxial compression, and is likened with existing data from experiments to validate the model's accuracy. Further simulations of different PVA fiber content and length in ECC are performed, and the mechanical properties of ECC under uniaxial compression are evaluated by yield stress, peak stress, EAC and Poisson's ratio.

Experimental Overview

According to the "Standard Test Method for Fiber Concrete", in this test, standard-sized cubic test blocks (100 mm × 100 mm × 100 mm) were used to study the compressive mechanical properties of ECC. The mechanical properties of ECC under compression were studied. The uniaxial compression test was conducted on a universal testing machine (200 t) in accordance with ASTM C469(ASTM 2002) standard. Transverse and longitudinal strain gauges were affixed to the symmetrical midpoints of the specimen to measure the axial and radial strains. At the same time, two LVDT-50 displacement gauges were symmetrically positioned on the specimen's side to detect axial strain. When loading, the specimen was first loaded continuously and uniformly at an average speed of 1 mm/min to 10 kN. In this process, the specimen was aligned and the effect of the gap between the pressure surface of the specimen and the pad on the test results was eliminated. During the formal loading, the displacement control approach was utilised with an average speed 0.2 mm/min. The specific experimental device can be seen in Figure 2. For detailed material properties and loading information, please refer to reference [20].

Fig. 2 – ECC compression test device

FE model

To examine and evaluate the failure mode of ECC and PVA fibers in ECC under uniaxial compression, a two-dimensional uniaxial compression model of the central section was established using ABAQUS to analyze the compression behavior of ECC. This section gives the two-dimensional modeling method of ECC, the fiber random placement algorithm, and the material constitutive law.

(1) Model establishment

To more realistically reflect the ECC compression test, the FE model size is set to 100 mm × 100 mm. A fixed constraint is set on the bottom surface of the FE model, and a coupling is set between the center point of the top surface and the top surface. A downward displacement load is set at the center point of the top surface, and the load size is 10 mm. In order to make the FE model converge better and be analyzed, the ECC matrix is divided into square grids with a grid size of 2 mm; the fiber is divided into a grid size of 1 mm, as illustrated in Figure 3.

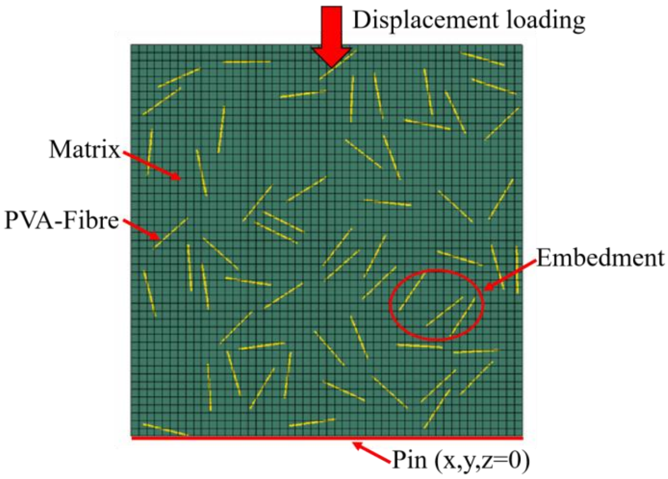

Fig. 3 – Finite element model

(2) Fiber placement algorithm

In order to avoid fiber agglomeration and uneven dispersion and give full play to the role of PVA fibers in ECC materials, PVA fibers should be evenly distributed in the ECC matrix during the ECC casting process. Unlike steel fibers, PVA fibers have a smaller cross-sectional diameter. When establishing a FE model, a large number of fibers in ECC materials often bring certain difficulties to numerical simulation and model establishment. Therefore, this paper uses the algorithm proposed by Yam [19] to simplify the fibers into straight lines. The calculation formula for the fiber number N is shown in Equation (1):

$$N = round\left(\frac{4\times W\times H\times V_f}{100\times\pi\times d^2\times L}\right) \tag{1}$$

Where W is the width of the sample, H is the height of the sample, L is the fiber length, d is the fiber diameter, the fiber volume fraction is V_f , and round (·) is the rounding function.

The fiber random placement geometric model studied by Wu [21] , the coordinates (x_i , y_i) of the center point O of the AB fiber are first determined, and the coordinates of the two end points A and B of the fiber are determined according to the fiber length and the fiber inclination angle, as shown in Figure 4.

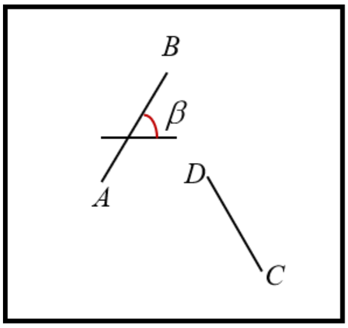

Fig. 4 – Graphic representation of random fiber dispersion

The specific coordinates of the endpoints can be calculated using Equations (2) to (5):

$$x_A = x_i - \frac{l}{2}\times\cos\beta \tag{2}$$

$$y_A = y_i - \frac{l}{2}\times\sin\beta \tag{3}$$

$$x_B = x_i + \frac{l}{2}\times\cos\beta \tag{4}$$

$$y_B = y_i + \frac{l}{2}\times\sin\beta \tag{5}$$

Where l is the fiber length, and β is the angle between the fiber and the horizontal line.

After randomly generating the endpoint coordinates of all fibers, the “Line()” geometric modeling method provided by the ABAQUS secondary development interface is used to connect the two endpoint coordinates of all fibers into a straight line, thereby obtaining a geometric model of random fiber placement.

(3) Material constitutive

In the FE method, the PVA fiber is considered to be a linear elastic material, and the specific values are provided in Table 1. Due to the random distribution characteristics of the fiber, a beam element is used for modeling, and its diameter is 0.1 mm. The fiber and the matrix are connected in an internal manner, that is, all the nodes of the fiber are connected to the ECC matrix.

Tab. 1 - Fiber parameters

Fiber name	Density (g/mm^3)	Tensile strength (MPa)	Modulus of elasticity (MPa)	Fiber diameter (μm)
PVA	1.3	1620	43	12

The concrete plastic damage model may properly explain the damage variation law of materials based on cement. Therefore, this research utilizes the elastic-plastic damage model in the constitutive model of the ECC matrix. For the constitutive model of the matrix, the literature [22,23] demonstrates that the mechanical characteristics of concrete are comparable to those of cement mortar, thus the concrete plastic damage model is employed to simulate the matrix.

The matrix strength in the FE simulation adopts the measured compressive capacity of the cubic specimen, which is 50 MPa, elastic modulus is 31 GPa, Poisson's ratio is 0.2, and density is 2.5 g/mm^3. In ABAQUS, several essential values in the plastic damage model need to be specified to specify the yield and failure criteria of the matrix. The particular parameter values are presented in Table 2.

Tab. 2 - Some special values in plastic damage model

Angle of expansion	Eccentricity	f_{b0}/f_c	K	Viscosity coefficient
38	0.1	1.16	0.6666667	1E-5

Results and discussion

The FE model was examined and the outcomes of the simulation were compared with the experimental findings of Xu [20] to verify the reliability of the FE model. Based on the model verification, a detailed parameter study was carried out. By analyzing different PVA fiber dosages and lengths, the stress-strain curves, yield stress, peak stress, EAC and Poisson's ratio of the specimens under different parameters were obtained to explore the mechanical properties of ECC under uniaxial compression.

(1) Stress-strain curve

The full stress-strain curves of ECC obtained by the FE model and the test are shown in Figure 5. It can be seen from the figure that both sets of stress-strain curves show a trend of increasing first and then decreasing. The yield stress and peak stress in the model analysis are 47.25 MPa and 54.96 MPa, respectively, which are 3.5% and 8.2% higher than the yield stress and peak stress obtained in the test. This is because the PVA fibers in the FE model are evenly distributed in the ECC, so that the load can be evenly stressed when bearing the load, resulting in a larger result. In addition, the FE model is simplified into a two-dimensional model to simulate the compression of the central section of the simulated specimen, which is larger than the test result. On the other hand , the peak strain in the FE analysis is 0.00339, which is slightly different from the peak strain of ordinary mortar and is also close to the peak strain of 0.004 in the test. It may also be determined by the study findings of the FE model that ECC can continue to bear a certain load after the peak stress, which is consistent with the results in the test and the law obtained by Li et al. [24].

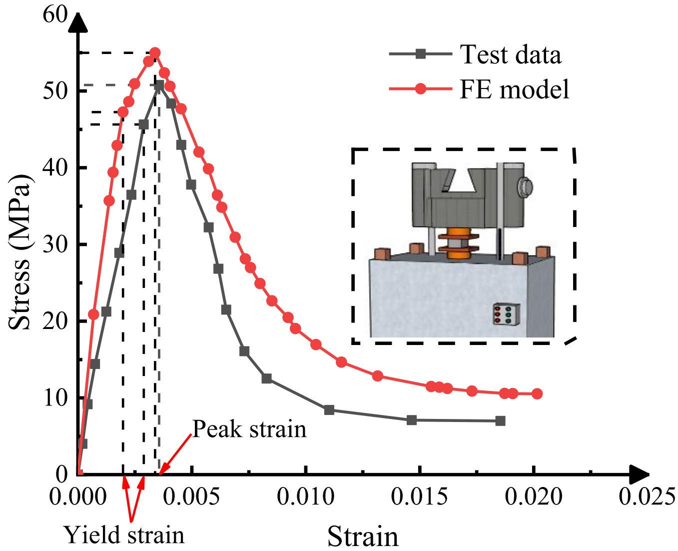

Fig. 5 – FE model analysis results and experimental stress-strain curve

(2) Destruction status

Figure 6 (a), the experimental phenomenon shows that the failed mode of ECC is different from the failure mode of the four-cornered pyramid surface of ordinary concrete. Through the bridging effect of the fiber at the break, the lateral expansion of the middle part of the cube becomes smaller, and the external bulging phenomenon of the fiber concrete in the middle part does not occur. At the same time, the strength of the test sample has been enhanced to a certain level. After reaching the peak load, ordinary concrete breaks rapidly and shows brittle failure. In the final failure stage of the ECC specimen, the hissing sounds of fiber splitting and pulling out can be distinctly heard. The specimen does not show brittle failure, and the specimen has good integrity, reflecting that ECC has good toughness.

Figure 6 (b) shows the compressive damage cloud map of the ECC compressive specimen. It can be seen that when the peak stress is reached, obvious damage occurs in the 45° direction inside the ECC compressive specimen, and the cracks in the middle area of the specimen continue to expand along the 45° direction until they are connected, resulting in X-shaped damage, which is consistent with the experimental results. Due to the existence of fibers between the connected fissures, when the stress continues to rise, the bridging effect of the fibers allows the ECC compressive specimen to continue to withstand larger loads, but at this time the internal damage of the ECC compressive specimen is already quite serious, and the cracks will continue to expand.

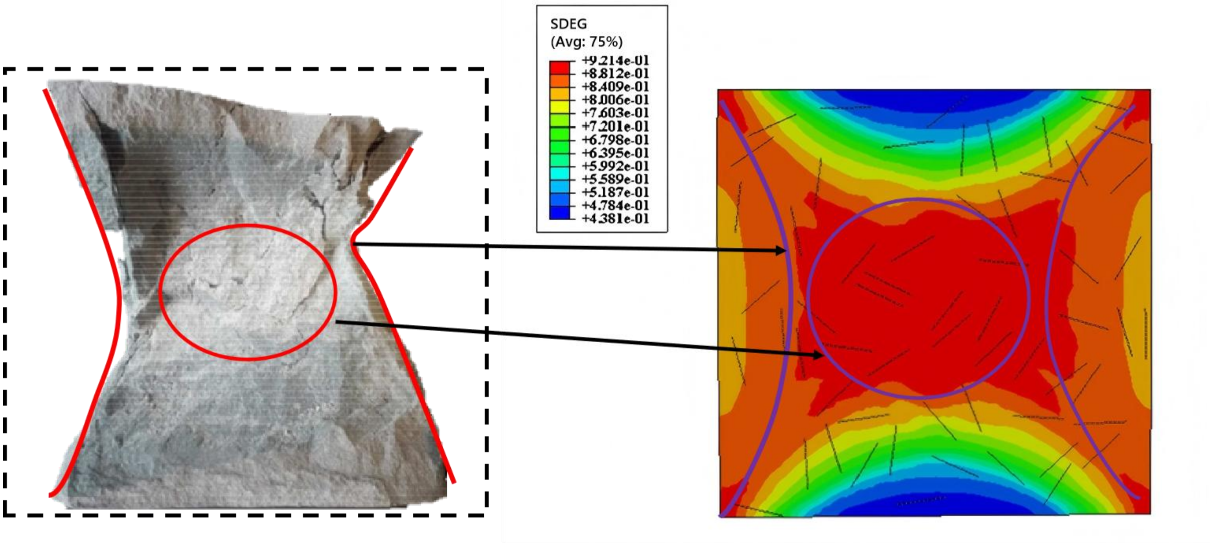

(a) Test (b) FE simulation

Fig. 6 – Comparison of FE model failure and experimental phenomena

In summary, by comparing the stress-strain curves and failure modes in the FE model and the experiment, it is shown that the FE model can better reflect the mechanical properties of ECC under compression.

Parameter study

Based on the model verification, the FE model was used to conduct parameter research. The mechanical features of ECC under compression were examined by varying the dosage and length of PVA fibers in the ECC mixture. The specific research variables are shown in Table 3.

Tab. 3 - Details of parametric analysis

Serial No.	Fiber ratio(%)	Fiber length(mm)
ECS-1	0.4	12
ECS-2	0.8	12
ECS-3	1.2	12
ECS-4	1.6	12
ECS-5	2	12
ECS-6	2.4	12
ECS-7	2.8	12
ECS-8	3.2	12
ECS-9	3.6	12
ECS-10	2	10
ECS-11	2	11
ECS-12	2	13
ECS-13	2	14

DOI 10.14311/CEJ.2026.01.0007

(1) Fiber content

The stress-strain relationship under uniaxial compression contains important mechanical performance indicators, which can fully reflect the deformation characteristics and the whole process of destruction of the material at each stress stage. It is a material physical condition necessary for structure and component design and nonlinear analysis. To investigate the influence of the fiber quantity on the compressive performance of ECC, the fiber content was incrementally raised by 0.4% for the parameter study. The ECC compressive stress-strain curve obtained by FE model analysis is shown in Figure 7.

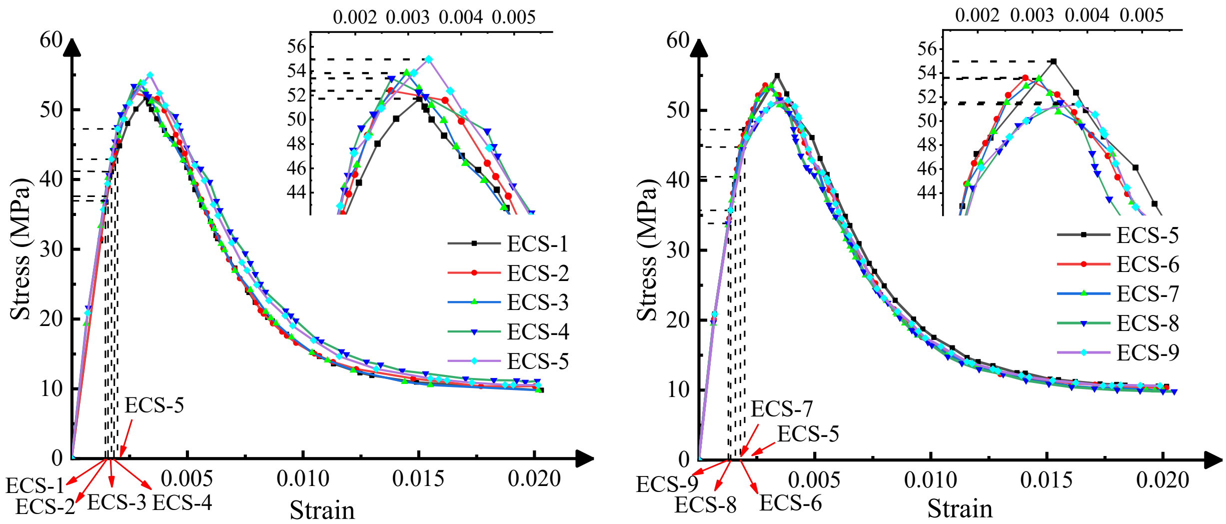

(a) Fiber content 0.4%~2% *(b) Fiber content 2%~3.6%*

Fig. 7 – Stress-strain curves of different fiber content

As illustrated in Figure 7, the shape of the stress-strain curve of ECC is similar to the compressive curve of ordinary concrete, which is a skewed single-peak curve. In the initial stage, the slope of the stress-strain curve of ECC is close to a straight line. As the load gradually increases, some fibers are broken, and the curve's slope alters markedly upon attaining the yield stress. When the fiber content is 0.4%~2%, as the fiber content increases, the yield strain increases from 0.0013 to 0.002, which is 1.5 times higher. The addition of fiber enhances the compressive capacity of ECC. When the fiber content is 2% to 3.6%, as the fiber content increases, the yield strain decreases from 0.002 to 0.0011, which is a decrease of 45%. After the curve enters the strengthening stage, the peak strains of ECS-1 to ECS-9 are between 0.0025 and 0.0035, and the change is not obvious. Overall, when the fiber length is 2%, the yield stress and peak stress of ECC reach the maximum value, and it has good compressive bearing capacity.

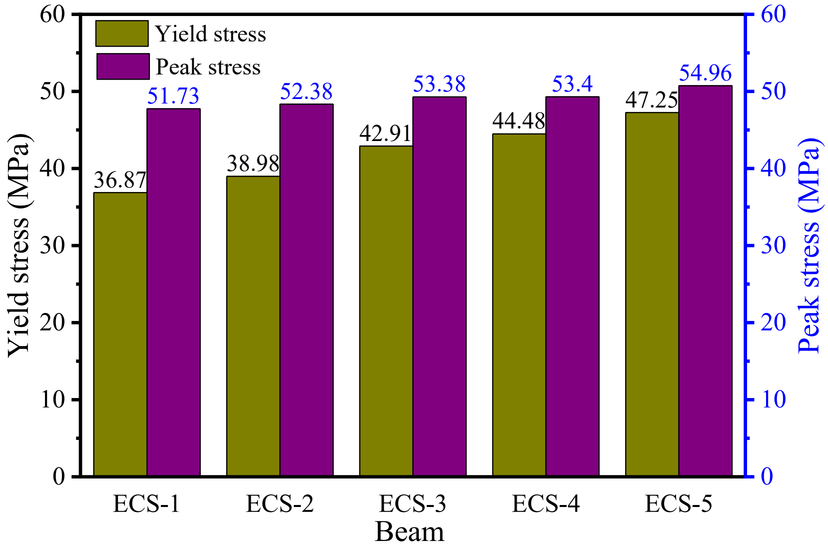

(a) Fiber content 0.4% to 2%

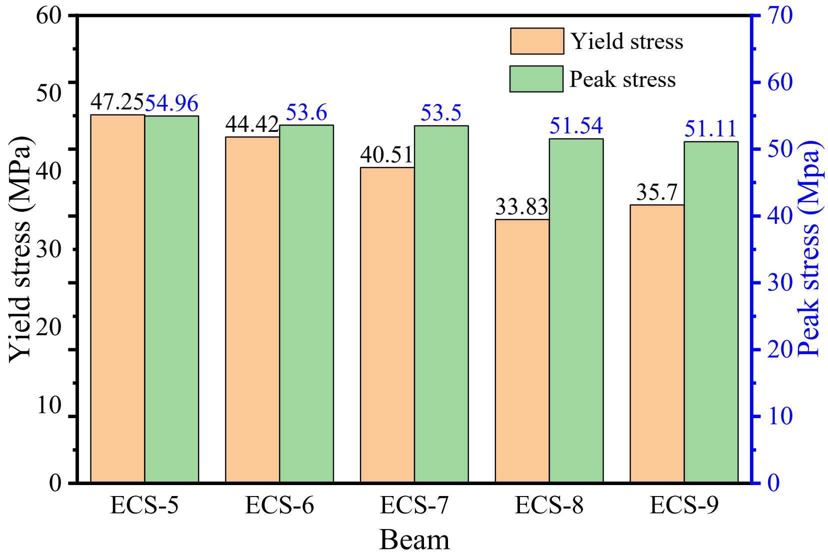

(b) Fiber content 2% to 3.6%

Fig. 8 – Yield and peak stress of different fiber contents

Figure 8 lists the yield stress and peak stress of ECC with different fiber content. As shown in Figure 8 (a), when the fiber content is 0.4% to 2%, the yield stress and peak stress of ECC gradually increase with the increase of fiber content. Compared with ECS-1, the yield stress and peak stress of ECS-5 are 47.25 MPa and 54.96 MPa, respectively, which are increased by 28.1% and 6.2%, respectively. This can be explained that the addition of fiber can enhance the ductility and toughness of ECC, improve the compressive strength of the material, and enable ECC to withstand greater stress. As illustrated in Figure 8 (b), when the fiber content is 2% to 3.6%, the yield stress and peak stress of ECC progressively diminish as fiber content increases. Compared with ECS-5, the yield stress of ECS-8 is 33.83 MPa, which is a decrease of 28.4%. Compared with ECS-5, the peak stress of ECS-9 decreases from 54.96 MPa to 51.11 MPa, which is a decrease of 7.0%. This result occurs because too many fibers are unevenly distributed inside the concrete, which causes the surrounding fibers to gather together, resulting in fiber bundling, which causes the ECC's compressive performance to decrease. Nonetheless, owing to the bridging action of the fibers, the ECC can persist in withstanding the pressure.

Tab. 4 - EAC and Poisson's ratio of different fiber content

Test block	ECS-1	ECS-2	ECS-3	ECS-4	ECS-5	ECS-6	ECS-7	ECS-8	ECS-9
EAC (J/m^2)	0.439	0.446	0.449	0.485	0.476	0.459	0.452	0.447	0.456
Poisson's ratio	2.63	2.71	2.89	2.96	2.98	3.00	2.93	2.91	2.90

The energy absorption capacity (EAC) of a material refers to the amount of energy it can absorb when subjected to external force or energy impact [25]. Table 4 illustrates that the EAC progressively rises from ECS-1 to ECS-4 as fiber concentration increases. The energy absorption of ECS-4 is 0.485 J/m^2, which is 10.5% higher than that of ECS-1. As the fiber content increases further, the energy absorption shows a decreasing trend. Compared with ECS-4, the energy absorption values of ECS-5 and ECS-8 are 0.476 J/m^2 and 0.447 J/m^2, respectively, which are 1.8% and 8.5% lower. The energy absorption of ECS-9 is 0.456 J/m^2, which is 2% higher than that of ECS-8, but the increase is small.

Table 4 gives the Poisson's ratio values of ECC with different fiber content. With an increase in fiber content, the Poisson's ratio initially rises and subsequently declines. Compared with ECS-1, the Poisson's ratio of ECS-6 is 3, an increase of 14.1%. Compared with ECS-6, the Poisson's ratio of ECS-9 is 2.9, a decrease of 3.3%. Simultaneously, it is evident that when fiber content increases, the magnitude of the Poisson's ratio tends to stabilize. The content of PVA fiber influences its interaction with the ECC matrix and the mechanical characteristics of ECC, resulting in a variation of the Poisson's ratio. In fiber-reinforced concrete, the fiber will support a portion of the load when the specimen is subjected to stress. The low elastic modulus of the fiber results in minimal impact on the Poisson's ratio of ECC from the surplus fiber.

(2) Fiber content

In order to study the impact of fiber length on the compressive performance of ECC, the fiber length was gradually increased with 1 mm as the benchmark for parameter study, and the compressive behavior of ECC was analyzed through 5 sets of simulation results. When ECC is subjected to force, relative slippage between fibers will occur, resulting in the fiber being broken. Under uniaxial compression, the strain of ECC changes with the increase of PVA length, as illustrated in Figure 9. As the fiber grows in length, the yield strain and peak strain of ECC initially rise and thereafter decline. Among them, the yield strain and peak strain of ECS-5 reach the maximum, which are 0.002 and 0.0034 respectively.

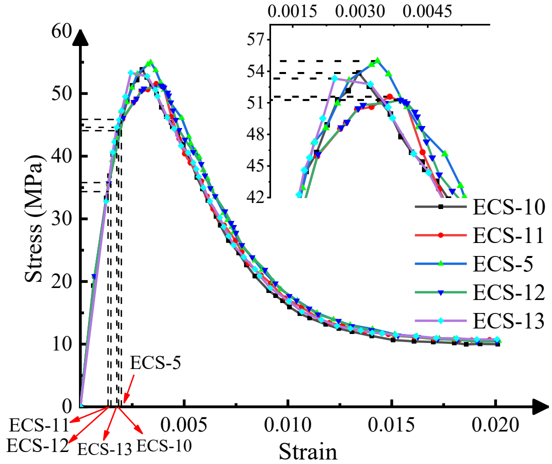

Fig. 9 – Stress-strain curves of different fiber lengths

Figure 10 (a) lists the yield stress values of different fiber lengths. Compared with ECS-10, the yield stress of ECS-11 is 32.81 MPa, which is 26.2% lower. Compared with ECS-11, the yield stress of ECS-5 reaches a maximum value of 47.25 MPa, which is 44.1% higher. The yield strength of ECS-12 is 32.81 MPa, which is 30.5% lower than that of ECS-5 and the same as the yield stress of ECS-11. The yield strength of ECS-13 is 44.60 MPa, which is 35.9% higher than that of ECS-12. The reason for the above pattern is that longer fibers sometimes produce problems such as agglomeration and entanglement in ECC, which in turn affects the uniformity and consistency of the ECC compressive properties, resulting in a decline in the ECC compressive performances.

The peak stress values of different fiber lengths are shown in Figure 10 (b). As the fiber length increases, the peak stress of ECS-5 reaches a maximum value of 54.96 MPa. Compared to ECS-5, the peak stresses of ECS-11 and ECS-12 are 51.57 MPa and 51.26 MPa, respectively, reduced by 6.5% and 7.2%. The peak stresses of ECS-10 and ECS-13 were 53.82MPa and 53.30MPa, respectively, which were reduced by 2.1% and 3.1%. The statistics indicate that a fiber length of 12 mm yields optimal compressive performance for ECC.

Tab. 5 - EAC and Poisson's ratio of different fiber content

Test block	ECS-10	ECS-11	ECS-5	ECS-12	ECS-13
EAC (J/m ^{2})	0.446	0.454	0.476	0.467	0.457
Poisson's ratio	2.92	3.07	2.98	2.89	2.94

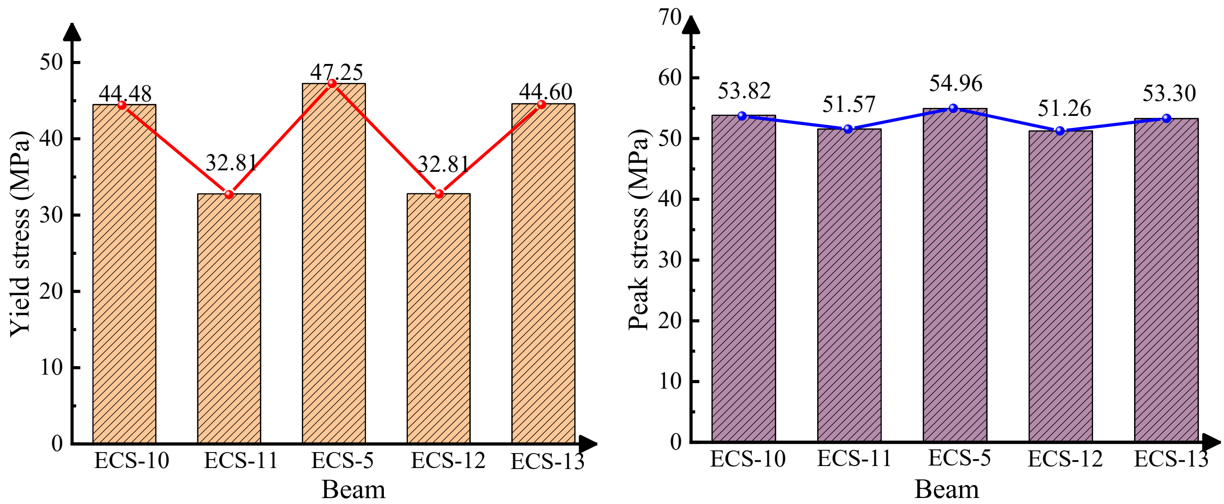

(a) Yield stress *(b) Peak stress*

Fig. 10 – Yield and peak stress values at different fiber lengths

Table 5 illustrates that with an increase in fiber length, both the EAC and Poisson's ratio initially rise and thereafter decline. The energy absorption values of ECS-10 and ECS-11 are 0.446 J/m^2 and 0.454 J/m^2, respectively, with a small difference. Compared with ECS-10, the energy absorption of EB-5 reaches a maximum value of 0.476 J/m^2, an increase of about 6.7%. As the fiber length increases further, the energy absorption shows a decreasing trend. Compared with ECS-5, the energy absorption values of ECS-12 and ECS-13 are 0.467 J/m^2 and 0.457 J/m^2, respectively, a decrease of about 1.8% and 3.6%. This shows that the EAC of ECS-5 is significantly improved compared with other test groups.

Compared with ECS-10, the Poisson's ratio of ECS-11 is 3.07, an increase of 5.13%. Compared with ECS-11, the Poisson's ratio of EB-12 is 2.89, a decrease of 5.8%. Simultaneously, it is evident that when the fiber length ranges from 10 mm to 14 mm, the augmentation of fiber

DOI 10.14311/CEJ.2026.01.0007

length little influences the Poisson's ratio of ECC and has a negligible impact on the overall stiffness of ECC.

CONCLUSIONS

This research studies the impact of PVA fiber content and fiber length on the compressive performance of ECC by numerical simulation method. The numerical model was first validated against experimental data to ensure its accuracy and practical applicability, and the following conclusions are drawn:

(1) The FE methods can be employed to model the uniaxial compression test of ECC. The derived stress-strain curve and damage occurrence closely align with the experimental findings.

(2) The stress-strain curve of ECC resembles the complete compressive strength curve of conventional concrete, characterized by a skewed single-peak shape.

(3) The optimal compressive performance of ECC occurs with a PVA fiber content of 2% and a fiber length of 12 mm. Within the PVA fiber content range of 0.4% to 2%, an increase in fiber content enhances the compressive performance of ECC. The yield stress and peak stress of ECS-5 attain maximum values of 47.25 MPa and 54.96 MPa, respectively. As fiber level exceeds 2%, the compressive performance of ECC diminishes with increasing fiber content.

(4) Augmenting the fiber length can significantly enhance the compressive characteristics of ECC. The yield stress and peak stress attain their greatest values with a fiber length of 12 mm. When the fiber length is greater than 12 mm, the yield stress, peak stress, and EAC will decrease as the fiber length increases.

(5) In future research, the authors will further precisely determine the dosage and length of PVA fibers to provide the optimal mechanical properties and offer reliable reference for engineering applications and designs.

ACKNOWLEDGEMENTS

This study is supported by 5 key funds: (1) Science and Technology Planning Project of Anyang, Henan Province, China (2025C01SF168), (2) Start-up Funding of Postdoctoral Innovation Practice Base in Anyang Institute of Technology, Henan Province, China (BHJ2025001), (3) Start-up Funding of Doctoral Research in Anyang Institute of Technology, Henan Province, China (BSJ2025010), (4) Training Program for Young Backbone Teachers in Higher Education Institutions of Anyang Institute of Technology, Henan Province, China (2025004), and (5) Annual Project of the College Students' Innovation and Entrepreneurship Training Program in Henan Province, China (202511330016).

REFERENCES

[1] Xu T, Zhou Z, Wang M, et al. Damage mechanism of pier concrete subjected to combined compressive stress, freeze-thaw, and salt attacks in saline soil. Construction and Building Materials, 2022, 324: 126567. 10.1016/j.conbuildmat.2022.126567.

[2] Ji J, Zhang Z, Lin M, Li L, Jiang L, Ding Y, et al. Structural application of engineered cementitious composites (ECC): A state-of-the-art review. Construction and Building Materials 2023;406:133289. 10.1016/j.conbuildmat.2023.133289.

[3] Hu Z, Elchalakani M, Yehia S, Ran H, Sadakkathulla MA, Guo X. Engineered cementitious composite (ECC) strengthening of reinforced concrete structures: A state-of-the-art review. Journal of Building Engineering 2024;86:108941. 10.1016/j.jobe.2024.108941.

[4] Wang LH, Shi WH, Qian LP, Bai YL, Liu SZ, Yang ZQ. Flexural behaviors of GFRP-reinforced Engineered Cementitious Composite (ECC)-concrete composite beams. Engineering Structures 2025;332:120097. 10.1016/j.engstruct.2025.120097.
[5] Shoji D, He Z, Zhang D, et al. The greening of engineered cementitious composites (ECC): A review. Construction and Building Materials, 2022, 327: 126701. 10.1016/j.conbuildmat.2022.126701.
[6] Guan X, Li Y, Liu T, et al. An economical ultra-high ductile engineered cementitious composite with large amount of coarse river sand. Construction and Building Materials, 2019, 201: 461-472. 10.1016/j.conbuildmat.2018.12.207.
[7] Li Y, Li J, Yang E H, et al. Mechanism study of crack propagation in river sand Engineered Cementitious Composites (ECC). Cement and Concrete Composites, 2022, 128: 104434. 10.1016/j.cemconcomp.2022.104434.
[8] Liu D. Development and application of high ductility fiber reinforced cement-based composites. Transport Business China, 2022(27): 146-148.
[9] Zhou J, Pan J, Leung C K Y. Mechanical Behavior of Fiber-Reinforced Engineered Cementitious Composites in Uniaxial Compression. Journal of Materials in Civil Engineering, 2015, 27(1): 04014111. 10.1061/(ASCE)MT.1943-5533.0001034.
[10] Fischer, G., and Li, V. C. (2002). "Effect of matrix ductility on deformation behavior of steel-reinforced ECC flexural members under reversed cyclic loading conditions." ACI Struct. J., 99(6), 781–790.
[11] Chunhong H, Yane G, Wancong D. Experimental research on compressive performance of ultra high toughness cementitious composites.Journal of Building Structures, 2013, 34(12):128-132+154.
[12] Singh M, Saini B, Chalak H D. Performance and composition analysis of engineered cementitious composite (ECC) – A review. Journal of Building Engineering, 2019, 26: 100851. 10.1016/j.jobe.2019.100851.
[13] Narimanifar K, Mousavi Ghasemi S A. Evaluating and comparing the bending performance of RC beams fabricated with lightweight aggregate concrete and normal concrete of equivalent strength. Buildings, 2024, 15(1): 45. 10.3390/buildings15010045.
[14] Ellithy M, Hassan A, El-Shafiey T F. Flexural strengthening of RC beams using PGFRP bars embedded in strain-hardening cementitious composites (SHCC). Engineering Structures, 2024, 317: 118628. 10.1016/j.engstruct.2024.118628.
[15] Subramanian N, Solaiyan E, Sendrayaperumal A, et al. Flexural behaviour of geopolymer concrete beams reinforced with BFRP and GFRP polymer composites. Advances in Structural Engineering, 2022, 25(5): 954-965. 10.1177/13694332211054229.
[16] Hung C C, Li S H. Three-dimensional model for analysis of high performance fiber reinforced cement-based composites. Composites Part B: Engineering, 2013, 45(1): 1441-1447. 10.1016/j.compositesb.2012.08.004.
[17] Gencturk B, Elnashai A S. Numerical modeling and analysis of ECC structures. Materials and Structures, 2013, 46(4): 663-682. 10.1617/s11527-012-9924-0.
[18] Li X Q, Ding J, Zhang T, et al. Influence of axial compression ratio on seismic performance of ECC frame nodes of different types. Journal of Vibration Engineering, 2022, 35(4): 793-805. 10.16385/j.cnki.issn.1004-4523.2022.04.002.
[19] Zhigang Ren, Bin Xu, Shuhuai Cheng. A two-dimensional stochastic modeling method for hybrid fiber concrete. Journal of Wuhan University of Technology, 2015, 37(4): 53-58.
[20] Xu Shi-shin, Cai Xiangrong, Zhang Ying-hua. Determination and analysis of full stress-strain curve test of ultra-high toughness cement-based composites under uniaxial compression. China Civil Engineering Journal, 2009, 42(11): 79-85. 10.15951/j.tmgcxb.2009.11.009.
[21] Wu Shaofeng. Study on basic mechanical properties of PVA-ECC materials based on microscopic finite element. Journal of Water Resources and Architectural Engineering, 2022, 20(6): 175-181. 10.3969/j. issn.1672－1144.2022. 06.026.
[22] Grote D L, Park S W, Zhou M. Dynamic behavior of concrete at high strain rates and pressures: I. experimental characterization. International Journal of Impact Engineering, 2001, 25(9): 869-886. 10.1016/S0734-743X(01)00020-3.
[23] Li V C. From micromechanics to structural engineering—the design of cementitous composites for civil engineering applications. Structural Engineering / Earthquake Engineering,1994,10(2) : 1-34. 10.2208/jscej.1993.471_1.
[24] Li Yan, Wen Congge. Study on uniaxial tensile properties of engineering fiber-reinforced cement-based composites PVA-ECC. Concrete, 2015(9): 31-35. 10.3969/j.issn.1002-3550.2015.09.009.

[25] Gopalaratnam V S, Gettu R. On the characterization of flexural toughness in fiber reinforced concretes. Cement and Concrete Composites, 1995, 17(3): 239-254. 10.1016/0958-9465(95)99506-O.

CIVIL ENGINEERING JOURNAL

Article no. 8

THE CIVIL ENGINEERING JOURNAL 1-2026

COMPARISON OF RENOVATION AND REPLACEMENT STRATEGIES FOR IMPROVING THE THERMAL PERFORMANCE OF HISTORIC BOX-TYPE WINDOWS IN 19TH-CENTURY APARTMENT BUILDINGS

David Skála and Klára Kroftová

Czech Technical University, Faculty of Civil Engineering, Department Architecture and Building, Prague, Thákurova 2077/7; e-mail: david.skala@fsv.cvut.cz, klara.kroftova@fsv.cvut.cz

Received:	*15.12.2025*
Received in revised form:	*02.03.2026*
Accepted:	*27.04.2026*

ABSTRACT

The article focuses on the possibilities of modifying the window assemblies of apartment buildings from the 19th and early 20th centuries. The issue is illustrated through a case study of a building constructed in 1873, located in Prague in the heart of Žižkov and protected as a cultural monument. It examines restoration, renovation, and maintenance strategies for historic window assemblies, addressing the methods of their repair as well as current technical and material possibilities for their renewal. The study concentrates on options for improving the technical performance of existing window structures, their comparison, and their adaptation to present-day standards required of modern window assemblies. The issue is evaluated from technical, economic, thermal, and hygrothermal perspectives.

KEYWORDS

Window renovation, Window heat resistance, Box-type windows, Window replacement, Historic apartment buildings

INTRODUCTION

The renovation of historic window assemblies from the 19th and early 20th centuries has become an important issue in both heritage conservation and energy efficiency. Original historic double and box-type windows are typically at the end of their service life after approximately 100–150 years and therefore require professional intervention. In many cases, this intervention leads to their replacement; however, from the perspective of heritage conservation, their preservation is generally preferable. Current trends and legislation often favour replacement with high-performance products, although renovation and technical upgrading remain viable alternatives.

If the designer decides to retain the existing windows, it is necessary to select an appropriate renovation strategy depending on their condition, heritage requirements, and desired building-physics performance. Despite its importance, comparative data on these approaches remain limited. The aim of this paper is to quantitatively compare renovation and replacement strategies for historic box-type windows in terms of thermal performance, condensation behaviour, and economic efficiency.

A brief literature review

At present, this issue is addressed primarily by joiners, who are required to declare the performance of refurbished window assemblies, and by designers responsible for their specification. Although some measurements have been carried out, publicly available and clearly documented research data remain limited, particularly with respect to comprehensive and comparable evaluations.

In the Czech Republic, the topic is discussed in the publication *Obnova okenních výplní a výkladců* ("Restoration of Window Infill Elements and Shopfronts") [1], in which Zbyněk Svoboda analyses four window assembly variants with different configurations of insulated glazing units using an atypical five-sash window as a reference case. Another relevant publication is *Repliky oken v památkových zónách* ("Window Replicas in Heritage Conservation Areas") [2], which marginally addresses condensation-related issues. Further works focusing on renovation methods include *Vady při obnově výplní otvorů u budov v památkových zónách* ("Defects in the Restoration of Opening Elements in Buildings Located in Conservation Areas") [3] and *Postupy při volbě oprav nebo zvolení výměny oken, dveří a dalších prosklených konstrukcí* ("Guidelines for Choosing Between Repair and Replacement of Windows, Doors, and Other Glazed Structures") [4]. These publications provide valuable practical insights but address building-physics aspects only to a limited extent. The production of window replicas is also briefly discussed in a conference contribution presented at the Faculty of Architecture of CTU in Prague in 2005 [5].

Thermal performance improvement is only marginally reflected in standards such as ČSN EN ISO 12567-1 (730579), ČSN 74 6101 and ČSN 73 0540-2. In popular literature, Jan Hollan addresses window renovation in *Co s okny? Upravená stará okna lepší než nová* ("What to Do with Windows? Refurbished Original Windows Are Better Than New Ones") [6]; however, this work does not provide quantified results. One of the co-authors of this paper previously contributed to the study *Stavební a architektonické detaily činžovních domů postavených na přelomu 19. a 20. století ve středoevropském regionu – hygrotermální analýza* ("Building and Architectural Details of Tenement Houses Built at the Turn of the 19th and 20th Centuries in the Central European Region—Hygrothermal Analysis") [7], which focuses on thermal performance and adaptation of envelope structures.

In the international context, thermal performance of historic windows has been investigated, for example, by studies conducted at the Berlin University [8] and the Vienna University [9], both presenting extensive experimental measurements. The influence of window installation within the building envelope is analysed in detail in *Documentation and assessment of conventional and innovative solutions for conservation and thermal enhancement of window systems in historic buildings* [10]. A key reference is also *Energetische Sanierung historisch wertvoller Fenster* issued by Bern University of Applied Sciences [11], although it focuses on window types less typical for 19th-century urban apartment buildings in the Czech context.

An overview of typical defects of historic windows

The preservation of historic window and door assemblies is one of the most demanding tasks in heritage conservation. In practice, both their heritage value and craftsmanship are often overlooked, and high-quality joinery elements are frequently replaced. This is often justified by claims of extensive damage, although such defects can often be repaired. In many cases, the current condition of windows results from a series of partial interventions, such as inserting new sashes into original frames. In these situations, expert assessment is essential, with emphasis on preserving as much original material as possible and replacing only later additions.

The most common defects include degradation of surface coatings and minor deterioration of timber, which can usually be prevented by regular maintenance. More serious problems include sagging of sashes, air leakage, warping of profiles, malfunctioning hardware, and biological degradation caused by rot, fungi, or insects. Weather-exposed elements are particularly vulnerable.

Each defect requires individual assessment to determine whether repair, partial replacement, or complete replacement is appropriate.

Sagging of window sashes is typically caused by loosened or displaced hinges. It can be addressed by re-fixing or repositioning the hinges. Corner braces are also commonly used; ideally, they should be inserted into prepared recesses. In practice, however, they are often only screwed on and covered with paint, which reduces their durability.

A discussion of possible intervension approaches

In the case of degraded timber in external window elements, it is first necessary to assess whether the defect is purely aesthetic. Irregularities such as nail holes or traces of previous repairs, which do not affect function, should generally be preserved. Minor losses of material can be repaired using wooden inserts or suitable repair compounds.

Air leakage between the sash and frame may result from settlement, timber shrinkage, or excessive paint layers. These defects can usually be remedied by sanding, local repairs, and renewal of the surface coating. Sealing profiles should be used only where sufficient airtightness cannot be achieved otherwise, as increased airtightness requires alternative ventilation. While metal profiles were used historically, rubber seals and bonded or milled-in profiles are now more common.

Timber decay caused by rot or fungi is often considered a reason for full replacement. However, local damage can usually be addressed by partial replacement, typically in the lower parts of sashes or frames. Extensive damage may require replacement of larger sections, which is technically demanding and may make full replacement economically preferable.

Replacing single glazing with insulated glazing units is one of the simplest ways to improve thermal and acoustic performance. However, the load-bearing capacity of existing frames and hinges must be verified. Thermal performance can also be improved by applying low-emissivity (Low-E) films. From a technical perspective, installing insulated glazing in the outer sashes, combined with improved airtightness, is generally preferable, as it reduces condensation risk and improves thermal performance.

From a heritage perspective, however, installing insulated glazing in the inner sash is often preferred because it preserves the external appearance. Two main approaches are used:

1. Installation into the existing rebate with additional glazing beads, which alters the external appearance.
2. Deepening of the rebate and bonding of the glazing, which is more demanding but visually more appropriate.

Decisions on window replacement require a sensitive approach, especially in heritage-protected buildings. The aim is to preserve original materials, opening mechanisms, and hardware. In buildings outside protected areas, economic considerations play a greater role, and repair and replacement should be evaluated in relation to energy savings and costs.

Inappropriate replacement can significantly damage the architectural character of a building. Typical examples include oversized timber profiles or plastic windows, which disrupt façade proportions and may negatively affect the thermal behaviour of adjacent structures. Changes in appearance may also result from the use of modern float glass with different optical properties compared to original glass.

CASE STUDY: SCHOOL AT ŠTÍTNÉHO 520/5

For this study, a specific type of inward-opening historic box-type window with a casement vent, operable transom, and subdivided sash was analysed. The windows are located in a Neo-Renaissance building in the Žižkov district of Prague, built in 1873. Although the building originally served as a school, the window design corresponds to common practice in 19th- and early 20th-century urban apartment buildings. Due to limited maintenance and economical operation, the original windows have been preserved in largely intact condition. The building has been listed as a cultural monument since 2003.

POSSIBILITIES FOR WINDOW IMPROVEMENT

Six variants were analysed, combining heritage requirements, energy performance, condensation behaviour, and cost. All variants represent solutions commonly used in practice.

Variant 1 – Basic renovation

This approach consists of careful repair of the existing windows, including cleaning, local replacement of damaged timber, surface treatment, and adjustment of hardware. Airtightness is improved by installing silicone sealing profiles. This intervention significantly improves airtightness (Figure 1) and reduces air exchange by up to approximately 70%. However, it increases the risk of condensation, particularly on the inner surface of the outer sash. Therefore, it is recommended to include drainage grooves and to consider alternative ventilation strategies.

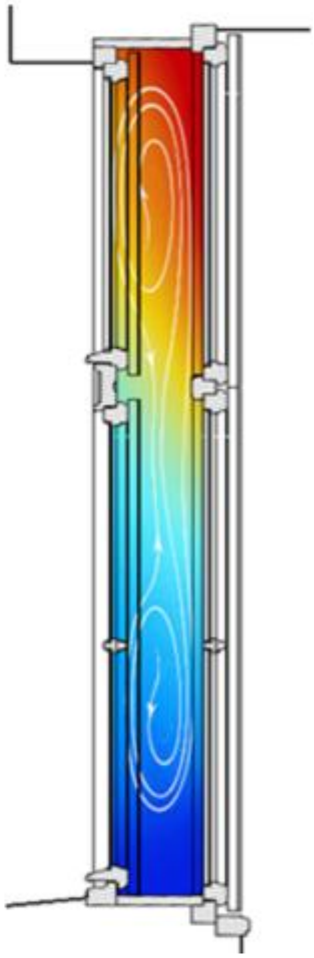

Fig. 1 - Schematic representation of airflow and distribution in the cavity between the outer and inner window.

Variant 2 – Renovation with Low-E film

A low-emissivity film is applied to both panes, reducing emissivity from 0.84 to 0.20 while maintaining high light transmittance. The intervention includes sealing of the outer sash and foaming of the window-to-wall joint. Although thermal performance improves, condensation on the inner surface of the outer sash persists and must be addressed similarly to Variant 1.

Variant 3 – Insulated glazing in outer sashes

Insulated glazing units (4–8–4 mm, krypton-filled) are installed into newly milled rebates in the outer sashes. The glazing is mechanically fixed and sealed, and structural reinforcement of the sashes is required. Sealing is applied to both sashes. This variant significantly improves thermal performance and reduces condensation risk. However, it requires modification of original elements and is not always feasible for larger windows.

Variant 4 – Insulated glazing in inner sashes

Insulated glazing is installed in the inner sashes, preserving the external appearance of the window. The intervention includes sealing and foaming of the reveals. This solution is less favourable from a building-physics perspective and, in this case, was not preferred due to the façade orientation.

The **final two variants involve complete replacement** with new window products, which excludes the preservation of the original historic fabric of the window assemblies.

Variant 5 – Replacement with a box-type replica

The original windows are replaced by new box-type windows made of laminated timber with modern sealing systems. These meet current technical requirements but differ in profile dimensions and detailing. From a heritage perspective, this solution is controversial and generally acceptable only outside strictly protected buildings.

Variant 6 – Replacement with a plastic window

This variant involves replacement with a standard plastic window. Although it offers a low initial cost, it significantly alters the appearance of the façade and results in the loss of historic value. For heritage-listed buildings, this solution is unacceptable.

THERMAL AND MOISTURE PERFORMANCE PARAMETERS

The assessment was not limited to the determination of the window thermal transmittance coefficient Uw as defined by the standard. However, the calculations were based on methodologies commonly used for evaluating window thermal performance. The assessed domain was extended to include 300 mm of adjacent brick masonry with internal and external plaster finishes surrounding the window opening. This made it possible to account for the influence of window installation on the overall heat losses of the building.

Particular emphasis was placed on evaluating the adverse impact of replacing box-type windows with single windows, especially in terms of increased heat transfer through the surrounding masonry, as addressed in Variant 6. The calculated values are therefore not directly comparable with catalogue data. However, they provide a more realistic basis for comparing the individual variants.

The window thermal transmittance coefficient Uw was calculated in accordance with EN ISO 10077-1 [12], which defines the total heat transfer as a combination of surface-related and linear components (Fig. 2). The calculation was performed using Equation 1:

$$U_w = \frac{A_g \cdot U_g + A_f \cdot U_f + L_g \cdot \psi_g + \sum L_k \cdot \psi_k + L_{inst} \cdot \psi_{inst}}{A} \qquad (1)$$

U_w – thermal transmittance of the window [W/m²K] according to EN 673,
U_g – thermal transmittance of glazing [W/m²K],
U_f – thermal transmittance of frame [W/m²K],
A_g – area of glazing [m²],
A_f – area of frame [m²],
ψ_g – linear thermal transmittance at the glass edge [W/mK],
ψ_k – linear thermal transmittance of muntins [W/mK],
ψ_{inst} – linear thermal transmittance of the window-to-wall junction [W/mK],
L_g, L_k, L_{inst} – corresponding lengths of thermal bridges [m],
A – total area of the window [m²].

Due to the atypical geometry of the assessed frames, all input values were determined using two-dimensional numerical simulation in THERM 7.8 (Lawrence Berkeley National Laboratory), in accordance with EN ISO 10077-2 and EN ISO 10211 [13]. Standard surface resistance conditions were applied (Rsi = 0.13 m²K/W and Rse = 0.04 m²K/W).

The model included individual material layers of the frame, glazing, and installation gaps. The temperature field was evaluated for a unit temperature difference of 1 K. Airflow within the window assembly was also considered, using boundary conditions corresponding to Prague (Ti = 20°C, Te = –12°C).

In parallel, air permeability was assessed in accordance with ČSN 73 0540-3 [14]. This was necessary due to the significant air leakage of the existing windows, which is not captured by EN ISO 10077-1 [12]. Although not included in the standard Uw calculation, air leakage represents an additional heat loss. Based on the volumetric airflow rate at reference pressure, the natural infiltration rate qv,nat was determined using a power-law relationship (n ≈ 0.67). The corresponding ventilation heat loss was calculated as Hinf = 0.34 W/K.

For comparison purposes, this component was expressed as an "effective" thermal transmittance value that includes the effect of air leakage (Equation 2). This parameter is not normative under EN ISO 10077-1 [12], but it allows a more comprehensive evaluation of the individual variants.

$$U_{w,\,eff} = U_w + \frac{H_{inf}}{A_w} \qquad (2)$$

$U_{w,\,eff}$ – "effective" thermal transmittance of the window [W/m²K],
U_w – thermal transmittance of the window [W/m²K] according to EN 673,
H_{inf} – ventilation heat loss due to air infiltration [W/K],
A_w – window area [m²].

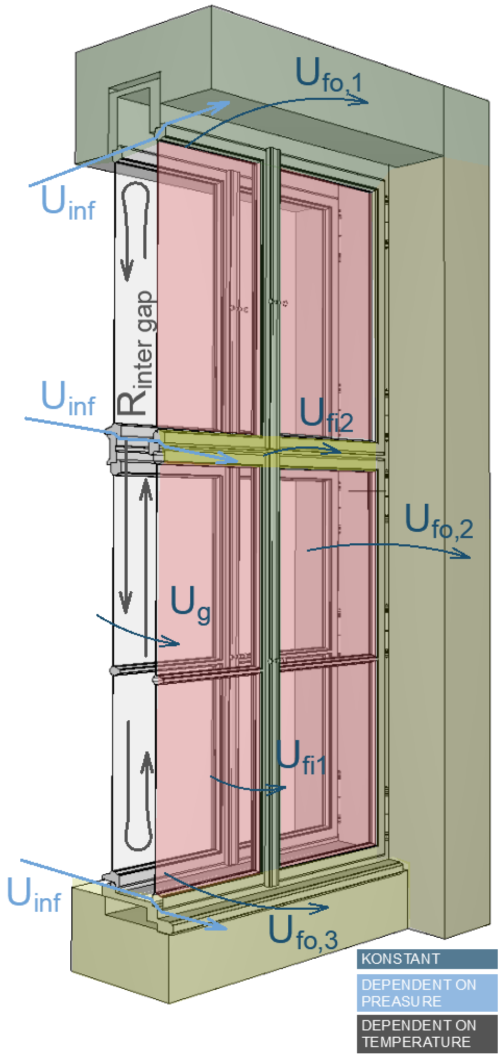

Fig. 2 - Schematic representation of the calculation procedure for the thermal transmittance of a box-type window.

WINDOWS OF THE BUILDING AT ŠTÍTNÉHO 520/5

A total of 16 similar windowss are located on the north-facing façade, four of which are tilt-opening. For their period, the windows are relatively large, with dimensions of 1200 × 2630 mm. Each window is divided into six panes with a thickness of 2.5–3.0 mm.

The frame includes an upper compartment for an inter-window blind or louvre. The hardware consists of espagnolette locking systems with decorative detailing. Hinges and fittings reflect classicistic design, and sash stays for the inner sashes are located at the lower part of the frame. The casement vent features a characteristic double ogee profile (Figures 3, 4).

Based on the original hardware, profile geometry, and preserved thin glass panes with optical imperfections typical of cylinder-blown glass, the windows can be reliably dated to the year of construction, i.e. 1873.

At present, the technical condition of the windows is unsatisfactory for school use. Sagging of the sashes limits operation, condensation has caused local timber decay, corner joints are loosened, frames are partially warped, and surface coatings are deteriorated on exposed sides.

According to heritage conservation requirements, it is necessary to preserve as much original material as possible while ensuring full functionality through renovation. The installation of insulated glazing and other modern elements is permitted, provided that the original geometry and architectural expression of the windows are maintained.

Article no. 8

THE CIVIL ENGINEERING JOURNAL 1-2026

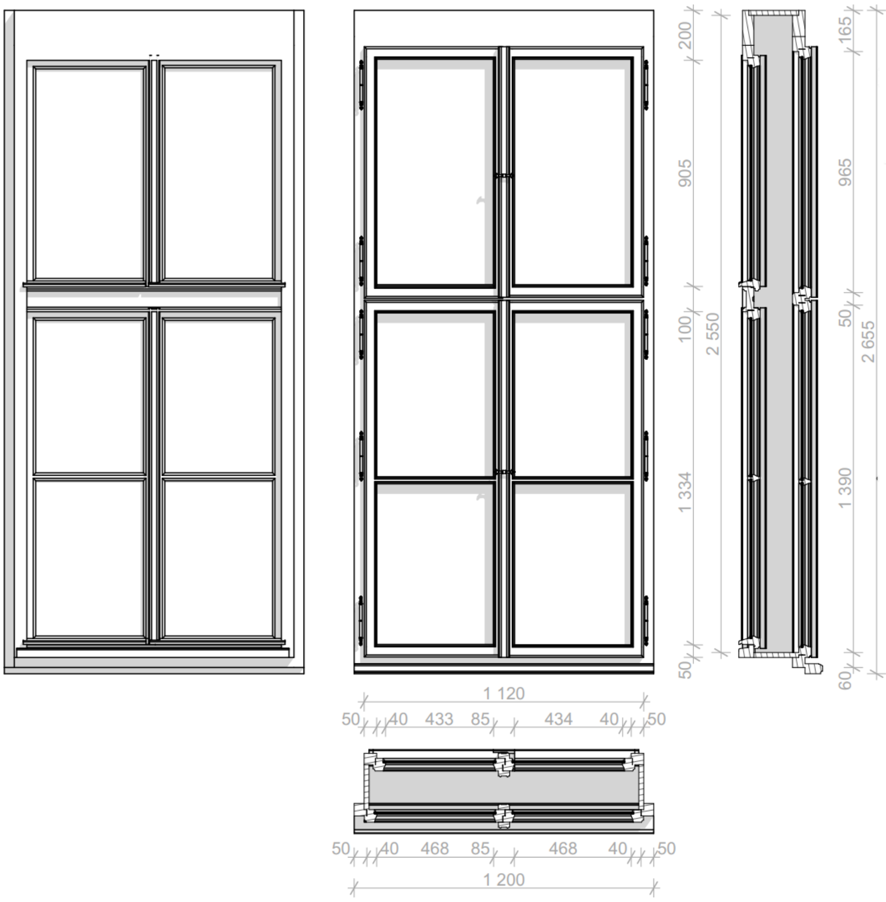

Fig. 3 - Analysed window at ZUŠ Štítného – drawing documentation.

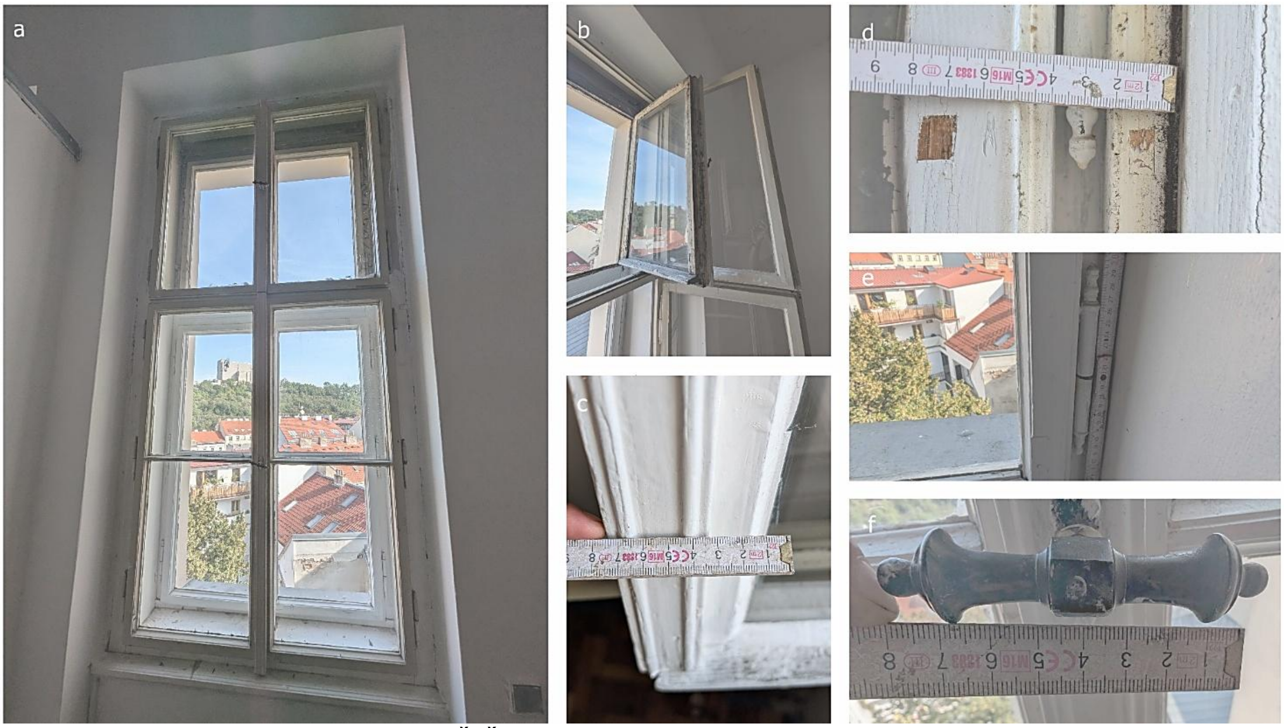

Fig. 4 - Analysed window at ZUŠ Štítného – photographic documentation a) front view of the window from the interior, b,c) detail of the profile, d,e,f) window ironmongery details.

The calculation considers two operating pressure differences representing different climatic situations: Q10 (10 Pa), corresponding to calm weather conditions, and Q50 (50 Pa), corresponding to windy conditions. The assessed window is exposed to strong north-western winds, further intensified by the morphology of the adjacent Vítkov Hill in the Žižkov district.

Due to the variable airflow within the window assembly, the thermal resistance of the internal cavity varies with surface temperatures. When evaluating results over a full model year, the contribution of airflow would be lower than under the presented design conditions. The results and comparisons of the individual variants are summarised in Tables 1 and 2.

1) Renovation of the existing window

From the condensation perspective, the introduction of sealing into the outer frame represents a deterioration of conditions, as ventilation is reduced compared to the original state. This effect can be mitigated by incorporating drainage grooves directing condensate towards the exterior and by protecting the structure against long-term moisture exposure. The measure reduces air infiltration during cold and windy conditions and contributes to extending the service life of the windows. The calculations indicate condensation within the window frame, which may migrate into the adjacent masonry and gradually evaporate towards the exterior (Figure 5).

2) Renovation with a Low-E film

Improving the radiative properties of the glazing increases the surface temperatures of both panes and shifts the condensation zone away from the critical threshold, particularly on the inner pane. On the outer pane, when sealing is applied only to the outer sash, condensation persists and must be addressed similarly to Variant 1. The results also indicate that foaming of the reveal reduces thermal bridging and lowers condensation risk (Figure 6).

3) Renovation with insulated glazing installed in the outer sashes

This variant provides a favourable temperature field distribution, with the main temperature gradients located in the outer sash. The transition from the colder masonry is moderated by the thermal properties of the box-type frame. The risk of condensation, associated with vapour penetration into the zone defined by the 12 °C isotherm, is reduced by internal sealing, which improves airtightness (Figure 7).

4) Renovation with insulated glazing installed in the inner sashes

Ventilation of the inter-window cavity and the shift of the thermal barrier towards the interior extend the colder zone into the window reveal. This may lead to condensation and freezing of adjacent masonry. The outer window is also exposed to freeze–thaw effects at sensitive locations. Effective drainage of condensate and meltwater is therefore essential (Figure 8).

5) Replacement with a modern replica of a box-type window

With proper installation, this solution provides favourable condensation behaviour and a smooth temperature transition. The critical point at the window-to-wall junction lies outside the condensation zone. However, increased airtightness reduces natural ventilation, which may be problematic, particularly in educational spaces (Figure 9).

6) Replacement with a modern plastic window

When installed in a conventional manner without specific treatment of the internal reveal, plastic windows show a lower degree of condensation on the masonry under standard indoor conditions. At the same time, a zone of increased heat loss occurs in the window reveal despite appropriate installation. The resulting thermal transmittance, including installation effects, is therefore less favourable than that of box-type windows in both renovated and new configurations (Figure 10).

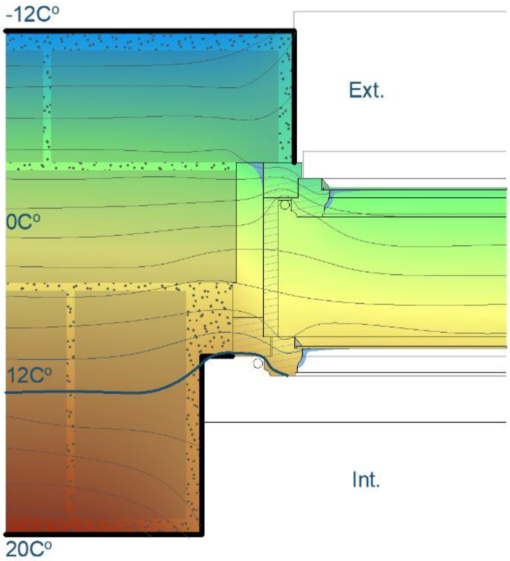

Fig. 5 - Distribution of temperature and moisture in the renovated window (WUFI 2D, Fraunhofer IBP)

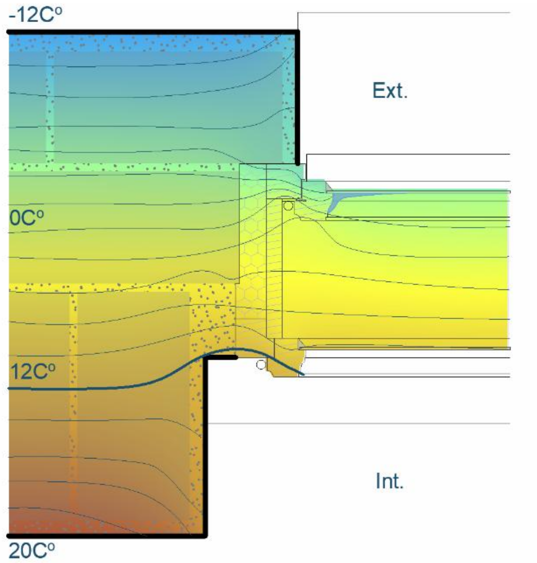

Fig. 6 - Distribution of temperature and moisture in the window fitted with a Low-E film (WUFI 2D, Fraunhofer IBP)

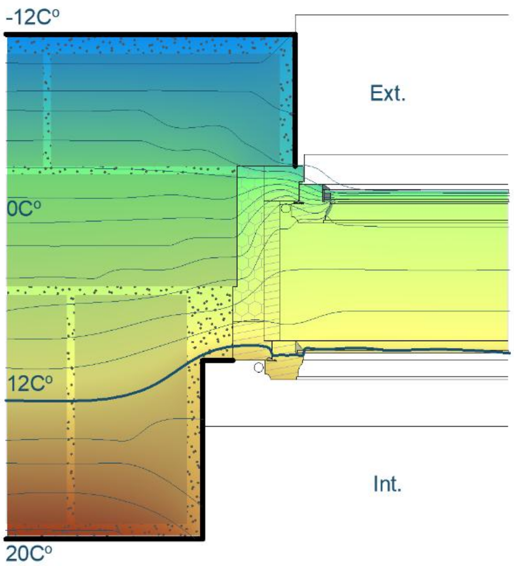

Fig. 7 - Distribution of temperature and moisture in a window with insulated glazing installed in the outer sashes (WUFI 2D, Fraunhofer IBP)

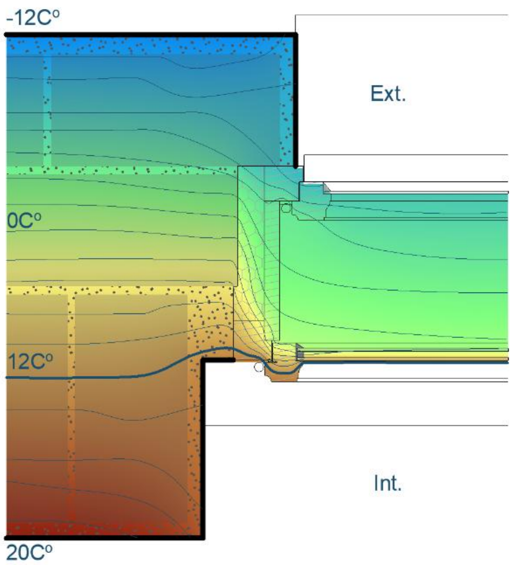

Fig. 8- Distribution of temperature and moisture in a window with insulated glazing installed in the inner sashes (WUFI 2D, Fraunhofer IBP)

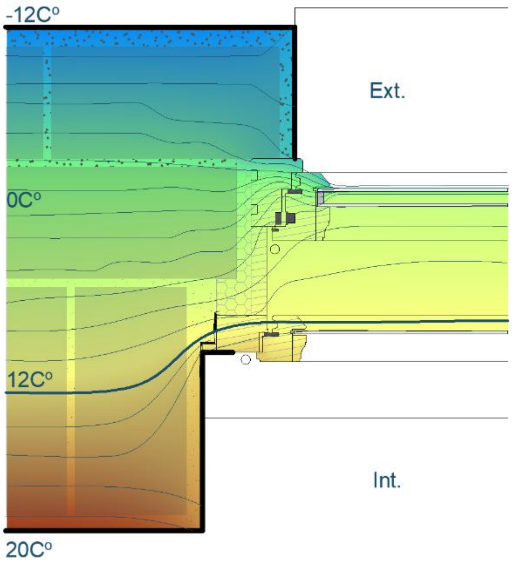

Fig. 9- Distribution of temperature and moisture in a new box-type window (WUFI 2D, Fraunhofer IBP)

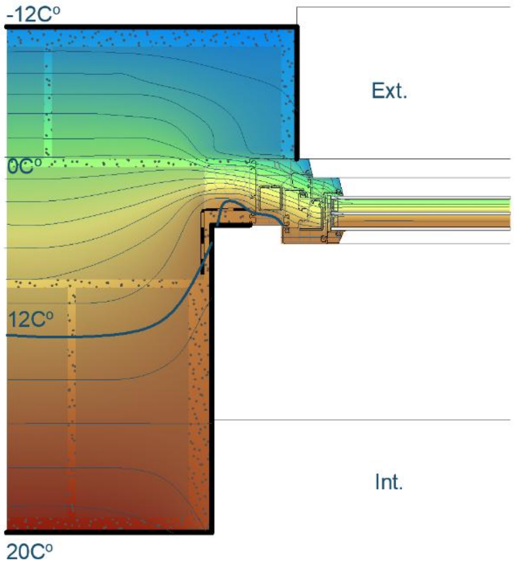

Fig. 10 - Distribution of temperature and moisture in a new plastic window (WUFI 2D, Fraunhofer IBP)

Tab. 1 - Calculation of thermal transmittance and air permeability of the existing windows

Variant	Thermal transmittance Uw according to EN ISO 10077-1 (W/m^2K)	Air permeability Q50 (m^3/h)	Air permeability Q10 (m^3/h)	Resulting Uw incl. Q50 + 300 mm masonry (W/m^2K)
Existing condition	1.897	0.837	0.284	2.734
Window repair	1.897	0.36	0.122	2.258
Low E film	1.732	0.36	1.22	2.092
Insulated glazing in outer sashes	1.399	0.11	0.071	1.760
Insulated glazing in inner sashes	1.399	0.392	0.133	1.792

Tab. 2 - Calculation of thermal transmittance including installation effects for new windows

Variant	Thermal transmittance U_w according to EN ISO 10077-1	+ 300 mm masonry effect	Resulting Uw incl. Q50 + 300 mm masonry
New box-type window	1.26	-0.07	1.19
New single plastic window	0.78	0.35	1.13

FINANCIAL COSTS AND INTERVENTION COMPLEXITY

To ensure a comprehensive assessment of the investigated issue, the financial costs associated with the individual interventions were quantified. All reported costs are expressed per single window and represent proportional shares of the total expenditure for the renovation of all 27 windows located on the courtyard façade. For most cost items, unit prices per window could be directly identified. For secondary budget items and costs related to waste disposal and material handling, proportional shares of either 1/27 or 1/20 (for renovated windows only) of the total costs were applied. The resulting values therefore include not only the direct costs of a new product or window renovation, but also all associated ancillary costs. This allows for an objective comparison of the individual variants.

The cost estimates were prepared on the basis of the URS pricing system (an integrated system of information, methodological guidance, and procedures for pricing construction works in the Czech Republic), using the KROS software (Kros a.s., Czech Republic). They are based on three quotations for window renovation for the analysed project, two quotations for replacement with plastic windows, and two quotations for replacement with box-type windows manufactured from laminated timber profiles. All prices are stated as of November 2025.

The overall comparison indicates that window renovation is fully cost-competitive with replacement. Interventions involving the installation of insulated glazing units approach the cost level of new products, while offering a substantial improvement in thermal performance and allowing the preservation of a significant portion of the original structure. In the case of new windows, the higher price of box-type window replicas is accompanied by additional costs related to demolition, waste disposal, material handling, site accessibility, and reinstatement of plaster finishes. These costs may be even higher in heritage-protected buildings.

A comparison of the individual variants in terms of financial costs is presented in Tables 3 and 4.

Tab. 3 - Cost analysis of the renovation of box-type windows

Variant	Partial costs of renovation					Total cost CZK (EUR)
	Joinery works	Low-E film	Insulated glazing	Foaming of reveals	Condensate drainage	
Window repair	33288				3761	37049 (1527 EUR)
Low E film	33288	5400		830	3761	43279 (2031 EUR)
Insulated glazing in outer sashes	33688		12043	830		48521 (2000 EUR)
Insulated glazing in inner sashes	33288		12043	830	3761	51882 (2138 EUR)

Tab. -: Cost analysis of window replacement options

Variant	Partial costs of renovation			Total cost CZK (EUR)
	Product cost	Demolition and waste disposal	General site costs	
New box-type window	52900	15902	7060	76121 (3137 EUR)
New single plastic window	17760	19661	7060	44481 (1833 EUR)

Replacement with plastic windows represents the lowest initial investment cost. However, this option is unacceptable in heritage-listed buildings and may have adverse effects on both the architectural appearance and the thermal stability of the masonry window reveal in the long term.

Considering the cost structure of the individual interventions, joinery works represent the largest investment component in renovation variants. For new window products, the dominant cost components are the price of the window itself, and demolition works, which are often underestimated or overlooked in comparative assessments.

An overall comparison of all variants is summarised in Table 5.

Tab. 5 - Comparison of renovation and replacement options for box-type windows (costs as of November 2025, excluding VAT)

Variant	Total cost (CZK excl. VAT)	U_w(Q50) (W/m²K)	U_w (Q10) (W/m²K)	Condensation	Heritage compatibility
Existing condition	-	2.734	2.182	Severe problem	-
Window repair	37049 (1527 EUR)	2.258	2.020	On inner and outer glazing	Maximum preservation
Low E film	43279 (2031 EUR)	2.092	1.855	On outer glazing	New glazing, change in reflection
Insulated glazing in outer sashes	48521 (2000 EUR)	1.510	1.466	Minimal, near sealing	New glazing, change in reflection
Insulated glazing in inner sashes	51882 (2138 EUR)	1.792	1.533	Occasional on outer glazing	Preserved external appearance
New box-type window	76121 (3137 EUR)	1.19	1.19	None	Profile not acceptable for listed buildings
New single plastic window	44481 (1833 EUR)	1.13	1.13	Occasional on masonry	Unacceptable for heritage buildings

RESULTS AND DISCUSSION

The main objective of this study was to compare the effectiveness of renovation and replacement strategies for historic box-type windows in terms of thermal performance, condensation behaviour, and economic aspects.

When interpreting the results, it should be noted that the calculations are based on conservative boundary conditions and therefore represent the upper limit of heat losses. Under more favourable conditions, particularly due to reduced internal airflow, the values can be expected to improve. In addition, due to the north-facing orientation of the model window, potential solar gains were not considered. As indicated by previous studies [6], such gains may further improve the performance of renovated windows.

The results show that even basic renovation can significantly improve thermal performance. In the analysed case, repair combined with sealing reduced the effective thermal transmittance from 2.734 to 2.258 W/m²K, i.e. by approximately 17%. The application of a low-emissivity film further reduced this value to 2.092 W/m²K.

More advanced renovation strategies achieved substantially better results. Installing insulated glazing in the outer sashes reduced the effective thermal transmittance to 1.760 W/m²K, corresponding to an improvement of approximately 36% compared to the original condition. A similar solution with glazing installed in the inner sashes resulted in a value of 1.792 W/m²K. These results confirm that significant improvements can be achieved without complete replacement of historic windows.

An important finding is the strong influence of installation effects on the performance of new window products. Although catalogue values suggest a clear advantage of plastic windows (typically 0.7–1.2 W/m²K), their performance in historic masonry is significantly less favourable. When installation effects are included, the effective thermal transmittance reaches 1.13 W/m²K for plastic windows and 1.19 W/m²K for new box-type windows. The difference between these solutions is therefore minimal. This indicates that the apparent advantage of plastic windows is largely reduced in real conditions, while their use leads to the loss of historic fabric and may negatively affect the hygrothermal behaviour of the structure.

In addition to thermal performance, condensation behaviour is a critical parameter. Increased airtightness reduces heat losses but also increases the risk of condensation, particularly within the inter-window cavity and at the window-to-wall junction. Variants with insulated glazing in the outer sashes showed the most favourable behaviour. In contrast, glazing installed in the inner sashes may increase moisture load in the window reveal and adjacent structures.

The results also highlight the importance of air permeability. Original windows allow natural ventilation with airflow rates of approximately 1.5–8 m³/h, which contributes to indoor air quality. New windows significantly reduce infiltration and therefore require additional ventilation measures, such as mechanical ventilation.

From a broader perspective, the results demonstrate that window performance is not determined solely by glazing type. The window-to-wall junction, airtightness, and behaviour of the inter-window cavity play a decisive role in the overall thermal and hygrothermal performance.

From the perspective of heritage conservation, the variants can be evaluated as follows: **Variant 1** (window repair) represents the most conservative approach, preserving the maximum extent of original material and being the most acceptable solution.

Variant 2 (Low-E film) retains the original window but alters optical properties, which may be problematic on prominent façades.

Variant 3 (insulated glazing in the outer sashes) significantly improves performance and minimises condensation but alters the external appearance.

Variant 4 (insulated glazing in the inner sashes) is less favourable from a building-physics perspective but allows preservation of original outer sashes in specific cases.

Variant 5 (new box-type window) provides high technical performance but is less suitable from a heritage perspective.

Variant 6 (plastic window) is unacceptable, as it fundamentally alters the appearance and reduces heritage value.

Overall, the results confirm that the choice of intervention is not purely technical. It requires a balanced assessment of building physics, heritage value, operational requirements, and economic factors. In many cases, high-quality renovation is not only cost-competitive but may also provide more appropriate long-term performance while preserving cultural value.

CONCLUSION

Key findings

The results demonstrate that renovation of historic box-type windows represents a technically and economically viable alternative to full replacement. Depending on the selected intervention, renovation can reduce the effective thermal transmittance by up to approximately 35% while preserving a substantial portion of the original structure.

The most effective solution was the installation of insulated glazing units in the outer sashes, achieving values of 1.760 W/m²K, which are close to those of new window products. Simpler interventions, such as repair combined with sealing or the application of low-emissivity films, also resulted in measurable improvements (up to approximately 17–24%).

A key finding is the strong influence of installation effects. When these are considered, the difference between new plastic windows (1.13 W/m²K) and new box-type windows (1.19 W/m²K) becomes minimal. This indicates that the apparent advantage of modern products is significantly reduced under real conditions.

Practical implications

The results confirm that the selection of an appropriate intervention strategy should not be based solely on catalogue thermal parameters. Instead, it must consider the interaction between the window, the surrounding masonry, and air permeability.

From a practical perspective, high-quality renovation is often a suitable and cost-competitive solution. It can provide substantial thermal improvement while preserving historic material and architectural value. In contrast, replacement—particularly with plastic windows—may lead to the loss of cultural value and negatively affect the hygrothermal behaviour of the structure.

At the same time, the reduced airtightness of historic windows can represent an advantage, as it supports natural ventilation and contributes to indoor air quality. This aspect is particularly relevant in buildings without mechanical ventilation systems. The results therefore provide a useful basis for decision-making by designers, conservation authorities, and building owners.

Limitations and future research

The study is limited by the use of numerical simulations under steady-state conditions and by the analysis of a single case study. The results therefore represent a specific but typical example of historic box-type windows.

Future research should focus on in-situ measurements, long-term monitoring of renovated windows, and dynamic simulations that better capture real operating conditions. Further work should also address the performance of exact replicas of historic windows, which are commonly used in practice but were not included in this study.

REFERENCES

[1] Báčová, M. et al. Obnova okenních výplní a výkladců. (“Restoration of Window Infill Elements and Shopfronts”). Praha: NPÚ, 2010.

[2] Šolc, M. (ed.). Repliky oken v památkových zónách. (“Window Replicas in Heritage Conservation Areas”). Brno: NPÚ, Metodické centrum moderní architektury v Brně, 2016.

[3] Stránský, F. Vady při obnově výplní otvorů u budov v památkových zonách. (“Defects in the Restoration of Opening Elements in Buildings Located in Conservation Areas”). TZB-info, 2015.

[4] Zápotocký, M. Postupy při volbě oprav nebo zvolení výměny oken, dveří a dalších prosklených konstrukcí. (“Guidelines for Choosing Between Repair and Replacement of Windows, Doors, and Other Glazed Structures”). Praha 7, 2017.

[5] Hájek, V. Možnosti splnění současných normových požadavků u replik historických okenních konstrukcí pro památkové objekty, (“Compliance with Current Technical Standards in Replicas of Historic Window Structures for Heritage Buildings”). Praha 2005.

[6] Hollan, J. *Co s okny? Upravená stará okna lepší než nová* (“What to Do with Windows? Refurbished Original Windows Are Better Than New Ones“). Eko Dostupné online: https://www.veronica.cz/co-s-okny

[7] Kroftová, K. et al. *Stavební a architektonické detaily činžovních domů postavených na přelomu 19. a 20. století ve středoevropském regionu – hygrotermální analýza* (“*Building and Architectural Details of Tenement Houses Built at the Turn of the 19th and 20th Centuries in the Central European Region—Hygrothermal Analysis*. Buildings 2023. Volume 13, Issue 2. Dhttps://doi.org/10.3390/buildings13020451.

[8] Rexorth, S. Zur energetischen Qualität von Kastenfenstern Besser als ihr Ruf, HTW Hochschule für Technik und Wirtschaft Berlin 2021.

[9] Schuss, M. et al. In-situ performance evaluation of historic box-type windows with vacuum glazing, J. Phys.: Conf. Ser. 2069 012128, 2021.

[10] Rieser, A. Documentation and assessment of conventional and innovative solutions for conservation and thermal enhancement of window systems in historic buildings, International Energy Agency, 2021.

[11] Gayer, Ch. et al. Energetische Sanierung historisch wertvoller Fenster - Broschüre für Planer, Berner Fachhochschule Architektur, Holz und Bau, 2012.

[12] EN ISO 10077-1. Thermal performance of windows, doors, and shutters - Calculation of the thermal transmittance coefficient. 2019.

[13] EN ISO 10211. Thermal bridges in building structures - Heat flows and surface temperatures - Detailed calculations. 2020.

[14] ČSN 73 0540-3. Thermal protection of buildings - Part 3: Design values of parameters. 2005.

[15] Kros a.s. *KROS* [software]. Žilina: KROS a.s., [2026]. Available from: https://www.kros.sk [accessed 2025-10-27].

[16] Lawrence Berkeley National Laboratory. *THERM 7.8* [software]. Berkeley, CA: Lawrence Berkeley National Laboratory, [2023]. Available from: https://windows.lbl.gov/software/therm [accessed 2025-10-27].

[17] Fraunhofer Institute for Building Physics IBP. *WUFI® – Wärme und Feuchte instationär (Heat and Moisture Transient Simulation)* [software]. Stuttgart: Fraunhofer Institute for Building Physics IBP [2026]. Available from: https://wufi.de [accessed 2025-10-27].

CIVIL ENGINEERING JOURNAL

Article no. 9

THE CIVIL ENGINEERING JOURNAL 1-2026

CHARACTERISTICS OF INCINERATION BOTTOM ASH AS A POTENTIAL SUBSTITUTE FOR AGGREGATES AND CEMENT

Yongzhen Cheng, Weiye Mu, Baoliang Li, and Mengdi Zhou

Huaiyin Institute of Technology, Faculty of Architecture and Civil Engineering, Huai'an, No.89 Beijing North Road, China; chengyongzhen198@163.com

Received:	*28.04.2025*
Received in revised form:	*15.09.2025*
Accepted:	*28.01.2026*

ABSTRACT

The disposal of bottom ash from municipal solid waste incineration (MSWI) in landfills may lead to ecological contamination and inefficient land resources utilization. The investigation assessed whether MSWI bottom ash could serve as a substitute for sand and supplementary binder components in concrete production. Multiple analytical techniques were employed to characterize the MSWI bottom ash and its recycled powder. X-ray fluorescence (XRF) and laser particle size analysis were used to determine chemical composition and particle size distribution, respectively. Microscopic morphology and pore structure were examined with scanning electron microscopy (SEM) and nitrogen adsorption analysis. Phase composition was identified by X-ray diffraction (XRD), complemented with simultaneous thermal analysis (TG/DTG) and Fourier transform infrared (FTIR) spectroscopy. Results show that incineration bottom ash is coarse-grained and even exceeds the gradation range of Zone Ⅰ sand stipulated by the Chinese standard. Soaking and sieving treatment yields coarse bottom ash particles with clean surfaces, while fine bottom ash particles contain organic contaminants that are difficult to treat. The soaked bottom ash showed low Cl and SO_3 content, containing mainly quartz, calcite, gypsum, and hematite. The particles of bottom ash-derived powder are gravel-shaped, with pore sizes ranging from 1 nm to 70 nm and a high specific surface area. The pores are mainly mesopores, accounting for 73.83% of the total pore volume. BET measurements revealed a specific surface area six times greater than that of cement. Except for Cr, all heavy metal leaching levels comply with Chinese regulatory limits. MSWI bottom ash shows potential for partial replacement of natural sand or cement in construction applications.

KEYWORDS

Incineration bottom ash, Particle characteristics, Chemical components, Mineral composition, Pore structure

INTRODUCTION

The rapid growth of consumerism and industrial activities has significantly increased municipal solid waste generation. During the 2011-2023 period, medium-sized and large cities in China experienced consistent growth in municipal solid waste collection volumes, with the annual quantity peaking at 242.06 million tons in 2019 [1]. Current municipal solid waste management primarily utilizes three approaches: thermal treatment, land disposal, and biological decomposition. However, landfills have issues such as occupation of land resources and environmental pollution [2-4]. Incineration can achieve waste reduction and harmlessness, and the waste heat can be used for power generation [5, 6]. Therefore, large waste incineration plants have been built in many cities in

China. Moreover, the volume of waste incineration has increased rapidly annually, while landfill volume has decreased significantly.

Through incineration, the mass of domestic waste drops by roughly 70%, and simultaneously, a 90% reduction in volume is achieved. After the incineration process, two main types of residues are produced. Bottom ash, coming from the incinerator, and fly ash, obtained from the flue gas cleaning mechanism, together form these two main residues of incineration. Specifically, bottom ash accounts for about 80% of the total residue weight [7]. Bottom ash comprises an assortment of solid particles with disparate sizes, and these sizes range from fine particles to coarse fractions that exceed the gradation of Zone I sand specified in the national standard for construction sand of China (GB/T 14684), which corresponds to coarse-grained sand with a relatively large particle size distribution. Among its components are glassy substances, ceramic elements, mineral components, along with unburned materials, giving rise to a heterogeneous composition. Since bottom ash contains a certain amount of metals, electromagnetic and eddy-current separation is utilized to recover these valuable resources and further process the bottom ash. As a result, this separation technique effectively extracts specific metals from bottom ash.

Recent investigations have explored MSWI bottom ash as partial replacements for conventional aggregates in various construction applications, including cementitious composites, bituminous mixtures, and pavement foundations [8-11]. However, aggregates must comply with industry standards governing their structural, material, and functional characteristics [12, 13]. MSWI bottom ash-derived powder can also be used in concrete as a substitute for cement [14-16], overcoming the limitations in particle shape and gradation associated with its direct application as fine aggregate. While these studies confirm MSWI bottom ash application potential, most focus on feasibility rather than systematic characterization of key properties. This gap makes it difficult to guide targeted utilization of MSWI bottom ash.

The development of sustainable construction materials has driven growing interest in the utilization of industrial by-products. Notable examples include micro silica and fly ash, which are highly effective pozzolanic materials commonly used as partial substitutes for cement. Their role in enhancing the mechanical properties and durability of cementitious composites, specifically through reactions with calcium hydroxide to form additional C-S-H gel, is well established [17, 18]. However, the supply of these high-quality materials can be limited in certain regions. For instance, areas in China far from coal-fired power plants, which are a major source of fly ash, often face shortages of such materials. Furthermore, the diversity of waste streams calls for the exploration of a broader range of valorization options.

MSWI bottom ash represents a distinctly different type of material from the aforementioned micro silica and fly ash. Its potential value lies not in high pozzolanic reactivity, but rather in its dual functionality as a partial replacement for both fine aggregate and cementitious filler. In contrast to fly ash, which is largely pozzolanic, bottom ash consists of a heterogeneous combination of crystalline and amorphous phases. Therefore, instead of focusing on direct reactivity comparisons, this study provides a comprehensive characterization to evaluate its suitability for specific applications where high chemical reactivity is not the primary requirement. This approach helps diversify the range of waste-derived construction materials and reduces reliance on any single type of supplementary material.

This study systematically characterized MSWI bottom ash through multiple analytical techniques including XRF, XRD, SEM, TG/DTG, FTIR, and particle size analysis. The investigation focused on the following key aspects: particle composition, gradation characteristics, chemical components, mineral composition, and pore structure. The aim was to guide the efficient utilization of MSWI bottom ash as fine aggregate and cement replacement additive.

MATERIALS AND METHODS

Materials and treatment

The study utilized bottom ash from a municipal solid waste incineration plant in Suqian, China, with an annual processing capacity of 300,000 tons. Unsorted waste was directly fed into the incinerator, where combustion temperatures were maintained at 850-950℃ to ensure complete dioxin decomposition. The resulting bottom ash was water-quenched upon discharge from the grate, then processed through sequential metal recovery: electromagnetic separation for ferrous metals and eddy current separation for non-ferrous components.

The collected MSWI bottom ash contained trace organic components, such as plant roots, bark, and plastic fragments. To minimize potential interference from these materials with the reactivity of MSWI bottom ash, a water immersion treatment was applied. The bottom ash was fully submerged in water at a water-to-ash ratio of 2:1 and stirred thoroughly to ensure complete flotation of light organic components. After 24 hours of soaking, the water along with the floating organics was drained. The remaining solids were air-dried completely, then ground in a planetary ball mill at 350 r/min for 45 minutes. The milled product was sieved through a 200-mesh sieve with an aperture of 75 μm to remove oversized particles. This process produced a dark-gray powder with a maximum particle size of 75 μm.

P·II 52.5cement was used in this research, and its physical and mechanical properties met the requirements of Chinese standards [19].

Material properties analysis

The chemical components of the samples were tested by XRF (manufactured by Thermo Electron Corporation, USA; instrument model: ARL; detector resolution: MnKa resolution < 155 ev, CPS > 3000).

The D8-Discover X-ray diffraction was employed to analyze the mineral composition of samples. Test conditions: Cu tube, 40 kV, 36 mA, 10-90°, 4°/min.

The morphology of the samples was examined by SEM (manufactured by FEI Corporation, instrument model: Nova Nano SEM NPE218).

Thermogravimetric analysis of the samples was conducted by a simultaneous thermal analyzer (manufactured by NETZSCH; instrument model: DTG-60AH). The heating process was set within a range starting from the ambient temperature up to 1500 °C, at a constant increment rate of 10 °C per minute. Throughout the analysis, the samples were exposed to an inert atmosphere of nitrogen gas.

The infrared analysis of the samples was performed by FTIR (manufactured by Thermo Scientific, USA; instrument model: Nicolet iS10).

A laser particle size analyzer (manufactured by Microtrac, Inc.; instrument model: Microtrac S3500; dispersion medium: anhydrous ethanol) was utilized to determine the particle size distribution of the samples.

The adsorption/desorption curves of the samples were obtained by an Autosorb-IQ2 physical chemical adsorption analyzer.

Environmental impact assessment

The Chinese standard was applied to carry out the leaching toxicity test of MSWI bottom ash [18]. 20 grams of MSWI bottom ash-derived powder was weighed, oven-dried at 60 ℃, and then underwent a series of steps including sieving with a 5-mesh polypropylene sieve, grinding, and acid extraction treatment to obtain the extraction solution. Inductively coupled plasma mass spectrometry (ICP–MS) was employed to analyze the concentrations of heavy metals in the extraction solution.

RESULTS AND DISCUSSION

Physical properties

Particle and gradation characteristics of MSWI bottom ash

MSWI bottom ash is dark-gray in color, and its particle size and composition are similar to those of natural sand. Figure1 shows the particle size distribution curve of the MSWI bottom ash. The sampled bottom ash has a nominal maximum particle size of 4.75 mm. In compliance with the national standard for construction sand of China [13], when preparing cement concrete, sand from Zone II is recommended as the preferred choice. However, the bottom ash particles are coarse and even beyond the gradation range of Zone I sand specified in this standard. Since the coarse nature of bottom ash particles may undermine the workability and strength of concrete, when preparing concrete with bottom ash serving as fine aggregate, a sufficient amount of cement should be used to compensate for the low cohesive force of coarse particles, along with an increase in the sand ratio. Although increasing the cement content affects economic and environmental sustainability, the overall lifecycle assessment includes diverting MSWI bottom ash from landfills to reduce landfill pollution and conserving natural sand resources to alleviate resource scarcity. This assessment may still render this approach beneficial on a broader scale.

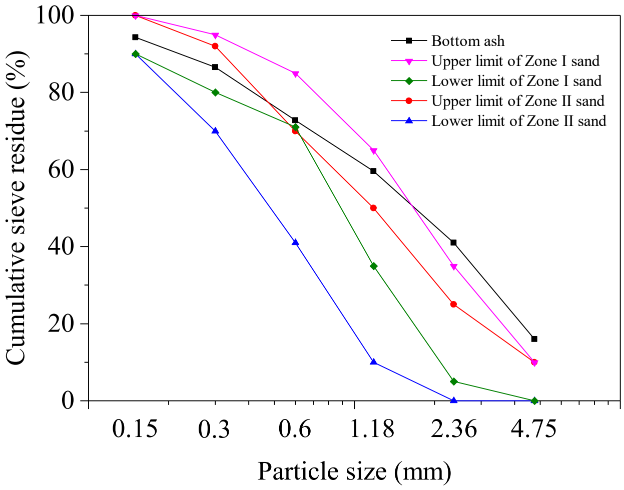

Fig. 1 - Gradation curve of MSWI bottom ash

The morphological features of MSWI bottom ash particles are illustrated in Figure 2. Morphological analysis reveals four predominant constituent components: quartz, glass fragments, ceramic shards, and slag. The composition further encompasses metallic oxides, especially iron-bearing particles.

Bulk analysis demonstrates that approximately 60% of bottom ash particles exhibit surface coatings comprising both fine-grained fractions and fused constituents. The fine particulate coatings develop on bottom ash surfaces through quenching-induced reactions during rapid water cooling [21]. During storage or transportation, bottom ash can be contaminated by the surrounding environment, resulting in the presence of some plant roots, bark and plastic products in it. Insufficient combustion of municipal solid waste can cause these pollutants to persist in bottom ash as well. In this research, water immersion effectively separated the majority of organic residues (including plant roots, skin debris, and plastic fragments) from the bottom ash. Consequently, the post-treated bottom ash exhibits clean particle surfaces without detectable fine particulate coatings. Additionally, MSWI bottom ash particles of varying sizes exhibit no substantial compositional differences. However, particle size influences phase distribution, with amorphous components (e.g., glass/ceramic fragments) showing enrichment in coarser fractions (>2.36 mm). Conversely, organic residues (plant matter, plastics) predominantly occur in finer fractions sized 0.6–1.18 mm, and there is a notable increase in their content in even finer particles below 0.6 mm.

It is evident that glass and ceramic particles are enriched in the coarser fractions of bottom ash. Thus, the powder regenerated from coarser bottom ash contains more amorphous reactive phases with higher reactivity, which is more suitable for replacing cement as a supplementary cementitious material. The finer particles of the bottom ash contain more residual organic matter, which has a negative impact on cement hydration.

Morphological characteristics of MSWI bottom ash-derived powder

Figure 3 shows the SEM image of MSWI bottom ash-derived powder. The powder primarily consists of irregular, gravel-like particles, a key characteristic reported by Tang et al. [22]. Unlike fly ash, which contains spherical particles and exhibits water-reducing effects, the bottom ash powder lacks these properties. Additionally, small particles adhere to larger ones, forming agglomerates due to electrostatic interactions [23]. These morphological characteristics of MSWI bottom ash and its derived powder, combined with its gradation features, further distinguish its application scenarios from those of traditional supplementary cementitious materials.

Fig. 2 - Particles of MSWI bottom ash. (a) ⩾2.36 mm; (b) 0.6–1.18 mm

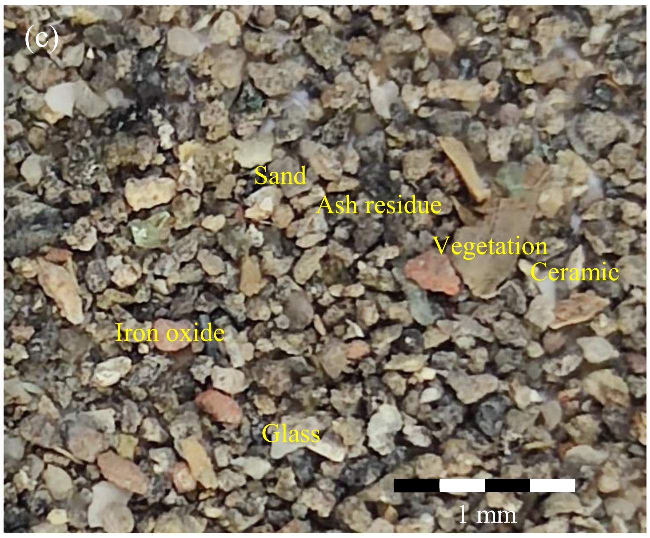

Fig. 2 - Particles of MSWI bottom ash.; (c) 0–0.6 mm

The morphological and gradation characteristics of MSWI bottom ash further clarify its application differences from traditional supplementary cementitious materials. For example, fly ash typically has spherical particles that improve concrete workability but require adjustment of sand ratio to compensate for poor gradation [24]; in contrast, the coarse-grained nature of bottom ash (exceeding Zone I sand) means it can partially replace natural sand in low-demand scenarios (e.g., pavement bases) without the need for additional "spherical particle modification"[10]. Meanwhile, compared with micro silica, which requires strict control of agglomeration due to fine particles [25], the gravel-like morphology of bottom ash-derived powder reduces agglomeration risk during mixing, which is more suitable for large-scale construction with simple mixing processes.

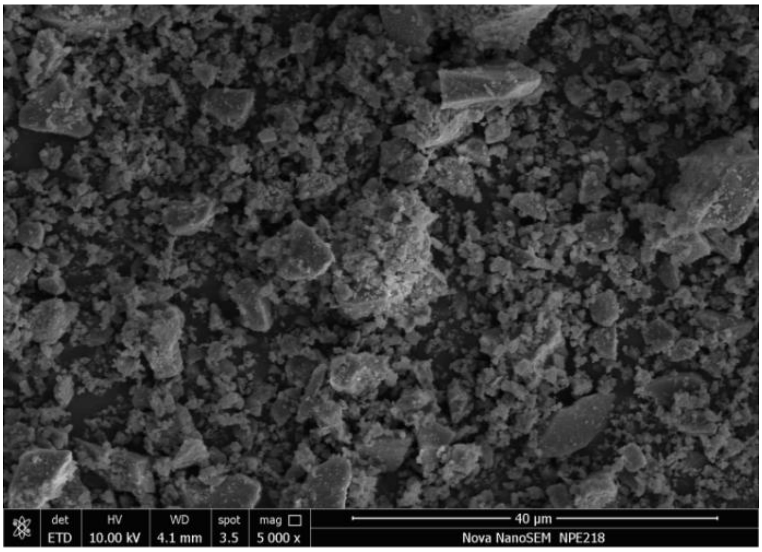

Fig. 3 - SEM image of MSWI bottom ash- derived powder. Scale bar: 40 μm.

Particle distribution of MSWI bottom ash-derived powder

Figure 4 illustrates the particle size distribution of the MSWI bottom ash-derived powder, with its granular characteristics summarized in Table 1. The powder particles are finer than cement particles, with all particles below 100 μm in size. This fineness results from high-speed milling with

DOI 10.14311/CEJ.2026.01.0009

sufficient duration, followed by sieving through a 75 μm mesh to remove large particles and impurities, yielding fine powder.

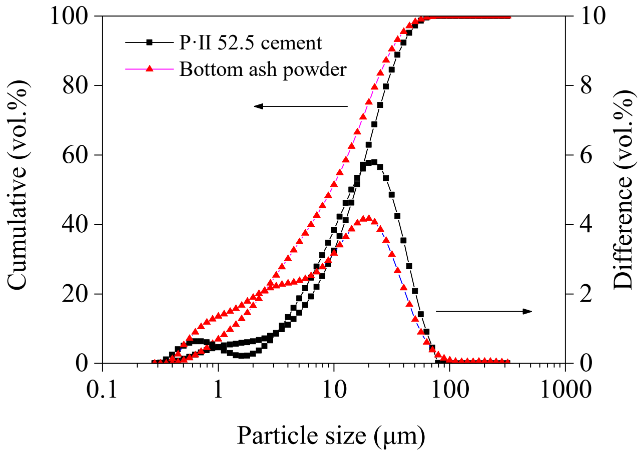

Fig. 4 - Particle size distribution of MSWI bottom ash-derived powder

Chemical components

Major oxides in both MSWI bottom ash and Portland cement (P·II 52.5) are quantified in Tab. 2. MSWI bottom ash exhibits a cement-like composition, primarily consisting of SiO_2, CaO, Al_2O_3, and Fe_2O_3. These four oxides collectively constitute over 85% of the bottom ash by mass. The bottom ash contains higher SiO_2 but lower CaO levels compared to cement. The contents of Al_2O_3 and Fe_2O_3 are 2 to 3 times greater than those in the cement. Na_2O, K_2O, and MgO are present in significant quantities in the bottom ash, representing typical alkali and alkaline earth oxides.

Tab. 1 - Particle size parameters of MSWI bottom ash-derived powder and cement

Particle size (μm)	P· II 52.5 cement	Bottom ash-derived powder
d (0.1)	3.634	1.348
d (0.5)	15.367	10.267
d (0.9)	36.877	36.492
D (3, 2)	5.722	3.720
D (4, 3)	18.171	15.498

Tab. 2 - Major oxides in MSWI bottom ash and cement (%)

Chemical components	MgO	Na_2O	Al_2O_3	SiO_2	P_2O_5	K_2O	CaO
P· II 52.5 cement	1.56	0.00	3.80	17.11	0.63	0.16	64.99
Bottom ash powder	2.49	3.87	9.22	49.45	2.31	2.29	19.37
Chemical components	TiO_2	MnO	Fe_2O_3	CuO	ZnO	Cl	SO_3
P· II 52.5 cement	0.27	0.09	3.59	0.02	0.15	2.00	3.96
Chemical components	0.87	0.15	7.40	0.13	0.29	0.46	0.78

Cl (0.46 wt.%) and SO_3 (0.78 wt.%) concentrations in bottom ash are significantly below literature values. Garcia-Lodeiro et al. reported bottom ash typically contains 1.29% Cl and 2.54% SO_3 [26], while Vizcarra et al. found 2.3-3.8 wt.% Cl and 1.3-3.6 wt.% SO_3 [27]. Fine bottom ash particles, like the fine particulate coatings, contain more chlorides and sulfates because of their large specific surface area. These particles form during water quenching and accumulate on the surface of coarse particles [28]. Saffarzadeh et al. showed that during water cooling and weathering, newly formed surface phases increase sites for chloride and sulfate absorption [29]. Immersing bottom ash in water causes dust on particle surfaces to separate and be carried away, reducing Cl and SO_3 levels in treated bottom ash.

The chemical composition shows that the sum of SiO_2, Al_2O_3, and Fe_2O_3 is about 62%, which is notably lower than the typical requirement of 70% for Class F fly ash as per ASTM C618 [30]. This quantitatively confirms the lower pozzolanic potential of MSWI bottom ash-derived powder compared to established supplementary cementitious materials. Consequently, its primary value in cement replacement applications may stem from its microfiller effect and its ability to provide nucleation sites for hydration products, rather than from significant pozzolanic contribution.

Mineral composition

XRD analysis (Figure 5) identifies quartz, calcite, gypsum, magnetite, and hematite as the dominant crystalline phases in MSWI bottom ash. Additionally, gehlenite, diopside and sodium feldspar are also detected in the bottom ash. Multiple active components, such as SiO_2, Al_2O_3, and CaO, exist in relatively high concentrations in MSWI bottom ash. However, MSWI bottom ash-derived powder lacks volcanic ash activity compared with fly ash [23]. This occurs since, rather than vitreous matter, most active components are present in stable crystal structures.

Stable crystalline phases (e.g., quartz, calcite) dominate over amorphous glassy phases, and these amorphous glassy phases are the primary source of reactivity in fly ash [31]. This further explains the limited pozzolanic activity observed in MSWI bottom ash-derived powder. This fundamental difference in phase composition between MSWI bottom ash and traditional supplementary cementitious materials (e.g., fly ash) underscores the need to identify applications that leverage its physical rather than chemical properties.

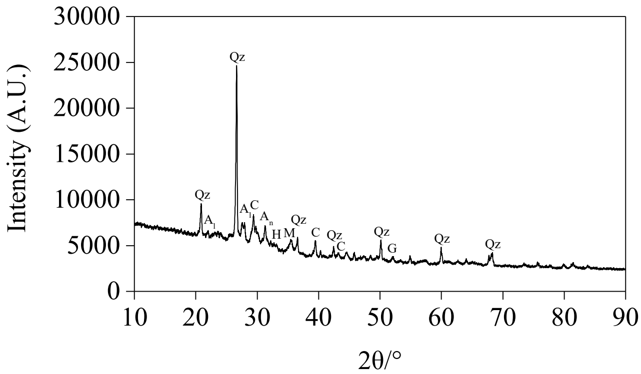

Fig. 5 - XRD pattern of MSWI bottom ash: Q: quartz (SiO_2); C: calcite ($CaCO_3$); G: gehlenite ($Ca_2Al_2SiO_7$); A_n: gypsum ($CaSO_4$); M: magnetite (Fe_3O_4); H: hematite (Fe_2O_3); D: diopside ($CaMgSi_2O_6$); A_l: sodium feldspar ($NaAlSi_3O_8$)

Figure 6 presents the FTIR spectrum of MSWI bottom ash, with key absorption bands assigned based on literature [32-36]: At 3420 cm^{-1}, the vibrational band corresponds to the stretching vibration of H-OH groups in free water. This band links to the adsorbed water and crystalline water of gypsum present in bottom ash; The 2520 cm^{-1} band corresponds to the vibrational mode of carbonate; The peak at 2360 cm^{-1} shows the vibrational mode of HPO_3^{-2}, indicating a small amount of phosphate in the bottom ash; The 1650 cm^{-1} absorption is characteristic of C=O asymmetric stretching, indicating surface-bound aromatic compounds, carboxylic acids, amino groups, or lipids; The peaks at 1450 cm^{-1}, 876 cm^{-1} and 730 cm^{-1} correspond to the asymmetric stretching vibration, out-of-plane bending vibration, and in-plane bending vibration of CO_3^{-2}; The antisymmetric stretching band at 1040 cm^{-1} and the symmetric stretching band at 780 cm^{-1} are due to the presence of quartz; The peak at 600 cm^{-1} corresponds to the vibrational mode of sulfate.

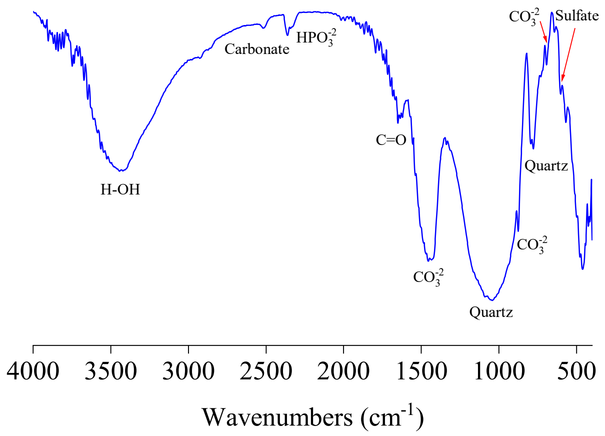

Fig. 6 - FTIR spectrum of MSWI bottom ash

Figure 7 displays TG/DTG curves for MSWI bottom ash. Based on these curves, bottom ash pyrolysis progresses through four sequential stages. Stage I: The bottom ash sample is heated to 114°C and experiences a mass loss of 0.85%. Evaporation of adsorbed water causes this mass reduction. Stage II: At 504°C and 570°C, a 3.34% weight loss occurs as hydrated silicate, chlorate, and other minerals undergo dehydration. Stage III: At 676°C, a weight loss of 2.32% corresponds to the decomposition of $CaCO_3$. Stage IV: At 1022°C, a weight loss of 0.7% corresponds to the decomposition of gypsum.

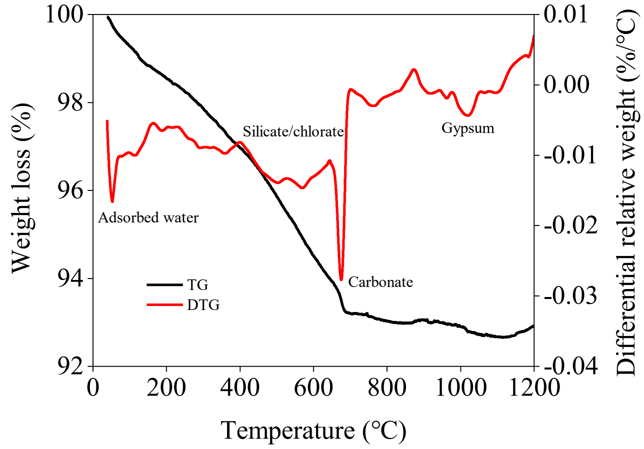

Fig. 7 - TG/DTG curves of MSWI bottom ash

The thermal decomposition of $CaCO_3$ (676 ℃, 2.32% mass loss) indicates two key implications: first, bottom ash may release CO_2 during cement hydration (a factor to consider in high-temperature scenarios like mass concrete) and a potential mass loss upon heating (critical for high-temperature applications); second, the presence of SiO_2 provides a basis for secondary hydration [37]. Beyond the contribution of SiO_2, the carbonate from $CaCO_3$ decomposition also plays a role in regulating the hydration process. More importantly, the presence of carbonate can affect the hydration process by interacting with calcium aluminate phases, potentially leading to the formation of carboaluminate phases, and these phases can densify the microstructure.

Pore structure of MSWI bottom ash-derived powder

Adsorption/desorption curves

The adsorption/desorption isotherm curves of MSWI bottom ash-derived powder are shown in Figure 8. According to the classification of gas physisorption isotherms [38], MSWI bottom ash-derived powder exhibits a Type II-like adsorption profile, though with less pronounced inflection at low relative pressures. These isotherms arise from unimpeded monolayer-to-multilayer adsorption under elevated pressure conditions, with distinct features as described below: For the condition where P/P0≤0.05, nitrogen adsorption enters its first stage. This initial stage is defined as the process of monolayer adsorption. When $0.05<P/P_0\leq0.9$, the adsorption isotherm rises slowly and multilayer adsorption begins to occur, corresponding to the second stage of nitrogen adsorption. Once P/P0 exceeds 0.9, capillary coalescence of nitrogen occurs. This leads to a rapid upward trend in the adsorption isotherm.

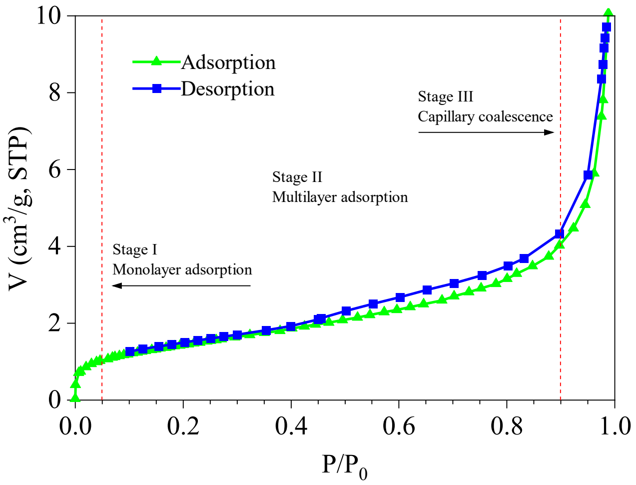

Fig. 8 - Adsorption/desorption isotherm curves of MSWI bottom ash-derived powder

Hysteretic behavior arises from non-overlapping adsorption-desorption isotherms. This hysteretic phenomenon varies significantly across systems, primarily governed by pore density, structural morphology, and size dispersity. Per IUPAC guidelines [38], MSWI bottom ash-derived powder exhibits combined H3-H4 type hysteresis, indicative of flexible lamellar particle aggregates containing interconnected macropores with partial capillary condensation.

Pore size distribution

The cumulative volume and differential size distribution of pores in MSWI bottom ash-derived powder are illustrated in Figure 9. Pores in porous materials can be categorized into three types: macroporous (＞50 nm), mesoporous (2–50 nm) and microporous (＜2 nm). As shown by the distribution curves, pores in MSWI bottom ash-derived powder vary significantly in size (1-70 nm). The average pore size, determined from cumulative pore volume analysis, measures 11.58 nm. Macropores represent 17.63% of the pore volume, while mesopores dominate at 73.83%, followed by micropores at 8.54%.

DOI 10.14311/CEJ.2026.01.0009

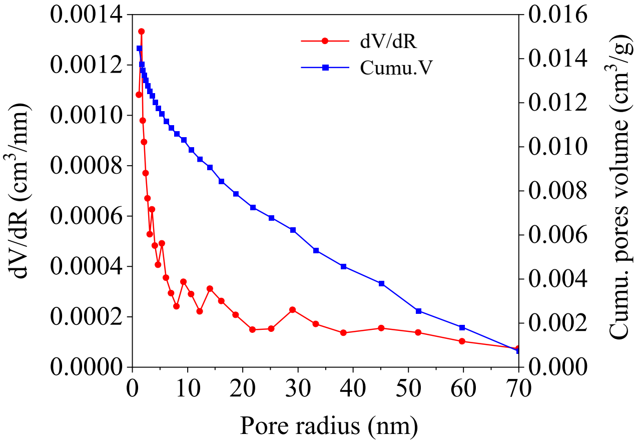

Fig. 9 - Cumulative pore volume and differential pore size distribution of MSWI bottom ash-derived powder

The BET surface area of MSWI bottom ash-derived powder measures 5.38 m²/g, showing good agreement with previous findings. As reported by Marieta et al. [36], one MSWI bottom ash-derived powder sample exhibited a specific surface area of 7.43 m²/g, while the other registered 5.30 m²/g. The BET method provides more reliable specific surface area measurements by eliminating the need for particle shape assumptions or semi-empirical corrections Marieta [39]. There is a significant correlation between the reactivity of powder and its particle size [40]. Powder fineness indicated by specific surface area directly correlates with the reactivity potential of bottom ash. Furthermore, adsorption capacity shows direct dependence on specific surface area in micro powders. Compared to ordinary Portland cement, the MSWI bottom ash-derived powder under study exhibits a significantly larger specific surface area. Li et al. [35] reported 0.88 m²/g for P·II 52.5 cement, merely one-fifth the specific surface area measured in MSWI bottom ash-derived powder.

Although this study primarily focuses on the fundamental characterization of municipal solid waste incineration (MSWI) bottom ash, its intrinsic properties, including particle size distribution, morphology, chemical and mineral composition, and pore structure, directly influence its potential mechanical performance in cementitious systems. Tang et al. [22] examined how the physicochemical properties of treated MSWI bottom ash and its cement replacement ratio affect the strength of cement-sand mortars. The results indicated that reducing the organic matter content mitigates its inhibitory effect on cement hydration, while the thermal decomposition of calcite ($CaCO_3$) generates new reactive phases, thereby enhancing the reactivity of the recycled ash. Finer ash powder was found to contribute to a denser mortar microstructure, leading to improved strength. The combined physical filling effect and favorable chemical composition, predominantly SiO_2–CaO–Al_2O_3, enable recycled MSWI bottom ash powder to serve effectively as a 30% cement replacement in low-strength mortars [41]. Physically, the mesoporous structure of the milled ash facilitates pore filling; chemically, its composition supports slow pozzolanic reactions and secondary hydration.

It is also important to note that, as with many single supplementary cementitious materials, the replacement ratio of MSWI bottom ash must be carefully optimized. Li et al. [23] reported that replacing 30% of cement with MSWI bottom ash resulted in an approximately 26% decrease in the 28-day compressive strength of mortar, which aligns with the replacement ratio of 30% or less as recommended in the environmental risk assessment section of this study. These findings suggest that MSWI bottom ash is most suitable for partial cement replacement in medium and low strength applications, such as non-structural concrete and pavement subgrades. It provides a sustainable alternative to conventional high-performance materials like microsilica or blended supplementary cementitious materials.

Environmental impact assessment

GB 5085.3 [20] mandates that leachate from hazardous waste must keep hazardous component concentrations below prescribed thresholds to ensure environmental and human health protection. The leaching behavior of MSWI bottom ash was characterized by ICP-MS, with quantitative results detailed in Tab. 3. The leaching amounts of all metals except Cr are lower than the limits set by Chinese legislation.

It is critical to emphasize that this standard leaching test was performed on the raw bottom ash powder in isolation. In practical cementitious applications, two key factors mitigate the environmental risk: (1) the incorporation rate of alternative materials like bottom ash is typically limited to below 30% [23], and (2) the encapsulation effect of the cement matrix is widely documented to significantly immobilize heavy metals, drastically reducing their leachability [42]. This encapsulation phenomenon represents the primary mechanism for risk reduction in real-world scenarios. Therefore, while the elevated Cr leaching from the raw powder is noted, its environmental impact in a solidified cementitious system is anticipated to be substantially lower. A comprehensive investigation into the long-term leaching behavior from engineered mortar/concrete composites remains a valuable focus for future studies.

Tab. 3 - The leaching properties of MSWI bottom ash-derived powder

Metals	As	Cr	Cd	Hg	Ni	Pb	Zn
Bottom ash powder (mg/L)	0.3943	8.7173	0.0005	0.0003	3.7926	1.9682	9.1731
Limits (mg/L)	5	5	1	0.1	5	5	100

CONCLUSION

(1) The gradation of MSWI bottom ash resembles that of Zone Ⅰ sand. In addition, bottom ash particles of varying sizes exhibit no significant disparity in their constituents. Coarse bottom ash fractions are enriched with ceramic and glass particulates, whereas finer fractions accumulate more residual plant matter and synthetic contaminants from incomplete combustion or external sources.

(2) MSWI bottom ash features a chemical composition similar to that of cement, with SiO_2-CaO-Al_2O_3-Fe_2O_3 being the main components. Compared to cement, MSWI bottom ash contains a relatively higher proportion of SiO_2 and a lower proportion of CaO, while mineralogical characterization reveals quartz, calcite, gypsum and hematite as major constituents.

(3) MSWI bottom ash-derived powder exhibits distinctive physical characteristics, featuring fine granulometry, high porosity, and a large surface area. Particle morphology analysis reveals gravel-like irregularity, with fine particulate matter adhering to coarser particle surfaces.

(4) The hybrid H3/H4 hysteresis loop observed in the Type II isotherm reflects the complex pore structure of MSWI bottom ash-derived powder, where mesopores constitute the primary void space within the broadly distributed pore network.

REFERENCES

[1] National Bureau of Statistics of China, 2011-2023. China Statistical Yearbook. China Statistics Press, Beijing.

[2] Shu S., Zhu W., Xu H.Q., Wang S.W., Fan X.H., Wu S.L., Shi J.Y., Song J., 2019. Effect of the leachate head on the key pollutant indicator in a municipal solid waste landfill barrier system. Journal of Environmental Management, vol. 239, p. 262-270.

[3] Peng W., Pivato A., Wang T.F., 2019. Stabilization of solid digestate and nitrogen removal from mature leachate in landfill simulation bioreactors packed with aged refuse. Journal of Environmental Management, vol. 232, p. 957-963.

[4] Sekhohola-Dlamini L., Tekere M., 2020. Microbiology of municipal solid waste landfills: a review of

microbial dynamics and ecological influences in waste bioprocessing. Biodegradation, vol. 31, no. 1-2, p. 1-21.

[5] Li M., Xiang J., Hu S., Sun L.S., Su S., Li P.S., Sun X.X., 2004. Characterization of solid residues from municipal solid waste incinerator. Fuel, vol. 83, p. 1397-1405.

[6] Sisani F., Maalouf A., Di Maria F., 2022. Environmental and energy performances of the Italian municipal solid waste incineration system in a life cycle perspective. Waste Management & Research, vol. 40, no. 2, p. 218-226.

[7] Chimenos J.M., Segarra M., Fernandez M.A., Espiell F., 1999. Characterization of the bottom ash in municipal solid waste incinerator. Journal of Hazardous Materials, vol. 64, no. 3, p. 211-222.

[8] Grazulyte J., Vaitkus A., Šernas O., Žalimienė L., 2022. The impact of MSWI bottom ash as aggregate on concrete mechanical performance. International Journal of Pavement Engineering, vol. 23, no. 9, p. 2903-2911.

[9] Singh A., Zhou Y.Y., Gupta V., Sharma R., 2022. Sustainable use of different size fractions of municipal solid waste incinerator bottom ash and recycled fine aggregates in cement mortar. Case Studies in Construction Materials, vol. 17, e01434.

[10] Suddeepong A., Buritatum A., Dasdawan S., Horpibulsuk S., Yaowarat T., Hoy M., Arulrajah A., 2023. Mechanical performance of porous asphalt concrete incorporating bottom ash as fine aggregate. Journal of Materials in Civil Engineering, vol. 35, no. 6, 04023129.

[11] Lu J.G., Yang X.L., Lai Y., Wan X.S., Gao J.J., Wang Y.D., Tan L.L., Deng F., 2024. Utilization of municipal solid waste incinerator bottom ash (MSWIBA) in concrete as partial replacement of fine aggregate. Construction and Building Materials, vol. 414, 134918.

[12] JTG F40. Technical Specifications for Construction of Highway Asphalt Pavement. 2004.

[13] JGJ 52. Standard for Technical Requirements and Test Method of Sand and Crushed Stone. 2006.

[14] Maldonado-Alameda A., Giro-Paloma J., Svobodova-Sedlackova A., Formosa J., Chimenos J.M., 2020. Municipal solid waste incineration bottom ash as alkali-activated cement precursor depending on particle size. Journal of Cleaner Production, vol. 242, 118443.

[15] Cheng L., Jin H.S., Wu Y.K., Ren Y.R., Liu J., Xing F., 2024. Influence of municipal solid waste incineration bottom ash particle size on cement hydration and performance. Construction and Building Materials, vol. 432, 136516.

[16] Song H., Fan S.J., Che J.H., Yao J.W., Lee Y.G., 2024. Physical & mechanical properties of pervious concrete incorporating municipal solid waste incineration bottom ash. Journal of Building Engineering, vol. 96, 110599.

[17] Szcześniak, A., Siwiński, J., Stolarski, A., Piekarczuk, A., Nasiłowska, B., 2024. The influence of the addition of microsilica and fly ash on the properties of ultra-high-performance concretes. Materials, vol. 18, no. 1, 28.

[18] Khankhaje, E., Kim, T., Jang, H., Kim, C.S., Kim, J., Rafieizonooz, M., 2023. Properties of pervious concrete incorporating fly ash as partial replacement of cement: a review. Developments in the Built Environment, vol. 14, 100130.

[19] GB 175. Common Portland Cement. 2007.

[20] GB 5085.3. Identification Standards for Hazardous Wastes-Identification for Extraction Toxicity. 2007.

[21] Yang S., Saffarzadeh A., Shimaoka T., Kawano T., 2014. Existence of Cl in municipal solid waste incineration bottom ash and dechlorination effect of thermal treatment. Journal of Hazardous Materials, vol. 267, p. 214-220.

[22] Tang P., Florea M.V.A., Spiesz P., Brouwers H.J.H., 2016. Application of thermally activated municipal solid waste incineration (MSWI) bottom ash fines as binder substitute. Cement and Concrete Composites, vol. 70, p. 194-205.

[23] Li X.G., Lv Y., Ma B.G., Chen Q.B., Yin X.B., Jian S.W., 2012. Utilization of municipal solid waste incineration bottom ash in blended cement. Journal of Cleaner Production, vol. 32, p. 96-100.

[24] Mishra, S.K., Upadhyay, B., Das, B.B., 2025. 3D printing aspects of fly ash and GGBS admixed binary and ternary blended cementitious mortar. European Journal of Environmental and Civil Engineering. https://doi.org/10.1080/19648189.2025.2521381

[25] Akmalaiuly, K., Berdikul, N., Pundienė, I., Pranckevičienė, J., 2023. The effect of mechanical activation of fly ash on cement-based materials hydration and hardened state properties. Materials, vol. 16, no. 8, 2959.

[26] Garcia-Lodeiro I., Carcelen-Taboada V., Fernández-Jiménez A., Palomo A., 2016. Manufacture of hybrid cements with fly ash and bottom ash from a municipal solid waste incinerator. Construction and Building Materials, vol. 105, p. 218-226.

[27] Vizcarra G.O.C., Casagrande M.D., da Motta L.M.G., 2014. Applicability of Municipal Solid Waste Incineration Ash on Base Layers of Pavements. Journal of Materials in Civil Engineering, vol. 26, no. 6,

06014005.
[28] Chen C.H., Chiou I.J., 2007. Distribution of chloride ion in MSWI bottom ash and de-chlorination performance. Journal of Hazardous Materials, vol. 148, p. 346-352.
[29] Saffarzadeh A., Shimaoka T., Wei Y.M., Gardner K.H., Musselman C.N., 2011. Impacts of natural weathering on the transformation/neoformation processes in landfilled MSWI bottom ash: a geoenvironmental perspective. Waste Management, vol. 31, no. 12, p. 2440-2454.
[30] ASTM C618-23, 2023. Standard specification for coal fly ash and raw or calcined natural pozzolan for use in concrete. ASTM International.
[31] Wei, G.Q., Dong, B.Q., Fang, G.H., Wang, Y.S., 2023. Understanding reactive amorphous phases of fly ash through the acidolysis. Cement and Concrete Composites, vol. 140, 105102.
[32] Martinez-Ramirez S., 1999. Influence of SO2 deposition on cement mortar hydration. Cement and Concrete Research, vol. 29, p. 107-111.
[33] Ismail I., Bernal S.A., Provis J.L., Nicolas R.S., Hamdan S., van Deventer J.S.J., 2014. Modification of phase evolution in alkali-activated blast furnace slag by the incorporation of fly ash. Cement and Concrete Composites, vol. 45, p. 125-135.
[34] Xu Y.F., Fu Y., Xia W., Zhang D., An D., Qian G.R., 2018. Municipal solid waste incineration (MSWI) fly ash washing pretreatment by biochemical effluent of landfill leachate: a potential substitute for water. Environmental Technology, vol. 39, no. 15, p. 1949-1954.
[35] Li B.L., Wang Y.H., Peng D., Yang L., Zhang Y.M., 2019. Composition and Suitable Application of Electric Furnace Ferronickel Slag Sand and Ferronickel Slag Powder. Materials Reports, vol. 33, no. 11, p. 3752-3756.
[36] Marieta C., Guerrero A., Leon I., 2021. Municipal solid waste incineration fly ash to produce eco-friendly binders for sustainable building construction. Waste Management, vol. 120, p. 114-124.
[37] McDonald, L.J., Carballo-Meilan, M.A., Chacartegui, R., Afzal, W., 2022. The physicochemical properties of Portland cement blended with calcium carbonate with different morphologies as a supplementary cementitious material. Journal of Cleaner Production, vol. 338, 130309.
[38] Thommes M., Kaneko K., Neimark A.V., Olivier J.P., Rodriguez-Reinoso F., Rouquerol J., Sing K.S.W., 2015. Physisorption of gases, with special reference to the evaluation of surface area and pore size distribution (IUPAC Technical Report). Pure and Applied Chemistry, vol. 87, no. 9-10, p. 1051-1069.
[39] Mantellato S., Palacios M., Flatt R.J., 2015. Reliable specific surface area measurements on anhydrous cements. Cement and Concrete Research, vol. 67, p. 286-291.
[40] Chen C.G., Sun C.J., Gau S.H., Wu C.W., Chen Y.L., 2013. The effects of the mechanical-chemical stabilization process for municipal solid waste incinerator fly ash on the chemical reactions in cement paste. Waste Management, vol. 33, p. 858-865.
[41] Zhang, S.P., Ghouleh, Z., He, Z., Hu, L.L., Shao, Y.X., 2021. Use of municipal solid waste incineration bottom ash as a supplementary cementitious material in dry-cast concrete. Construction and Building Materials, vol. 266, 120890.
[42] Wang, D.Q., Wang, Q., 2022. Clarifying and quantifying the immobilization capacity of cement pastes on heavy metals. Cement and Concrete Research, vol. 161, 106945.

CIVIL ENGINEERING JOURNAL

Article no. 10

THE CIVIL ENGINEERING JOURNAL 1-2026

FINITE ELEMENT ANALYSIS OF BONDED PRESTRESSED STRENGTHENED HOLLOW SLAB BEAMS

Xilong Zheng

School of Intelligent and Architectural Engineering, Harbin University, No.109 Zhongxing Road, Harbin, Heilongjiang Province, China; Zhengxilong88@163.com

Received: *28.05.2025*

Received in revised form: *21.01.2026*

Accepted: *19.03.2026*

ABSTRACT

With the continuous increase in traffic loads, the insufficient bearing capacity of existing bridges has become increasingly prominent, necessitating effective strengthening technologies to enhance their performance. This study focuses on bonded prestressed strengthened hollow slab beams. A finite element analysis method was employed to establish a discrete model comprising concrete (SOLID65 elements), composite mortar (SHELL41 elements), and prestressed tendons (LINK8 elements), with nonlinear spring elements used to simulate the interaction at the bonding layer. A three-point loading method was adopted to analyze the stress distribution characteristics of the strengthened beam under 10 kN and 80 kN loads, with emphasis on the stress responses in the anchorage zone, mid-span cross-section, and reinforcement. The results indicate significant stress concentration in the anchorage zone, requiring reinforcement in engineering design. When the cross-section approaches the destressed state (stress range: 0.1 MPa to -0.2 MPa), there is a notable discrepancy between finite element simulation results and material mechanics theoretical values. However, good agreement is observed in non-destressed states. Additionally, the stress variation trend of prestressed tendons under increasing loads aligns with theoretical predictions, with an error margin below 0.8%. This research provides theoretical and numerical references for the engineering application of bonded prestressed strengthening techniques.

KEYWORDS

Bonded prestressing, Hollow slab beams, Finite element analysis, Stress distribution, Strengthening technology, ANSYS simulation

INTRODUCTION

With rapid socio-economic development and improved living standards, vehicle load capacities and traffic volumes have significantly increased, leading to substantial increases in highway bridge loads [1,2]. However, bridges constructed in China's early years have low bearing capacities due to technological limitations, and prolonged use has exacerbated their deterioration [3]. In recent years, even newly constructed bridges have exhibited varying degrees of damage after years of operation, severely impacting transportation and economic development [4,5]. Therefore, strengthening damaged bridges to enhance their load-bearing capacities is crucial for maintaining their functionality.

Section enlargement is a common bridge strengthening method. It involves removing damaged or loose parts of the structure and recasting concrete to expand the compression zone, thereby improving bending resistance, crack resistance, and stiffness [6-8]. While this method minimizes traffic disruption by working beneath the bridge, it faces constraints in special geographical or structural conditions, leading to increased costs, prolonged construction periods, and traffic impacts. Moreover, enlarging the section increases structural self-weight, potentially reducing load-bearing capacity [9-12].

Externally bonded reinforcement methods, such as attaching steel plates or high-strength materials (e.g., carbon fiber) to the surfaces of bridge components, enhance load-bearing capacity with minimal weight impact. These methods improve bending performance, control crack propagation, and enhance durability. However, issues like stress lag and adhesive quality limitations restrict their applicability [13-17].

Active strengthening techniques, such as prestressing, effectively utilize materials and mitigate strain lag effects inherent in passive methods [18-21]. Bonded prestressed composite mortar steel strand systems offer advantages such as convenient tensioning, simple anchorage, and high durability, making them widely recognized in engineering. While experimental studies on bonded prestressed hollow slab beams exist, finite element simulations remain limited. This study conducts a full-scale finite element simulation of a hollow slab beam to analyze stress distributions under varying loads and compares results with material mechanics theoretical values.

FINITE ELEMENT MODEL ESTABLISHMENT

An 8-meter full-scale beam model was simulated based on actual engineering parameters (Figure 1), incorporating eight prestressed steel strands. A discrete model was established using constraint equations. Schematic diagram of the anchoring system for hollow plate reinforcement is shown in Figure 2.

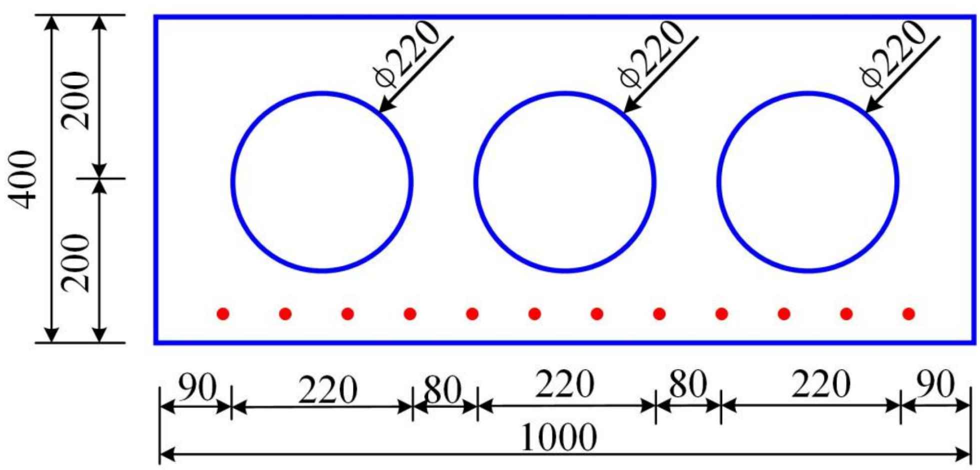

Fig. 1 - Cross-sectional Schematic of the 8 m Hollow Slab Beam (mm)

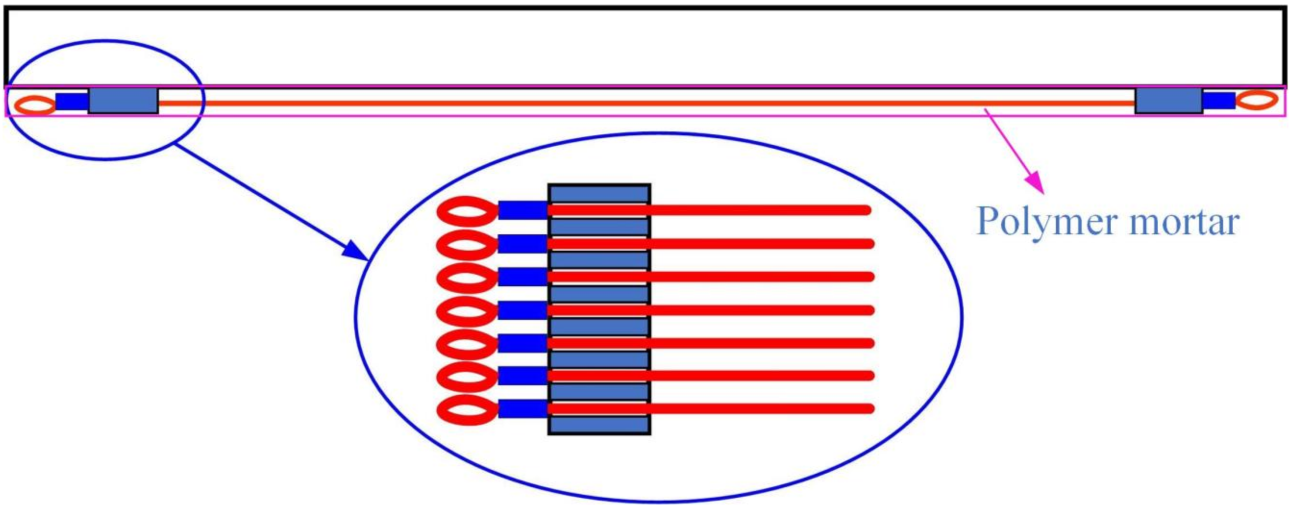

Fig. 2 - Schematic Diagram of the Anchoring System for Hollow Slab Reinforcement

Concrete was modelled using SOLID65 elements, composite mortar with SHELL41 elements, and reinforcement/prestressed tendons with LINK8 elements. In ANSYS, beam and truss elements are represented by two-node lines, requiring manual input of cross-sectional properties (e.g., area, inertia). The standard value of the compressive strength of concrete is 40 MPa.

The yield strength of ordinary steel bars is 335 MPa, and their elastic modulus is 200 GPa steel wire ropes with a moderate diameter of 4 mm were selected, offering high strength, low creep rate, and adequate ductility. The ropes possess a cross-sectional area of 10.55 mm², an ultimate tensile stress of 1200 MPa, an ultimate tensile strain of 0.02, and an elastic modulus of 130 GPa.

Meshing for composite mortar and concrete utilized element sizes of approximately 50 mm × 50 mm × 125 mm. The finite element model is shown in Figures 3–4. Full displacement compatibility between reinforcement and concrete was assumed, neglecting slippage.

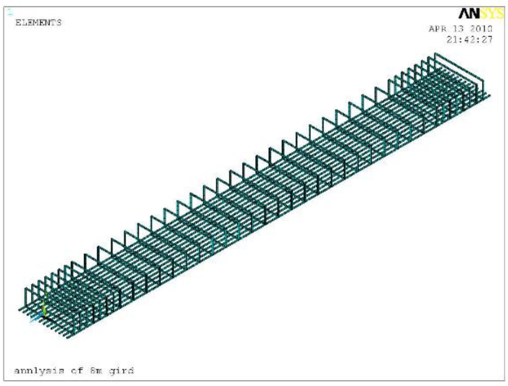

Fig. 3 - Reinforcement Simulation

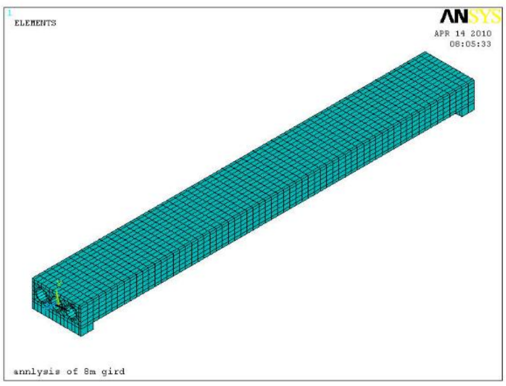

Fig. 4 - Meshing Results

Composite mortar-concrete interaction was modelled using nonlinear spring elements (CONBIN39) in three directions: normal (perpendicular to the interface), longitudinal shear (parallel to beam length), and transverse shear (perpendicular to beam length) (Figures 5–6). To achieve pure bending at mid-span, three-point loading was applied at 2.5 m from the supports. Surface loads and support pads were used to improve convergence.

DOI 10.14311/CEJ.2026.01.0010

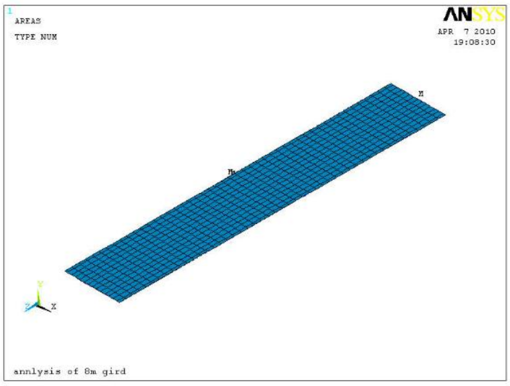

Fig. 5 - Composite Mortar Simulation

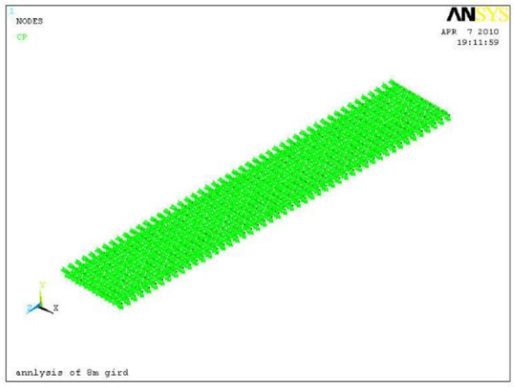

Fig. 6 - Spring Element Simulation

STRESS ANALYSIS UNDER THREE-POINT LOADING

Post-processing extracted displacements, stresses, strains, and deformations. Stress analyses under 10 kN and 80 kN loads (excluding self-weight) are detailed below.

Stress Analysis Under 10 kN Load

1) Global Stress Distribution

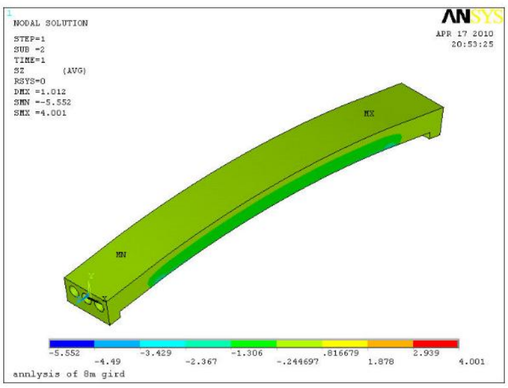

Fig. 7 - Global Equivalent Stress Contour (MPa)

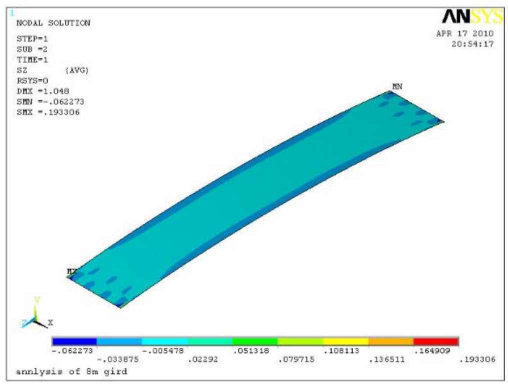

Fig. 8 - Composite Mortar Equivalent Stress Contour (MPa)

Maximum tensile stress (4.00 MPa) occurred at the bottom anchorage zone, while minimum stress (5.55 MPa) appeared near the top at 1/3 span from supports. Stress concentration in the anchorage zone necessitates localized reinforcement.

2) Cross-Sectional Stress Analysis

Z-direction stress contours at 1/8, 1/4, 3/8, and mid-span sections are shown in Figures 8–11. Under 10 kN, tensile stresses (0.17–0.24 MPa) increased toward mid-span, while compressive stresses (0.66–1.29 MPa) dominated the bottom. Complex stresses were observed at 1/8 span due to anchorage effects.

DOI 10.14311/CEJ.2026.01.0010

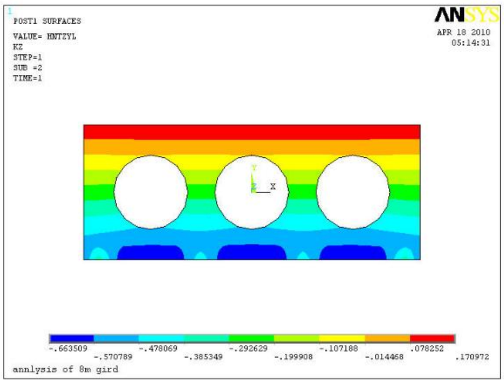

Fig. 9 - 1/8 Section Z-Direction Stress Contour (MPa)

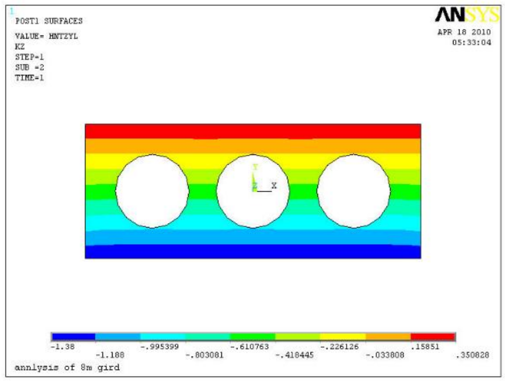

Fig. 10 - 2/8 Section Z-Direction Stress Contour (MPa)

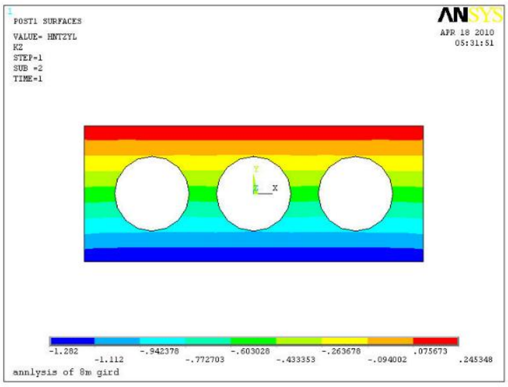

Fig. 11 - 3/8 Section Z-Direction Stress Contour (MPa)

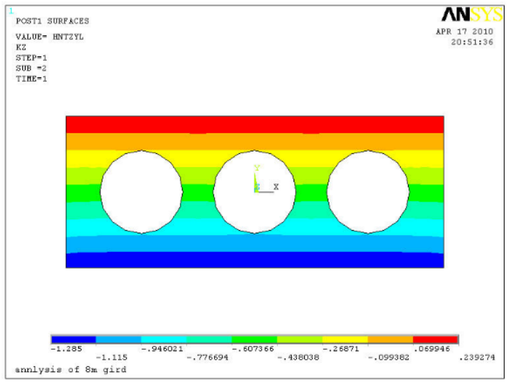

Fig. 12 - Mid-Span Section Z-Direction Stress Contour (MPa)

In ANSYS, the system defaults to tensile stress as positive and compressive stress as negative. As shown in Figures 9-12, under a total load of 10 kN (excluding beam dead load), the sections from the 1/8-span to mid-span exhibit tensile stress, varying from 0.17 MPa to 0.24 MPa. Conversely, the beam bottom sections show compressive stress, ranging from 0.66 MPa to 1.29 MPa. At the 1/8-span section, stress distribution is more complex due to the anchor device effect.

DOI 10.14311/CEJ.2026.01.0010

3) Main Reinforcement Stress Analysis

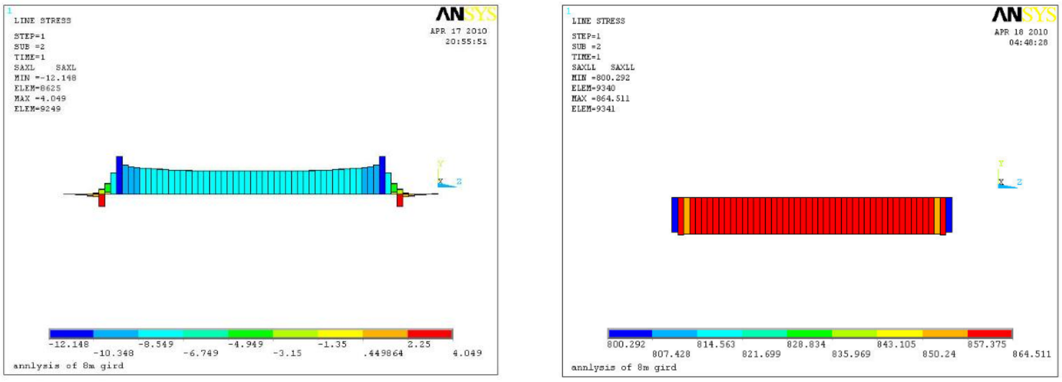

(a) Ordinary Reinforcement Stress Diagram

(b) Prestressed Reinforcement Stress Diagram

Fig. 13 - Stress Contour of Internal Reinforcement in Post-Strengthened Beam (MPa)

Figure 13 illustrates the stress contour of internal reinforcement in a post-strengthened beam under a concentrated load of 10 kN. As shown in the diagram, the maximum stress of ordinary reinforcement occurs in the mid-span region, reaching 5.76 MPa under tension. Conversely, the minimum stress of ordinary reinforcement, measured at 12.15 MPa under compression, appears between the concentrated force application point and the support. Additionally, the stress of prestressed reinforcement in the mid-span region is recorded as 864.51 MPa.

Stress Effect Analysis of the Beam Under 80 kN Load Application

1) Integral Beam Stress Analysis

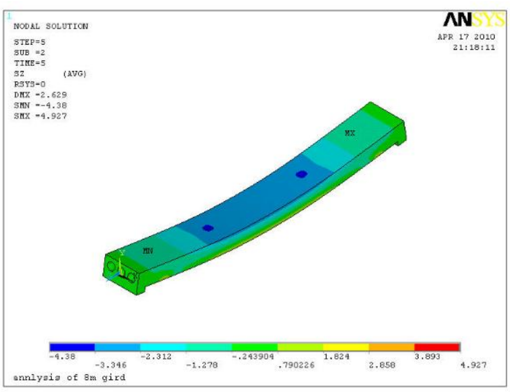

Fig. 14 - Integral Beam Equivalent Stress Contour (MPa)

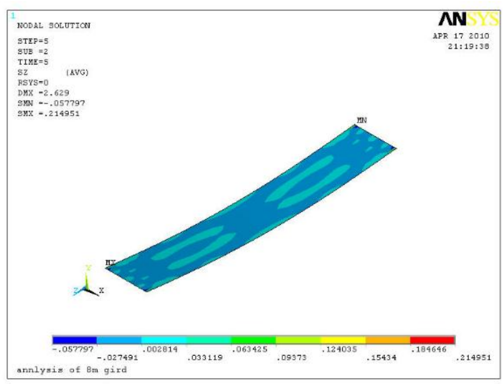

Fig. 15 - Composite Mortar Equivalent Stress Contour (MPa)

As shown in Figure 14, under the applied load, the integral beam exhibits maximum tensile stress (4.93 MPa) at the bottom anchorage region and maximum compressive stress (4.38 MPa) at the top slab, located 1/3 span away from the support. The primary cause of the maximum tensile stress is excessive local stress concentration at the anchorage point. Figure 15 presents the equivalent stress contour of composite mortar, where maximum tensile stress also appears in the anchorage region. This indicates that the anchorage zone is a structural weakness requiring localized reinforcement design in engineering strengthening.

DOI 10.14311/CEJ.2026.01.0010

2) Main Beam Stress Analysis at Calculated Sections

Z-direction stress contours were extracted for the 1/8-span, 2/8-span, 3/8-span, and mid-span sections of the main beam, as illustrated in Figures 15-18.

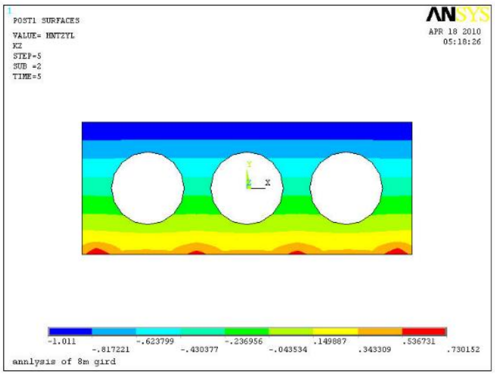

Fig. 16 - Z-Direction Stress Contour of the 1/8-Span Section (MPa)

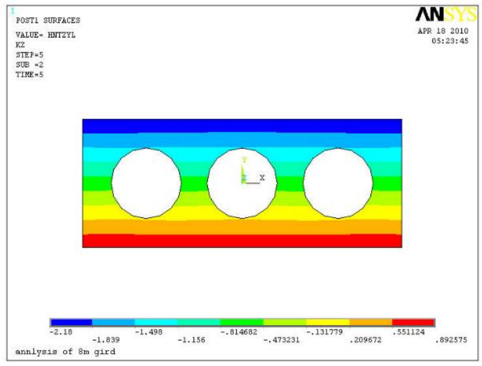

Fig. 17 - Z-Direction Stress Contour of the 2/8-Span Section (MPa)

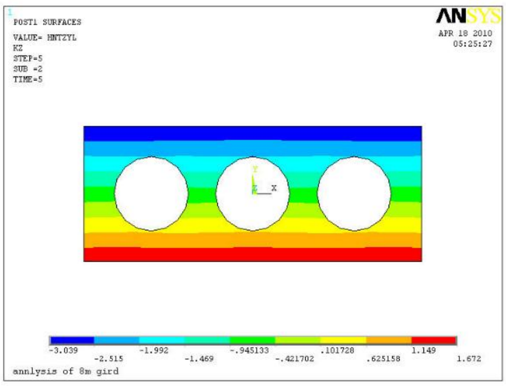

Fig. 18 - Z-Direction Stress Contour of the 3/8-Span Section (MPa)

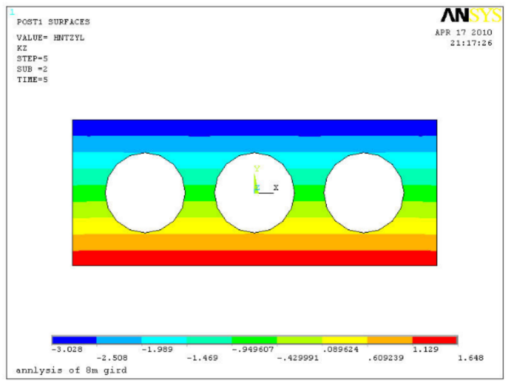

Fig. 19 - Z-Direction Stress Contour of the Mid-Span Section (MPa)

In ANSYS, tensile stress is defined as positive by default, while compressive stress is negative. As observed in Figures 16-19, under a total load of 80 kN, compressive stresses (excluding self-weight and dead loads of the main beam) are observed across sections from the 1/8-span to mid-span, ranging from 1.01 MPa to 3.03 MPa. Tensile stresses are observed at the beam bottom sections, ranging from 0.73 MPa to 1.65 MPa. At the 1/8-span section, stress distribution is more complex due to the influence of anchorage devices.3) Main Reinforcement Stress Analysis

DOI 10.14311/CEJ.2026.01.0010

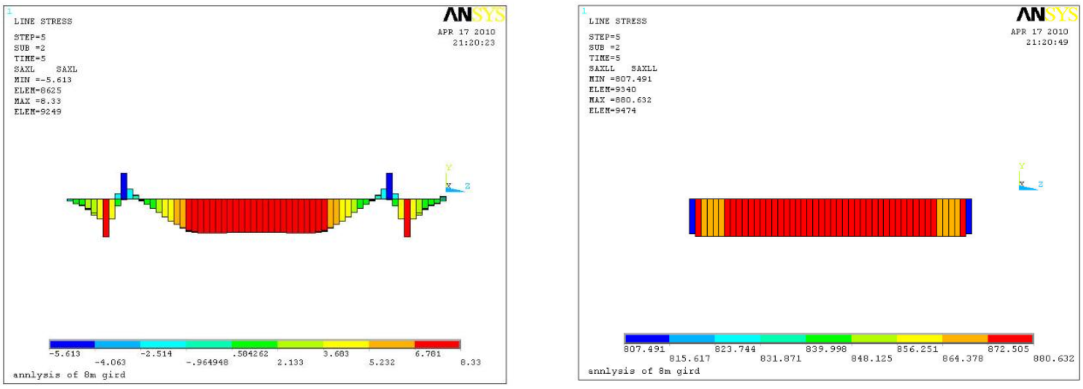

(a) Stress Contour of Ordinary Reinforcement *(b) Stress Contour of Prestressed Reinforcement*

Fig. 20 - Stress Contour of Internal Reinforcement in Post-Strengthened Beam (MPa)

Figure 20 illustrates the internal reinforcement stress distribution in the post-strengthened beam under an 80 kN concentrated load. As shown in the figure, the maximum tensile stress of ordinary reinforcement occurs in the mid-span region, reaching 8.33 MPa, while the minimum compressive stress (5.61 MPa) is observed in the 1/8-span region. The prestressed reinforcement at mid-span exhibits a stress level of 880.63 MPa.

COMPARATIVE ANALYSIS BETWEEN ANSYS-CALCULATED VALUES AND THEORETICAL SOLUTIONS FROM MECHANICS OF MATERIALS

To validate the accuracy of numerical simulations, stress values calculated via solid element simulations at the mid-span section were compared with analytical results derived from mechanics of materials under applied loads of 10 kN, 20 kN, 40 kN, 60 kN, and 80 kN. Detailed computational data are provided in Table 1 and Table 2.

Tab. 1 - Post-Strengthened Beam Concrete Stress Calculation Results (MPa)

Load kN	Calculated Section Top Edge Stress				Calculated Section Bottom Edge Stress			
	Theoretical Value from Mechanics of Materials	Solid Element Simulation Value	Difference Between Simulation and Theory	Percentage Difference (%)	Theoretical Value from Mechanics of Materials	Solid Element Simulation Value	Difference Between Simulation and Theory	Percentage Difference (%)
10	-0.30	-0.24	0.06	19.8	1.35	1.29	-0.06	4.7
20	0.19	0.23	0.04	22.7	0.92	0.87	-0.05	5.7
40	1.13	1.16	0.03	2.8	0.08	0.03	-0.05	66.3
60	2.09	2.10	0.01	0.2	-0.76	-0.81	-0.05	6.6
80	3.05	3.03	-0.02	0.7	-1.61	-1.65	-0.04	2.4

DOI 10.14311/CEJ.2026.01.0010

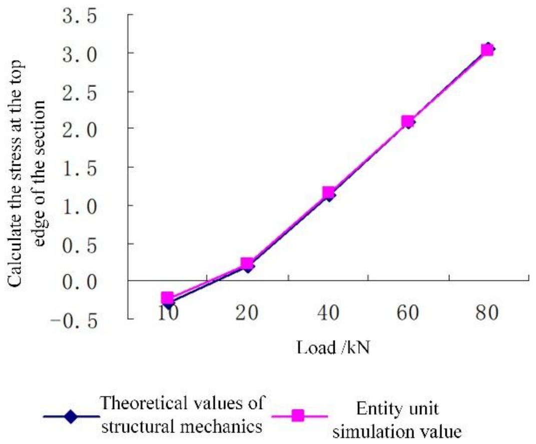

Fig. 21 - Post-Strengthened Beam Top Edge Stress Under Varying Load Levels

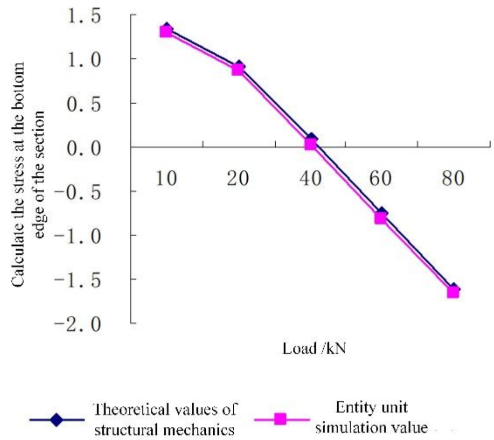

Fig. 22 - Post-Strengthened Beam Bottom Edge Stress Under Varying Load Levels

Figures 21 and 22 depict the top/bottom edge stresses at the mid-span section of the post-strengthened beam under varying load levels. As shown, discrepancies exist between solid element simulation results and theoretical solutions from mechanics of materials, with the magnitude of differences progressively decreasing as load intensity increases. This phenomenon primarily arises from the inherent assumptions embedded in classical mechanics of materials theories, such as the plane section assumption and homogeneous material assumption, which derive sectional stresses through inverse calculation of member bending moments. In contrast, solid element simulations adhere to finite element principles by directly capturing internal force distributions at discrete locations through structural behavior modeling. Consequently, theoretical deviations are inevitable between these two methodologies. The application of solid element modeling enables refined structural analysis by accounting for localized stress variations and complex geometric/material interactions.

Tab. 2 - Post-Strengthened Beam Reinforcement Stress Calculation Results (MPa)

Load kN	Calculated Section Top Edge Stress				Calculated Section Bottom Edge Stress			
	Theoretical Value from Mechanics of Materials (MPa)	Solid Element Simulation Value (MPa)	Difference Between Simulation and Theory (MPa)	Percentage Difference (%)	Theoretical Value from Mechanics of Materials (MPa)	Solid Element Simulation Value (MPa)	Difference Between Simulation and Theory (MPa)	Percentage Difference (%)
10	6.00	5.76	-0.24	4.0%	-863.09	-864.51	-1.423	0.2%
20	3.49	3.27	-0.22	6.3%	-866.58	-865.76	0.814	0.1%
40	-0.08	-0.13	-0.05	62.5%	-873.55	-869.05	4.504	0.5%
60	-4.88	-5.08	-0.20	4.0%	-880.53	-874.84	5.689	0.6%
80	-10.84	-11.08	-0.24	2.2%	-887.50	-880.63	6.868	0.8%

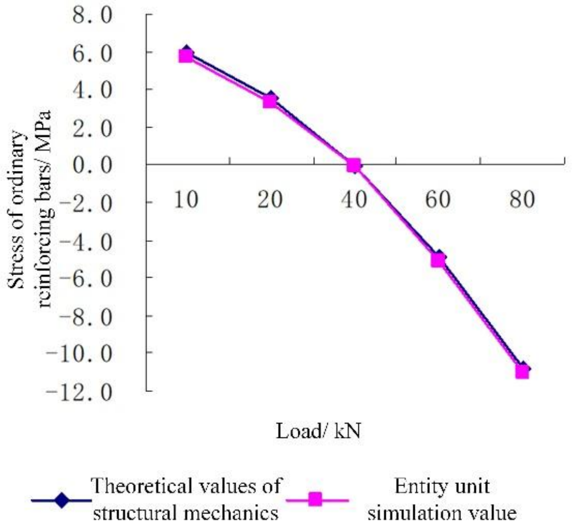

Fig. 23 - Post-Strengthened Beam Ordinary Reinforcement Stress Under Varying Load Levels

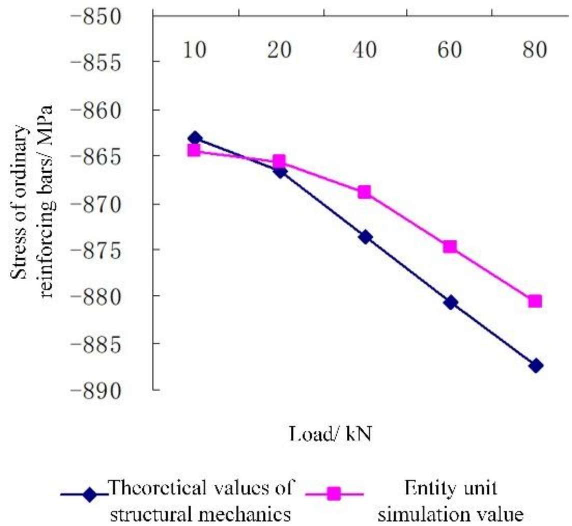

Fig. 24 - Post-Strengthened Beam Prestressed Reinforcement Stress Under Varying Load Levels

Figures 23 and 24 illustrate the stress variations of ordinary reinforcement and prestressed reinforcement, respectively, in the post-strengthened beam under varying load levels. Observations reveal that at lower load magnitudes, the discrepancy between solid element simulation results and theoretical values from mechanics of materials for ordinary reinforcement remains relatively small. However, as load intensity increases, the deviation for prestressed reinforcement stress exhibits a progressive growth trend, though the percentage difference remains minimal (0.1%–0.8%).

Correlation analysis with Table 1 and Table 2 data reveals notable discrepancies between calculation methods under specific loading conditions. At 20 kN total load, the mid-span top edge concrete compressive stress exhibits significant variation: 0.185 MPa (theoretical) vs. 0.23 MPa (simulation). Similarly, at 40 kN total load, the mid-span ordinary reinforcement tensile stress shows marked divergence: 0.08 MPa (theoretical) vs. 0.13 MPa (simulation). These phenomena stem from the beam's stress state transition: at 20 kN, the top edge approaches stress neutralization (zero stress), while at 40 kN, the bottom edge enters stress neutralization. Consequently, when sectional stresses range between 0.1 MPa (tension) and -0.2 MPa (compression) during stress neutralization transitions, the two calculation methodologies produce pronounced discrepancies due to the complexity of stress redistribution. Conversely, when sectional stresses are from the neutralization state (i.e., at higher stress magnitudes), both calculation methods demonstrate consistent results.

COMPARATIVE ANALYSIS OF FINITE ELEMENTS BEFORE AND AFTER REINFORCEMENT

In order to clearly understand the improvement effect of the beam reinforced with bonded prestress, studies were conducted on the unreinforced beam, the beam reinforced with 8 prestressed steel strands, and the beam reinforced with 12 prestressed steel strands. The mid-span section was simulated using solid elements and the calculated values were compared with the theoretical values based on material mechanics under loads of 10kN, 20kN, 40kN, 60kN, and 80kN. The specific calculation values are shown in Tables 3 and 4. The top edge concrete stress and bottom edge steel bar stress before and after reinforcement are shown in Figures 25 and 26.

DOI 10.14311/CEJ.2026.01.0010

Tab. 3 - Top Edge Stress Results Before and After Reinforcement (MPa)

Load kN	Calculated Section Top Edge Stress				
	Unstrengthened	Strengthened with 8 prestressed steel strands	Percentage Difference (%)	Strengthened with 12 prestressed steel strands	Percentage Difference (%)
10	0.57	-0.24	-141.9%	-0.87	-253.2%
20	1.36	0.23	-83.3%	-0.12	-109.0%
40	2.54	1.16	-54.3%	0.88	-65.4%
60	2.97	2.10	-29.5%	1.56	-47.4%
80	4.32	3.03	-29.9%	2.20	-49.2%

Tab. 4 - Steel Bar Stress Results Before and After Reinforcement (MPa)

Load kN	Calculated Steel Bar Stress				
	Unstrengthened	Strengthened with 8 prestressed steel strands	Percentage Difference (%)	Strengthened with 12 prestressed steel strands	Percentage Difference (%)
10	-1.02	5.76	-664.7%	6.25	-712.8%
20	-4.37	3.27	-174.8%	5.37	-222.9%
40	-6.28	-0.13	-97.9%	2.64	-142.1%
60	-14.36	-5.08	-64.6%	-1.73	-88.0%
80	-22.59	-11.08	-51.0%	-5.65	-75.0%

From Table 3 and Figure 25, it can be seen that when the load is 20kN, the compressive stress at the top edge of the 8 prestressed steel strand reinforced beam is 0.23 MPa, which is 83.3% lower than that of the un-reinforced beam, indicating that the application of prestress reduces the tensile stress generated at the top edge during the loading process and thereby lowers the top edge pressure. The tensile stress of the top edge concrete of the 12 prestressed steel strand reinforced beams is -0.12 MPa, indicating that with the increase in the number of prestressed steel strands, the tensile stress of the top edge concrete increases, but it is still under tension at this time. When the load is 80kN, the compressive stress of the 8 prestressed steel strand reinforced beams is 3.028MPa, which is 29.9% lower than the compressive stress of the top edge concrete of the un-reinforced beam. The compressive stress of the top edge concrete of the 12 prestressed steel strand reinforced beams is 19.3% lower than that of the 8 prestressed steel strand reinforced beams, indicating that with the increase in the number of prestressed steel strands, the compressive stress at the top edge decreases.

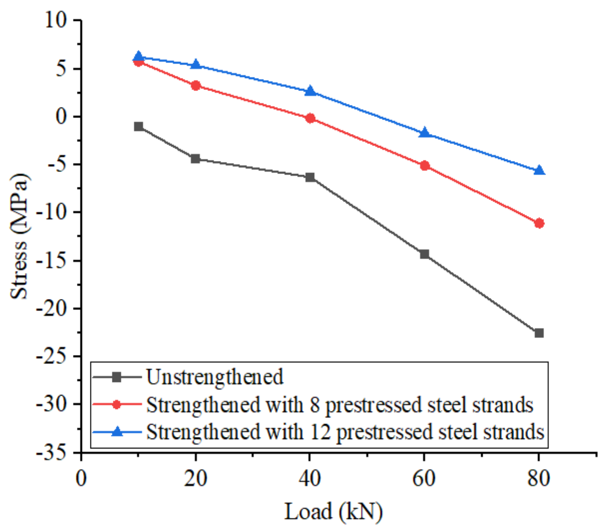

Fig. 25 - Stress of the top edge concrete under different loads

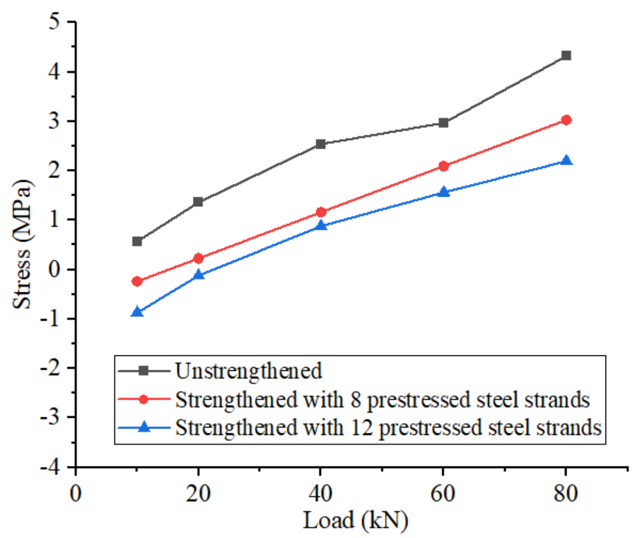

Fig. 26 - Stress of ordinary reinforcing bars under different loads

From Table 4 and Figure 26, it can be seen that when the load is 20 kN, the tensile stress of the unreinforced beam is -4.37 MPa, and the bottom edge compressive stress of the 8 prestressed steel strand reinforced beams is 3.27 MPa. This indicates that the application of prestress causes compressive stress at the bottom edge of the beam. The compressive stress of the bottom edge of the 12 prestressed steel strand reinforced beams is 48.1% higher than that of the 8 prestressed steel strand reinforced beams, indicating that as the number of prestressed steel strands increases, the compressive stress at the bottom edge increases. When the load is 80 kN, the tensile stress of the 8 prestressed steel strand reinforced beams' steel bars is -11.08 MPa, which is 51.0% lower than that of the unreinforced beam. The tensile stress of the bottom edge steel bars of the 12 prestressed steel strand reinforced beams is 24.0% lower than that of the 8 prestressed steel strand reinforced beams, indicating that as the number of prestressed steel strands increases, the compressive stress at the top edge decreases.

In order to clearly understand the improvement effect of the beam reinforced with bonded prestress, studies were conducted on the unreinforced beam, the beam reinforced with 8 prestressed steel strands, and the beam reinforced with 12 prestressed steel strands. The mid-span section was simulated using solid elements and the calculated values were compared with the theoretical values based on material mechanics under loads of 10kN, 20 kN, 40 kN, 60 kN, and 80 kN. The crack width before and after reinforcement are shown in Figures 25 and 26.

Tab. 5 - Crack Width Before and After Reinforcement (mm)

Load kN	Calculated Steel Bar Stress				
	Unstrengthen	Strengthened with 8 prestressed steel strands	Percentage Difference (%)	Strengthened with 12 prestressed steel strands	Percentage Difference (%)
10	0	0	/	0	/
20	0	0	/	0	/
40	0.03	0	-100%	0	-100%
60	0.07	0.02	-71.4%	0	-100%
80	0.15	0.06	-60.0%	0.04	-73.3%

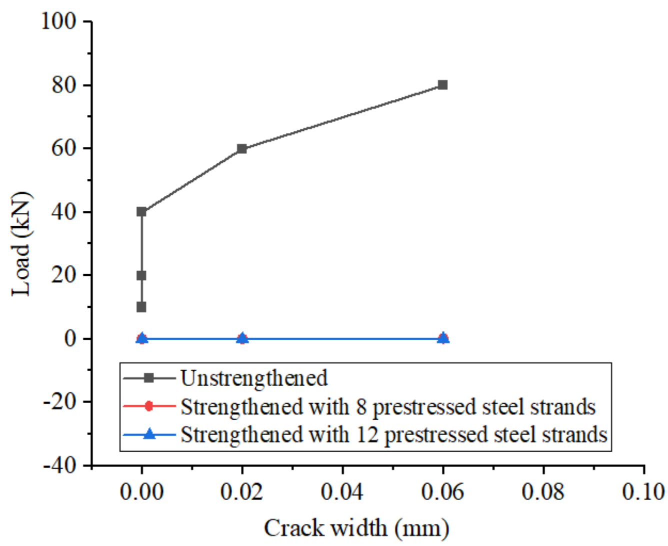

Fig. 27 – Crack width under different loads

From Table 5 and Figure 27, it can be seen that when the load is 20kN, Neither the reinforced beams nor the un-reinforced beams showed any cracks, indicating that the beams were still in the elastic working stage at this point. When the load is 40kN, the crack width of the unreinforced beam is 0.03mm, while the reinforced beam does not crack. When the load is 60kN, the crack width of the unreinforced beam is 0.07mm, and the crack width of the 8 prestressed steel strand reinforced beam is 0.02mm, while the 12 prestressed steel strand reinforced beams do not crack. When the load is 80kN, the crack width of the unreinforced beam is 0.15mm, the crack width of the 8 prestressed steel strand reinforced beam is 0.06mm, and the crack width of the 12 prestressed steel strand reinforced beam is 0.04mm, indicating that the prestressed steel strand reinforcement can effectively delay the appearance of cracks and limit the expansion of cracks.

STRESS ANALYSIS OF REINFORCED BEAMS

For components that have been reinforced by certain means, when considering the combined section bearing live loads, and fully taking into account the effect of the added reinforcing materials, the calculation of the section stress should still be based on the cracked section of the component.

The calculation of the section stress is to calculate the geometric characteristic values of the converted section of the combined section after reinforcement based on the cracked section, and then calculate according to the relevant formulas in material mechanics. Finally, the stress calculated at each stage needs to be superimposed to obtain the final result.

According to the force analysis, the concentrated load and the bending moment caused by the live load generated by the prestressed reinforcement will increase the compressive stress in the compression zone at the top of the original beam, while the bending moment generated by the prestressed reinforcement will reduce the compressive stress in the compression zone. The concentrated load and the bending moment generated by the prestressed reinforcement will reduce the tensile stress of the main reinforcement of the original beam, while the standard value of the bending moment caused by the live load will also reduce the tensile stress of the main reinforcement. Stress calculation diagram for the main section is shown in Figure 28. Strain calculation diagram for the main section under the ultimate state is shown in Figure 29.

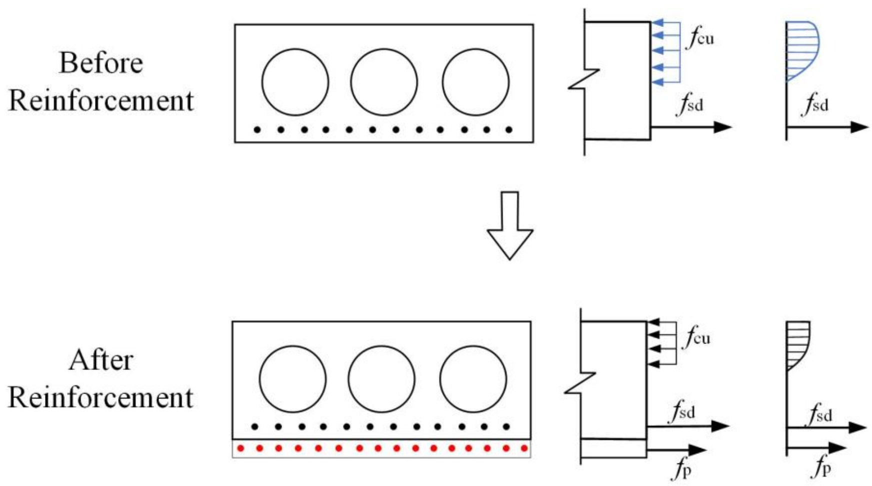

Fig. 28 – Stress calculation diagram for the main section

After the reinforcement of the beam with load, both the stress and strain will change. To simplify the calculation, the final strain is divided into two parts: before reinforcement and the ultimate state. ε_{c2} is taken as the strain increment of the concrete compression zone at the upper edge from before reinforcement to the ultimate state, and ε_{s2} is taken as the strain increment of the main reinforcement of the original beam from before reinforcement to the ultimate state. The stress calculation diagram of the reinforced beam under the ultimate state is shown below.

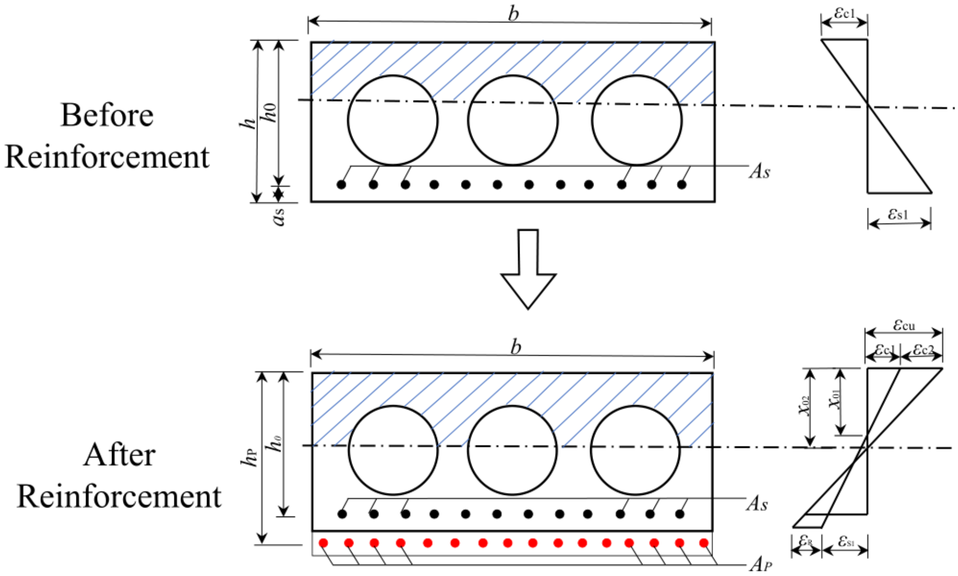

Fig. 29 Strain calculation diagram for the main section under the ultimate state:

$$\xi_b = \frac{\beta\varepsilon_{cu}}{\varepsilon_{s1} + \varepsilon_{s2} + \varepsilon_{cu}} \tag{1}$$

$$\varepsilon_{s2} = \frac{h_0}{h_p}\left(\varepsilon_R + \varepsilon_{c2}\right) - \varepsilon_{c2} \tag{2}$$

$$\varepsilon_R = \frac{\sigma_R - \sigma_{con}}{E_R} \tag{3}$$

In the formula:

ε_R — Strain after adding prestressed reinforcement;

σ_{con} — Control of prestressed reinforcement tensioning for controlling prestress;

σ_R — The stress of the post-installed reinforcement in the ultimate state;

E_R — The elastic modulus after adding reinforcing bars;

h_P — The distance from the combined action point of the prestressed reinforcing bars to the compressive edge of the section.

CONCLUSION

This paper introduces a numerical analysis methodology for finite element simulation of bonded prestressed reinforcement systems, analyzing the stress distribution in post-strengthened beams under varying load levels and comparing results with theoretical solutions from mechanics of materials. The key conclusions are summarized as follows:

(1) ANSYS enables accurate simulation of bonded prestressed reinforcement systems, particularly in beam end anchorage zones where complex stress states exist. Classical mechanics of materials theories often lack precision in such regions due to localized stress concentrations, necessitating the use of solid element modeling for detailed analysis at beam end sections.

DOI 10.14311/CEJ.2026.01.0010

(2) When the calculated section approaches stress neutralization (0.1 MPa tension to -0.2 MPa compression), significant discrepancies arise between finite element simulation results and theoretical predictions. This phenomenon stems from the complex stress redistribution occurring at sectional edges during neutralization transitions, where conventional theoretical assumptions fail to capture localized stress variations.

(3) At mid-span sections under non-neutralized stress states, solid element simulations and theoretical calculations demonstrate good agreement. For routine engineering design where sections operate away from neutralization conditions, classical mechanics of materials theories provide sufficiently accurate results with acceptable computational efficiency.

REFERENCE

[1] Li X, Wu G, Popal M S,. 2018. Experimental and numerical study of hollow core slabs strengthened with mounted steel bars and prestressed steel wire ropes. Construction and Building Materials, 2018, 188: 456-469. ISSN: 0950-0618, https://doi.org/10.1016/j.conbuildmat.2018.08.073

[2] Wang Z, Wang M, Xu Q,. 2021. Experimental research on prestressed concrete hollow-core slabs strengthened with externally bonded bamboo laminates. Engineering Structures, vol. 244, p. 112786. ISSN: 0141-0296, https://doi.org/10.1016/j.engstruct.2021.112786

[3] Yang J, Hou P, Pan Y,. 2021. Shear behaviors of hollow slab beam bridges strengthened with high-performance self-consolidating cementitious composites. Engineering Structures, vol. 242, p.112613. ISSN: 0141-0296, https://doi.org/10.1016/j.engstruct.2021.112613

[4] Yang J, Guo H, Yang C,. 2024. Experimental investigation and evaluation of shear performance of hollow slab beams strengthened by cavity grouting method. Case Studies in Construction Materials, vol. 20, p. e03184. ISSN: 2214-5095, https://doi.org/10.1016/j.cscm.2024.e03184

[5] Li X H, Wu G, Wang S,. 2019. Flexural behavior of hollow-core slabs strengthened with prestressed basalt FRP grids. Journal of Composites for Construction, vol. 23, n. 3, p. 04019016. ISSN: 1090-0268, https://doi.org/10.1016/j.cscm.2024.e03184

[6] Pachalla S K S, Prakash S S,. 2027. Load resistance and failure modes of GFRP composite strengthened hollow core slabs with openings. Materials and Structures, vol. 50, p. 1-14. ISSN: 1359-5997, https://doi.org/10.1617/s11527-016-0883-8

[7] Song S, Deng M, Zhang Y,. 2024. Effects of textile type on the flexural properties of prefabricated hollow-core slabs strengthened with PVA fibers-improved TRM. Journal of Building Engineering, vol. 87, p. 109103. ISSN: 2352-7102, https://doi.org/10.1016/j.jobe.2024.109103

[8] Zhang H, Huang W, Liu B,. 2022. Flexural behavior of precast concrete hollow-core slabs with high-strength tendons. Journal of Building Engineering, vol. 59, p. 105050. ISSN: 2352-7102, https://doi.org/10.1016/j.jobe.2022.105050

[9] Di J, Sun Y, Yu K,. 2020. Experimental investigation of shear performance of existing PC hollow slab. Engineering Structures, vol. 211, p. 110451. ISSN: 0141-0296, https://doi.org/10.1016/j.engstruct.2020.110451

[10] Chen X, Ma Q,. 2024. Experimental study on the flexural performance of concrete hollow composite slabs with tightly connected panel sides. Scientific Reports, vol. 14, n. 1, p. 20784. ISSN: 2045-2322, https://doi.org/10.1038/s41598-024-71880-8

[11] Elharouney O, Elkateb M, Khalil A,. 2021. Behaviour of prestressed hollow core slabs strengthened with NSM CFRP strips around openings: A finite element investigation. Engineering Structures,vol. 238, p. 112262. ISSN: 0141-0296, https://doi.org/10.1016/j.engstruct.2021.112262

[12] Badran H, Alkloub A,. 2025. Strengthening of precast pretensioned hollow core slabs exposed to fire. Journal of Structural Integrity and Maintenance, vol. 10, n. 1, p. 2471156. ISSN: 2470-5314, https://doi.org/10.1080/24705314.2025.2471156

[13] Zhang S, Du S, Ang Y,. 2021. Study on performance of prestressed concrete hollow slab beams reinforced by grouting with ultra-high performance concrete. Case Studies in Construction Materials, vol. 15, p. 83. ISSN: 2214-5095, https://doi.org/10.1016/j.cscm.2021.e00583

[14] Chen J, Li X, Zhu Q,. 2023. Experimental research on mechanical behavior and strengthening technologies of joints in hollow-core slab bridge. Structures, vol. 49, p. 223-239. ISSN: 2352-0124, https://doi.org/10.1016/j.istruc.2023.01.103

[15] Xun S, Shiping Y, Yuhou Y,. 2022. Comparative analysis of flexural performance of old full-scale hollow slab beams reinforced with fiber composites. Construction and Building Materials, vol. 338, p. 127657. ISSN: 0950-0618, https://doi.org/10.1016/j.conbuildmat.2022.127657

[16] Wang J, Jia Y, Zhang G,. 2018. Experimental study on prestressed concrete hollow slabs in service strengthened with prestressed CFRP plates. International Journal of Structural Integrity, vol. 9, n. 5, p. 587-602. ISSN: 1757-9864, https://doi.org/10.1108/IJSI-08-2017-0049

[17] Al-Rubaye M, Manalo A, Alajarmeh O,. 2020. Flexural behaviour of concrete slabs reinforced with GFRP bars and hollow composite reinforcing systems. Composite structures, vol. 236, p. 111836. ISSN: 0263-8223, https://doi.org/10.1016/j.compstruct.2019.111836

[18] Kankeri P, Prakash S S,. 2017. Efficient hybrid strengthening for precast hollow core slabs at low and high shear span to depth ratios. Composite structures, vol. 170, p. 202-214. ISSN: 0263-8223, https://doi.org/10.1016/j.compstruct.2017.03.034

[19] Yang L, Shen Q, Lu M,. 2025. Experimental Study on Bending Behaviors of Ultra-High-Performance Fiber-Reinforced Concrete Hollow-Core Slabs. Buildings, vol. 15, n. 5, p. 812. ISSN: 2075-5309, https://doi.org/10.3390/buildings15050812

[20] Xiao J L, Liu Y F, Feng H L,. 2025. Field tests and structural performance evaluation of existing reinforced concrete hollow slab beam bridges. Engineering Structures, vol. 333, p. 120128. ISSN: 0141-0296, https://doi.org/10.1016/j.engstruct.2025.120128